Copyright

by

Margaretha Catharina Maria Rijken

2005

The Dissertation Committee for Margaretha Catharina Maria Rijken Certifies that this is the approved version of the following dissertation:

MODELING NATURALLY FRACTURED RESERVOIRS: FROM EXPERIMENTAL ROCK MECHANICS TO FLOW SIMULATION

Committee:

Jon E. Olson, Supervisor

Jon T. Holder

Larry W. Lake

Stephen E. Laubach

Randall A. Marrett

Sanjay Srinivasan

MODELING NATURALLY FRACTURED RESERVOIRS: FROM EXPERIMENTAL ROCK MECHANICS TO FLOW SIMULATION

by

Margaretha Catharina Maria Rijken, M.S.

Dissertation

Presented to the Faculty of the Graduate School of
The University of Texas at Austin
in Partial Fulfillment
of the Requirements
for the Degree of

Doctor of Philosophy

The University of Texas at Austin
May, 2005

Dedication

To my mother: for wanting for her children what she herself never had the chance to pursue.
To my father: for his patience, presence and support.

Voor mijn moeder: omdat ze voor haar kinderen altijd wil waar ze zelf nooit de kans voor heeft gekregen.
Voor mijn vader: voor zijn geduld, aanwezigheid en ondersteuning.

Acknowledgements

I want to extend my sincerest gratitude to Dr. J.E. Olson for his support and guidance throughout my time at The University of Texas at Austin. I feel fortunate to have been his student. Likewise, I am immensely grateful to have had the pleasure to work with Dr. J. Holder, without whom no experiment would have succeeded. Furthermore, I want to extend my sincerest appreciation to my committee members, Dr. Lake, Dr. Srinivasan, Dr. Laubach, and Dr. Marrett, for answering my questions and taking the time to read and correct my dissertation.

I also would like to thank Dr. Sepehrnoori, Dr. Srinivasan and Dr. Bryant for letting me use their computer clusters. Without their generosity, large parts of this work would not exist. Furthermore, I would like to thank Glen Baum and Bob Savicki for helping me with my strange requests for equipment and always coming through with a solution. Also, I want to thank Tony Bermudez for his help with the instrument design and Greg Thompson for his advice on polishing and thin-sections.

I am grateful for all the help I received from Steve Laubach, Kitty Milliken, Astrid Makowitz, Julia Gale, Rob Reed, Leonel Gomez, and Edgar Pinzon regarding thin-section analysis and image processing. I am also extremely grateful to the FRAC consortium for allowing me to use their microscope and their image acquisition system.

I would like to extend my genuine gratitude to the entire POR team for helping me better understand the POR reservoir. Specifically, I would like to thank Fernando Cardenosa and Jason Cansler for their discussions and guidance, both during and after my summer internship.

In addition, I want to extend many thanks to Jennifer Liang, Eileen Paclibon and Precious Williams for taking time out of their schedule to help me with the extremely

boring job of cutting, polishing and grooving samples. No marble floor or granite countertop will ever look the same to them! I also want to thank F.O. Alpak, for his help with ECLIPSE, inversion, computers and more of such matters.

Furthermore, I would like to thank all my officemates for being patient with me all these years. Specifically, I would like to thank Namsu Park, who had to put up with me the most. Thank you all for your advice and above all for listening. I also want to thank Michele Cooke, who inspired me to attempt this Ph.D.

This study was made possible in large part through the FRAC consortium and through direct funding by ChevronTexaco. I am very grateful for their support and confidence.

This material is based in part on work supported by the US Department of Energy under Award No. DE-FC26-00BC15308 and by a grant from the Chemical Sciences, Geosciences and Biosciences Division, Office of Basic Energy Sciences, Office of Science, U.S. Department of Energy program "Predicting fracture porosity evolution in sandstone".

Lastly, I want to thank my extended family, Mam, Pap, Inge, Dave, Debbie, Mitch, Omer, en Wendy, in no particular order, for picking up the phone, for answering emails, for writing, and for simply being.

MODELING NATURALLY FRACTURED RESERVOIRS: FROM EXPERIMENTAL ROCK MECHANICS TO FLOW SIMULATION

Publication No._____________

Margaretha Catharina Maria Rijken, Ph.D.
The University of Texas at Austin, 2005

Supervisor: Jon E. Olson

Fractures have a big impact on reservoir production but are inherently difficult to quantify. This study gives a robust and practical workflow to obtain a mechanically consistent naturally fractured reservoir model without direct sampling of the fracture network. The three tiers of the workflow are: 1) subcritical testing, 2) geomechanical modeling, and 3) flow modeling.

Subcritical fracture index, a rock property, has been shown to influence fracture attributes such as length, spacing and connectivity. Subcritical tests show that the average subcritical index for sandstones in ambient air is around 62, whereas the average value for microstructurally comparable carbonates samples is 120. Thin-section analysis shows that an increase in cement content increases the subcritical index. Furthermore, sandstone samples containing more than 15% carbonate cement, sandstone samples containing more than 40% clay, and pure carbonate samples exhibit a large drop in subcritical index when the environment is changed from ambient air or oil to fresh water or brine.

Geomechanical modeling has shown that the mechanical bed thickness has a large influence on fracture pattern characteristics and has the potential to overshadow fracture pattern changes due to strain level, strain anisotropy and subcritical index. Furthermore, an increase in strain anisotropy reduces the number of dominant through-going fracture sets and decreases the fracture spacing between the through-going fractures. This spacing variation not only influences the preferential drainage direction, it can also enhance the drainage efficiency, because more rock is exposed to the through-going fractures which are more likely to be intersected by a borehole.

The level of detail provided by the geomechanical model greatly exceeds the level of detail normally used in reservoir simulation. Therefore, upscaling of the geomechanically generated fracture patterns is necessary for practical flow modeling. This study shows that different upscaling methods can lead to large variations in permeability prediction. A Local Grid Refinement around the well should be maintained, because it will almost always ensure accurate production prediction. This method is preferred over the dual permeability approach, which can be calibrated to match production data in some cases, but often requires using an unrealistic representation of the fracture pattern.

Table of Contents

List of Tables

List of Figures

Chapter 1 Introduction

1.1 OBJECTIVE

Many of the hydrocarbon reservoirs present in the world are naturally fractured (Aguilera, 1980; van Golf-Racht, 1982, Nelson, 1985). Better description of the fracture network characteristics, improved understanding of mechanisms controlling fracture growth, and more accurate fluid flow simulation of naturally fractured reservoirs, promises more efficient and economical production. The objective of this study is to supply a complete workflow, starting at the core scale and ending at the well scale, which can be used as a blue print to describe and model many of the naturally fractured reservoirs in the world. The three main tiers of the workflow are: 1) subcritical testing of the reservoir rock to obtain the governing rock property information (Chapter 2), 2) geomechanical modeling to create a natural fracture model of the reservoir (Chapter 3), and 3) flow modeling of the naturally fractured reservoir to obtain a production estimate (Chapter 4).

The first stage of the workflow sets out to determine the subcritical index (a rock property) from core and outcrop samples. The subcritical index has been observed to have a considerable effect on the resulting fracture pattern characteristics (Olson, 1993; Olson et al. 2001; Olson, 2004) and is, amongst others, a function of the rock's microstructure as well as the chemical environment (Atkinson and Meredith, 1987a). Therefore, Chapter 2 sets out to determine how the petrology of the sample and chemical environment influence the subcritical index value, to ultimately provide a basis for predicting changes in the subcritical index (and thus the fracture pattern) over time.

The objective of the second stage of the workflow is to determine fracture pattern attribute distributions, such as length, spacing and aperture without direct observation of the fracture pattern. In this study, a geomechanical fracture growth model as described by Olson (2004) is employed. This geomechanical model uses rock properties such as subcritical index, Poisson's ratio, Young's modulus and remote stresses/strains as input. In Chapter 3, the Point of Rocks (POR) reservoir in California is used as a field example to illustrate how to predict the fracture attributes of a naturally fractured reservoir.

Finally, after creating a suitable natural fracture model, the fracture pattern is imported into an industry standard reservoir simulator (ECLIPSE) to allow for well scale flow simulations. However, computer limitations do not allow the same level of detail as provided by the geomechanical model to be used in the flow simulations. Therefore, upscaling of the geomechanically created fracture pattern is required. Chapter 4 sets out to determine the applicability of both the industry standard dual permeability approach as well as flow based upscaling techniques, to naturally fractured reservoirs.

This first chapter supplies the background information for this study. Specifically it gives information on: 1) the type of methods used to characterize natural fracture patterns (Section 1.2), 2) the fracture laws employed (Section 1.3), and 3) the techniques used to flow-simulate fractured reservoirs (Section 1.4).

1.2 METHODS IN FRACTURE CHARACTERIZATION

Two different approaches exist to quantify fracture pattern characteristics. The first approach uses field observations (e.g. Laubach 1997; Ortega and Marrett, 2000) to quantify fracture pattern attributes. The second approach employs geomechanical principles (e.g. Bai and Pollard, 2000; Olson, 2004) to predict fracture pattern characteristics.

1.2.1 Field observations

Many different fracture pattern attribute distributions have been observed in the field and are summarized by Olson et al. (2001). These observed distributions are used as analogs for subsurface fracture patterns. Accurate prediction of the fracture distributions present in the subsurface allows for usage of these distributions in discrete flow simulations (e.g. Long et al., 1982; Andersson and Dverstorp, 1987). However, ambiguity about the representative fracture distribution complicates the selection of a suitable distribution. Rives et al. (1992) show that the fracture spacing distribution changes with the saturation level of the fracture pattern, where the saturation level is defined as the stage of joint set development. The spacing distribution is a negative exponential for young or relatively undeveloped patterns and transitions into log normal and ultimately normal as the pattern is fully saturated (Rives et al., 1992). Therefore, prediction using field observations is limited, since the underlying processes are normally not investigated, and extrapolation of the results to other regions can be problematic.

In general, large amounts of data are necessary to construct a single fracture attribute distribution, and obtaining this data can be challenging. Fracture attributes such as length, spacing and aperture are parameters important to fluid flow (e.g. Snow, 1969, 1970; Long et al., 1982; Schwartz et al., 1983; Dverstorp and Andersson, 1989; Zhang et al., 1992; Bear, 1993; Lee and Farmer, 1993; Wels and Smith, 1994; Sanderson and Zhang, 1999; Gudmundsson, 2000; Nakashima et al., 2000), but are inherently difficult to quantify. Fractures in the subsurface are predominantly vertical and vertical wells have a small probability intersecting them (Narr, 1996). Direct fracture observation in outcrop is susceptible to similar restrictions as those present in wells. Although most attributes are more easily determined in outcrop, it is rare to have the opportunity to quantify length, spacing and aperture at the same time. Fracture length determination is restricted to the size of the outcrop. Aperture is often difficult to determine due to the presence of vegetation and weathering of the fracture walls. Spacing, in general, has been the most frequently measured fracture attribute. However, like all other parameters it is restricted by the outcrop size. Moreover outcrops are not samples of the reservoir, and inadequate subsurface sampling makes it challenging to verify that a given outcrop is a good analog for a particular reservoir.

In order to circumvent this sampling problem, one approach has been to use small scale microfracture observations as analogs for larger scale fracturing (Laubach, 1997; Ortega and Marrett, 2000). In this technique, small scale fractures are used to predict large scale attributes such as orientation (Laubach, 1997) fracture openness (Laubach et al., 2000; Laubach, 2003) and sizes (Marret et al., 1999). Fracture orientations found at micro-scales are used as direct proxies for the orientation of the large or macro-fractures. Fracture openness is predicted based on the determination of the amount of cement deposited after fracture formation, termed post-kinematic cement (Laubach, 1997, 2003). If large amounts of the pore space are filled after fracture development, macro-fracture openness will degrade considerably and the fracture may be cemented shut. Likewise, if small amounts of pore space are filled with postkinematic cement, macro-fractures should be open. By dividing the postkinematic cement volume by the post-fracture pore volume, the degradation index is obtained (Laubach et al., 2000). The degradation index can predict fracture openness. If the degradation index is larger than 50%, the macro-fractures are expected to be closed, whereas degradation index values below 50% predict the macro-fractures to be at least partly open. Although these techniques are an important advancement over conventional fracture measurements, they require samples from the subsurface and thus at best provide point data (albeit with greater density than conventional methods). Moreover, they do not provide information on length distribution or connectivity. Thus they are best used in conjunction with geomechanical modeling.

1.2.2 Geomechanical fracture pattern modeling

The second approach to natural fracture prediction employs geomechanical models. This approach uses fracture mechanics laws to predict fracture attributes as well as to explain fracture pattern observations. A detailed description of the two main fracture mechanics laws is given in the next section. The main advantage of using a mechanical approach is that an understanding of the underlying mechanism allows for prediction of fracture attributes in different situations and locations, including parts of the subsurface that have not been sampled. The main problem with this approach is that it requires *a priori* knowledge of rock properties and boundary conditions present during formation of the fractures which are usually in the geological past and therefore difficult to determine. Also, the laws are normally highly idealized and therefore limited in their application.

Using geomechanics, many theories have been developed explaining fracture observations with respect to spacing, orientation, length and aperture. Fracture spacing theories were first proposed in the 1960’s (Lachenbruch, 1961; Hobbs 1967) and later improved by others (Nur, 1982; Pollard and Segall, 1987; Gross et al., 1995; Bai and Pollard, 2000). These principles developed from the observation that fracture spacing is often proportional to the mechanical bed thickness (Bogdanov, 1947; Price, 1966; McQuillan, 1973; Segall and Pollard, 1983; Narr and Lerche, 1984; Huang and Angelier, 1989; Narr and Suppe, 1991; Gross, 1993; Gross and Engelder, 1995; Wu and Pollard, 1995; Becker and Gross, 1996; Ji and Saruwatari, 1998; Laubach et al., 1998). Due to a reduction in stress level, there exists a region around the fracture, termed the stress shadow, where fracture propagation is inhibited (Lachenbruch, 1961; Nur, 1982; Pollard and Segall, 1987; Gross et al., 1995). Bai and Pollard (2000) further investigated the stress distribution between an array of parallel fractures under tension. They found that at certain spacing to bed thickness ratios, the stress regime between the fractures converts from tension to compression, further inhibiting fracture growth (Bai and Pollard, 2000). Therefore, a minimum spacing results which is proportional to the fracture height and thus the mechanical unit thickness. However, fracture swarms or clusters are not explained by this theory. Olson (2004) used fracture dynamics and the three-dimensional nature of lateral fracture propagation to numerically generate fracture clusters. Using subcritical crack-propagation, he showed that fractures form clusters at high subcritical index values. At intermediate subcritical index values, the model generates the previously described linear spacing to bed thickness relationship.

Opening-mode joints propagate perpendicular to the least compressive stress, which is typically the minimum horizontal stress (Lawn and Wilshaw, 1975, p. 65-72; Pollard and Aydin, 1988). Thus joint trends can be predicted if the horizontal stress regime at the time of fracturing is known. Borehole breakouts, drilling induced fractures, strain relaxation, and acoustic velocity anisotropy can be used to determine the present day horizontal stress orientations in the subsurface. These present day stress orientations and magnitudes should be adjusted to reflect the expected stress regime present during fracturing. Olson and Pollard (1989) show that the magnitude of the differential stress plays an important role in fracture orientation development, where larger differential stresses result in straighter fractures than fractures formed under lower differential stresses. Thus, knowledge of the stress regime present during fracturing allows for the determination of the expected fracture orientation and planarity of the fractures.

The observation that the fracture length distribution is sometimes a negative exponential has been explained using a fracture interaction premise (Olson et al., 2001; Qui, 2002). This model uses the mechanical observation that, dependent on the overlap of two fractures, a fracture will either experience an increase or decrease in its crack tip stress intensity factor (Pollard et al., 1981; Olson et al., 2001). This allows for the quantification of zones where fractures are captured and propagation is hindered. Likewise, zones where fractures are not hindered in their propagation can also be delineated. This ultimately governs what length the fractures are able to reach.

Using linear elastic fracture mechanics and assuming a constant driving stress, the maximum fracture aperture is linearly related to the fracture length (Pollard and Segall, 1987). However, field observations indicate that not all data sets follow this linear scaling law (Delaney and Pollard, 1981; Vermilye and Scholz, 1995; Renshaw, 1997; Moros, 1999). Olson (2003) proposed a sub-linear relation between fracture length and aperture using the premise that all fractures in a body have the same stress intensity factor. The resulting aperture to length scaling is of a negative ½ power. This closely resembles fracture aperture data from outcrop as presented by Delaney and Pollard (1981), Vermilye and Scholz (1995), and Moros (1999).

In the present study, the mechanically based fracture pattern simulator described by Olson (2004) is employed. This numerical fracture pattern simulator uses the subcritical fracture growth law as its fracture propagation criterion. The model predicts fracture attributes based on measurable rock properties such as Young’s modulus, Poisson’s ratio, subcritical index and loading conditions. These present day measurements need to be adjusted to reflect the properties present during fracturing. This geomechanical approach is chosen here, over distributions obtained from field observations, because it allows for prediction of the fracture pattern characteristics outside the wellbore region, allowing for fracture pattern characterization for the entire reservoir given the correct variation of input parameters and boundary conditions.

1.3 FRACTURE GROWTH THEORY

There are two main propagation regimes for opening-mode fractures: 1) critical growth and 2) subcritical growth. Critical fracture growth velocities are typically larger than subcritical fracture growth velocities. An example of a process governed by critical fracture propagation is hydraulic fracturing. Subcritical fracture growth occurs when rocks are exposed to small loads over long periods of time, conditions which are generally present in the subsurface (Anderson and Grew, 1977; Atkinson, 1984; Kirby, 1984; Segall 1984). Both theories will be discussed in greater detail in the following paragraphs.

1.3.1 Critical fracture growth

Fracture mechanics started with the theory that materials fail under tension when the critical strength or the macroscopic tensile strength of the material is exceeded (Love, 1934). However, experiments conducted by Griffith (1921) showed that fracturing could occur below the critical strength of the material, dependent on the size of the specimen. This moved Griffith (1924) to postulate that flaws concentrate stresses and allow fractures to propagate at stress levels below the material's macroscopic tensile strength. The stress concentration at the fracture tip can be quantified using the stress intensity factor, K_I (Lawn and Wilshaw, 1975). The stress intensity factor for a blade shaped fracture in an infinite body has been determined to be (e.g. Rossmanith, 1983; Pollard and Aydin 1988; Anderson, 1995):

$$K_I = \sigma_I \sqrt{\pi a} \text{ ,} \qquad \text{Eq. 1.1}$$

where a is the fracture half-length and σ_I is the net driving stress. At a critical driving stress level the material fails. The stress intensity reached at this point is called the fracture toughness (K_{Ic}), which is a material property. When the fracture toughness of a material is known, one can determine under which conditions the fracture is likely to propagate.

1.3.2 Subcritical fracture growth

Grenet (1899) was the first to observe that the failure of glass could occur due to prolonged low level loading. This process has been termed slow fracture growth, fatigue cracking, or subcritical fracture growth. Three different regions of subcritical fracture growth have been observed in glass and other materials (Fig. 1.1) (Wiederhorn, 1967; Evans, 1972; Pletka et al., 1979; Atkinson and Meredith, 1987a). In region 1, the crack velocity is governed by stress corrosion (Wiederhorn, 1967; Atkinson and Meredith, 1987a). Region 1 is important because most of the fracture growth occurs in this region prior to catastrophic failure (Pletka et al., 1979). In region 2, the crack velocity is constant and independent of the stress intensity factor. This region is controlled by the transport of the reactive species to the crack tip (Wiederhorn, 1967; Wiederhorn et al., 1982; Atkinson and Meredith, 1987a). In region 3, crack growth is believed to be almost independent of the chemical environment, and crack growth is mainly controlled by the mechanical rupture (Evans, 1972; Atkinson and Meredith, 1987a). Ultimately, when the stress intensity factor reaches the fracture toughness, crack growth becomes unstable and the crack propagates at the rupture velocity, which is the maximum velocity at which the stress can travel through the body. As outlined in Figure 1.1 subcritical fracture growth occurs between the fracture toughness value and the threshold stress intensity factor below which the stress concentration at the crack tip is too low to allow for subcritical fracture growth (Evans, 1972). This lower limit has been termed the stress corrosion limit (K_I^*).

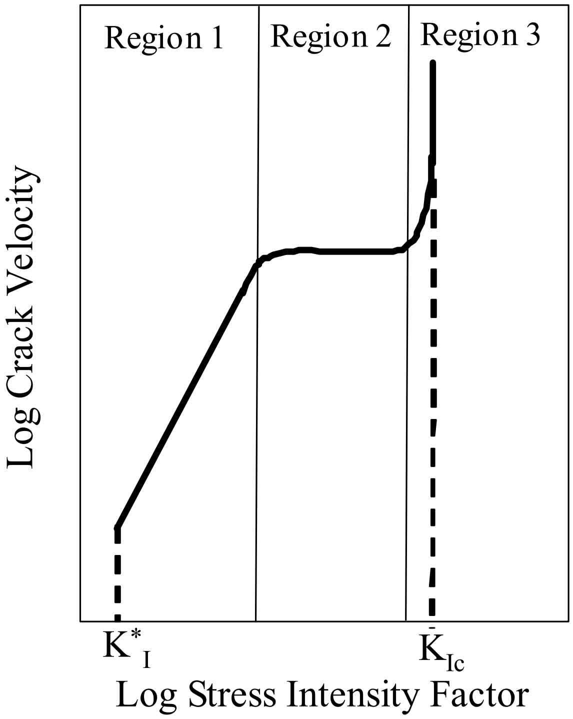

Figure 1.1: Log stress intensity factor vs. log crack velocity. Three different regions have been observed to exist: Region 1) dominated by stress corrosion, Region 2) controlled by the transport of reactive species to the crack tip, and Region 3) dominated by mechanical rupture. Subcritical fracture growth occurs between the stress corrosion limit (K_I^*) and the fracture toughness (K_{Ic}) (after Atkinson and Meredith, 1987a).

Stress corrosion has been proposed to be the main physical process behind subcritical fracture growth (Charles and Hillig, 1961; Evans, 1972; Atkinson and Meredith, 1987a). Hillig and Charles (1964) state that critical failure occurs when the tip of a flaw reaches a certain amount of sharpening. In general, a flaw will not propagate when the crack tip is not sharp enough for fracture propagation. Sharpening can occur due to stress enhanced corrosion. In subsurface rocks, where diagenetic reactions such as cement precipitation occur, a major cause of blunting is likely preferential cement precipitation in narrow crack tips (Laubach, 2003). Blunting can also occur when the flaw is uniformly increased in size (such as etching of glass which makes it less susceptible to time/stress dependent failure). Due to differential stress corrosion, the stress tip is sharpened and the fracture can grow subcritically. Catastrophic or critical fracturing will only occur if the crack tip is further sharpened to reach the geometry at which critical fracturing is dominant.

Subcritical fracture growth is generally considered to be a chemically driven process, in which chemicals, such as water, have the ability to attack the strained bonds more easily and weaken them to the point of bond-failure. Stress corrosion has been most often described in glass, a material very different from rock. However, the observations made in glass form a framework against which other tests can be compared. Freiman (1984) states that the activity of the corrosive agent is the governing factor controlling stress corrosion. The proposed reaction of glass in water environments is (Scholz, 1972; Martin, 1972; Swain et al., 1973; Atkinson, 1979; Atkinson and Meredith, 1987a):

$$H-O-H+\left[\equiv Si-O-Si\equiv\right]\Leftrightarrow\equiv Si-OH\cdot HO-Si\equiv\Leftrightarrow 2\left[\equiv Si-OH\right] \text{............ React. 1.1}$$

In basic environments Charles (1958a) describes:

$$\equiv Si-O-Si\equiv+OH^{-}\Leftrightarrow\equiv Si-O^{-}+\equiv Si-OH \text{ .... React. 1.2}$$

Although these reactions were developed for glass, many authors assume these reactions to be true for silicate materials as well. To date, no such reactions have been proposed for calcite rocks (Atkinson and Meredith, 1987a).

1.3.2.1 Stress intensity factor-velocity relationship: power-law vs. exponential fit

Two schools have developed quantifying the fracture velocity vs. stress intensity factor relationship of region 1 (Fig. 1.1). The first is the power-law approach as outlined by Charles (1958b). The second is the exponential approximation as proposed by (Charles and Hillig, 1961; Wiederhorn and Bolz, 1970). Charles (1958b) postulates that the fracture tip will be sharpened and the fracture velocity will increase as a function of the applied stress, until the stress tip is sharpened to the point where critical failure will occur. Based on experimental results, Charles (1958b) arrived at the following power-law equation including the stress intensity factor:

$$V = V_0' \exp\left(\frac{-H}{RT}\right) K_I^n \quad \text{.......... Eq. 1.2}$$

where V is the fracture velocity, V_0' is a constant, H is the activation enthalpy, R is the gas constant, T is the temperature, K_I is the stress intensity factor and n is the subcritical index (a rock property).

Charles and Hillig (1961) state that subcritical fracture growth is governed by the chemical reaction between glass and water. Since chemical reactions are activated processes, they argue that subcritical fracture growth should follow the behavior of an activated process (Charles and Hillig, 1961). Based on the reaction rate theory and with the aid of experimental results, Wiederhorn and Bolz (1970) arrived at:

$$V = V_0 \exp^{\left(\frac{-E^* + bK_I}{RT}\right)}, \quad \text{.......... Eq. 1.3}$$

where V_0, E^* and b are experimental constants, K_I is the stress intensity factor, R is the gas constant and T is the temperature. Equation 1.3 is a simplification of the equation proposed by Charles and Hillig (1961).

Within the experimental range of stress intensity factor and fracture both approximations hold true. In other words, one can obtain a good fit with both the power-law (Charles, 1958b) and the exponential (Wiederhorn and Bolz, 1970) approximation. No compelling evidence exists favoring one equation over the other and although close agreement between the different methods is reached, extrapolation to regimes outside that of the experimental realm give greatly differing predictions of the crack velocity and the stress intensity factor.

Loading conditions present in the subsurface are often favorable for subcritical fracture growth, since rocks are loaded for long periods of time below their fracture toughness value (Anderson and Grew, 1997; Atkinson, 1984; Kirby, 1984; Segall, 1984). Many authors employ the subcritical fracture growth theory as a basis to explain natural fracture observations (e.g. Anderson and Grew, 1977; Olson, 1993; Renshaw, 1996; Olson, 2004). Likewise, this study employs subcritical fracture growth as its fracture propagation criterion. The power-law approximation as postulated by Charles (1958b) is chosen in this study. Specifically, the formulation as given by Pletka and Wiederhorn (1978) is used:

$$V = V^{*}\left(\frac{K_I}{K_0}\right)^{n} \quad ,\text{..........} \quad \text{Eq. 1.4}$$

where V^{*} is a constant and K_0 is an arbitrary constant (with units identical to the stress intensity factor) used to normalize K_I. In the geomechanical model as described by Olson (2004), the fracture toughness is used as a normalization factor. The power-law approximation is chosen, since a body of data exists for geologic materials (Atkinson, 1984; Atkinson and Meredith, 1987a, 1987b), which report the subcritical index values. Such information is not available for the function constants proposed by Wiederhorn (1967).

1.4 FLOW MODELING OF FRACTURED RESERVOIRS

Geomechanical modeling of the subsurface fracture network through use of the subcritical fracture growth law is a powerful first step in an attempt to model naturally fractured reservoirs. The numerical model described by Olson (2004) can complete this step. The second step is to quantify the influence of fracturing on subsurface fluid flow. Historically two approaches have been developed to model fluid flow in naturally fractured reservoirs: 1) the continuum approach, and 2) discrete fracture pattern simulation. Both techniques are discussed in the following sections.

1.4.1 Double porosity/double permeability

Continuum reservoir simulation is based on the idea that a heterogeneous hydrocarbon reservoir can be represented by an equivalent homogenous medium. Warren and Root (1963) expanded this approach to a naturally fractured reservoir. They proposed to describe the fractured reservoir with two types of porosity: 1) the primary or matrix porosity, and 2) the secondary or fracture porosity. This approach is called the double porosity or dual porosity approach. The two systems are linked through a transfer function, which represents the exchange of fluid between them. These transfer functions depend on the shape and dimensions of the matrix block, transmissibility of the block, relative permeability, capillary pressure, and density differences between phases (Mattax and Dalton, 1990).

Warren and Root (1963) acknowledge that a naturally fractured reservoir is inherently heterogeneous (Fig. 1.2A). However, if the scale of heterogeneity is small compared to the scale of the reservoir, the reservoir is considered homogeneous (Warren and Root, 1963). Warren and Root (1963) derive the analytical solution for the response of an infinite reservoir based on the following assumptions: 1) the matrix porosity is homogeneous, isotropic, and contained within a systematic array of identical, rectangular parallelepipeds; 2) the fracture system consists of an array of uniform orthogonal fractures, aligned with the principal axes of permeability (Fig. 1.2B); 3) flow can occur between the matrix and the fractures, but flow from matrix to matrix block cannot occur; 4) quasi-steady state exists in the matrix blocks at all times; and 5) only single phase flow of a slightly compressible liquid is considered. Warren and Root (1963) define the following dimensionless parameters:

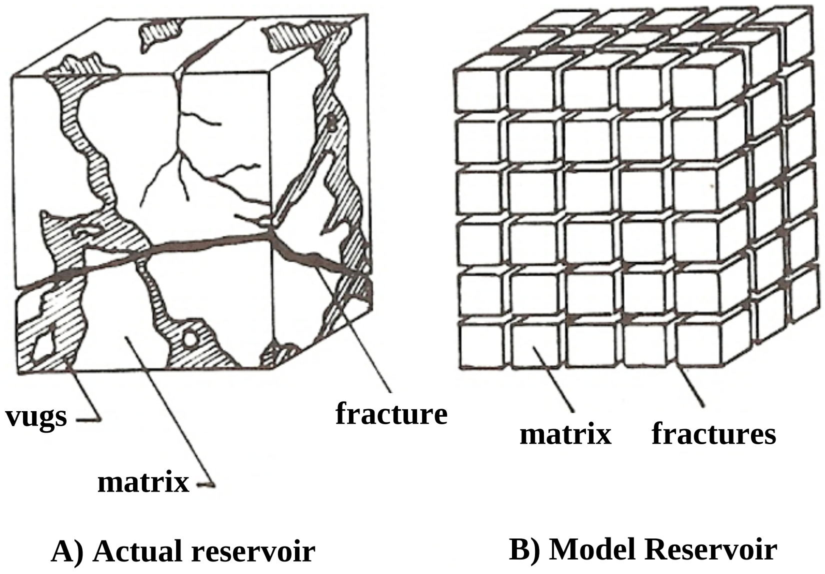

Figure 1.2: Conceptual naturally fractured reservoir model, where A) depicts an actual naturally fractured reservoir, and B) depicts the conceptual naturally fractured reservoir (reproduced from Warren and Root, 1963).

$$P_D = \left(\frac{2\pi k_f h}{q\mu}\right)\left[P_0 - P(r,t)\right], \qquad \text{Eq. 1.5}$$

$$t_D = \frac{k_f t}{\left(\varphi_f C_f + \varphi_m C_m\right)\mu r_w^2}, \qquad \text{Eq. 1.6}$$

and

$$r_D = \frac{r}{r_w}, \qquad \text{Eq. 1.7}$$

where k is the permeability, h is the reservoir thickness, q is the flow rate at the wellbore, μ is the viscosity, P_0 is the initial reservoir pressure, $P(r,t)$ is the pressure at radius, r, and time, t, ϕ_f and ϕ_m are the porosity of the fracture and matrix system respectively, C_f and C_m are is the total compressibility of the fracture and matrix system respectively, and r_w is the wellbore radius. With these dimensionless parameters, Warren and Root (1963) derive the following solution for pressure drawdown in an infinite reservoir:

$$P_{2D}(1,t_D)=\frac{1}{2}\left[0.80908+\ln t_D+Ei\left(-\frac{\lambda t_D}{\omega(1-\omega)}\right)-Ei\left(-\frac{\lambda t_D}{1-\omega}\right)\right], \text{.............................} \quad \text{Eq. 1.8}$$

where,

$$Ei(-x)=-\int_x \frac{e^{-u}}{u}du \text{ ....} \quad \text{Eq.1.9}$$

Equation 1.8, as derived by Warren and Root (1963), shows that the pressure drawdown observed at a well can be completely described by two parameters ω and λ, where ω is a measure of the fluid capacitance or storativity due to the secondary porosity (or fracture) and is determined through:

$$\omega=\frac{\varphi_f C_f}{\varphi_f C_f+\varphi_m C_m}, \text{...} \quad \text{Eq. 1.10}$$

The second parameter, λ, is related to the flow capacity of the matrix blocks and the contrast between the matrix and fracture permeability, and is determined through (Warren and Root, 1963):

$$\lambda=\alpha\frac{k_m}{k_f}r_w^2, \text{..} \quad \text{Eq. 1.11}$$

where α is a shape factor defined as (Warren and Root, 1963):

$$\alpha=\frac{4m(m+2)}{l^2}, \text{...} \quad \text{Eq. 1.12}$$

and *m* is the number of orthogonal fracture sets. The variable, *l*, is defined by (Warren and Root, 1963):

$$l=x \qquad m=1$$

$$l=\frac{2xy}{(x+y)} \qquad m=2, \text{..} \quad \text{Eq. 1.13}$$

$$l=\frac{3xyz}{(xy+yz+zx)} \qquad m=3$$

where *x*, *y* and *z* are the dimensions of the matrix blocks.

The dual porosity model predicts drawdown tests to exhibit 2 parallel straight lines on a dimensionless pressure-time plot that are connected by a transition curve of non-constant slope (Fig. 1.3) (Warren and Root, 1963). The placement of the parallel straight lines is directly related to the relative storage capacity of the fractures (ω). The dimensionless pressure drop value at the transition curve is related to the flow capacity and the contrast between fracture and matrix properties (λ). In the limiting cases, where $\omega \rightarrow 1$ and $\lambda \rightarrow \infty$, the solution reduces to that of a homogeneous reservoir, where $\omega \rightarrow 1$ indicates that all storage occurs in the fracture system and $\lambda \rightarrow \infty$ indicates there is no impedance to interporosity flow. Kazemi (1969) observed a response similar to that in Figure 1.3 for a finite radial fractured reservoir.

A natural extension of the double porosity approach is to allow for flow between matrix blocks, called the double or dual permeability model. To solve for fluid flow through the matrix block as well as the fracture system one has to solve the Barenblatt-Zheltov equations (Barenblatt and Zheltov, 1960). Chen (1990) gives a summary of some of the analytical solutions available. The advantage of this dual permeability approach is that it allows for flow between matrix blocks, however the dual permeability approach is computationally more expensive than the dual porosity approach.

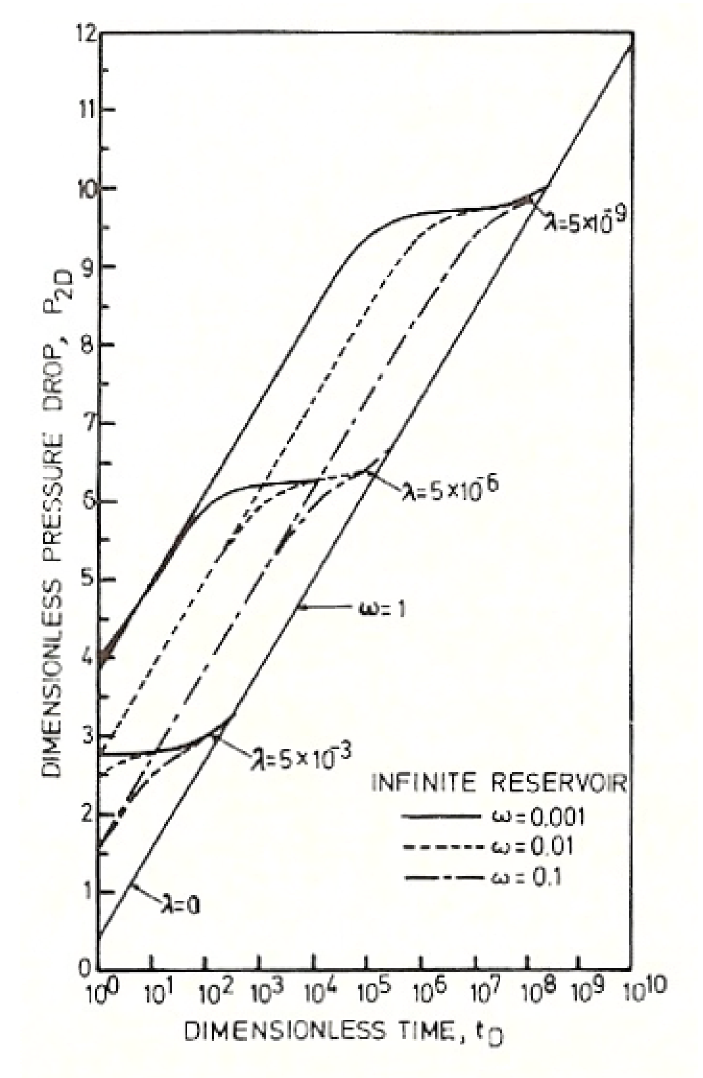

Figure 1.3: Dimensionless time vs. dimensionless pressure drop for a double porosity infinite reservoir as obtained by Warren and Root (1963) (Reproduced from Warren and Root, 1963).

1.4.2 Discrete fracture network modeling

Fractured media do not necessarily behave like continua (Long et al., 1982; Long and Witherspoon, 1985; Long et al., 1985b), because the assumption that the fracture length is small compared to the continuum dimensions is often violated. Dverstorp and Andersson (1987) used a discrete fracture approach to explain the non-uniform sweep observed during a migration experiment performed at the Stripa research mine in Sweden. A continuum approach would not have been able to predict this non-uniform sweep. Another shortcoming of the continuum approach is that the porous matrix blocks are normally assumed to have simple geometries with uniform size and shape (Sudicky and McLaren, 1992). Such simple geometries are seldom observed in nature.

The first attempts to model flow through discrete fracture networks consisted of two-dimensional, infinite fractures in an impermeable matrix (Snow, 1969). Long et al. (1982) argued that this greatly overestimates the contribution of the fractures to fluid flow since no fractures are infinite. Finite fractures are less likely to intersect other fractures. Therefore, the flow rate in a finite fracture length model is lower than that predicted for an infinite fracture length model (Long et al., 1982). Long et al. (1985a) expanded their approach to 3D, but no flow through the matrix is possible with their method. Sudicky and McLaren (1992) showed that matrix flow is not negligible in many groundwater flow and solute transport cases. Therrien and Sudicky (1996) present a 3D discrete numerical fracture model which includes advection, mechanical dispersion, molecular diffusion and sorption in the matrix.

The discrete fracture network modeling discussed above, requires prior knowledge of the statistical distributions of the fracture attributes (Snow, 1970; Long et al., 1985a; Dershowitz and Einstein, 1988). Therefore, either direct or indirect field data are used to populate the fractured regions (Long and Billaux, 1987; Andersson and Dverstorp, 1987; Dverstorp and Andersson, 1989). Other approaches use previously published fracture attribute distributions (Wilson and Witherspoon, 1974; Long et al., 1982; Smith and Schwartz, 1984, Long and Witherspoon, 1985; Long et al., 1985a; Berkowitz, 1995). Using statistical distributions in the subsurface requires that: 1) the fracture pattern exhibits statistical homogeneity; 2) it is possible to obtain a statistically representative sample; 3) the spatial distribution of fractures can be described by a simple stochastic process; and 4) the characterized fractures are the ones that conduct fluid in the subsurface (National Research Council, 1996). Assuming that these conditions are satisfied, the fracture attribute distributions can be implemented. The disaggregate method implements each fracture attribute separately (Dershowitz and Einstein, 1988). However, the aggregate method honors not only the individual fracture attribute characteristics, it also honors the internal correlations between the different fracture attributes (for instance, fracture aperture and length), thus leading to more realistic fracture patterns (Dershowitz and Einstein, 1988).

The previously described methods are powerful tools to estimate the influence of certain fracture pattern characteristics on the overall flow response. However, these methods are only weakly linked, if at all, to the underlying mechanical processes forming the fracture patterns in the subsurface. Thus, meaningful extrapolation outside the area of interest is difficult or impossible. In the present study, fracture patterns are generated using a pseudo-3D numerical fracture pattern simulator as described by Olson (2004). This model allows the user to assume the boundary conditions and material properties appropriate for the area interest, and does not require *a priori* knowledge of the fracture pattern distributions.

Chapter 2 Petrographic and Chemical Controls on Subcritical Fracture Growth

2.1 INTRODUCTION

The sparse amount of available fracture attribute information makes quantification of the fracture pattern in the interwell region difficult. A number of geomechanical phenomena have been explained using subcritical fracture growth theory (Atkinson and Meredith, 1987a), and numerical simulations have demonstrated subcritical crack growth controls on fracture spacing and length distributions (Segall, 1984; Olson, 1993; Olson, 2004), connectivity (Renshaw, 1996; Olson, 1997) and fracture aperture (Renshaw and Park, 1997; Olson et al., 2001). Specifically, it has been observed that the subcritical index has a considerable effect on the overall fracture pattern characteristics (Olson, 1993; Olson et al. 2001; Olson, 2004) (Fig. 2.1). The subcritical index value is, amongst others, a function of the rock's microstructure as well as the chemical environment (Atkinson and Meredith, 1987a), which are both expected to change with time. Variations in subcritical index over time can be used to explain field observations. An example is the fracture pattern from the Pennsylvanian-Permian Rico Formation, Monument upwarp, southeastern Utah, where the clustered appearance of the younger north-south set is attributed to an increase in subcritical index over time (Fig. 2.2.) (Olson and Pollard, 1989). Therefore, the objective of this part of the study is to predict differences in subcritical index expected over geologic time.

Subcritical fracture testing has been performed on many different materials, such as glasses (Charles, 1958a, 1958b; Wiederhorn, 1967; Kies and Clark, 1969; Wiederhorn and Bolz, 1970; Evans, 1972; Pletka et al., 1979; Wiederhorn et al., 1980; Michalske et al., 1981; Simmons and Freiman, 1981; Wiederhorn et al., 1982; Yaoguang and

Shengyan, 1982; Stravrinidis and Holloway, 1983; Cook and Liniger, 1993; Bhatnagar et al., 2000), metals (Williams and Evans, 1973), ceramics (Evans et al., 1974; Freiman et al., 1974; Wu et al., 1978; Wiederhorn et al., 1980; Rice et al., 1980; Rice et al., 1981; Bhatnagar et al., 2000), cement/cement paste (Mindess et al., 1974; Beaudoin, 1985a; Beaudoin, 1985b; Beaudoin, 1987; Taylor and Tait, 1999), minerals (Atkinson, 1979;

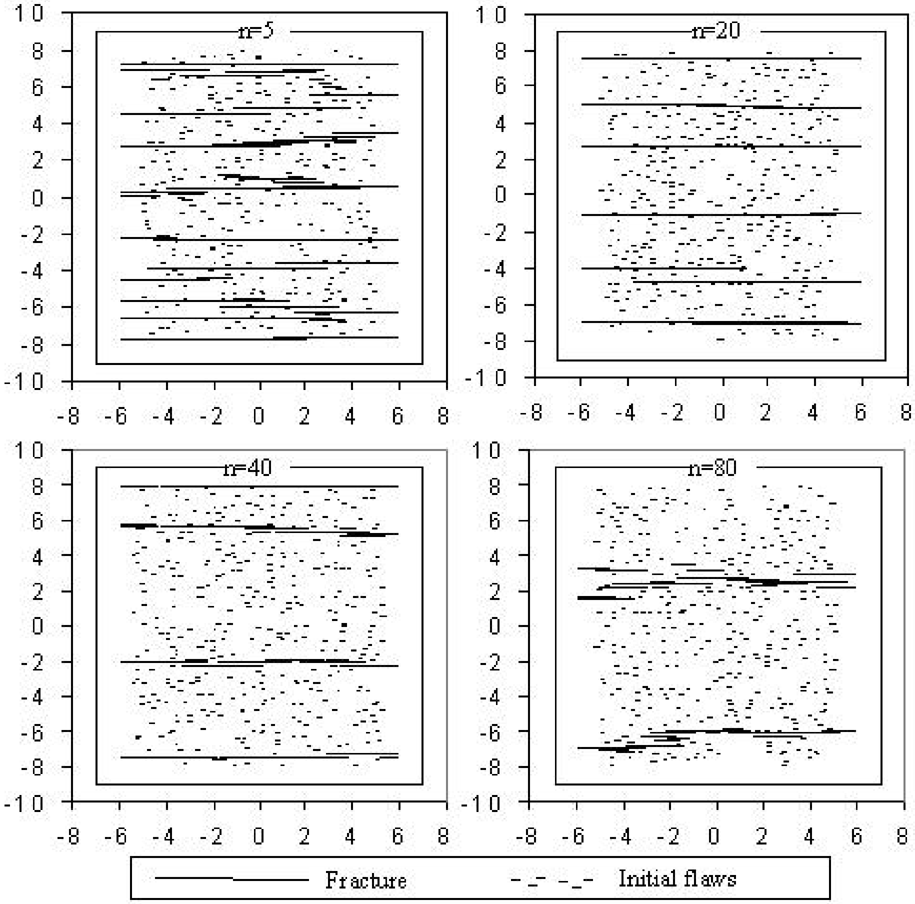

Figure 2.1: Fracture trace maps for numerical subcritical crack propagation simulations for different subcritical crack indices (n), using 400 initial flaws. The numbers along the axis indicate the size of the fracture patterns (in m). Each case used an identical crack-perpendicular extensional strain rate. Note increasing fracture density with decreasing n, and fracture clustering for n = 40 (with clusters at 6, -2 and -8 m) and n = 80 (with clusters at 3 and -6 m). From Olson et al. (2001).

Atkinson and Meredith, 1981; Meredith and Atkinson, 1982; Darot and Gueguen, 1986) and rocks (Swanson, 1984; Atkinson, 1980, 1984; Atkinson et al., 1980; Sano and Ogino, 1980; Waza et al., 1980; Wilkins, 1980; Atkinson and Rawlings, 1981; Atkinson 1982; Costin and Mecholsky, 1983; Meredith and Atkinson, 1983, 1985; Winter, 1983; Atkinson et al., 1984a, 1984b). However, systematic studies on sedimentary materials are

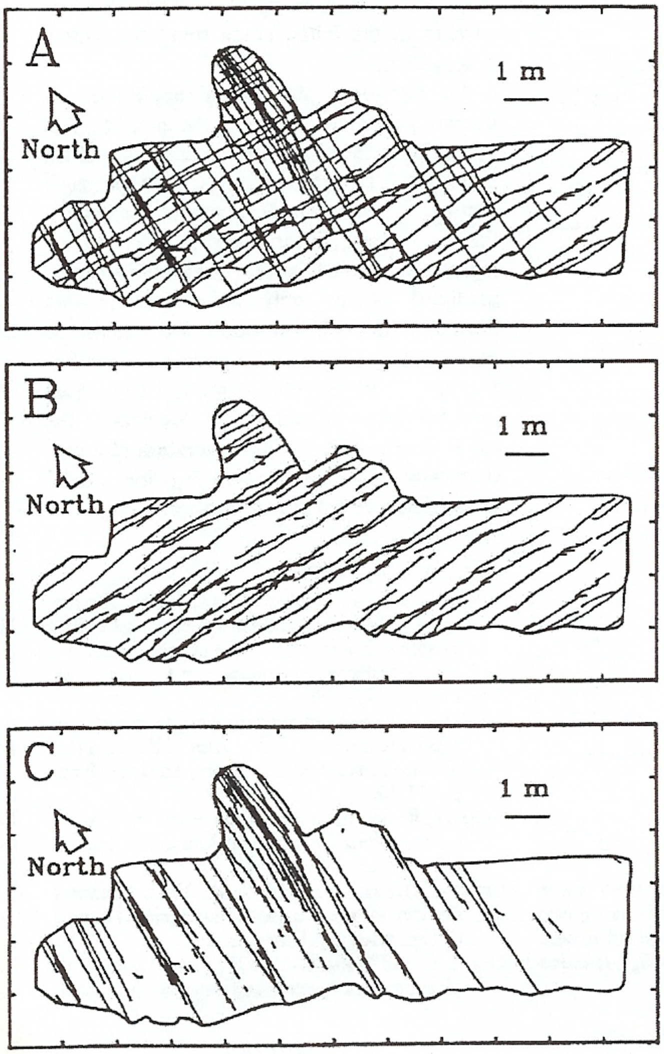

Figure 2.2: Fracture trace maps from the bedding surface of the Rico Formation, Monument upwarp, southeastern Utah: A) fracture trace map showing both fracture sets, B) fracture trace map of only the east-west striking fracture set, C) fracture trace map of only the north-south striking fracture set. Reproduced from Olson and Pollard (1989).

lacking (Holder et al., 1999). In this chapter such a systematic study is presented, with special emphasis on sandstones. Petrologic features as well as chemical environment changes believed to control subcritical index variations are investigated. Given that the changes in both the chemical environment and the diagenetic history of the area are known, understanding how petrologic features and chemical environment influence the subcritical index value provides a basis for predicting changes in the subcritical index expected over time.

This chapter begins with a review of published subcritical fracture growth correlations. After a description of the employed test procedure, the obtained experimental results are discussed. The effects of petrologic as well as chemical environment changes are addressed successively.

2.2 LITERATURE SURVEY

Atkinson and Meredith (1987a) postulated that the following 6 parameters influence subcritical fracture growth: 1) temperature, 2) chemical environment, 3) pressure, 4) microstructure, 5) residual strain, and 6) stress intensity factor. Since the dependence of crack velocity on stress intensity factor was extensively discussed in the previous chapter, the discussion is omitted here (Fig. 1.1). The remaining five parameters are discussed successively.

2.2.1 Temperature

On the basis of Equation 1.2 and 1.3 subcritical fracture growth is dependent on temperature (Charles, 1958b; Wiederhorn and Bolz, 1970), where an increase in temperature results in an increase in fracture velocity. Experimental results tabulated by Atkinson and Meredith (1987b) report mixed correlations between subcritical index and temperature. Meredith and Atkinson (1982) show an increase in subcritical index (from

40 to 46) with an increase in air temperature (from 20 to 300 °C) for quartz. However, the opposite holds true for a water vapor environment, where the subcritical index decreased from 18 to 12 with an increase in temperature from 20 to 200 °C. Tests of Tennessee sandstone in water showed that the subcritical index increased (from 14 to 26) as the temperature increased (20 to 60 °C) (Atkinson, 1984). Although variations in subcritical index with temperature are observed, no clear trends have been found for sedimentary materials. In this study, subcritical index value variations obtained from the same material, tested under constant temperature conditions, were as large as the variation in subcritical index values reported in literature due to temperature changes. Therefore, changes in subcritical index values due to temperature variations are expected to fall within the experimental scatter, specifically, since the anticipated temperature changes in the subsurface lie within the temperature range tested in literature. Although no direct correlation between temperature and the subcritical index is observed, temperature can influence subcritical fracture growth indirectly. For instance, an increase in temperature might alter the stress corrosion reaction speed and therefore the subcritical index. Likewise a temperature increase might increase the cementation rate and thus alter the rock's microstructure and subcritical index. However, since these expected subcritical index changes are only indirectly linked to temperature, and because of the limited variations in subcritical index values observed in literature due to temperature changes, temperature variations are not addressed in this study.

2.2.2 Chemical environment

Subcritical fracture growth has been extensively studied for materials in aqueous environments (Charles, 1958a; Charles and Hillig, 1961; Wiederhorn, 1967; Wiederhorn and Bolz, 1970; Evans, 1972; Scholz, 1972; Lawn, 1975; Atkinson, 1979, 1980, 1982, 1984; Wiederhorn et al., 1980; Atkinson and Meredith, 1981; Atkinson and Rawlings, 1981; Simmons and Freiman, 1981; Wiederhorn et al., 1982; Stravrinidis and Holloway, 1983; Meredith and Atkinson, 1983, 1985; Beaudoin, 1985a, 1985b; Darot, 1986; Cook and Liniger, 1993). Stress corrosion is a chemically-based process which governs subcritical fracture growth in region 1 of Figure 1.1 (Charles and Hillig, 1961; Evans, 1972; Atkinson and Meredith, 1987a). Stresses are enhanced at the fracture tip, increasing the solubility of the rock (Hillig and Charles, 1964). The fracture propagates as long as the soluble material is removed from the fracture tip (Atkinson and Meredith, 1987a). If the material is not removed, precipitation may occur, blunting the fracture tip and arresting propagation (Ito and Tomozawa, 1982). Therefore, solubility of the material influences the subcritical fracture behavior. Solubility of calcite minerals is much higher than that of quartz at room temperature and is much higher in sea water than in fresh water (Atkinson and Meredith, 1987a). Quartz solubility is not affected by dissolved salts and is fairly independent of pH below a pH of 9 (Atkinson and Meredith, 1987a). On this basis, calcite minerals are expected to show a stronger dependence on the presences of aqueous liquids than quartz.

Although many subcritical index tests have been performed in aqueous conditions, no clear correlation between subcritical index and presence of water is evident in sedimentary materials. Winter (1983) found a marked decrease in subcritical index from 63-151 to 8-11 when water is introduced to the Ruhr Sandstone. Similar tests performed by Atkinson (1984) also showed a decrease in subcritical index as water was introduced to the Tennessee sandstone, but the decrease was much less pronounced (from 17 to 14) and falls within the expected experimental scatter. Unfortunately, no mineralogical information is available for the tested Tennessee sandstone samples to allow for an explanation of the differences in sample response. For granite Atkinson et al. (1984a) gave mixed results, where sometimes the subcritical index decreased with water and sometimes it increased. Similar results were obtained by Atkinson and Rawlings (1981) for Black gabbro. To date, no systematic testing has been performed in chemical environments of interest to the petroleum industry. In sedimentary basins, during fracturing in the subsurface, either water, brine, gas or oil is expected to be present. Given that water/hydroxyl ion has the ability to react with the rock material and impact subcritical fracture growth (reaction 1.1 and 1.2), the largest differences are expected between aqueous and oil or gas environments.

2.2.3 Pressure

The effect of fluid pressure or confining pressure on subcritical fracture growth is not straight-forward since it affects: 1) the stress tensor of the solid undergoing crack growth, 2) the mechanical properties of the fluid in the crack, and 3) the chemical reactions taking place between the fluid in the crack and the solid material at the crack tip (Anderson and Grew, 1977). These three effects can either work to increase or decrease the crack velocity. For instance, Anderson and Grew (1977) describe that an increase in pressure can increase the viscosity of the fluid. This retards the transport abilities of the chemicals in the fluid, which attack the bonds in the solid, and thus one would expect a decrease in crack propagation rate. However, if simultaneously the reaction speed increases through an increase in pressure, then both effects might cancel. Therefore, no *a priori* determination can be made with respect to the expected behavior of the material with a change in pressure (Anderson and Grew, 1977; Atkinson, 1984). Due to the inherent experimental difficulty, and the possibility that different processes cancel each other to produce no observable change in subcritical fracture growth response, pressure was not considered in this study.

2.2.4 Microstructure

Sedimentary materials are inherently different from ceramics in that they generally have more complex microstructures including coarser grain size, porosity, and unstable mineralogical phases. Swanson (1984) found that the subcritical index increases as the material becomes micro-structurally more complex, based on the comparison of results from single crystals/glasses (subcritical index ranges from 10 to 25), single phase polycrystals (subcritical index ranges from 24 to 60), multiphase ceramics (subcritical index ranges from 40 to 160) and rocks (subcritical index ranges from 70 to 170). Single phase crystals are considered least complex, since they do not have the grain-to-grain contacts nor the material differences such as present in the more complex sedimentary materials. If, for the sedimentary materials of interest, there exists a limited range in fracture toughness and rupture velocities as compared to the total range of stress intensity factor and crack velocity than all curves on a stress intensity factor vs. crack velocity plot will converge to one point (Fig. 2.3). This hinge point will be at the fracture toughness-rupture velocity intersection. Given the existence of such a hinge point, an expected change in fracture velocity at a given stress intensity factor completely defines the change in subcritical index. Specifically, the subcritical index is expected to increase as the macro-fracture velocity decreases at a given stress intensity factor (arrow Fig. 2.3). Swanson (1984) states that as the material becomes more complex (i.e. moving from a single crystal material to a sedimentary rock), the fracture path becomes more tortuous, effectively decreasing the macro-crack velocity and thus increasing the subcritical index.

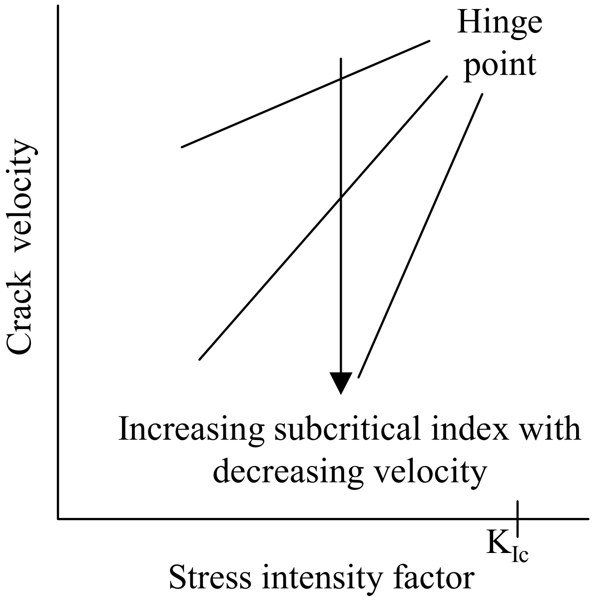

Figure 2.3: Stress intensity vs. the crack velocity. The graph illustrates that all curves come together at a common hinge point, due to a limited range in rupture velocity and fracture toughness. If the velocity decreased at identical stress intensity factor values the subcritical index decreases.

Gesing and Bradt (1983) find that in polycrystalline ceramics an increase in grain size decreases the subcritical index. They assume that grain boundaries provide low resistance pathways for the fracture to follow. The main crack extends when a flaw at a three-grain junction ahead of the crack propagates and links up with the main crack (Fig. 2.4). The crack extension force that has to be applied to the main crack in order to extend the flaw can be calculated from the stress field analysis around the main crack tip. This crack extension force is a function of the flaw size, the fracture toughness and the distance from the main crack tip. Since a flaw that links up to the main crack is always one grain facet away from the crack tip, the crack extension force can be expressed in terms of grain size (Gesing and Bradt, 1983). Combining this expression with the expression for subcritical index, which is a function of crack velocity and crack extension force (or stress intensity factor), a dependence of the subcritical index on grain size follows. Specifically, Gesing and Bradt (1983) show that as the grain size increases the subcritical index decreases. Their theoretical analysis is validated by experiments on alumina (Gesing and Bradt, 1983).

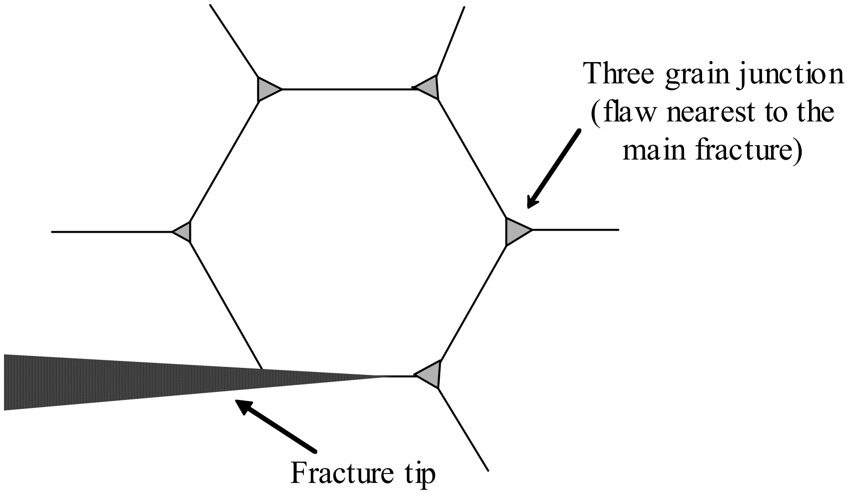

Figure 2.4: Geometry of a three grain junction flaw in the stress field of a main crack (adapted from Gesing and Bradt, 1983).

2.2.5 Residual strain

Strains can become locked into the fabric of the rock during deposition, compaction, cementation, uplift and burial. These residual strains alter the stress field at the crack tip, which in turn influences the stress corrosion process. The presence of residual strains has been reported to change both the stress corrosion limit (Vosikovsky et al., 1980) as well as the fracture toughness of the material (Atkinson, 1984). The influence of residual strains on the subcritical index is as of yet unknown. A major problem in determining the influence of residual strains on the subcritical index in sedimentary materials is determining what the residual strain level is of the rock. Atkinson and Meredith (1987a) state that residual strains can be very local (on grain size level) and highly heterogeneous. If this is the case, the effect of residual strains will closely resemble the microstructure in the rock (Atkinson and Meredith, 1987a), further complicating the determination of the dependence of residual strains on subcritical fracture growth. Due to these difficulties, residual strain is not considered in this study.

2.3 THE DOUBLE TORSION BEAM TEST

Previous sections have shown that the subcritical index value varies widely both within rocks (Swanson, 1984; Atkinson, 1984; Atkinson and Meredith 1987b) as well as with the chosen chemical environment (Winter, 1983; Atkinson 1984). Therefore this study sets out to: 1) determine the petrology of the samples tested, and 2) vary the chemical environment to resemble that of a hydrocarbon reservoir. Subcritical crack growth measurements were carried out with a constant-displacement, double-torsion beam (DTB) apparatus (Fig. 2.5) (Evans, 1972; Williams and Evans, 1973). In this configuration, stress intensity factor is independent of fracture length, and a complete propagation velocity vs. stress intensity factor curve can be obtained from a single load decay measurement on opaque samples. The sample is placed on 4 bearing balls. The two

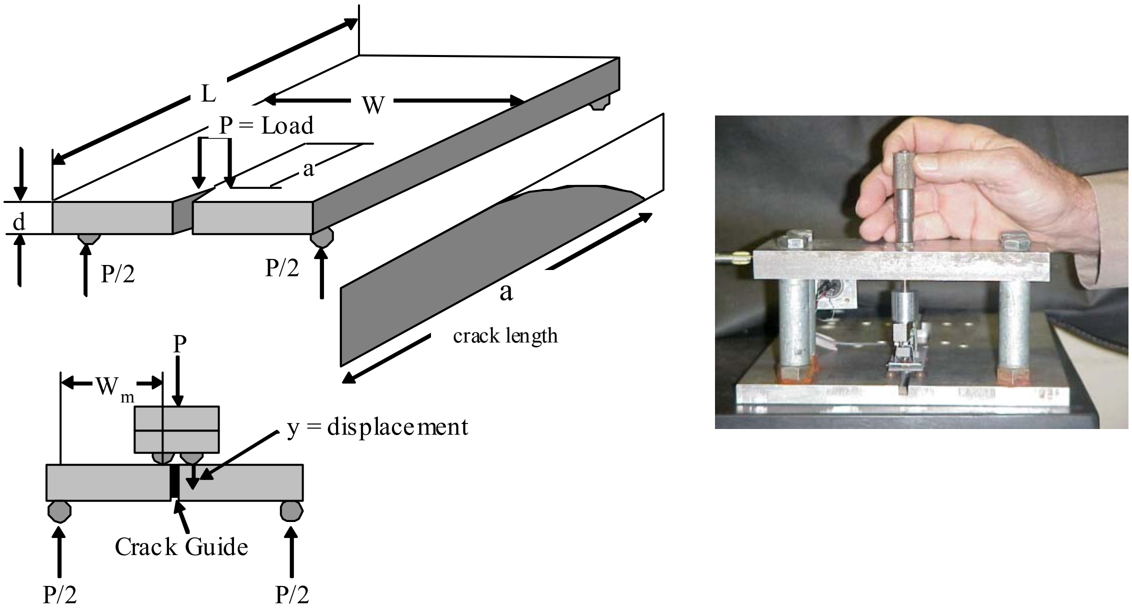

Figure 2.5: Test configuration for the Double Torsion Beam tests.

balls that straddle the machined groove apply a bending moment to the sample. This applied load propagates a fracture at the bottom of the sample. The displacement, *y*, is applied manually using a micrometer, and the load decay is recorded. The double torsion beam (DTB) test was first introduced by Kies and Clark (1969) as a method to determine crack speeds as a function of the driving force. A complete mathematical description of the relationship between the stress intensity factor and the specimen dimensions was first reported by Williams and Evans (1973). A brief synopsis is given in the following section.

2.3.1 Theory

DTB tests are based on the observation that the sample compliance (*S*) (Defined in Eq. 2.1) is a linear function of the crack length (*a*) (Evans, 1972; Williams and Evans, 1973):

$$S = \frac{y}{P} = S_0 + Ba \text{ , } \ldots\ldots \text{Eq. 2.1}$$

where *y* is the displacement in the y-direction at the loading point, *P* is the load, S_0 is the compliance of the intact specimen, and *B* is an experimental constant. Differentiating Equation 2.1 with respect to time, *t*, at constant displacement, *y*, gives the following relationship for crack propagation velocity (*V*) (Williams and Evans, 1973):

$$V = \left(\frac{\delta a}{\delta t}\right)_y = -\frac{(S_0 + Ba)}{BP}\left(\frac{\delta P}{\delta t}\right)_y \ldots\ldots \text{Eq. 2.2}$$

For a constant displacement setup, Equation 2.1 can be rewritten to form:

$$P(S_0 + Ba) = P_i(S_0 + Ba_i) = P_f(S_0 + Ba_f), \ldots\ldots \text{Eq. 2.3}$$

where the subcripts *i* and *f* stand for the intial and final conditions. Combining Equations 2.2 and 2.3 leads to:

$$V = \left(\frac{\delta a}{\delta t}\right)_y = -\frac{P_{i,f}(S_0 + Ba_{i,f})}{BP^2}\left(\frac{\delta P}{\delta t}\right)_y = -\frac{P_{i,f}\left(a_{i,f} + \frac{S_0}{B}\right)}{P^2}\left(\frac{\delta P}{\delta t}\right)_y \ldots\ldots \text{Eq. 2.4}$$

For all except very low modulus materials, $S_0/B<<a$, so that Equation 2.4 reduces to (Williams and Evans, 1973):

$$V=\left(\frac{\delta a}{\delta t}\right)_y=-\frac{P_{i,f}\,a_{i,f}}{P^2}\left(\frac{\delta P}{\delta t}\right)_y \quad \text{Eq. 2.5}$$

Equation 2.5 allows for the determination of the crack velocity from the load relaxation curve obtained during a constant displacement test.

To determine the stress intensity factor, the expression as determined by Pletka et al. (1979) is used:

$$K_I=P\cdot W_m\cdot\sqrt{\frac{3}{W\cdot d^3\cdot d_n\cdot(1-\nu)}} \quad ,\ \text{Eq. 2.6}$$

where W_m is the moment arm, W is the specimen width, d is the specimen thickness, d_n is the thickness of the specimen measured at the central groove, and ν is the Poisson's ratio.

2.3.2 Data analysis

Crack velocity is determined from the time vs. load decay curve using Equation 2.5, which requires the derivative of the load decay curve. Direct numerical computation of load-time slopes from individual data points is generally not suitable because of measurement scatter. Therefore, raw data are usually smoothed by fitting a high order polynomial to the load-time behavior (Swanson, 1984), and the derivative is calculated from the polynomial fit. However, a good fit may require dividing the data in multiple regions to be fit separately. Unfortunately, this method often computes velocity-load variations which deviate from a well-defined power-law.

In this study, a new method developed by Holder (Pers. Comm., 2001) is used which directly fits the measured data to an integration of Equation 2.5, circumventing the need for a derivative of the empirical data. At the start of the test:

$$y=\frac{S_0}{P_i} \quad \text{Eq.2.7}$$

Combining Equation 2.7 and 2.1:

$$P = \frac{P_i}{\left(1+\frac{B}{S_0}\cdot a\right)}, \qquad \text{Eq. 2.8}$$

where P_i is the initial value of applied load. Differentiating this expression with respect to time gives:

$$\frac{\partial P}{\partial t} = \frac{-\frac{B}{S_0}P_i}{\left(1+\frac{B}{S_0}a\right)^2}\frac{\partial a}{\partial t} = \frac{-\frac{B}{S_0}P_i}{\left(1+\frac{B}{S_0}a\right)^2}V = \frac{-\frac{B}{S_0}P^2}{P_i}V\,. \qquad \text{Eq. 2.9}$$

Using the power-law dependence of crack velocity on the load, i.e. $V = A(P)^n$, gives:

$$\frac{\partial P}{\partial t} = \frac{-\frac{B}{S_0}P^2}{P_i}A(P)^n = -\frac{A\frac{B}{S_0}}{P_i}(P)^{n+2} \qquad \text{Eq. 2.10}$$

From Equation 2.10, the constants A and $\frac{B}{S_0}$ can be related to initial values of load, P_i, and its time derivative, $P_i^{'}$:

$$A\frac{B}{S_0} = -\frac{P_i^{'}}{P_i^{(n+1)}} \qquad \text{Eq. 2.11}$$

Integrating Equation 2.10 gives:

$$P = \frac{P_i}{\left[1-(n+1)\cdot\left(\frac{P_i^{'}}{P_i}\right)\cdot t\right]^{\frac{1}{n+1}}} \qquad \text{Eq. 2.12}$$

In principle, P_i and $P_i^{'}$ could be determined from measurements of the initial load-time behavior, and the subcritical index could be determined by a least square fit of load and time to this power-law expression. However, experimental scatter is too high, especially during the initial portion of the load decay, to directly determine these parameters. Instead, an iterative procedure (such as Excel's SOLVER utility) is used to determine all three parameters from a least square fit of all load decay data to Equation 2.12. Crack velocity is then determined from Equation 2.4. The primary benefit of this method is that it creates a single power-law curve which fits the entire data set. Also, this process can easily be set up in an Excel template, and the entire curve fit can be carried out within a few seconds.

2.3.3 Sample preparation

Samples were cut into slabs of approximately 0.068 by 1 by 3 inch (= 1.7 by 25.4, by 76.2 mm) from rocks obtained from either outcrop or core. This particular combination of length, width and thickness has been shown to result in a sizeable region where crack length is independent of the stress intensity factor (Evans et al., 1974; Pletka et al., 1979). Cutting was done using saws that were oil cooled. After cutting, the samples were polished to a shine on the fracture propagation side, to eliminate possible bumps in the fracture propagation path as well as to help visualize the crack. Polishing was performed on a polishing table cooled with water. The samples were glued to a backing plate using salol (Phenyl Salicylate $HOC_6H_4COOC_6H_5$). This organic compound is solid at room temperature but melts at ~40° C. Water sensitive samples were polished with sandpaper and no salol was necessary. Samples tested in fluid were saturated in the specified fluid for 48 hours under vacuum prior to testing after Beaudoin (1987). During testing, samples were submerged in their respective fluid environments.

To eliminate the influence of oil and salol from the preparation procedures on the test results, all samples were soaked in Toluene over-night and then oven dried. The temperature in the oven never exceeded 100 degrees Celsius to ensure that clay bound water was not lost. Benchmark tests were performed to determine if the use of salol and soaking in Toluene altered the subcritical index value. Samples were polished without salol, by using wax to adhere the sample to the backing plate. Wax was applied at the corners away from the center of the sample, where the fracture propagates. The high viscosity of the wax prevented it from penetrating into the sample, removing the need for Toluene cleaning. The samples were placed in the oven for 2 days to remove any remaining oil. Five sandstone samples prepared with salol and cleaned with Toluene had an average subcritical index of 53±11 (11 tests) whereas the two samples prepared with wax had a subcritical index of 59±11 (5 tests). These tests show that sample preparation with salol followed by Toluene cleaning does not change the subcritical index value.

Pletka et al. (1979) argued that the absence of a pre-crack should influence the subcritical fracture response. Specifically, the stress intensity factor required for initiating a fracture when the sample is not pre-cracked should be larger than the stress intensity obtained during subsequent testing (Pletka et al., 1979). However, test results from 3 Travis Peak samples (sandstones) indicate no systematic variations between the length of the pre-crack and the subcritical index value (Fig. 2.6A) or the stress intensity factor obtained at a crack velocity of 5×10^{-6} (m/s) (Fig. 2.6B). The changes in subcritical growth response from one sample to another are far larger than those found within one sample. Identical results were obtained for notched, un-notched, and pre-cracked samples. None of these showed systematic changes in subcritical index or stress intensity factor due to the pre-crack or notch configuration. Nevertheless, to ensure uniformity, all but the Travis Peak samples were notched prior to testing.

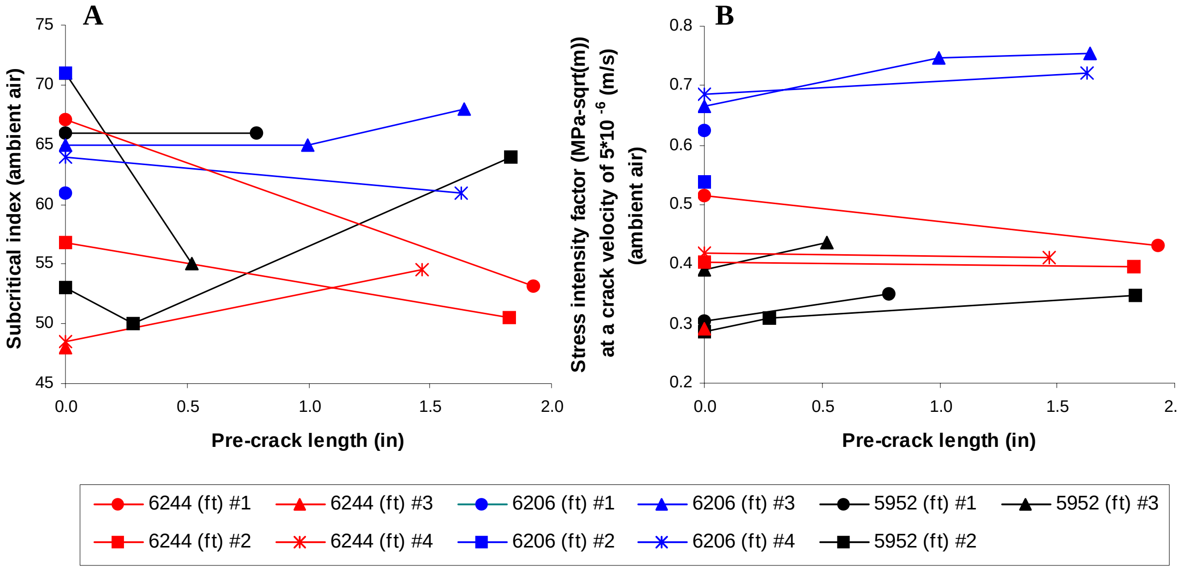

Figure 2.6: A) Pre-crack length (in) vs. subcritical index in ambient air. B) Pre-crack length (in) vs. the stress intensity factor (MPa-sqrt(m)) at a crack velocity of 5×10^{-6} (m/s) in ambient air. All samples are from the Travis Peak Formation, where black curves are from a depth of 5952 ft, blue curves are from 6206 ft depth, and red curves are from 6244 ft depth. No apparent correlation is found between the length of the pre-crack and the subcritical index value or the stress intensity factor.

2.4 TEST RESULTS

Unlike, for instance, Young's modulus and Poisson's ratio testing, subcritical index testing of sedimentary materials has been limited. Atkinson and Meredith (1987b) list a number of authors who have performed subcritical tests on rocks. However, only 4 sandstone formations are reported, totaling 9 different subcritical index values (Atkinson and Meredith, 1987b). Therefore, comparison of the obtained subcritical measurements to a large body of data is not possible. The present study is the largest single body of subcritical index measurements on sedimentary rocks available to date. Furthermore, comparison of individual subcritical index values to values obtained in literature is difficult because microstructure and mineral content are not the same between the samples presented in literature and this study. The method employed here has been extensively described in metals and ceramics, and tests performed in glass will be discussed to calibrate the method used in this study. Following this calibration, results obtained in sedimentary materials are discussed.

2.4.1 Glass

Subcritical fracture growth in glass has been investigated extensively (Charles, 1958a, 1958b; Wiederhorn, 1967; Wiederhorn and Bolz, 1970; Evans, 1972; Cook and Liniger, 1993; Bhatnagar et al., 2000). The results show that the subcritical index for Soda Lime Silica (SLS) glass ranges from 14 to 23 in water and can range from 17 to 26 in dry conditions (either air or dry N_2) (Wiederhorn, 1967; Evans, 1972; Bhatnagar et al., 2000).

Wiederhorn (1967) performed tests on glass microscope slides with varying Relative Humidity (RH) (0.17% to 100%) using the Double Cantilever Cleavage (DCC) arrangement (Fig. 2.7). A DCC test is different from a Double Torsion Beam (DTB) test in that the velocity of the crack is directly measured during a DCC test. In a DTB test

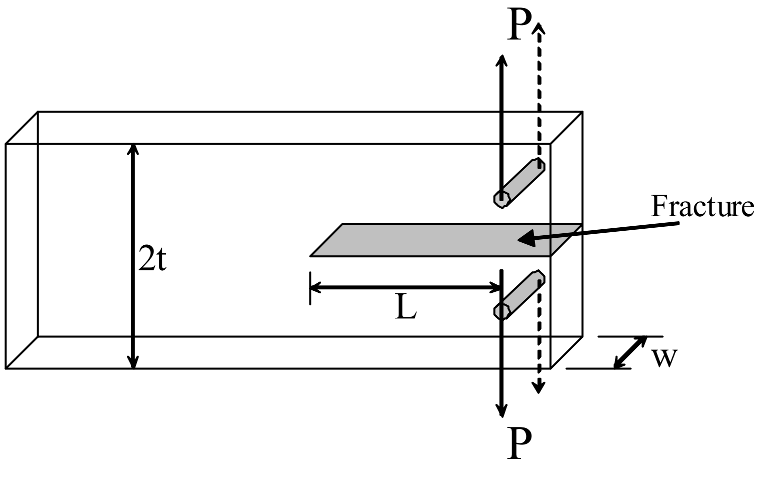

Figure 2.7: Double Cantilever Cleavage arrangement (after Wiederhorn, 1976), where P signifies the applied loading.

crack velocity is not measured but calculated based on the sample compliance. The subcritical indices, as calculated from the curves presented by Wiederhorn (1967), range from approximately 20 to 26. Based on these results, Wiederhorn (1967) concluded that an increase in RH decreases the subcritical index. He also noticed that the stress intensity factor at a given crack velocity decreases as the RH increases (Fig. 2.8). Wiederhorn's (1967) tests in water were matched by Evans (1972) who used a Double Torsion Beam (DTB) setup. Therefore, Wiederhorn's (1967) results are used to calibrate the employed experimental setup.

Figure 2.8 shows both the results as published by Wiederhorn (1967) and the results obtained in the present study. Each line represents a separate test (red curves = 5 ambient air tests, and blue curves = 4 fresh water tests). It is unclear if the data presented by Wiederhorn (1967) is an average over multiple tests or not. Figure 2.8 shows a close match between the published data and the experimental results obtained here. When performing tests on samples in ambient air the RH is not controlled. Also the sample dimensions and pre-crack length are not identical for all samples, nor does the crystal configuration remain the same between each sample. All these factors explain the observed data spread. Figure 2.8 also shows a direct transition from region 1 behavior to region 3 behavior. This could indicate that transport of reactive species to the crack tip is not a limiting factor in these experiments. Interpreting the vertical portion of the plots as the fracture toughness value, implies an experimental fracture toughness range from ~0.6-0.7 MPa-sqrt(m) for glass. This is only slightly lower than the range (~0.7-0.8 MPa-sqrt(m)) reported in literature (Wiederhorn et al, 1982; Bhatnagar et al., 2000). The obtained subcritical index value for glass in ambient air is 26±6, and in water the subcritical index drops to 20±3.

From the experimental scatter as shown in Figure 2.8, it is apparent that the correlations found by Wiederhorn (1967) between RH and subcritical index cannot be substantiated by the test results presented in this study. The subcritical index does not show a variation outside one standard deviation as water is introduced to the sample. However, the reduction in stress intensity factor at a given crack velocity when water is introduced into the environment (Fig. 2.8) is similar to that observed here.

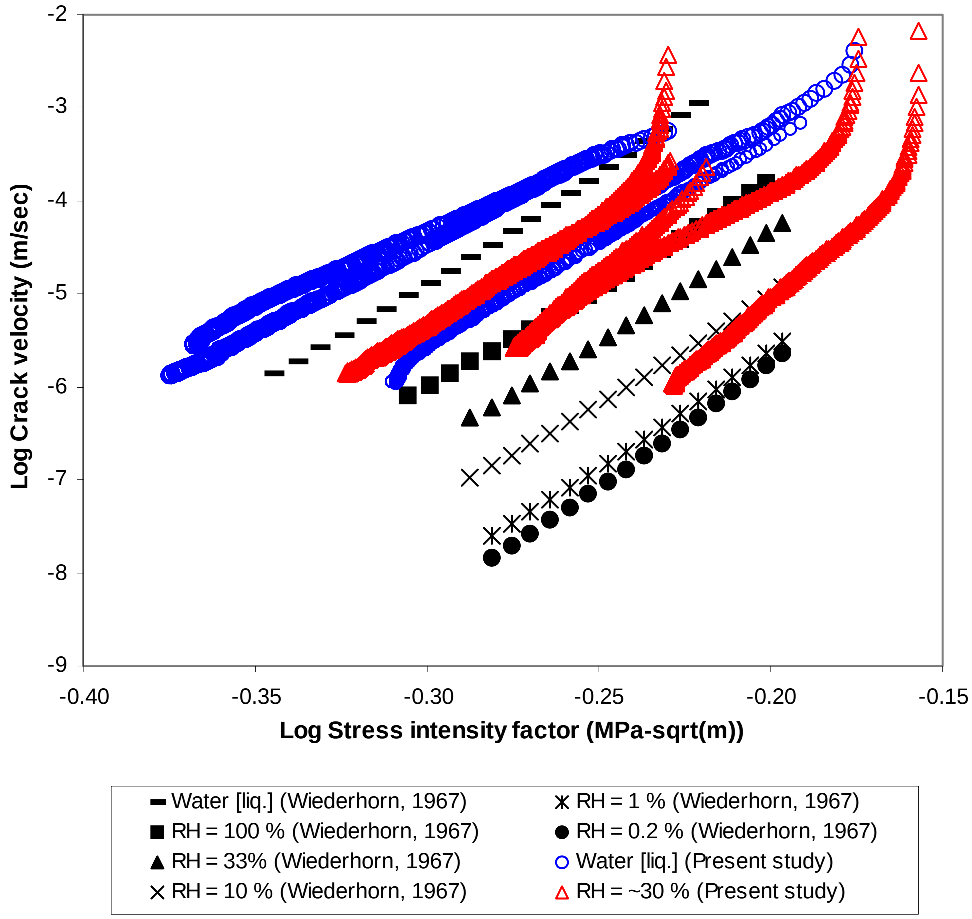

Figure 2.8: Log of stress intensity factor vs. log of crack velocity for glass samples. The black curves are recreated from test data published by Wiederhorn (1967), for varying Relative Humidity (RH) values. The red symbols show results from the present study in ambient air (5 tests). The blue symbols show the results obtained in fresh water (4 tests). The results from the study presented here match the results obtained by Wiederhorn (1967).

2.4.2 Sedimentary materials

Subcritical tests were performed on 109 different rock samples from 38 different formations (Table 2.1). Of these samples 82 were sandstones, 4 were siltstones, 1 was a mudstone, and 20 were carbonate rocks. One chert and one shale sample were also tested. Petrographic analysis was performed on 56 samples (Table 2.2). The average stress intensity factor vs. crack velocity curves for 67 samples performed in ambient air are plotted in Figure 2.9. The stress intensity factor shown in the plot is the average stress intensity factor value for all tests performed on the sample (average of ~4 tests). The velocity range in this figure is artificial and resembles the velocity range normally observed during testing. Figure 2.9 shows both a wide spread in stress intensity factor (from 0.02 MPa-sqrt(m) to 2.41 MPa-sqrt(m)) and subcritical index (from 20 to 306).

The average subcritical index of all sandstones is 62±25 (Fig. 2.10). In general, the subcritical indices of carbonate rocks are significantly higher, averaging (120±87). Exceptions are vuggy carbonates (Yates Formation and sample no. 90 from the 2nd Carbonate Formation, Table 2.1), dolopackstones (Clear Fork samples from 6091 ft, 6367 ft, 6484 ft, and 6520 ft) and a dolowackestone (Clear Fork Sample from 6385 ft), which tend to have indices more similar to sandstones. The larger grain sizes and the vuggy porosity are believed to affect the resulting fracture path, and thus the subcritical fracture response, explaining their outlying position.

Table 2.1: Subcritical test results.

Formation	No.	Depth ft	Subcritical index				Relative fracture strength (MPa-sqrt(m))				
			Dry	Wet	Oil	Brine	Dry	Wet	Oil	Brine	
Siliciclastic rocks											
Ankereh	1	outcrop	85 ± 12				1.61 ± 0.13				h*
“	2	outcrop	151 ± 40				1.97 ± 0.11				r*
Berea	3	outcrop	54 ± 6	60 ± 7	65 ± 5	58 ± 7	0.21 ± 0.02	0.14 ± 0.01	0.21 ± 0.03	0.14 ± 0.01	r*
Capaya	4	13449.6	62 ± 11	17							h*
"	5	13464.1	60 ± 6	55							h*
"	6	13468	59 ± 5	37							h*
"	7	13481.5	52 ± 15	48							h*
"	8	13497.1	66 ± 6	46							h*
"	9	13501	62 ± 9	58							h*
"	10	13502	48 ± 16	35							h*
"	11	13513	54 ± 9	55							h*
Cedar Mesa	12	outcrop	42 ± 8	27 ± 3			0.13 ± 0.03	0.08 ± 0.01			r*
“	13	outcrop	50 ± 3	35							h*
Clear Fork	14	6138	40	34							p*
Cloverly	15	outcrop	154 ± 20	88 ± 12	97 ± 11	109 ± 26	2.02 ± 0.16	1.43 ± 0.08	1.56 ± 0.23	1.58 ± 0.11	r*
“	16	outcrop	68 ± 7	81 ± 12	53 ± 16	68 ± 10	1.16 ± 0.06	1.01 ± 0.04	1.23 ± 0.08	1.01 ± 0.02	r*
Cozzette	17	7892	66 ± 17	39 ± 4							h*
"	18	7892	64 ± 16	67 ± 18							h*
"	19	9002	58 ± 6	45 ± 4	60 ± 2	42 ± 7	0.70 ± 0.09	0.47 ± 0.06	0.66 ± 0.02	0.42 ± 0.05	r*
"	20	9041	54 ± 16	43 ± 3	59 ± 15	41 ± 3	0.93 ± 0.09	0.58 ± 0.04	0.94 ± 0.06	0.59 ± 0.04	r*
"	21	9071	50 ± 9	41 ± 3	50 ± 7	41 ± 3	0.92 ± 0.12	0.58 ± 0.07	0.94 ± 0.06	0.63 ± 0.09	r*
Dakota	22	7068	57 ± 12	38 ± 12							h*
"	23	7090	47 ± 11	20 ± 4							h*
"	24	7099	60 ± 8	41 ± 1							h*
"	25	7112	46 ± 5	11 ± 1							h*
"	26	7186	62 ± 9	37 ± 8							h*
"	27	7198	44 ± 5								h*
"	28	7205	37 ± 4								h*
"	29	7218	41 ± 7								h*
"	30	7225	74 ± 10	50 ± 8							h*

Table 2.1: Cont.

Formation	No.	Depth ft	Subcritical index				Relative fracture strength (MPa-sqrt(m))				
			Dry	Wet	Oil	Brine	Dry	Wet	Oil	Brine	
Siliciclastic rocks (cont.)											
Dakota	31	7227	84 ± 11	90 ± 39							h*
"	32	7236	138 ± 36	93 ± 30							h*
"	33	7210.5	59 ± 7								h*
Flathead	34	outcrop	77 ± 11	66 ± 26	119 ± 16		1.59 ± 0.07	1.35 ± 0.15	1.76 ± 0.11		r*
Fort Union	35	outcrop	50 ± 6	23 ± 2	45 ± 7	24.5 ± 1	0.53 ± 0.05	0.22 ± 0.02	0.62 ± 0.03	0.25 ± 0.02	r*
Frontier	36	outcrop	15 ± 5								h*
“	37	outcrop	41 ± 7				0.02 ± 0.01				r*
“	38	outcrop	96 ± 7	46 ± 4	85 ± 8	35 ± 4	0.97 ± 0.14	0.69 ± 0.09	0.87 ± 0.19	0.64 ± 0.08	r*
Gannett	39	outcrop	151 ± 51	90 ± 8	268		1.79 ± 0.22	1.90 ± 0.12	2.25		r*
“	40	outcrop	70 ± 9	62 ± 5	73 ± 11	53 ± 4	0.96 ± 0.11	0.74 ± 0.11	0.98 ± 0.11	0.66 ± 0.11	r*
Honaker Trail	41	outcrop	63 ± 9	25			1.59 ± 0.19	1.14			h*
La Boca	42	outcrop	43 ± 10				0.22 ± 0.03				r*
"	43	outcrop	60 ± 6				0.81 ± 0.09				r*
Moenkopi	44	outcrop	43 ± 5		51 ± 5	21 ± 7	0.57 ± 0.04		0.58 ± 0.04	0.10 ± 0.03	r*
Nugget	45	outcrop	27 ± 9				0.02 ± 0.01				r*
“	46	outcrop	77 ± 15	70 ± 11			1.42 ± 0.06	1.34 ± 0.12			r*
Point of Rocks	47	9025.8	45 ± 2	29 ± 2	53 ± 2	38 ± 2	0.21 ± 0.04	0.08 ± 0.01	0.21 ± 0.03	0.10 ± 0.03	r*
"	48	9038.8	44 ± 3	28 ± 3	47 ± 3	35 ± 3	0.22 ± 0.02	0.07 ± 0.01	0.27 ± 0.02	0.11 ± 0.01	r*
"	49	9239.9	52 ± 5	24 ± 2	52 ± 6	40 ± 3	0.33 ± 0.15	0.08 ± 0.02	0.34 ± 0.14	0.27 ± 0.03	r*
"	50	9615.8	20 ± 4				0.02 ± 0.01				r*
"	51	9707.7	54 ± 2	30 ± 3	49 ± 3	36 ± 3	0.32 ± 0.03	0.12 ± 0.01	0.26 ± 0.05	0.15 ± 0.02	r*
"	52	9710.6	82 ± 9	27 ± 2	74 ± 7	26 ± 2	0.77 ± 0.19	0.50 ± 0.04	0.83 ± 0.08	0.50 ± 0.04	r*
"	53	9738.8	53 ± 3		63 ± 2	40 ± 1	0.40 ± 0.10		0.45 ± 0.04	0.30 ± 0.04	r*
"	54	9771.9	34 ± 6	23 ± 4	41 ± 4	22 ± 3	0.09 ± 0.02	0.04 ± 0.01	0.09 ± 0.02	0.04 ± 0.01	r*
"	55	9804	45 ± 4		46 ± 2	29 ± 9	0.16 ± 0.04		0.12 ± 0.02	0.07 ± 0.00	r*
"	56	10033.9	41 ± 3	37 ± 5	41 ± 3	33 ± 4	0.10 ± 0.02	0.08 ± 0.01	0.12 ± 0.01	0.07 ± 0.01	r
Rosa Blanco	57	5929	78 ± 8								h*
Sandstone 1	58	core	89 ± 8				0.96 ± 0.05				r*
"	59	core	87 ± 6				1.08 ± 0.03				r*
"	60	core	90				1.53				r*
"	61	core	72 ± 11				0.90 ± 0.04				r*
San Juan	62	14327	46 ± 12	59 ± 8							h*
“	63	14547	59 ± 17	50 ±							h*

Table 2.1: Cont.

Formation	No.	Depth ft	Subcritical index				Relative fracture strength (MPa-sqrt(m))				
			Dry	Wet	Oil	Brine	Dry	Wet	Oil	Brine	
Siliciclastic rocks (cont.)											
San Juan	64	13979	47 ± 6	45 ± 2	49 ± 8	38 ± 3	0.60 ± 0.05	0.52 ± 0.08	0.59 ± 0.02	0.47 ± 0.10	r*
Scioto	65	outcrop	35	25							p*
“	66	outcrop	52 ± 17	36							p*
“	67	outcrop	42 ± 2	44 ± 3		43 ± 3	0.39 ± 0.03	0.26 ± 0.03		0.27 ± 0.02	r*
Spraberry	68	core	48 ± 6	54 ± 2	47 ± 12		0.98 ± 0.05	0.83 ± 0.05	0.97 ± 0.02		r*
Stump	69	outcrop	41 ± 6	53.5 ± 12		51 ± 2	0.34 ± 0.07	0.15 ± 0.06		0.23 ± 0.02	r*
“	70	outcrop	82 ± 15				1.54 ± 0.02				h*
Thermopolis	71	outcrop	53 ± 3				0.38 ± 0.01				r*
Tennessee	72	2746 m	75 ± 9	74 ± 4	69 ± 8	58 ± 5	0.85 ± 0.17	0.55 ± 0.02	0.78 ± 0.05	0.61 ± 0.08	r*
Tensleep	73	outcrop	70 ± 8	60 ± 6	80 ± 11		0.74 ± 0.05	0.69 ± 0.02	0.77 ± 0.04		r*
Travis Peak	74	5952	61 ± 8	70 ± 7			0.34 ± 0.05	0.23 ± 0.05			r*
"	75	5962	50 ± 12	26			0.77 ± 0.11	0.15			r*
"	76	6206	65 ± 3	66 ± 5			0.67 ± 0.08	0.53 ± 0.09			r*
"	77	6244	54 ± 6	52	56 ± 8	49 ± 3	0.47 ± 0.07	0.27	0.54 ± 0.04	0.49 ± 0.03	r*
"	78	6270	61 ± 14	54 ± 16			0.91 ± 0.17	0.73 ± 0.09			r*
"	79	6295	51 ± 12	58 ± 7			0.85 ± 0.15	0.66 ± 0.16			r*
"	80	6633	78 ± 17				1.23 ± 0.26				r*
"	81	7457	57 ± 17	56 ± 9			0.62 ± 0.21	0.73 ± 0.05			r*
"	82	7506	59 ± 15	70 ± 8			0.83 ± 0.17	0.85 ± 0.08			r*
"	83	7737	41 ± 8	63 ± 9			1.06 ± 0.17	1.13 ± 0.12			r*
"	84	9817	56 ± 11	60 ± 15			0.86 ± 0.21	0.93 ± 0.14			r*
"	85	9837	69 ± 8		82 ± 4		0.86 ± 0.10		0.71 ± 0.07		r*
"	86	9880	54 ± 8	87 ± 7	70 ± 1		0.50 ± 0.08	0.83 ± 0.03	0.80 ± 0.07		r*
"	87	10141	73 ± 22	54 ± 16			1.36 ± 0.24	1.29 ± 0.24			r*
Carbonate rocks											
Carbonate 1	88	2620 m	64 ± 19			25 ± 4	0.54 ± 0.10			0.35 ± 0.06	r*
Carbonate 2	89	7771.7	179 ± 15	103 ± 20	144 ± 4	91 ± 17	1.32 ± 0.14	1.12 ± 0.15	1.56 ± 0.42	1.04 ± 0.14	r*
"	90	7727.5	59 ± 4				0.59 ± 0.07				r*
Carbonate 3	91	2076 m	76 ± 6			29 ± 8	0.88 ± 0.06			0.53 ± 0.05	r*
“	92	1807 m	151 ± 40			21 ± 9	0.75 ± 0.20			0.52 ± 0.07	r*
Clear Fork	93	6091	43 ± 8	37 ± 9							p*
"	94	6367	60 ± 18	53 ± 15							p*
"	95	6385	81 ± 15	70 ± 4							p*

Table 2.1: Cont.

Formation	**No.**	**Depth ft**	**Subcritical index**				**Relative fracture strength (MPa-sqrt(m))**				
			Dry	**Wet**	**Oil**	**Brine**	**Dry**	**Wet**	**Oil**	**Brine**	
Carbonate rocks (cont.)											
Clear Fork	96	6484	43 ± 10	37							p*
"	97	6520	38 ± 8	30 ± 6							p*
Cupido	98	outcrop	262 ± 44	104 ± 7	238 ± 21		1.24 ± 0.12	1.18 ± 0.26	1.05 ± 0.11		r*
"	99	outcrop	306 ± 33	145 ± 17			0.95 ± 0.09	1.13 ± 0.08			r*
Honaker Trail	100	outcrop	271 ± 58	41 ± 22							h*
"	101	outcrop	250 ± 113								h*
Austin Chalk	102	5585	124	42							p*
"	103	5573	95	20							p*
Knox	104	14516	97 ± 23	56 ± 6							h*
Texas Crème	105	outcrop	98 ± 31	41 ± 7	42 ± 3	20 ± 4	0.28 ± 0.11	0.14 ± 0.01	0.23 ± 0.06	0.18 ± 0.07	r*
Yates	106	1347	32 ± 6	44 ± 8							h*
"	107	1427	64 ± 13								h*
Others											
Barnett Shale	108	7692	289 ± 50				1.05 ± 0.05				r*
Devonian Chert	109	13690	286 ± 35				2.41 ± 0.10				r*
Glass	110	na	26 ± 6	20 ± 3			0.54 ± 0.05	0.48 ± 0.04			r*

*h = tests performed by J. Holder, p = tests performed by Z. Philip, r = tests performed by P. Rijken.

Table 2.2: Thin-section information.

Formation	No.[1]	Depth	RH[2]	Grain size	Quartz		Carbonate cement		Feldspars		Clay	Porosity	Tortuosity
					Grains	Cement	Ferroan Dolomite	(Ferroan) Calcite	Plagioclase	K-Spar			
		ft	%	mm	%[3]	%[3]	%[3]	%[3]	%[3]	%[3]	%[3]	%[3]	
Siliciclastic rocks													
Ankereh	1	outcrop	41	0.14 ± 0.09	44.50	12.00	0.00	0.00	16.50	2.50	23.50	1.00	-
Berea	3	outcrop	49	0.16 ± 0.07	59.75	3.25	0.75	0.25	2.00	5.50	8.75	19.75	1.16
Cedar Mesa	12	outcrop	56	0.13 ± 0.05	57.83	16.67	0.17	0.17	0.00	4.50	4.33	16.33	1.15
Cloverly	15	outcrop	28	0.10 ± 0.04	57.25	25.25	0.00	0.00	11.00	5.25	1.00	0.25	1.08
"	16	outcrop	28	0.13 ± 0.04	62.50	19.00	0.00	0.00	0.00	18.25	0.00	0.25	1.10
Cozzette	19	9002	43	0.23 ± 0.11	55.50	21.50	0.00	0.00	0.00	4.00	19.00	0.00	1.13
"	20	9041	38	0.19 ± 0.07	57.50	18.00	0.00	0.00	0.50	5.00	18.50	0.50	1.15
"	21	9071	40	0.15 ± 0.05	56.00	20.50	0.50	0.00	1.50	1.50	20.00	0.00	1.12
Flathead	34	outcrop	38	0.33 ± 0.29	67.75	13.00	0.00	0.00	0.00	18.25	0.00	1.00	1.13
Fort Union	35	outcrop	22	0.02 ± 0.01	40.33	0.00	9.50	0.17	2.17	1.17	46.67	0.00	1.04
Frontier	37	outcrop	54	0.20 ± 0.07	54.00	1.00	0.00	0.00	2.00	0.00	3.50	39.50	1.19
"	38	outcrop	38	0.18 ± 0.06	52.00	1.00	0.00	25.75	0.00	13.00	8	0.25	1.16
Gannett	39	outcrop	47	0.09 ± 0.03	57.50	5.25	0.00	29.50	0.00	0.75	7.00	0.00	1.06
"	40	outcrop	53	0.18 ± 0.05	61.00	19.00	0.00	0.00	0.75	3.25	16.00	0.00	1.16
Honaker Trail	41	outcrop	44	0.05 ± 0.02	52.00	0.00	0.00	26.00	0.00	3.00	19.00	0.00	1.06
Moenkopi	44	outcrop	55	0.05 ± 0.03	50.75	0.00	1.00	0.50	0.25	10.25	37.25	0.00	1.09
Nugget	45	outcrop	27	0.19 ± 0.10	58.00	4.88	0.00	0.25	0.13	9.63	2.63	24.50	1.14
"	46	outcrop	55	0.13 ± 0.04	59.00	27.00	0.00	0.00	0.00	11.75	0.75	1.50	1.10
Point of Rocks	47	9025.8	45	0.31 ± 0.17	45.00	0.25	0.50	2.00	10.75	15.00	15.75	10.75	1.16
"	48	9038.8	45	0.32 ± 0.19	42.50	0.00	1.50	1.50	12.25	17.25	16.25	8.75	1.14
"	49	9239.9	37	0.26 ± 0.21	43.75	0.25	1.75	2.00	17.75	19.75	12.5	2.25	1.12
"	50	9615.8	45	0.26 ± 0.14	36.17	0.83	0.00	0.50	16.00	24.17	15.50	6.83	1.20
"	51	9707.7	26	0.28 ± 0.18	48.67	0.00	0.00	2.50	17.50	14.67	10.83	5.83	1.19
"	52	9710.6	25	0.26 ± 0.14	37.25	0.00	11.00	10.50	14.25	17.50	9.25	0.25	1.20
"	53	9738.8	25	0.27 ± 0.14	47.50	0.25	2.50	5.50	11.75	17.25	11.75	3.50	1.21
"	54	9771.9	26	0.22 ± 0.13	36.38	1.00	0.00	1.38	21.38	21.13	12.38	6.38	1.26
"	55	9804	34	0.34 ± 0.18	43.33	0.33	1.67	3.00	19.17	17.17	11.67	3.67	1.25
"	56	10033.9	43	0.32 ± 0.19	48.50	2.25	0.00	0.38	10.63	18.25	10.13	9.88	1.21
San Juan	64	13979	43	0.28 ± 0.15	67.33	13.00	0.00	0.00	0.00	3.00	7.83	8.83	1.17
Scioto	67	outcrop	27	0.06 ± 0.02	49.00	3.00	0.50	0.00	1.00	11.50	18.25	16.75	1.12

Table 2.2: Cont.

Formation	No.[1]	Depth	RH[2]	Grain size	Quartz		Carbonate cement		Feldspars		Clay	Porosity	Tortuosity
					Grains	Cement	Ferroan Dolomite	(Ferroan) Calcite	Plagioclase	K-Spar			
		ft	%	mm	%	%	%	%	%	%	%	%	
Siliciclastic rocks (cont.)													
Spraberry	68	core	49	0.05 ± 0.02	56.00	6.25	1.00	1.75	0.25	6.25	27.75	0.75	1.09
Stump	69	outcrop	28	0.26 ± 0.11	72.93	7.02	0.00	0.00	0.00	11.53	0.50	8.02	1.23
Thermopolis	71	outcrop	45	0.16 ± 0.05	61.00	19.00	0.00	0.00	0.00	1.00	2.50	16.50	1.16
Tennessee	72	2746 m	40	0.11 ± 0.04	66.00	12.00	0.00	0.00	1.50	3.25	15.25	2.00	1.15
Ten Sleep	73	outcrop	56	0.13 ± 0.05	52.00	18.50	0.00	0.00	4.50	16.75	1.00	7.25	1.17
Travis Peak	74	5952	49	0.15 ± 0.06	65.38	12.38	1.13	0.75	0.00	1.75	0.88	17.75	1.18
“	75	5962	42	0.15 ± 0.06	41.75	0.75	40.25	16.00	0.00	0.75	0.50	0.00	1.07
“	76	6206	52	0.11 ± 0.04	58.67	16.83	1.17	1.00	0.00	6.67	1.50	14.17	1.13
“	77	6244	48	0.14 ± 0.04	53.50	21.50	0.00	0.00	2.50	6.50	0.00	16.00	1.17
“	78	6270	48	0.09 ± 0.04	49.00	10.50	37.50	1.00	0.00	0.50	0.50	1.00	1.10
“	79	6295	42	0.11 ± 0.03	60.00	14.00	1.75	1.25	4.25	9.25	0.75	8.75	1.09
“	80	6633	34	0.10 ± 0.03	55.00	14.50	14.00	5.00	1.25	4.50	1.25	4.50	1.08
“	81	7457	41	0.16 ± 0.06	66.50	20.00	0.00	0.00	2.00	3.50	1.50	6.50	1.16
“	82	7506	50	0.15 ± 0.06	61.00	23.00	0.00	0.50	1.50	5.00	3.50	5.50	1.11
“	83	7737	33	0.07 ± 0.03	63.25	16.50	1.00	0.25	0.00	2.75	13.50	2.75	1.10
“	84	9817	45	0.17 ± 0.05	73.50	18.50	0.00	0.00	1.00	3.50	1.00	2.50	1.13
“	85	9837	48	0.20 ± 0.05	54.00	21.00	17.50	0.00	0.00	1.50	0.00	6.00	1.11
“	86	9880	38	0.23 ± 0.06	66.50	19.50	0.00	0.00	0.00	5.00	5.00	4.00	1.13
“	87	10141	47	0.07 ± 0.04	60.50	19.00	4.00	3.50	0.00	5.00	8.00	0.00	1.10
Carbonates													
Carbonate 2	89	7771.1	47	-	0.00	0.00	0.00	99.50	0.00	0.00	0.50	0.00	1.07
“	90	7727.5	50	0.21 ± 0.15	0.00	0.00	0.00	87.50	0.00	0.00	1.00	11.50	1.11
Carbonate 3	91	2076 m	55	0.03 ± 0.01	0.00	0.00	48.00	0.00	0.00	0.00	52.00	0.00	1.04
“	92	1807 m	55	0.01 ± 0.01	0.00	0.00	45.00	0.50	0.00	0.00	54.50	0.00	1.03
Cupido	98	outcrop	33	0.02 ± 0.01	0.00	0.00	92.13	0.00	0.00	0.00	7.88	0.00	1.04
“	99	outcrop	44	-	0.00	0.00	100.00	0.00	0.00	0.00	0.00	0.00	1.01
Others													
Barnett shale	108	7692	39	-	0.00	0.00	0.00	0.00	0.00	0.00	100.00	0.00	1.01

[1] numbers in this column correspond to the numbers in Table 2.1

[2] RH = Relative Humidity

[3] Volume percent

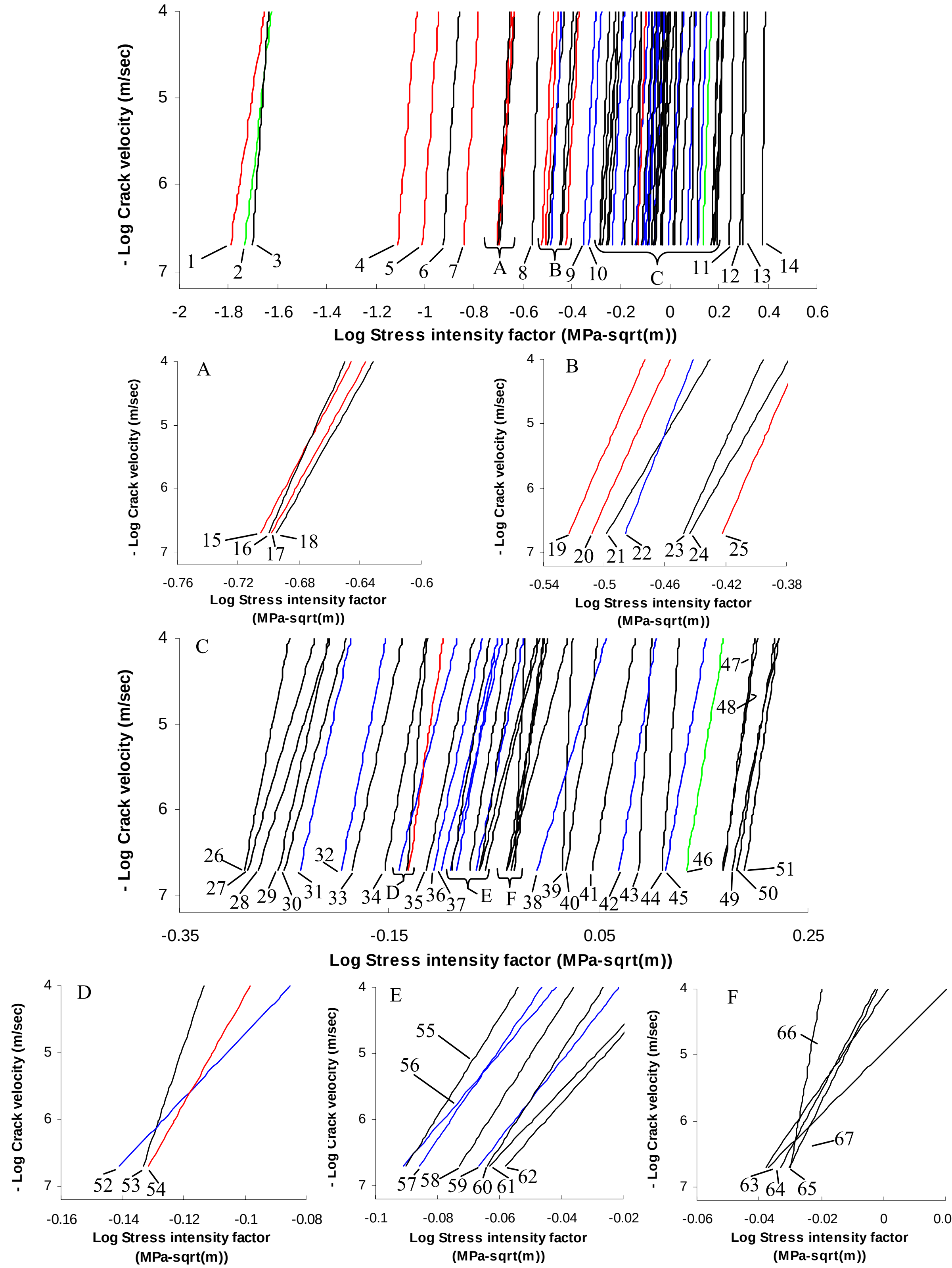

Fig. 2.9 (see caption on following page)

Legend table

No.	Formation	Depth (ft)	No.	Formation	Depth (ft)
1.	Point of Rocks	9615.8	35.	La Boca	outcrop
2.	Nugget	outcrop	36.	Travis Peak	7506
3.	Frontier	outcrop	37.	Travis Peak	6295
4.	Point of Rocks	9771.9	38.	Travis Peak	7737
5.	Point of Rocks	10033.9	39.	Barnet Shale	7692
6.	Cedar Mesa	outcrop	40.	Sandstone 1	core
7.	Point of Rocks	9804	41.	Cloverly	outcrop
8.	Texas Crème	outcrop	42.	Travis Peak	6633
9.	Travis Peak	6244	43.	Cupido	outcrop
10.	Travis Peak	9880	44.	Carbonate 2	7771.7
11.	Gannett	outcrop	45.	Travis Peak	10141
12.	Ankereh	outcrop	46.	Nugget	outcrop
13.	Cloverly	outcrop	47.	Sandstone 1	core
14.	Devonian Chert	13690	48.	Stump	outcrop
15.	Point of Rocks	9025.8	49.	Honaker Trail	outcrop
16.	Berea sandstone	Outcrop	50.	Flathead	outcrop
17.	Point of Rocks	9038.8	51.	Ankereh	outcrop
18.	La Boca	outcrop	52.	Travis Peak	5962
19.	Point of Rocks	9707.7	53.	Carbonate 3	1807 (m)
20.	Point of Rocks	9239.9	54.	Point of Rocks	9710.6
21.	Stump	outcrop	55.	Tennessee Sst.	core
22.	Travis Peak	5952	56.	Travis Peak	9817
23.	Thermopolis	outcrop	57.	Travis Peak	9837
24.	Scioto	outcrop	58.	Carbonate 3	2076 (m)
25.	Point of Rocks	9738.8	59.	Travis Peak	6270
26.	Gaviota	2620 (m)	60.	Sandstone 1	core
27.	Moenkopi	outcrop	61.	Cozzette	9071
28.	Fort Union	outcrop	62.	Cozzette	9041
29.	Carbonate 2	7727.5	63.	Gannet	Outcrop
30.	San Juan	13979	64.	Sprayberry	core
31.	Travis Peak	7457	65.	Sandstone 1	core
32.	Travis Peak	6206	66.	Cupido	outcrop
33.	Cozzette	9002	67.	Frontier	outcrop
34.	Ten Sleep	outcrop			

Figure 2.9: Log of stress intensity factor vs. log of crack velocity for 67 samples. The curves are average curves of approximately 4 tests each. The numbers on the plots correspond to the formation given in the legend table. Red curves are the Point of Rocks Formation, blue curves are Travis Peak Formation and green curves are the Nugget Formation, all other curves are black.

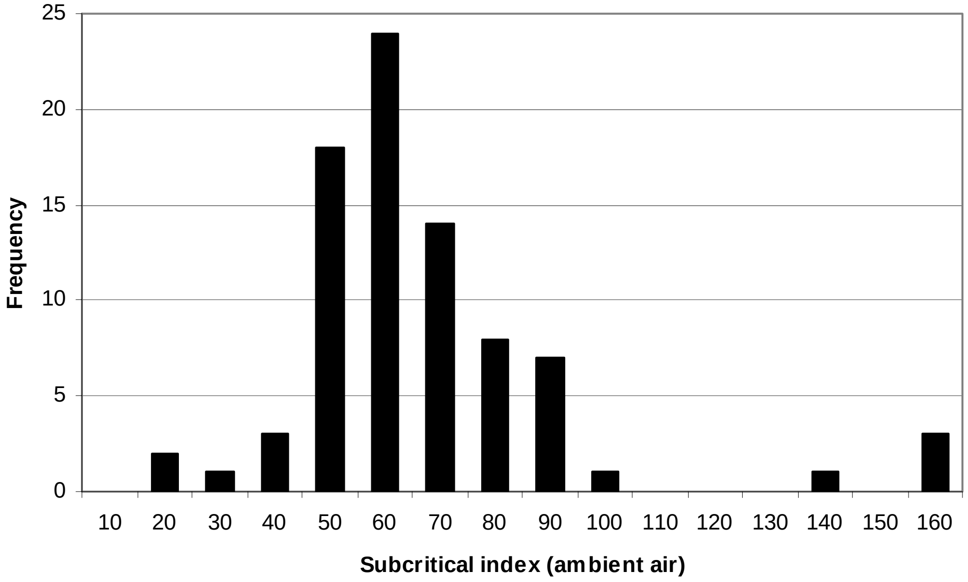

Figure 2.10: Histogram of the subcritical index values measured in ambient air for all 82 sandstone samples.

Some formations exhibit distinct clustering about particular regions of the stress intensity factor axis. For instance, the Point of Rocks Formation falls at the low end of the stress intensity factor axis (red curves in Figure 2.9). Since the stress intensity factor required for fracturing is a measure of the material's strength, the Point of Rocks Formation is considered weaker than the other formations tested. Less energy is required to initiate a subcritical fracture in this formation than, for instance, the Travis Peak Formation (blue curves in Figure 2.9). The Travis Peak Formation clusters around a value of 0.8 MPa-sqrt(m), which is very close to the average stress intensity factor value obtained from all tests (average stress intensity factor = 0.79 MPa-sqrt(m)).

However, not all formations show this consistent stress intensity factor clustering. The two Nugget Formation samples place on opposite ends of the stress intensity factor axis (green curves in Figure 2.9). This increase in stress intensity factor from 0.02 MPa-sqrt(m) to 1.42 MPa-sqrt(m) is accompanied by an increase in subcritical index from 27 to 77. Similarly, the Point of Rocks Formation shows a variation in subcritical index from 20 to 80, corresponding to a stress intensity factor range of 0.02 MPa-sqrt(m) to 0.77 MPa-sqrt(m).

To investigate the relationship between placement on the stress intensity factor axis and subcritical index a new parameter is introduced, called the relative fracture strength (RFS). The RFS is defined as the stress intensity factor at a velocity of $5x10^{-6}$ m/s. A crack velocity of $5x10^{-6}$ m/s is chosen since most cracks exhibit this velocity during testing. A plot of the RFS vs. the subcritical index in ambient air for sandstones and carbonates shows a clear correlation for sandstones (Fig. 2.11). As the RFS in sandstones increases, the subcritical index increases. Due to the small range in fracture toughness and rupture velocities of sedimentary materials, all curves on a log-log plot of crack velocity vs. stress intensity factor meet close to one point, as discussed earlier (Atkinson, 1984; Swanson, 1984) (Fig. 2.3). This implies that stronger rocks have steeper slopes (i.e. higher subcritical indices) than weaker rocks, which is consistent with what is observed in Figure 2.11.

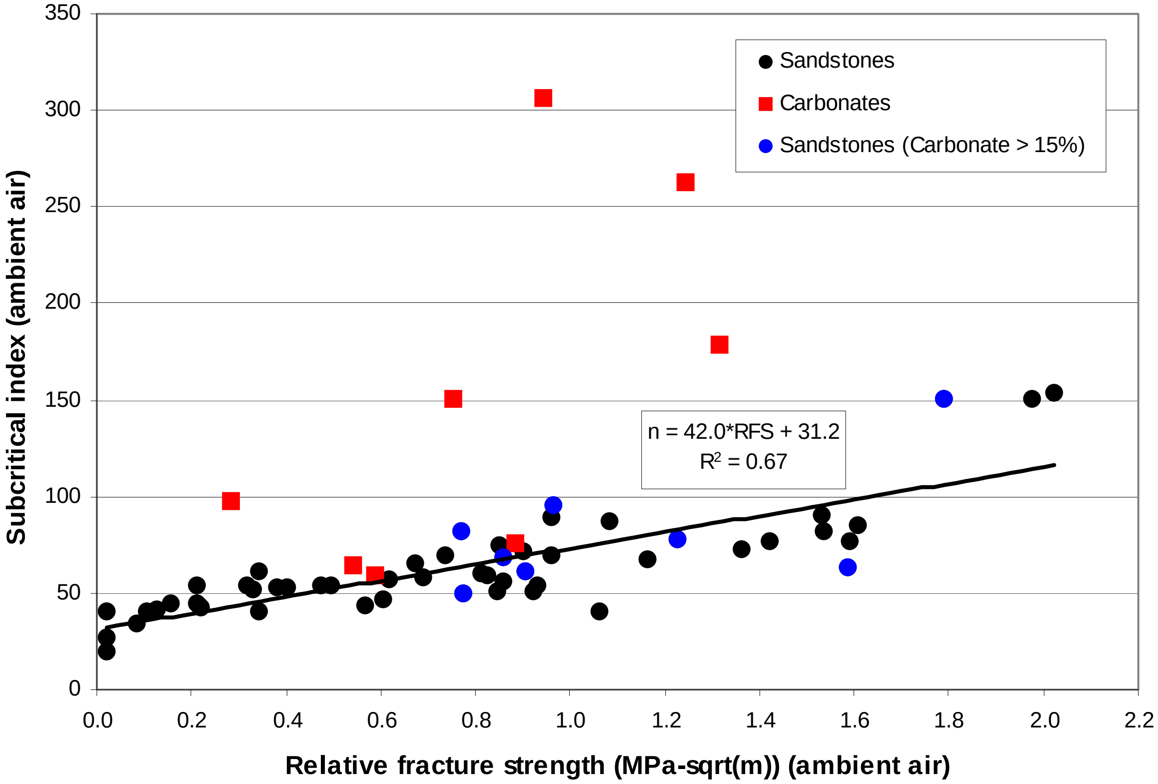

Figure 2.11: Relative fracture strength vs. the subcritical index in ambient air for sandstones and carbonate samples. Sandstones are represented by black symbols and carbonate samples are represented by red symbols. Blue circles represent those sandstone samples with more than 15% carbonate content. The plot shows that the carbonate samples do not follow the same trend as the sandstone samples.

2.4.2.1 Microstructure/petrology

The microstructural aspects controlling subcritical behavior are poorly understood (Atkinson and Meredith, 1987a). It has been shown that different rocks have different subcritical indices (Swanson, 1984; Atkinson, 1984; Atkinson and Meredith, 1987b). Therefore, accurate knowledge of the rock’s composition should aid in understanding the experimental results. For this reason, petrographic analysis was performed on 56 test samples (Table 2.2) after the samples were experimentally cracked. Point-counts were performed on two thin-sections per sample lithology and 200 counts per thin-section were made. The count classifications used were:

- Porosity
- Quartz grains
- Quartz cement
- Ferroan dolomite (grains and cement)
- (Ferroan) calcite = Ferroan calcite and Calcite (grains and cement)
- Clay (detrital and authigenic – undifferentiated)
- Plagioclase
- K-spar

This classification scheme works particularly well for "clean" sandstones (i.e. lacking substantial clay minerals, lithic grains etc.), but is less useful outside this range. If materials were encountered which fell outside the above categories, they were ignored. Normally this was less than 5% of the total count.

2.4.2.1.1 Fracture path

Photomicrographs (Fig. 2.12) of experimental cracks show the inherent complexity of fractures in sedimentary materials, where the blue coloring is blue epoxy filling the void of the artificial crack. Fractures have tortuous traces (Fig. 2.12A), exhibit en echelon (step-like) arrangements (Fig. 2.12B), and display dramatic lateral variation in aperture (Fig. 2.12C). The images show that fractures in these DTB tests grow predominantly through the cement between the grains (intergranular propagation), but fractures occasionally propagate through grains (transgranular propagation) (Fig. 2.12A). Laubach (1988) showed that this pattern typifies some natural fractures formed at depth in basins. Swanson (1980), Mecholsky (1981), Atkinson and Rawlings (1981), and

Meredith and Atkinson (1983) also found experimental fractures predominantly propagate between the grains.

Figure 2.13 shows an example of two natural fractures observed in the Weber Formation and the Nugget Formation. The Weber Formation shows a clear example of an open natural fracture, which has grown between the quartz grains (Fig. 2.13A). The Nugget Formation, on the other hand, shows a clear example of a partially open natural fracture with quartz cement lining, where the fracture propagated through the grains (transgranular) (Fig. 2.13B).

In nature fractures are observed to propagate both transgranularly as well as intergranularly (Fig. 2.13). Transgranular fracture growth might be more common in the subsurface because the compressive stresses in the subsurface might increase the strength of the grain to grain contacts, decreasing the chance of fractures growing along the grain boundaries. Furthermore, all fractures observed in the subsurface need not have propagated subcritically. Another fracture mechanism discussed in literature is dynamic fracture growth, occurring when the energy in the system exceeds the energy required to form new surface area (Sagy et al, 2001). The excess energy is used to accelerate the fracture, leading to large fracture velocities. A few fracture geometries have been associated with dynamic fracture growth: 1) mirror-mist-hackle zonation (Ravi-Chandar and Knauss, 1984; Ravi-Chandar, 1998), where the mirror zone is attributed to the acceleration of the fracture and the mist zone to the stabilization of the fracture at high velocities, 2) large scale branches which propagate away from the main crack (Schardin, 1959; Lawn and Wilshaw, 1975), and 3) small scale or micro-branching (Ravi-Chandar and Knauss, 1984; Sharon and Fineberg, 1996, 1999). Large fracture velocities might lead to an independence of the fracture to small scale heterogeneities, possibly leading to transgranular growth.

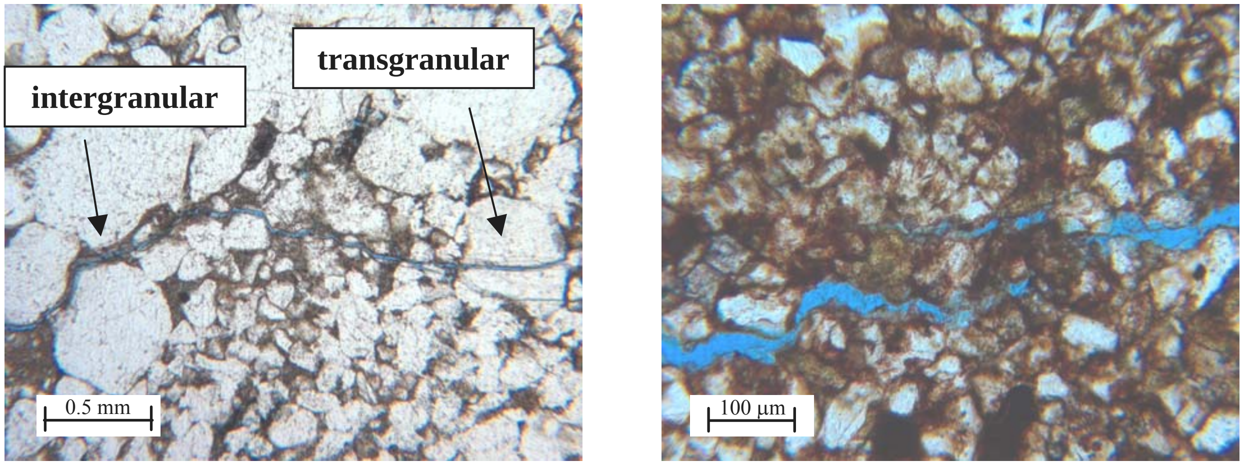
A) Sandstone (Flathead Fm.)

B) Sandstone (Moenkopi Fm.)

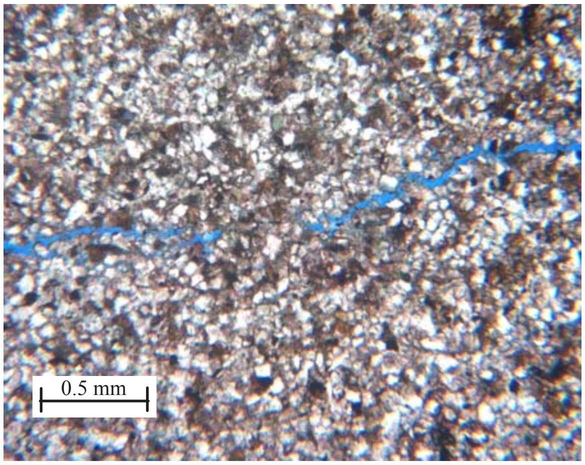
C) Sandstone (Scioto Fm.)

Figure 2.12: Photomicrographs of experimental fractures of 3 test specimens, where the blue coloring delineates the epoxy filled fractures. A) Evidence of growth both through the grains (transgranular) as well as along the grain boundaries (intergranular). B) En echelon character of the crack. C) Changes in fracture aperture.

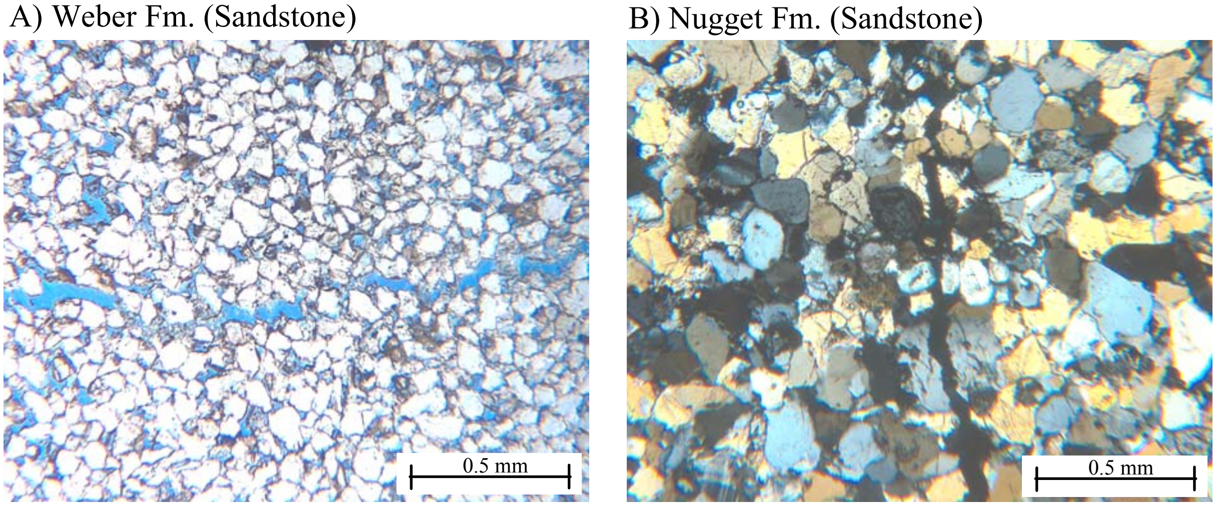

A) Weber Fm. (Sandstone)

B) Nugget Fm. (Sandstone)

Figure 2.13: Photomicrographs of natural fractures. A) Natural fracture which has propagated between the grains (intergranular) (Weber Fm., plane polarized light), B) Natural fracture propagating through the grains (transgranular, crossed polars) (Nugget Fm.). (Pictures by Rob Reed)

The higher subcritical index for carbonates versus sandstones might be related to their microstructural differences. Figure 2.14 shows photomicrographs of experimentally created fractures, one in sandstone and one in carbonate. Gesing and Bradt (1983) have shown an inverse dependence of subcritical index on grain or facet size in polycrystalline ceramics, where an increase in grain size decreases the subcritical index. Although other factors are likely to play a role, the systematically higher indices in carbonates and the smaller effective grain sizes of the carbonate samples vs. the sandstone samples is consistent with the trend predicted by Gesing and Bradt (1983). This observation is further substantiated by the considerably lower subcritical indices of the Texas Crème, the 1st Carbonate Fm. (no. 88), and the Clear Fork Formation (Table 2.1). These samples were larger grained than other carbonate samples and showed considerable lower subcritical index values than, for instance, the small grained Cupido Formation.

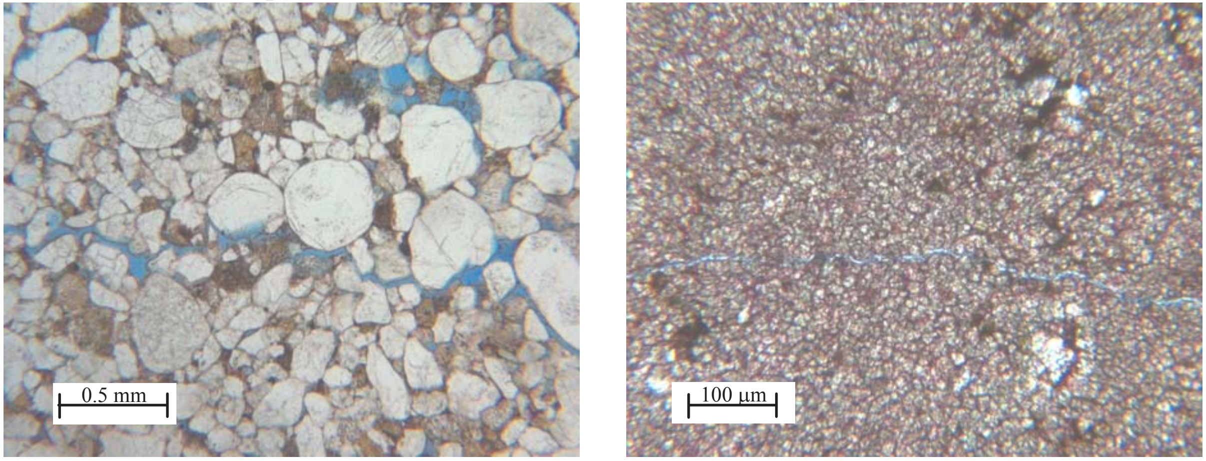

A) Sandstone (Stump Fm.)

B) Carbonate (Cupido Fm.)

Figure 2.14: Photomicrographs of experimental fractures in A) a sandstone, and B) a carbonate rock. The sandstone is larger grained and the crack experiences more fracture wandering. The carbonate is smaller grained and the crack path is straighter. The analysis by Gesing and Bradt (1983) suggests a smaller grain size results in a higher subcritical index.

To investigate the dependence of subcritical index on grain size and fracture path tortuosity, the grain size of 15 grains was measured in two directions (long and short direction) for each thin-section (Table 2.2). Fracture tortuosity was also measured, where tortuosity is defined as the trace length of the fracture divided by the straight tip-to-tip length. If a fracture were perfectly straight the tortuosity would be 1. The more tortuous the fracture path the larger this value becomes. The tortuosity was measured along a path of at least 20 grain lengths through the center of the crack (the average number of grains crossed was 76). Both grain size and tortuosity measurements are limited by the resolution of the microscope. Tortuosity measurements could be made on samples for which the grain size could not be determined. This indicates a measurement truncation exists for the tortuosity values, since the magnification limit does not allow for determination of small scale fracture wandering. Due to this measurement truncation small values of fracture tortuosity are considered suspect. However, a good correlation was found between the tortuosity of the crack and the grain sizes measured in thin-section, even if the small tortuosity (< 1.05) cracks would have been excluded from the fit (Fig. 2.15). Those samples plotting far above the trend line were samples which had more intergranular growth. Plotting the results of all samples tested in air suggests an inverse dependence of subcritical index on tortuosity as well as grain size, in sedimentary materials (Figure 2.16A and B). The grain size correlation is consistent with the theory from polycrystalline ceramics as proposed by Gesing and Bradt (1983) and indicates that this theory might be used as a first approximation to explain subcritical fracture growth in sedimentary materials. However, more data are required to confirm the observed trend, since it could be argued that the observed trend is an artifact of the material type (i.e. quartz vs. carbonate) and not the grain size.

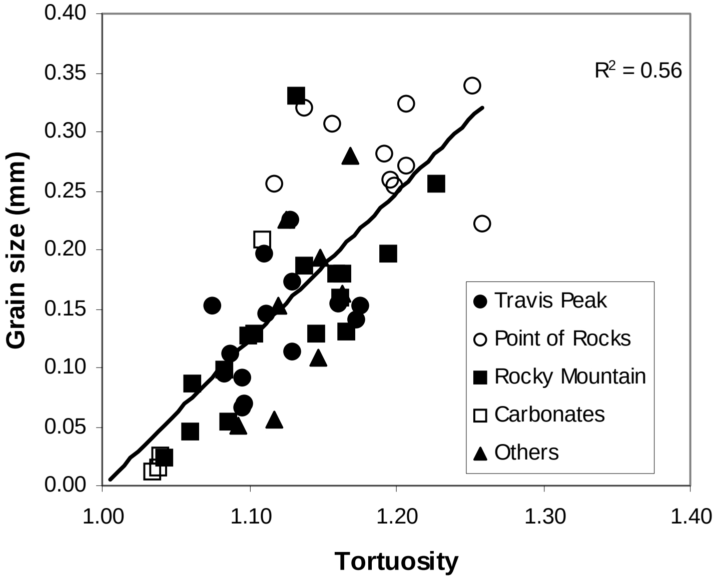

Figure 2.15: Tortuosity vs. grain size. As the grain size increases the tortuosity increases.

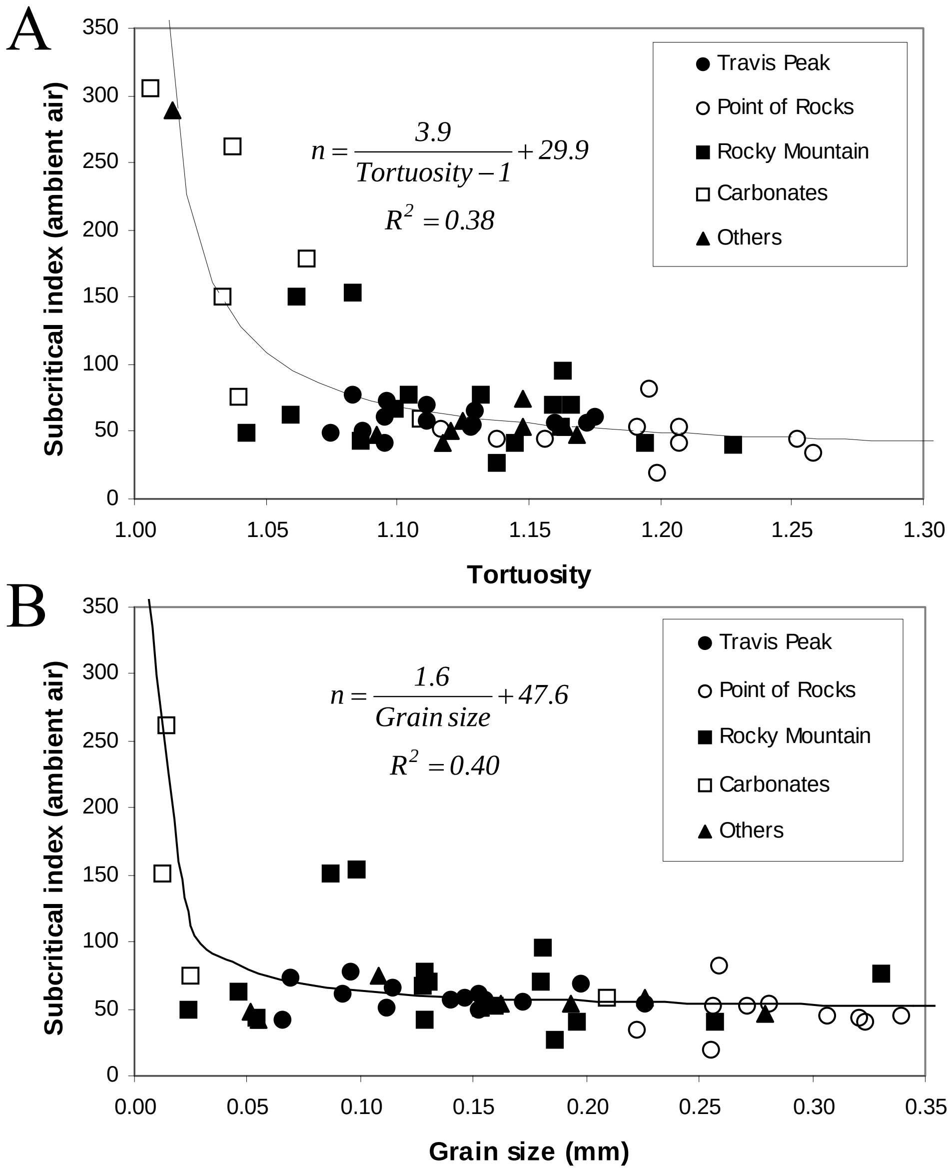

Figure 2.16: A) Tortuosity vs. subcritical index. B) Grain size vs. subcritical index. The analysis by Gesing and Bradt (1983) suggests a smaller grain size results in a higher subcritical index.

2.4.2.1.2 Cement content

A clear increase in subcritical index is observed with an increase in total (ferroan) calcite content (Fig. 2.17). Both carbonate cemented sandstones and a carbonate rock are included in this figure, where the carbonate rock is the open symbol at 100% (ferroan) calcite. As discussed in section 2.4.2, the subcritical index of carbonate samples is higher than that of sandstone samples. Also, as noted in section 2.4.2.1, most experimental fractures grow intergranularly. Therefore, it is logical to assume that the material present between the grains, i.e. the cement, largely governs subcritical fracture growth, and one would expect that an increase in carbonate cement would increase the subcritical index. This point is illustrated by examining the trend of the (ferroan) calcite cemented sandstones only (i.e. eliminating the open symbol in Fig. 2.17). A clear increase in subcritical index is observed as the carbonate cement content increases. Cracks grow through only carbonate material in the 100% carbonate sample, explaining the additional increase in subcritical index this sample exhibits. Since Figure 2.17 is on a logarithmic scale, sandstones without any (ferroan) calcite cement cannot be plotted. Those samples are represented by a range of subcritical index values marked on the y-axis (Fig. 2.17).

One of the main problems in comparing natural rock samples is that with a change in carbonate content other constituents change as well. These other varying factors might obscure the existing correlation. For this reason, only roughly comparable samples were used in Figure 2.17. This means that those samples containing more than 15% clay, 15% feldspars, 15% ferroan dolomite, and 15% quartz cement were eliminated. Those samples exhibiting vuggy porosity were also eliminated since they were microstructurally different. The siltstones were also eliminated from the analysis, but the grain size was not constant in the remaining data set, so it is unclear if its variation affected the results. To determine which effect is most important, a suite of tests should be performed in which the grain size is kept constant and the amount of (ferroan) calcite is systematically increased. Unless a very large number of samples are tested, sampling natural rocks is not a good method to solve this problem, since the composition and grain size of the sample is only known after testing has occurred. It is unclear if a similar correlation, as found for (ferroan) calcite, exists for ferroan dolomite since few comparable samples containing varying amounts of ferroan dolomite were tested.

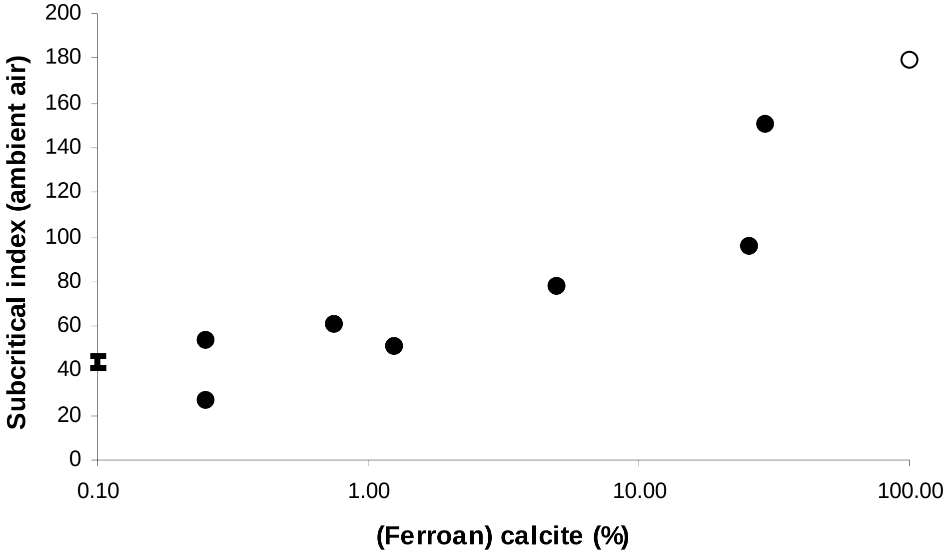

Figure 2.17: (Ferroan) calcite content (%) vs. subcritical index in ambient air for carbonate (open symbols) and sandstone samples (closed symbols) A clear increase in subcritical index occurs with an increase in (ferroan) calcite content.

Since an increase in subcritical index is observed with an increase in relative fracture strength (Fig. 2.11), an increase in subcritical index with quartz cement content is expected. The same criteria as for the (ferroan) calcite correlation are applied, i.e. eliminating those samples containing more than 15% clay, 15% feldspars, 15% ferroan dolomite, and 15% (ferroan) calcite, as well as the siltstones. A very weakly increasing trend with increasing quartz cement content is visible (Fig. 2.18). The subcritical index varies from 27 to 77 for an increase in quartz cement from 0 to ~25%. This is a much narrower range of subcritical index values than found previously for (ferroan) calcite cement content (for an increase from 0 to ~30% in (ferroan) calcite cement the subcritical index increased from 27 to 151). Thus, small amounts of (ferroan) calcite have the ability to overshadow the quartz cement correlation. Nonetheless, even though the trend with quartz cement is weak, it is considered to be noteworthy. For the two samples from the Nugget Formation, a clear increase in subcritical index with an increase in quartz cement is observed (red symbols in Fig. 2.18). These two samples are virtually identical in their composition except for their quartz cement content, and they show a clear increase in subcritical index with an increase in quartz cement. An increase in cement content, keeping all things equal, will decrease the porosity. Therefore, the trend with quartz cement content could also reflect a trend showing that samples with smaller porosities have higher subcritical index values. However, if the observed trends were solely porosity related then the type of cement would not be a factor, which is not consistent with observations.

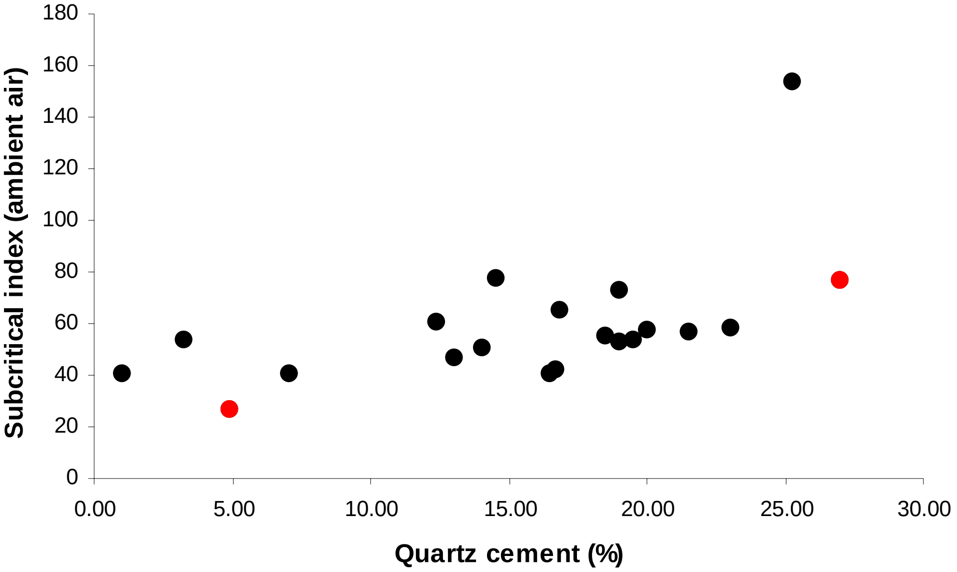

Figure 2.18: Quartz cement content (%) vs. the subcritical index in ambient air. A faint increase (from in subcritical index with an increase in quartz content is observed. The red symbols are for the Nugget Formation, which show an increase in subcritical index with an increase in quartz cement content.

To further investigate the effects of cement type, two samples of different depths from the Travis Peak Formation were artificially cemented (9817 ft and 9880 ft). Samples from 9817 ft were cemented with one of two types of cement, sodium silicate and salol. Samples from 9880 ft were only cemented with salol. Since salol contains a hydroxyl group which has a strong influence on subcritical fracture growth (React. 1.2), sodium silicate ($2Na_2O.SiO_2$) was used as a second cement. It does not contain a hydroxyl group. Salol melts at temperatures above 40° C, so samples were placed in molten salol and kept in the oven for some time. The samples were then taken out of the bath and left to solidify. Sodium silicate is soluble in water and comes in gel format. The samples were soaked in the sodium silicate gel and then placed in the oven to solidify and remove the excess water.

A distinct decrease in subcritical index, as well as a distinct increase in stress intensity factor, was observed for the artificially cemented samples (Fig. 2.19 and 2.20). This is in contrast to the trend found in nature, where an increase in cement content increases the subcritical index. These results suggest that the subcritical index of sodium silicate and salol in ambient air is lower than that of quartz or (ferroan) calcite. However, attempts to test pure sodium silicate and/or salol were unsuccessful, and this statement cannot be substantiated with experimental results. However, these results do substantiate that the type of cement present in rock has a strong influence on the subcritical behavior of the rock.

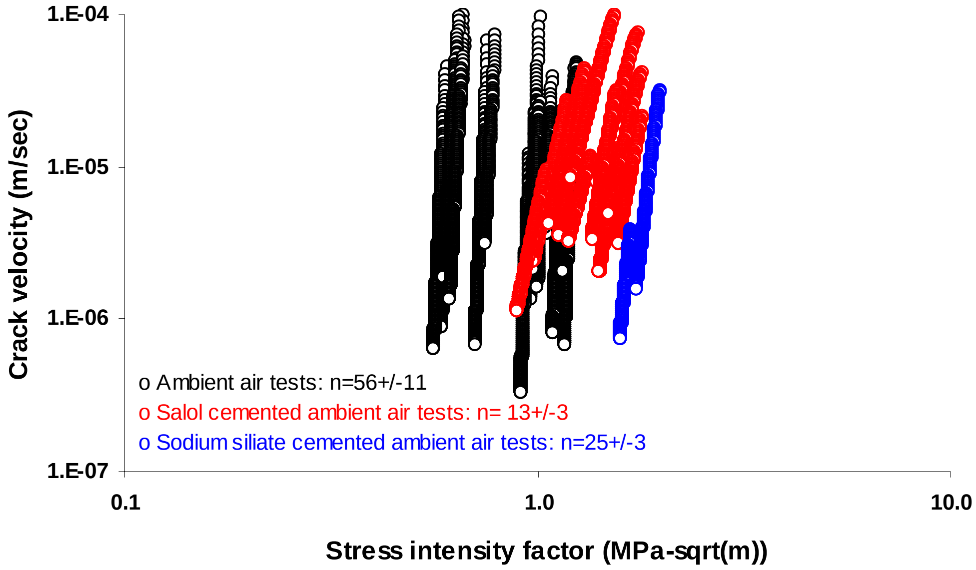

Figure 2.19: Stress intensity factor vs. crack velocity for the Travis Peak Formation from 9817 ft depth. Black curves correspond to ambient air test of the virgin material. Red curves are the results of test performed in ambient air after the samples have been cemented with salol. Blue curves are the results of test performed in ambient air after the samples have been cemented with sodium silicate. A clear decrease in subcritical index and a clear increase in stress intensity factor is observed when the samples are artificially cemented.

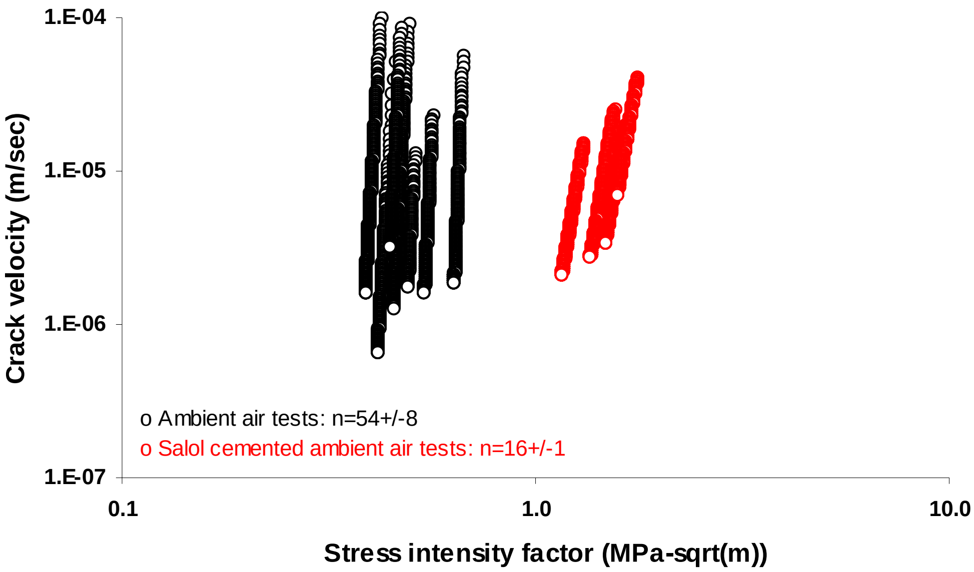

Figure 2.20: Stress intensity factor vs. crack velocity for the Travis Peak Formation from 9880 ft depth. Black curves correspond to ambient air tests of the virgin material. Red curves are the results of tests performed in ambient air after the samples have been cemented with salol. A clear decrease in subcritical index and a clear increase in stress intensity factor is observed when the samples are artificially cemented.

2.4.2.1.3 Step-wise regression analysis: microstructure/petrology

Variations in composition of sedimentary materials are not isolated. An assessment of petrographic controls on subcritical crack indices requires the use of techniques that couple observed variations in subcritical index (dependent variable) with simultaneous variations in several petrographic features (independent variables). The step-wise regression analysis described by Draper and Smith (1981) is used here. The advantage of this method is that it successively (step-wise) adds variables to the regression fit, working only with a small or limited number of variables, and thus reducing the computational requirements. The objective of this method is to select that sub-set of parameters which gives the optimum regression equation. Variables are added into the sub-set based on the magnitude of their correlation coefficient, where variables with large correlation coefficients are introduced into the sub-set first. The selected variable is then used to create a regression fit. A fit is deemed successful if it passes an F-test analysis with significance level of 0.1 or less, meaning that there is a one in ten chance of allowing the wrong variable into the regression analysis. If the variable is considered significant, the parameter with the next larger correlation coefficient is selected and used in the regression analysis, and the resultant fit is again tested for its significance using the F-test. Individual parameters are also tested using the partial F-test. This allows a parameter which was initially highly correlated to be eliminated at a later stage if it turns out that parameters which were added later have rendered the parameter superfluous. One of the limitations of this method is that it assumes a linear regression. The method also assumes that the variables under investigation are independent.

In this analysis, 11 variables are considered: 1) relative humidity (RH) (ambient air tests only), 2) grain size (mm) (Gs), 3) quartz grain % (Qg), 4) quartz cement % (Qc), 5) ferroan dolomite % (Fd), 6) (ferroan) calcite % (Fc), 7) plagioclase % (Pc), 8) K-spar % (Ks), 9) clay % (Cl), 10) porosity % (ϕ), and 11) tortuosity (Tt). Table 2.3 shows the correlation coefficient of each variable with respect to the other variables under investigation. Correlation coefficient values close to 1 or -1, indicate that two variables are highly correlated. The obtained correlation coefficient values indicate that the assumption that the variables under investigation are independent is not strictly valid (i.e. Plagioclase and K-spar are highly correlated). However, the following obtained regression equations form the best possible fit given the available data and can be used as general guidelines to estimate subcritical index values from thin-section analysis.

Table 2.3: Correlation coefficients of variables under investigation.

	RH^{1}	**Gs**^{2}	**Qg**^{3}	**Qc**^{4}	**Fd**^{5}	**Fc**^{6}	**Ks**^{7}	**Cl**^{8}	**Pc**^{9}	ϕ^{10}	**Tt**^{11}	**n**^{12}
RH	1.00	-0.18	0.22	0.31	-0.01	-0.03	-0.32	-0.15	-0.39	0.20	-0.14	0.00
Gs	-	1.00	-0.19	-0.28	-0.15	-0.15	0.57	-0.18	0.57	0.11	0.70	-0.26
Qg	-	-	1.00	0.64	-0.31	-0.21	-0.47	-0.40	-0.67	0.07	-0.15	0.18
Qc	-	-	-	1.00	-0.12	-0.38	-0.42	-0.43	-0.49	-0.13	-0.25	0.30
Fd	-	-	-	-	1.00	0.17	-0.27	-0.14	-0.11	-0.21	-0.30	0.02
Fc	-	-	-	-	-	1.00	-0.08	0.01	-0.06	-0.28	-0.23	0.46
Ks	-	-	-	-	-	-	1.00	0.03	0.71	-0.09	0.49	-0.22
Cl	-	-	-	-	-	-	-	1.00	0.12	-0.29	-0.19	-0.24
Pc	-	-	-	-	-	-	-	-	1.00	-0.05	0.54	-0.14
ϕ	-	-	-	-	-	-	-	-	-	1.00	0.36	-0.37
Tt	-	-	-	-	-	-	-	-	-	-	1.00	-0.36
n	-	-	-	-	-	-	-	-	-	-	-	1.00

[1]RH = relative humidity (%); [2]Gs = grain size (mm); [3]Qg = quartz grain (%); [4]Qc = quartz cement (%); [5]Fd = ferroan dolomite (%); [6]Fc = (ferroan) calcite (%); [7]Pc = plagioclase (%); [8]Ks = K-spar (%); [9]Cl = clay (%); [10]ϕ = porosity (%);[11]Tt = tortuosity; [12]n = subcritical index.

Carbonate samples were not included in this analysis. All data were normalized, where the maximum value of the each variable was set to equal 1 and the minimum value of the each variable was set to equal 0, such that the coefficients of the regression fit indicate the relative importance of each parameter to the fit. The multivariate linear regression analysis was applied to all siliciclastic rocks (45 sandstones, 2 siltstones, and 1 mudstone) for which petrographic data was collected. Comparison of measured and predicted values are shown in Figure 2.21. The solid line shows the trend of a perfect correlation between predicted and measured values. The dashed lines are situated at plus and minus one standard deviation. The resultant regression fit is:

$n_{ambient\ air} = 27.5 + 72.6 \times Fc + 44.5 \times Pc + 41.7 \times Qc - 32.1 \times Tt + 28.3 \times Qg$ .... Eq. 2.13

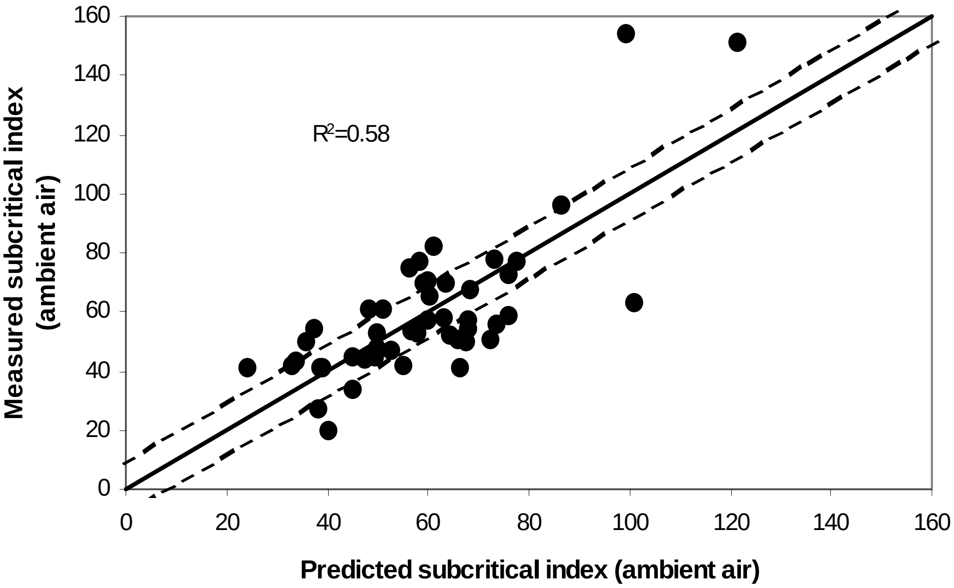

$$n_{\text{ambient air}} = 27.5 + 72.6*Fc + 44.5*Pc + 41.7*Qc - 32.1*Tt + 28.3*Qg$$

Figure 2.21: Predicted subcritical index (ambient air) vs. measured subcritical index (ambient air). Plot shows the results of the stepwise regression analysis performed on all samples tested in ambient air. In the regression fit Fc stands for (ferroan) calcite, Pc stands for plagioclase, Qc stands for quartz cement, Tt stands for tortuosity and Qg stands for Quartz grains. All variables were normalized, where the maximum measured value was set equal to 1 and the minimum measured value was set equal to 0, so that the magnitude of the coefficient reflects the relative importance of each variable to the fit.

The regression results substantiate the earlier found trends with (ferroan) calcite and quartz cement, where the regression equation shows that an increase in either of these parameters increases the subcritical index. This regression analysis also indicates that plagioclase has a slightly stronger influence on the subcritical index value than quartz cement. The dependence on quartz grains is less than either plagioclase or quartz cement. These trends were not evident prior to the regression analysis. A possible explanation for the stronger dependence of the regression fit on plagioclase than quartz cement is that plagioclase weathers more easily than quartz, making it more likely for the fracture to grow through this weaker material and thus more strongly affect the subcritical index. The sign of the trend indicates that an increase in plagioclase increases the subcritical index. This contradicts the previously observed trend, where weaker rocks with smaller relative fracture strength (RFS) values had lower subcritical index values. This might indicate that, like salol and sodium silicate, which showed an increase in RFS but a decrease in subcritical index, plagioclase might also be a material which does not follow the observed general trends, where an increase in plagioclase is believed to decrease the RFS but increase the subcritical index. Further testing is required to substantiate this claim.

A similar multivariate regression analysis was performed with respect to the relative fracture strength (RFS) of the same 48 samples. The resulting regression fit shown in Figure 2.22, is:

$$RFS_{ambient\ air} = 1.70 - 1.40 \times \phi - 0.99 \times Tt - 0.95 \times Cl - 0.69 \times Fd - 0.31 \times Ks - 0.30 \times Fc$$

.... Eq. 2.14

Eq. 2.14 shows that the relative fracture strength depends predominantly on porosity and clay content, such that an increase in porosity or clay content leads to a corresponding decrease in relative fracture strength. This is a reasonable behavior, since pores are void spaces, which provide no strength, and clay is a weaker material than the surrounding quartz or carbonate matrix. Tortuosity exhibits a slightly higher correlation with RFS than the clay content, where an increase in tortuosity decreases the RFS. It is currently unclear what drives this trend. It is interesting to observe that although the relative fracture strength and subcritical index correlate well to each other, their individual regression analyses show a dependence on different variables. Furthermore, the RFS measurements fit the predicted trend better than the subcritical index measurements, indicating that the measured variables are better able to predict the relative fracture strength than the subcritical index. Both observations hint towards the existence of other unquantified factors, having a larger influence on subcritical index than on relative fracture strength. Examples of such factors might be: grain sorting, grain contact type and grain contact size.

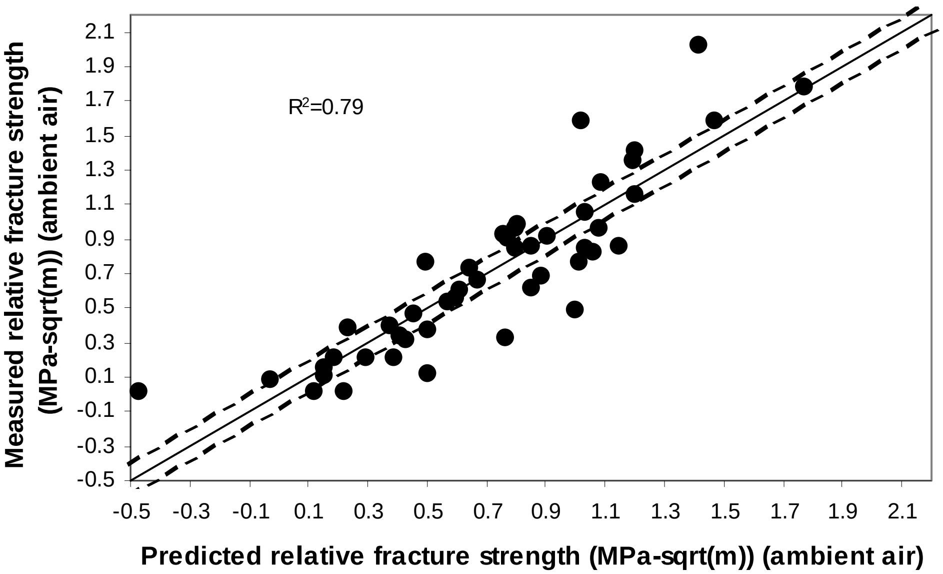

$$RFS_{\text{ambient air}} = 1.70 - 1.40{*}\phi - 0.99{*}Tt - 0.95{*}Cl - 0.69{*}Fd - 0.31{*}Ks - 0.30{*}Fc$$

Figure 2.22: Predicted relative fracture strength (ambient air) vs. measured relative fracture strength (ambient air). Plot shows the results of the stepwise regression analysis performed on all samples tested in ambient air. In the regression fit ϕ stands for porosity, Tt stands for tortuosity, Cl stands for clay, Fd stands for ferroan dolomite, Ks stands for K-spar, and Fc stands for (ferroan) calcite. All variables were normalized, where the maximum measured value was set equal to 1 and the minimum measured value was set equal to 0, so that the magnitude of the coefficient reflects the relative importance of each variable to the fit.

2.4.2.2 Chemical environment

The correlations in Figures 2.21 and 2.22 are for tests in ambient air. Since a more representative environment for rocks from a subsurface hydrocarbon reservoir would be water, brine or hydrocarbon saturation, correlations for samples tested in fresh water, brine (40,000 ppm NaCl) and oil (EXXSOL D110, technical white oil), were investigated. Fluid inclusion analysis could determine which fluids were present during fracturing for a particular rock, but this study is conducted to find general trends. Therefore, general fluids such as a technical white oil and 40000 ppm NaCl solution are used as proxies for the fluid changes expected in the subsurface.

The smaller standard deviation in subcritical index values observed in fresh water, brine, and oil (Table 2.1) is an artifact of the environmental control and the testing sequence. The environment is more controlled in oil, fresh water and brine, than in ambient air. Each sample is submerged in its respective fluid environment (oil, fresh water or brine) during testing. However, in ambient air, the relative humidity (RH) is measured, but not controlled. It has been documented (Wiederhorn, 1967) that RH alters the subcritical response in glass, hence an increase in subcritical index variability in sedimentary materials with RH is expected. Additionally, more tests (on a larger group of samples) were performed in ambient air than in oil, brine or fresh water. Since the microstructure is not identical between samples from the same sedimentary material, this effectively increases the heterogeneity in the ambient air testing as compared to the other testing environments, resulting in a the decrease in standard deviation in fresh water, brine and oil as compared to ambient air.

Tests performed on glass indicate that the subcritical index and the relative fracture strength (RFS) decrease when testing in an aqueous environment. Correspondingly, the subcritical index and the RFS are expected to increase when testing in oil, since all water is eliminated from the environment. Figure 2.23 shows that the subcritical index decreases when testing in fresh water or brine as opposed to testing in oil or ambient air. The distribution of the difference between the subcritical index in ambient air and the subcritical index in oil averages around zero. Likewise the distribution of difference between the subcritical index in fresh water and the subcritical index in brine also clusters around zero. Both observations indicate that there is very little change between subcritical index values obtained in oil or ambient air and those obtained in fresh water and brine. The spread of the data around zero indicates that not all samples exhibit identical responses. However, the distributions of the difference between the subcritical index in ambient air and the subcritical index in fresh water, and the distribution of the difference between the subcritical index in oil and the subcritical index in brine average at higher values of around 10 to 15. Therefore, the subcritical index in ambient air or oil is higher than the subcritical index obtained in fresh water or brine.

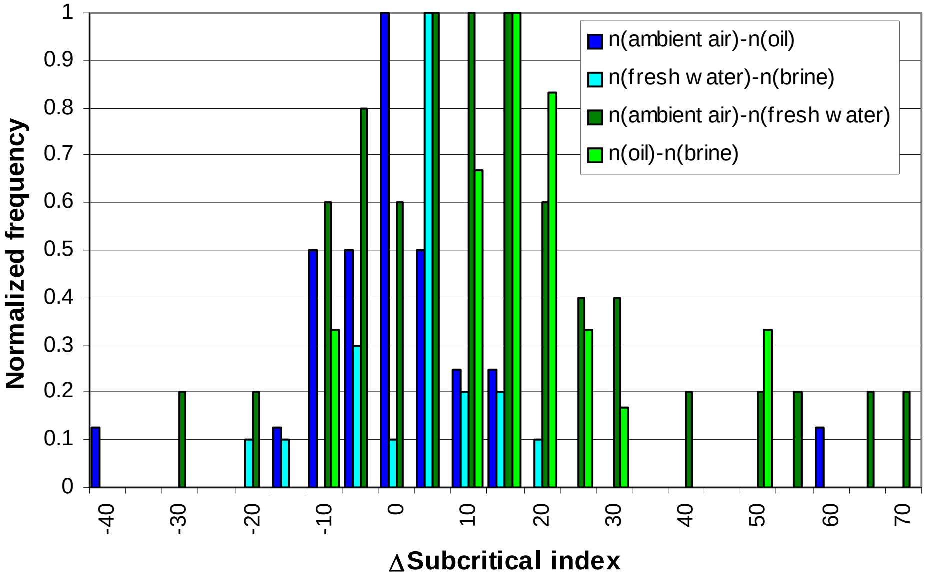

Figure 2.23: Histogram of difference in subcritical index values between: 1) ambient air tests and oil tests (dark blue), 2) fresh water tests and brine tests (light blue), 3) ambient air tests and fresh water tests (dark green), and 4) oil tests and brine tests (light green). Since the blue curves cluster around the zero, the ambient air tests and oil tests have similar subcritical index values. Likewise the fresh water and brine tests have similar subcritical index values. The green curves indicate that the ambient air tests and oil tests have a larger subcritical index than the fresh water and brine tests.

This observation matches the observations made by Wiederhorn (1967) in glass. The spread of the distribution around zero indicates that the subcritical index response of some samples is a function of more than just the presence or absence of water. Some clays are known to swell and react in the presence of fresh water, but not in the presence of brine. Calcite is more soluble in brine than in fresh water. Other minerals in the samples might have similar responses which will influence subcritical fracture growth and thus the subcritical index, explaining the observed data spread.

Comparison of the relative fracture strength (RFS) and subcritical index in ambient air, fresh water, oil and brine for the Cozzette Formation (9041 ft) shows a clear clustering of tests performed in ambient air or oil at higher RFS values than those tests performed in fresh water or brine (Fig. 2.24). This clustering at lower stress intensity factor values for aqueous conditions corresponds to a decrease in material's bond strength due to stress corrosion at the fracture tip. Also, the subcritical index for the oil and ambient air tests are relatively higher (54±16 to 59±15) than those for the brine and fresh water tests (41±3 to 43±3). Thus the Cozzette Formation sample (a sandstone) follows the trend found in glass. Likewise, the Forth Union Formation sample (a mudstone) exhibits a strong dependence on relative humidity (RH) (Fig. 2.25). A clear decrease in subcritical index and RFS is observed when the amount of water is increased. The Forth Union sample tested has a large clay percentage (>40%), which might explain its dependence on moisture content. Clays are known to be water sensitive and may even exhibit swelling when in contact with fresh water. However, no swelling was observed in the Forth Union samples tested. Also the differences between the fresh water tests and brine tests were minimal (Fig. 2.25), indicating that swelling was not causing this subcritical fracture growth dependence.

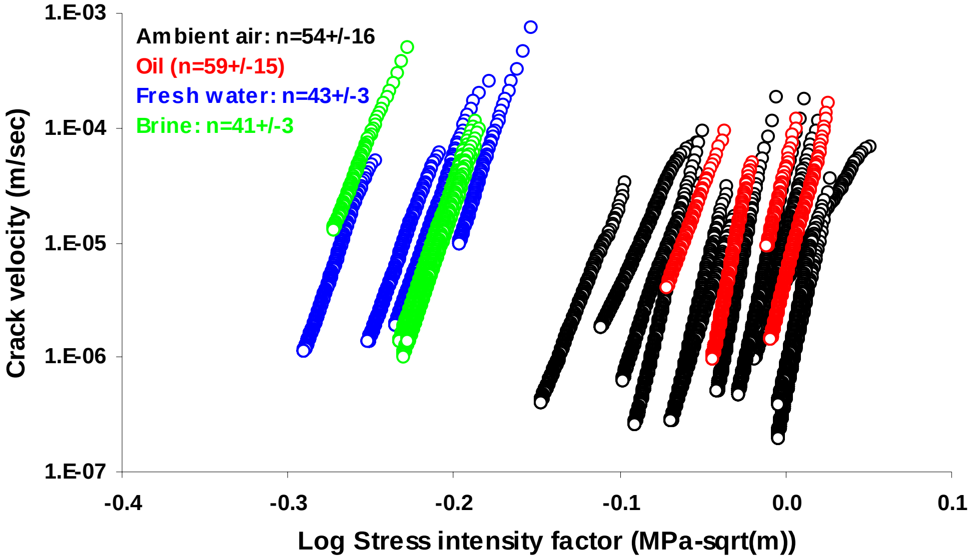

Figure 2.24: Log of stress intensity factor vs. crack velocity for the Cozzette Formation from 9041 ft. Black, red, blue and green curves represent individual tests performed in ambient air, oil, fresh water, and brine respectively. A clear clustering of the ambient air and oil tests vs. the fresh water and brine tests is observed. The oil and ambient air tests show a higher subcritical index and stress intensity factor then those tests performed in fresh water and brine.

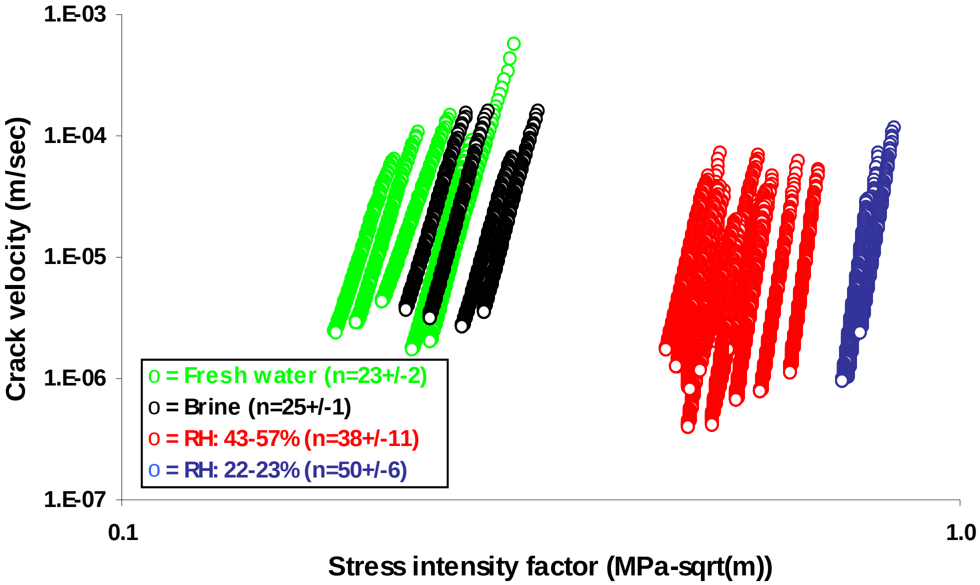

Figure 2.25: Log of stress intensity factor vs. crack velocity for the Forth Union Formation. The blue curves represent individual tests performed in ambient air with a relative humidity (RH) ranging from 22 to 23%, red curves represent individual tests performed in ambient air with a RH ranging from 43 to 57%, green curves represent individual tests performed in fresh water, and the black curves represent individual tests performed in brine. A clear dependence on RH is observed for the Forth Union Formation, where an increase in RH/water content decreases both the subcritical index and the stress intensity factor.

This clear dependence on RH was not found in any other samples. The results for the Travis Peak Formation even show the opposite trend, where the subcritical index and the RFS tend to increase with water content (Fig. 2.26, 7737 ft depth). This Travis Peak Formation sample contains very little clay, possibly indicating that some larger clay content is necessary to obtain a RH dependence in sedimentary materials.

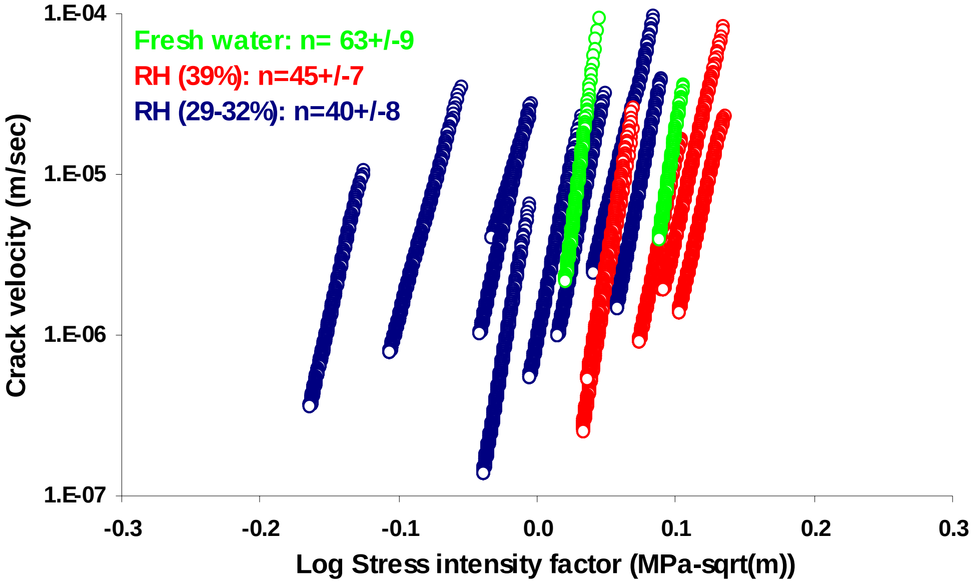

Figure 2.26: Log of stress intensity factor vs. crack velocity for the Travis Peak Formation (a sandstone) from a depth of 7737 ft. The blue curves represent individual tests performed in ambient air with a RH ranging from 29 to 32%, red curves represent individual tests performed in ambient air with a RH ranging from 39%, and the green curves represent individual tests performed in fresh water. An opposing trend with RH is found for this sample as compared to the Forth Union Formation (a mudstone) (Fig. 2.22). An increase in RH/water content increases both the subcritical index and the stress intensity factor for this sample.

The relative fracture strength (RFS) decreases for most samples when water or brine are added to the test environment (Fig. 2.27). Air and oil environments show consistently higher fracture strength values (by 0.1-0.2 MPa-sqrt(m)). This implies that as hydrocarbons migrate into the reservoir, more energy is required to propagate subcritical fractures. This trend is more compelling than the trend found with subcritical index. It is noteworthy that oil and air tests have similar relative fracture strength values. The same can be found for fresh water and brine tests.

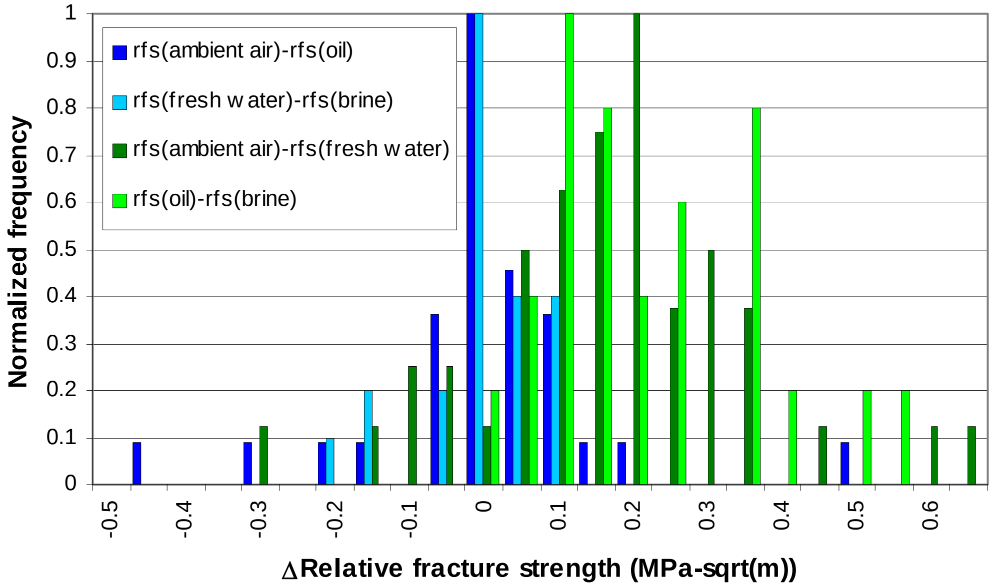

Figure 2.27: Histogram of difference in relative fracture strength between: 1) ambient air tests and oil tests (dark blue), 2) fresh water tests and brine tests (light blue), 3) ambient air tests and fresh water tests (dark green), and 4) oil tests and brine tests (light green). Since the blue curves cluster around the zero, the ambient air tests and oil tests have similar relative fracture strength values. Likewise the fresh water and brine tests have similar relative fracture strength values. The green curves indicate that the ambient air tests and oil tests have a larger relative fracture strength than the fresh water and brine tests.

In ambient air, the subcritical index increases as the RFS increases. Similar observations are made for the correlation between the subcritical index and the RFS in fresh water, brine and oil (Fig. 2.28). Those samples containing more than 15% carbonate (plotted as blue circles) exhibit a larger drop in subcritical index as compared to other samples in identical aqueous environments. In ambient air and oil (Fig. 2.21 and Fig. 2.28C), the subcritical indices of these samples fell within the general trend. However, in brine and fresh water, these samples tend to drop towards the bottom of the trend, i.e. to

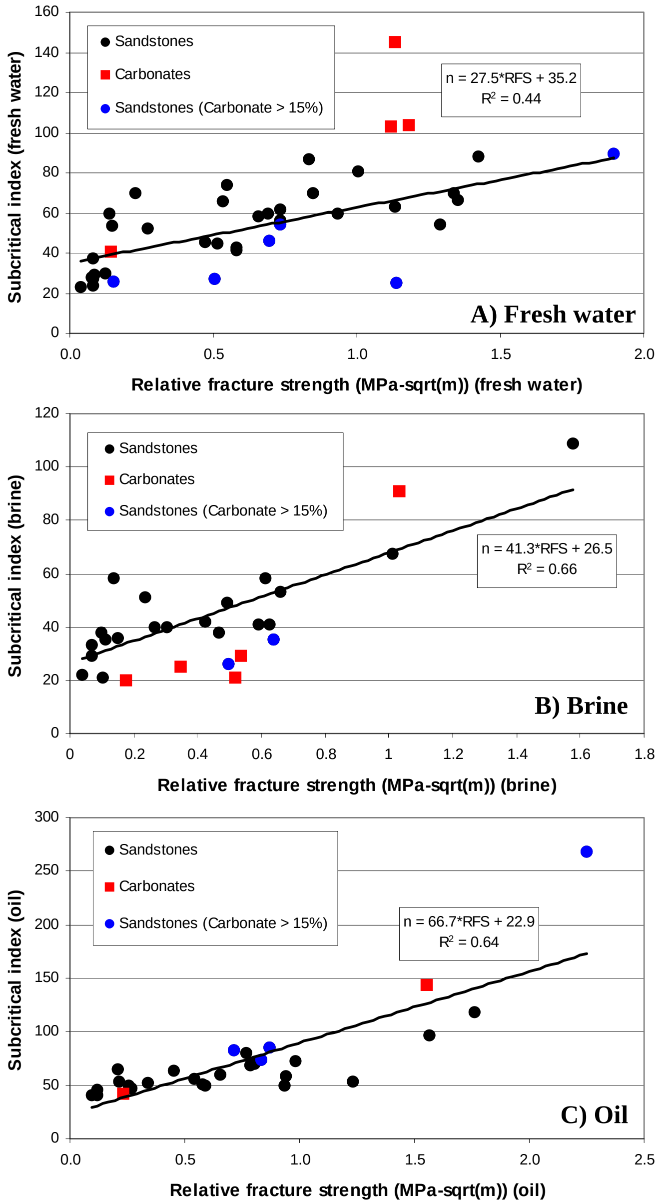

Figure 2.28: The relative fracture strength vs. the subcritical index for both sandstones and carbonate samples in: A) fresh water, B) brine, and C) oil. Sandstones are represented by black symbols and carbonate samples are represented by red symbols. Blue circles represent those sandstone samples with more than 15% carbonate content. The plots show that the carbonate samples and carbonate rich sandstones exhibit a larger drop in subcritical index than those sandstone samples containing less than 15% carbonate cement.

lower subcritical index values. Since the carbonate samples had such high subcritical indices in ambient air to begin with, they still plot above the sandstones in fresh water. The average drop in subcritical index for the carbonate samples shown in Figure 2.28A is 113. The subcritical index of carbonate samples in brine drops even more than compared to fresh water, since solubility of calcite is much higher in sea water than in fresh water (Fig. 2.28B).

2.4.2.2.1 Step-wise regression analysis: chemical environment

Regression analyses, with the subcritical index as dependent variable, were performed on the results from all 3 environments for siliciclastic rocks only (fresh water = 39 samples, brine = 24 samples, and oil = 28 samples, all variables were normalized, where the maximum value of the each variable was set to equal 1 and the minimum value of the each variable was set to equal 0, such that the coefficients of the regression fit indicate the relative importance of each parameter to the fit) (Fig. 2.29):

$$\begin{aligned} n_{\text{fresh water}} &= 23.5+37.6\times Qg+19.4\times Qc \\ n_{\text{brine}} &= 77.6+14.0\times Qc-42.4\times Tt-57.1\times Cl \qquad \text{Eq. 2.15} \\ n_{\text{oil}} &= 27.1+53.9\times Qg+129.4\times Fc \end{aligned}$$

Common correlating factors in most testing environments (including ambient air, Eq. 2.13) are quartz cement and quartz grains. In all environments an increase in subcritical index correlated with an increase in quartz cement. In oil, the correlation coefficient of the subcritical index with quartz cement was 0.49 and that with quartz grains was 0.50. This resulted in the quartz cement correlation not appearing in the fit. However, the small correlation coefficient difference between the two variables indicates that both variables are important to the fit. If quartz cement is used as a variable, the regression fit is still statistically significant and the R^2 is also 0.62. Therefore, in the oil environment quartz cement is also considered an important parameter. In all environments, except brine, an increase in subcritical index correlated with an increase in quartz grains. For the brine tests, the correlation with quartz grains followed the same trend (i.e. an increase in quartz grains increases the subcritical index), but the trend was too weak to be of statistical significance. In general, an increase in quartz grains or cement correlates with an increase in the subcritical index. Furthermore, the strong dependence on (ferroan) calcite in ambient air disappeared in fresh water and brine but not in oil, indicating that (ferroan) calcite is subcritically different in oil/ambient air vs. fresh water/brine. This is explained by the difference in solubility of calcite in aqueous vs. non-aqueous environments, which influences subcritical fracture growth and thus the subcritical index.

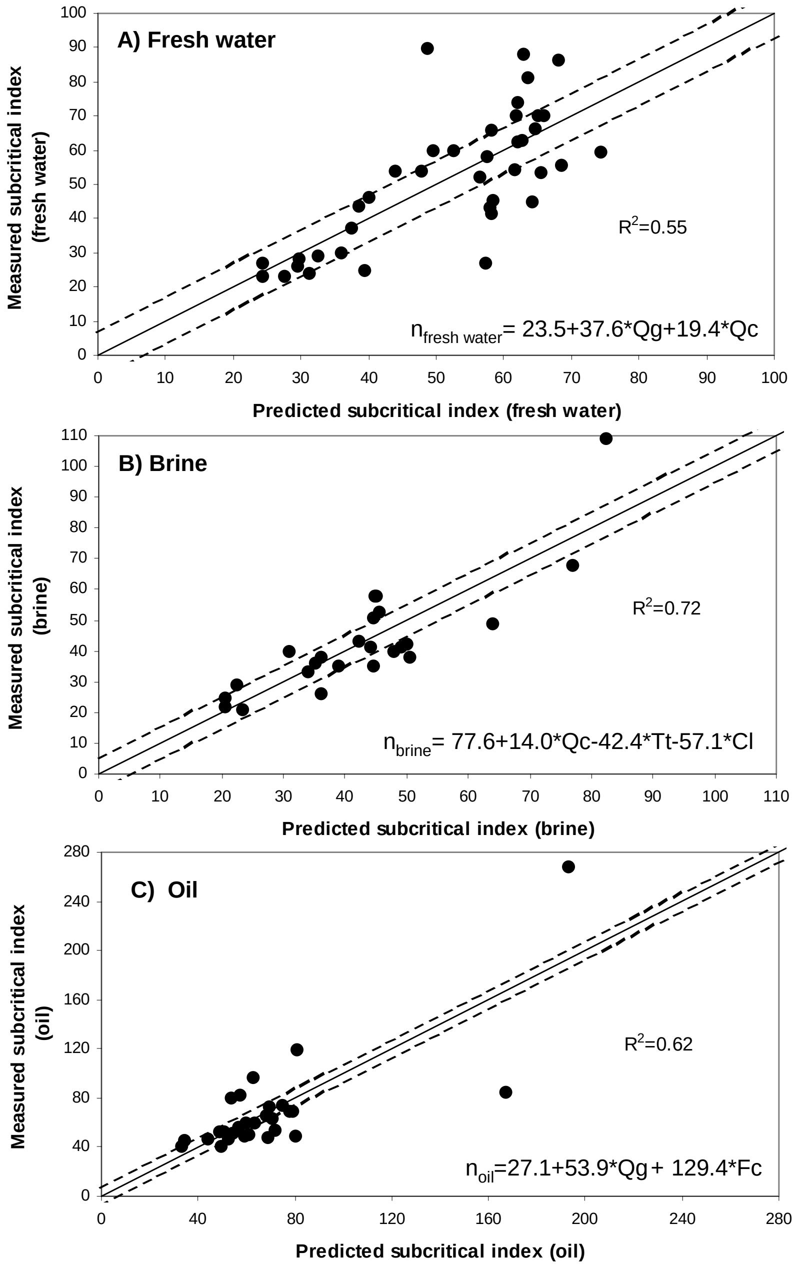

Figure 2.29: Predicted subcritical index vs. measured subcritical index for: A) fresh water, B) brine, and C) oil. The plots shows the results of the stepwise regression analysis performed on all samples tested in their respective environments. In the regressions fit Qg stands for Quartz grains, Qc stands for quartz cement, Tt stands for tortuosity, Cl stands for clay, and Fc stands for (ferroan) calcite. All variables were normalized, where the maximum measured value was set equal to 1 and the minimum measured value was set equal to 0, so that the magnitude of the coefficient reflects the relative importance of each variable to the fit.

A regression analysis performed with the relative fracture strength (RFS) as the dependent variable shows that, independent of the environment, an increase in porosity or clay content leads to corresponding decreases in the RFS (Fig. 2.30):

$$\begin{aligned} RFS_{\text{fresh water}} &= 1.70 - 0.89\times\phi - 0.82\times Tt - 1.18\times Cl - 0.42\times Gs - 0.95\times Fd \\ RFS_{\text{brine}} &= 1.26 - 0.51\times\phi - 0.53\times Tt - 1.09\times Cl - 0.36\times Gs + 0.24\times Qc \\ RFS_{\text{oil}} &= 1.24 - 0.77\times\phi - 0.94\times Tt - 0.80\times Cl - 0.42\times Gs + 0.55\times Fc + 0.49\times Qg \end{aligned} \qquad \text{.......... Eq. 2.16}$$

The decrease in relative fracture strength with an increase in grain size coincides with what is found in literature, where an increase in grain size decreases the rock strength (Eberhardt et al., 1999; Přikryl, 2001; Cheema et al., 2004). A possible explanation for this dependence is given by Eberhardt et al. (1999). They propose that large grained materials have longer grain boundaries which provide a longer path of weakness for growing cracks to propagate along. These longer planes of weakness coalesce at lower stresses, effectively reducing the material's strength. Equation 2.16 also shows a strong dependence of the RFS on tortuosity, where the higher the tortuosity the smaller the RFS, consistent with what is observed in ambient air. It is currently unclear what controls this trend.

In a hydrocarbon reservoir, the most likely fluid change is from brine to oil. Figure 2.31 and Equation 2.17 show that an increase in (ferroan) calcite and clay content both increase the drop in subcritical index from oil to brine:

$$\Delta(n_{oil} - n_{brine}) = -13.4 + 48.7 \times Fc + 40.3 \times Cl + 23.3 \times Tt \quad \text{.................................... Eq. 2.17}$$

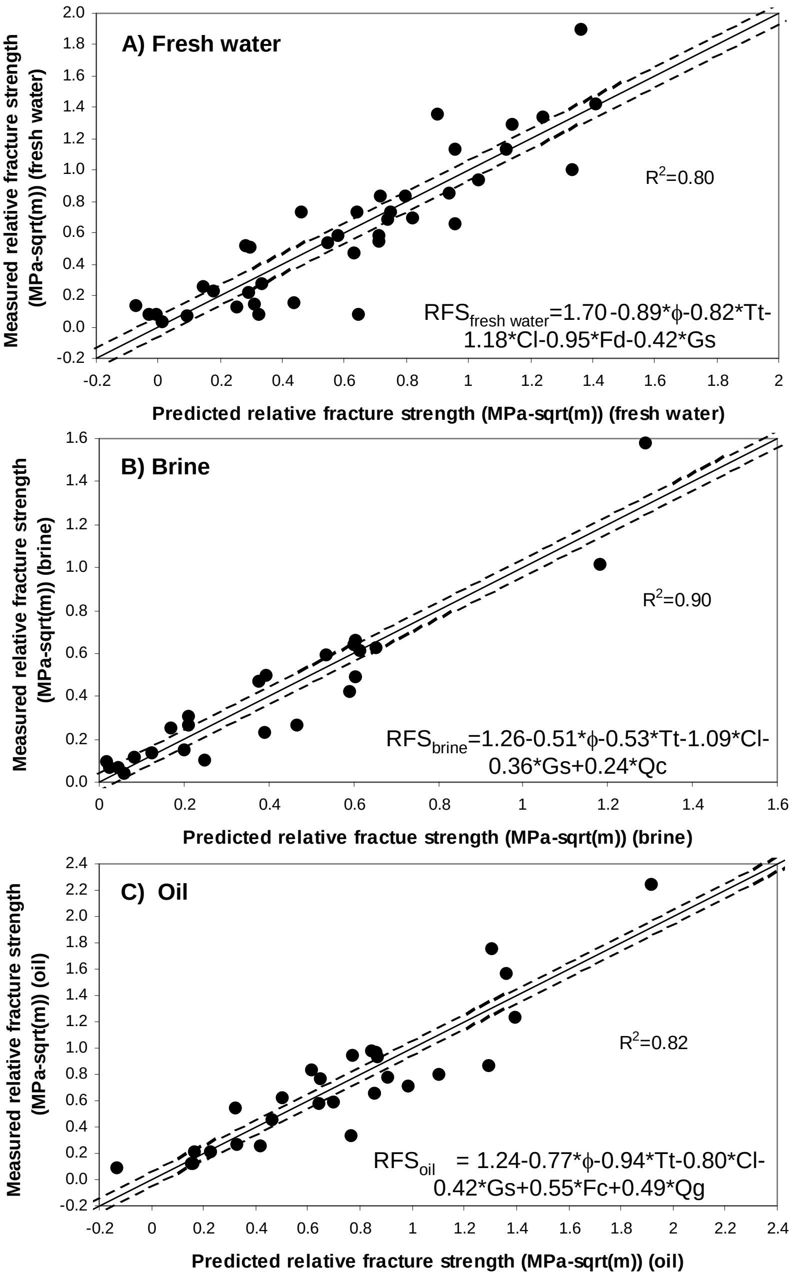

Figure 2.30: Predicted relative fracture strength vs. measured relative fracture strength for: A) fresh water, B) brine, and C) oil. The plots shows the results of the stepwise regression analysis performed on all samples tested in their respective environments. In the regression fit ϕ stands for porosity, Tt stands for tortuosity, Cl stands for clay, Fd stands for ferroan dolomite, Gs stands for grain size, Qc stands for quartz cement, Fc stands for (ferroan) calcite, and Qg stands for quartz grains. All variables were normalized, so that the magnitude of the coefficient reflects the relative importance of each variable to the fit.

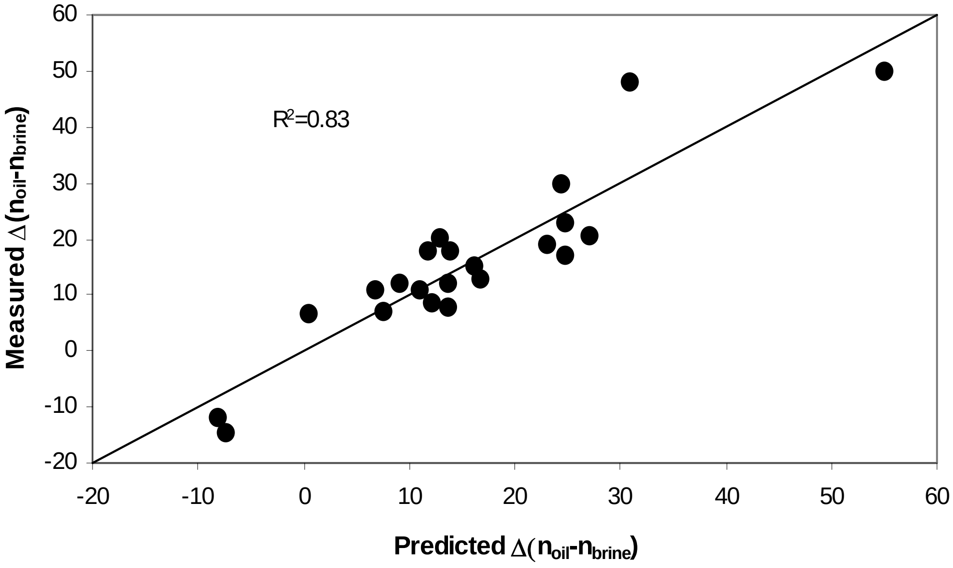

$$\Delta(n_{oil}-n_{brine}) = -13.4 + 48.7*Fc + 40.3*Cl + 23.3*Tt$$

Figure 2.31: Predicted difference between the subcritical index in oil and the subcritical index in brine vs. the measured difference between the subcritical index in oil and the subcritical index in brine. The plot shows the results of the stepwise regression analysis. In the regression fit Fc stands for (ferroan) calcite, Cl stands for Clay, and Tt stands for tortuosity. All variables were normalized, so that the magnitude of the coefficient reflects the relative importance of each variable to the fit.

Some clays are known to be water sensitive, and a dependence on clay content is not surprising. However, the dependence on (ferroan) calcite is surprising and is stronger than the clay effect. Therefore, the presence of water in a clay and (ferroan) calcite rich sample increases the likelihood of atomic bond activation and lowers the subcritical index. A possible reason for the deviations found to the trend is an unknown variation in mineral wettability. Wettability characterizes the surface tension of a fluid in the presence of another immiscible fluid. Almost all clean reservoir minerals are strongly water-wet (Gant and Anderson, 1988), but exposure to different pore fluids can alter this state to preferentially oil-wet. Moisture in a preferentially water-wet sandstone will adhere to the grain surfaces more so than in an oil-wet rock. Holder et al. (2001) postulate that this preferential distribution of water along the grain surfaces provides for greater water-weakening of silicate bonds.

2.5 DISCUSSION AND CONCLUSIONS

Tests performed on sedimentary rocks show that the subcritical index and the relative fracture strength (RFS) depend on both the rock's microstructure and the chemical environment. The most distinct observation is that in tests in ambient air the subcritical index for carbonates and carbonate cemented sandstones is higher than that for quartz-cemented sandstones without carbonate content. The average subcritical index in ambient air for sandstones is approximately 62, whereas the average value for comparable carbonate samples is 120. A strong relationship exists between the subcritical index and the relative fracture strength (RFS), where an increase in RFS increases the subcritical index. Sedimentary materials have a limited span in fracture toughness and rupture velocity, so that all curves on a stress intensity factor vs. crack velocity plot converge to one hinge-point (Fig. 2.3). Therefore, if the RFS of a sample is low, the sample has a larger range of stress intensity factor it can cross before reaching the fracture toughness limit as compared to a sample with a high RFS value. This results in low subcritical index values for rocks with low RFS values, which matches the measured trends.

The larger subcritical index values for carbonates in comparison to sandstones could, in part, be attributed to the smaller "grain" sizes for the carbonate samples. The carbonate samples tested consisted predominantly of very fine grains or facets. Sandstone samples with relatively lower subcritical index values had much larger grain sizes. This observation matches the theory as postulated by Gesing and Bradt (1983), which states that the subcritical index increases as the grain or facet size decreases. However, more testing is required to corroborate this trend in sedimentary materials.

Petrographic analysis of the sedimentary materials tested showed that an increase in cement content increases the subcritical index. Specifically, an increase in (ferroan) calcite cement results in a large increase in subcritical index. Quartz cement follows a similar, yet, less obvious trend. Two virtually identical (except for their quartz cement content) Nugget Fm. samples exhibit a clear increase in subcritical index with an increase in quartz cement, supporting the observed trend. These observations coincide with the theory that materials with large RFS values (for instance larger quartz cement content) have higher subcritical index values, since both types of cementation increase the RFS value. Thus, additional cementation in nature is expected to increase both the RFS as well as the subcritical index. However, measurements for artificial cementation of rock samples show that this natural trend can be reversed. The artificially cemented samples exhibited an increase in RFS, but a decrease in subcritical index, indicating that the subcritical index value of the material present in the pore is the governing factor in determining the subcritical index and not the RFS of the framework itself. However, in nature, carbonate samples have a larger subcritical index value than sandstones, either due to the material type itself or due to the relatively smaller crystal/grain size. An increase in quartz cement in a quartz framework reduces the pore space, effectively increasing the subcritical index. Thus, additional cementation in nature is expected to increase both the RFS as well as the subcritical index.

In general, the subcritical index value, as well as the RFS value, changes as the chemical environment is altered. Tests in oil and ambient air cluster at higher RFS and subcritical index values than tests in fresh water or brine. The Forth Union Formation samples (a mudstone) showed a clear decrease in RFS and subcritical index with an increase in relative humidity (RH). However, this trend was not found in all samples. A possible reason for the strong trend obtained in the Forth Union Formation is its high clay content (>40%).

Those sandstones containing more than 15% carbonate cement as well as pure carbonate samples exhibit a larger drop in subcritical index when the environment is changed from ambient air or oil to fresh water or brine than sandstones containing less than 15% carbonate cement. This indicates that carbonates and carbonate cemented sandstones are more susceptible to environment changes than quartz cemented sandstones. Calcite is much more soluble in water than quartz, effectively explaining the disproportional drop in subcritical index when water is introduced to these samples. When changing the environment from brine to oil, a larger decrease in subcritical index is observed when the sample has a large clay content. Therefore, clay rich sandstones which are (ferroan) calcite cemented exhibit the strongest response to fluid changes.

Given these observations, predictions can be made regarding fracture trends expected in the subsurface. In general, two processes are expected to occur as the reservoir matures: 1) cementation, and 2) the influx of hydrocarbons displacing water. Both processes increase the subcritical index, especially, if the later cement consists of (ferroan) calcite. A subcritical index increase of 50 due to a change in fluid environment from brine to oil has been observed for a (ferroan) calcite rich (>15%) sandstone. Both processes also increase the RFS, where the expected increase in RFS as a result of hydrocarbon influx is approximately 0.01-0.02 MPa-sqrt(m). Larger RFS values result in higher energy levels to initiate fractures. Thus, if the reservoir remains under constant extensional loading conditions and undergoes the maturing processes as described, the present study predicts that further fracturing might be inhibited. If fracturing does occur, the resultant fracture pattern is expected to be more clustered in appearance, due to the expected increase in subcritical index.

Numerical simulations have demonstrated subcritical crack growth controls on fracture spacing and length distributions (Segall, 1984; Olson, 1993; Olson, 2004), connectivity (Renshaw, 1996; Olson, 1997) and fracture aperture (Renshaw and Park, 1997; Olson et al., 2001). This study has focused on determining the subcritical index value of sedimentary rocks. The results reported can be used to estimate the current-day average subcritical index value of sedimentary rock from thin-section analysis. Corrections need to be made to account for changes in cementation and compaction that occurred from the time of fracturing to the present day. Furthermore, test results have shown that determination of the type of pore fluid present during fracturing is essential for correct determination of the subcritical index value. Combining this knowledge of the subcritical index value with geomechanical modeling based on subcritical fracture growth allows for determination of fracture pattern characteristics without abundant sampling.

Chapter 3 Numerical Modeling of a Naturally Fractured Reservoir: The Point of Rocks Reservoir

3.1 OBJECTIVE

The objective of this chapter is to outline a methodology for generating a representative fracture pattern, using a geomechanical model. The procedure will be demonstrated for the meso-fractures in 2nd and 4th Point of Rocks (POR) reservoir intervals, an oil reservoir located in southern California. Fracture pattern attributes are estimated, using a numerical fracture pattern simulator based on subcritical fracture growth (Olson, 2004). This simulator allows for fracture attribute prediction without direct observations and uses rock properties such as subcritical index, Poisson's ratio, Young's modulus and remote stresses/strains as input.

This chapter starts with a brief explanation of the numerical model employed to create the fracture patterns. This is followed by a discussion of the POR reservoir fracturing and the POR structure, successively. After this, a summary of the remaining input parameters necessary to run the fracture pattern simulator is given. More detailed information on each input parameter is presented in Appendix A through D (Appendix A: Static Young's Modulus; Appendix B: Static Poisson's Ratio; Appendix C: Bed Thickness; and Appendix D: Subcritical Index). A sensitivity analysis with respect to Poisson's ratio, Young's modulus, flaw orientation, strain rate, strain anisotropy, the total amount of strain, bed thickness, and subcritical index is presented. Following this sensitivity study, a brief summary of the distributions predicted for the 2nd and 4th POR intervals is given. Conclusions derived from the results are presented in the final section.

3.2 BOUNDARY ELEMENT CODE

A discrete fracture pattern simulator as described by Olson (2004) is employed to simulate natural fracture patterns. A brief synopsis of the employed simulator is given here, for a more complete description the reader is referred to Olson (2004). This simulator uses subcritical fracture growth as its underlying propagation criterion and is based on the displacement-discontinuity, boundary element method as presented by Crouch and Starfield (1983). Crack interaction, an important factor controlling fracture pattern development, is taken into account using the following expression (Olson, 2004):

$$\sigma_n^i = \sum_{j=1}^{N} G^{ij} C_{ns}^{ij} D_s^j + \sum_{j=1}^{N} G^{ij} C_{nn}^{ij} D_n^j \text{ ,} \quad \text{Eq. 3.1}$$

where σ_n^i is the normal stress acting on element i and G^{ij} is a three dimensional correction factor. This correction factor corrects the normal stress to adjust for the limited fracture dimensions. C_{ns}^{ij} are the plane strain, elastic influence coefficients giving the normal stress at element i due to a shear and opening displacement discontinuities at element j denoted by D_s^j and D_n^j, respectively. A similar equation can be written for the shear stress acting on the i^{th} element. The three dimensional correction factor is determined using (Olson, 2004):

$$G^{ij} = 1 - \frac{d_{ij}^{2.3}}{\left[d_{ij}^2 + h^2\right]^{2.3/2}} \text{ ,} \quad \text{Eq. 3.2}$$

where h is the bed thickness or fracture height, and d_{ij} is the distance between the centers of elements i and j. This correction factor accounts for the influence of fracture height on the fracture induced stress field. However, fracture height growth is not explicitly simulated in this model. The initial starter flaws are assumed to span the entire bed height. Fracture velocity is calculated using Equation 1.4, and fracture propagation is simulated by adding equi-length boundary elements to the starter flaws (Olson, 1993).

3.3 POINT OF ROCKS FRACTURING

The Point of Rocks (POR) reservoir is a low matrix permeability reservoir. Hydrocarbon production depends heavily on the natural fractures. The fracture model for this reservoir is based on examination of stress magnitudes/directions, core, outcrop, aerial photographs, Formation Micro Imager (FMI), Oil-Base Micro Imager (OBMI), micro-seismic, well-logs and rate and pressure transient analyses. The proposed fracture model in the POR reservoir consists of 3 hydraulic systems: 1) matrix: location for fluid storage, 2) meso-fractures: giving continued production, and 3) macro-fractures: fluid flow “highways” connecting the meso-fractures (Fig. 3.1). The hydrocarbon is stored in the matrix and the small or meso-fractures break the matrix up into smaller sized blocks, which provide for continued hydrocarbon production in the POR reservoir. The big or macro fractures connect the meso-fractures and form fluid “highways” along which oil or water is produced.

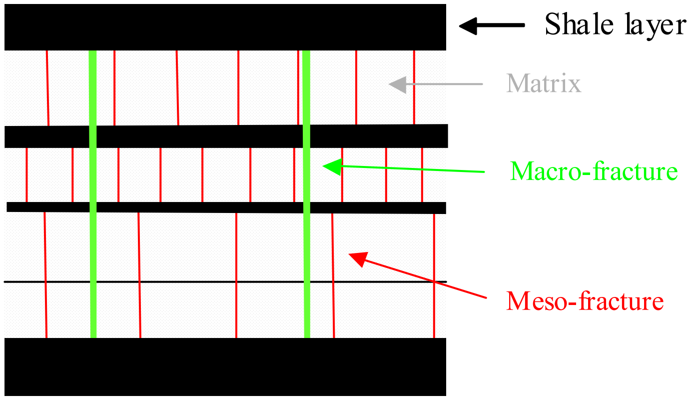

Figure 3.1: Natural fracture model hypothesized to be present in the POR reservoir. The matrix stores the hydrocarbon. The meso-fractures divide the reservoir into small blocks and allow for continued reservoir production since they greatly increase the effective surface area of the reservoir. The macro-fractures connect the meso-fractures and form fluid “highways” which increases oil or water production.

FMI and OBMI logs as well as the micro-seismic indicate that 3 fracture orientations are present in the POR reservoir: 1) N20E, 58NW, 2) N35W, 70NE, and 3) N43E, 63SE. Consequently this investigation attempts to simulate growth of 3 orientations of fractures. Fracture set 1 coincides with the present day maximum horizontal stress direction. The local and regional stress orientations were obtained from breakout data and regional stress information as given by Reinecker et al. (2003). Solely based on the current in-situ stress field, fracture set 1 would be expected to be most conductive because it is perpendicular to the least compressive horizontal stress (Crampin, 1987; Crampin and Lovell, 1991). Laubach et al. (2004) point out that this statement is only true if no cementation occurred prior to or after the end of fracturing. Cementation can cause fracture bridging, keeping the fracture open to flow regardless of its orientation with respect to the in-situ stress field. Cementation of the host rock after fracturing can lock in the fracture displacement, propping it open to flow independent of the in-situ stress field. Examination of POR core showed a high degree of cementation, indicating that fracture conductivity in the reservoir need not necessarily align with the present day in-situ stress field.

In this analysis, the word fracture is used synonymously with opening-mode joint. The numerical fracture simulator employed for this study simulates opening-mode fractures only. In core and outcrop, both opening-mode fractures (joints) and shear fractures (faults) were observed. Core and outcrop showed that the joints had steeper dips than the shear fractures, where the shear fractures showed clear offset in core. However, from FMI it is unclear if the observed fractures are shear or opening-mode fractures. The average dips of the fracture clusters does not allow for determination of the fracture origin, i.e. opening-mode fractures or shear fractures.

As stated earlier, the POR structure consists of three hydraulic units: 1) matrix, 2) meso-fractures, and 3) macro-fractures (Fig. 3.1). The big or macro fractures are observed in micro-seismic and aerial photographs of the exposed reservoir unit. The average natural fracture spacing of these macro-fractures determined from micro-seismic is on the order of 100-200 ft. The current hydraulic fracture design of 125 ft will most likely only intersect one or two macro-fractures. The average fracture length of the macro-fractures as determined from aerial photographs is on the order of 1000 ft. These features are believed to greatly enhance oil production, but also increase the likelihood of water production and therefore control stand-off from the Oil Water Contact (OWC). These macro-fractures are not believed to cross the faults present in the POR structure. This observation is based on the differences in API gravity and water resistivity observed between the fault blocks in the reservoir. Although highly important to fluid flow, these macro-fractures are not characterized in this study, since no direct observations (except for micro-seismic and aerial photos) are available for these macro-fractures. They have not been observed in core, although one would expect that core would not be retrieved from rocks containing such fractures. Therefore, it is unknown if these macro-fractures are faults or opening-mode joints. Also, no information is available on the vertical containment of these fractures, making assessment of the control/simulation volume challenging. Because of these uncertainties, this study focuses on the more readily observed meso-fracture trends only.

3.4 THE POR STRUCTURAL HISTORY

The POR structure is an anticline formed due to compression of the region against the San Andreas fault (Mann, 2000). Mann (2000) postulates that folding of the POR region occurred during the Miocene Epoch. Therefore, it is assumed that strains in the structure occurred sometime between 24 and 6 million years ago. The POR reservoir is a deep-water deposit, ranging from Middle to possibly Lower Eocene in age (Mann, 2000). Calcite concretions are present in the POR reservoir. These concretions can be relatively small in size (on the order of 30 cm) or they can form layer type features, which can be traced from well to well. A petrographic description of 10 samples obtained from the POR reservoir is given in Table 2.2.

A structural strain analysis of the POR structure was performed by E. Flodin (ChevronTexaco, CEPSCO) assuming strains result from bending associated with folding. The calculated strain values were predicted to vary from extension at the top of the structure to shortening/contraction at the bottom. In the area of interest, which encompasses wells 10, 4 and 8, an almost isotropic extension is predicted on the order of 3% (Fig. 3.2). Because this structural model predicts a decrease in extension with depth, the 2nd POR reservoir should have slightly higher strain than the 4th POR interval, suggesting higher fracture intensity in the 2nd POR, all other factors being equal. Figure 3.2 also shows that the strain anisotropy gradually increases towards the flanks of the reservoir, which should influence the resulting fracture pattern.

To determine the amount of strain accommodated by jointing, a rough estimate of the fracture spacing is required of fractures that span the mechanical layer thickness. To predict an average fracture spacing from FMI, a technique as described by Narr (1996) was employed. This technique is based on the probability of fractures intersecting the borehole. By equating the fracture porosity in core to the fracture porosity in the reservoir and assuming that 1) fractures occur in an array of parallel fractures, 2) fractures are perpendicular to bedding, and 3) the fractures are very long relative to the core diameter, Narr (1996) derived the following relationship for fracture spacing:

$$S_{av} = \frac{d_c \times H_c}{\sum_{i-1}^{n} H_i}, \qquad \text{Eq. 3.5}$$

where d_c is the core diameter, H_c is the core or interval height, and H_i is the height of fracture i as measured in core. Equation 3.5 assumes that the average aperture of the fracture is a good representation of the fracture apertures present in the subsurface. Since apertures measurements are limited in the POR reservoir, there is no alternative but to use the core-measured values. This technique also assumes that fracture spacing is related to

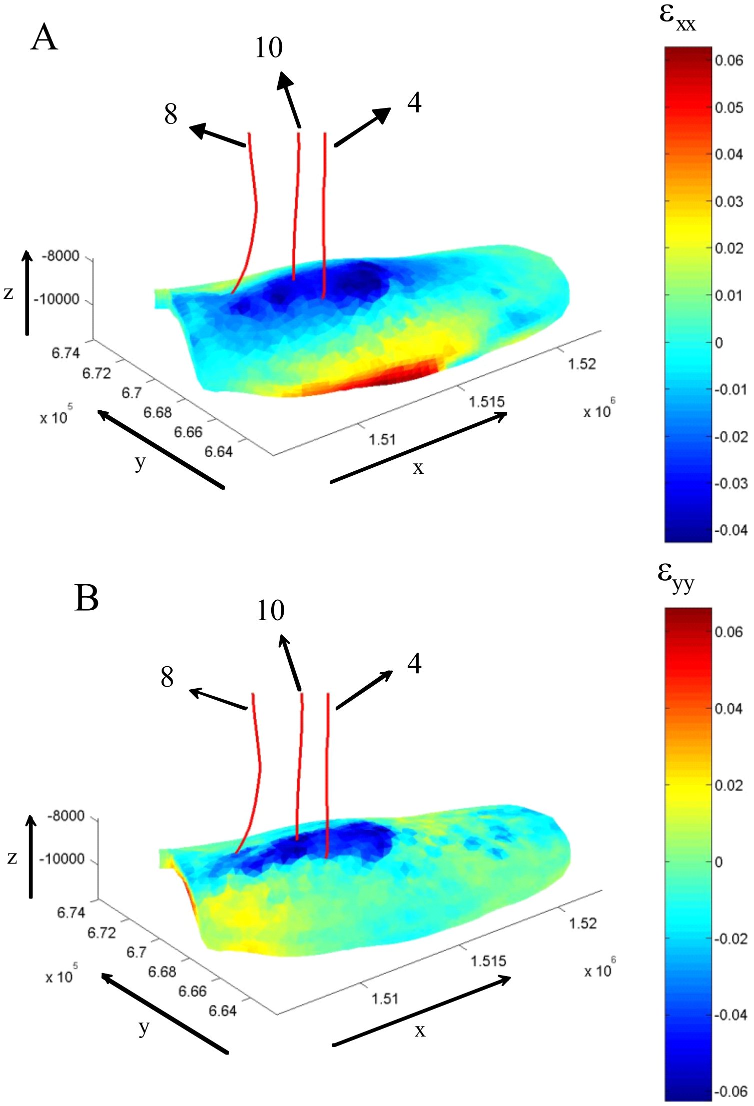

Figure 3.2: Strains in the x (A) and y (B) direction in the POR structure (Data provided by E. Flodin, CEPSCO). The analysis indicates that 3 % extensional strain seems to be reasonable for the POR area under investigation.

mechanical bed thickness and requires knowledge of the height of each mechanical unit. A strong relationship of bed height vs. fracture spacing was qualitatively observed in outcrop of the POR reservoir (Fig. 3.3). However, the technique as described by Narr (1996) requires a full study of the mechanical or fracture stratigraphy of the POR reservoir. In the present study only a rough estimate of the fracture spacing is required. Therefore, a uniform investigation interval of 50 ft was chosen to obtain an estimate of the average fracture spacing over the different POR intervals. The obtained values are tabulated in Table 3.1.

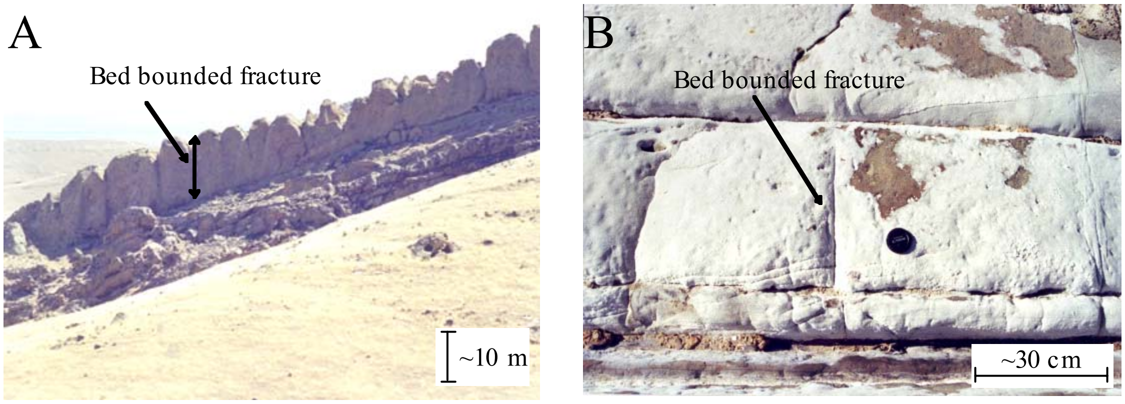

Figure 3.3: Pictures of Point of Rocks outcrops. A) Carneros Canyon; evidence of fracturing related to mechanical unit thickness on a large scale. The height of the beds is approximately 10 m. B) Salt creek; evidence of fracturing related to mechanical unit thickness on a small scale (lens-cap for scale).

Table 3.1 shows that the average fracture spacing determined from core ranges from ~2 ft to ~42 ft in the 2nd POR reservoir and from ~20 ft to ~142 ft in the 4th POR reservoir (Table. 3.1). The average fracture aperture obtained from core was 0.4 mm (an average of only 8 measurements). With this information, the total strain accommodated by the jointing can be calculated as (Jaeger and Cook, 1979, p. 35):

$$\varepsilon = \frac{\sum aperture}{L} \approx \frac{average\ fracture\ aperture}{average\ spacing} \quad \text{... Eq. 3.6}$$

where *L* is the total scan-line length. Using the values obtained for the POR reservoir, the strain accommodated by the jointing ranges from:

$$\frac{0.4\times 10^{-3}\,m}{142\,ft\times 0.3048\,\frac{m}{ft}}\times 100\% < \varepsilon < \frac{0.4\times 10^{-3}\,m}{2\,ft\times 0.3048\,\frac{m}{ft}}\times 100\% \Rightarrow 0.0009\% < \varepsilon < 0.07\% \qquad \text{Eq. 3.7}$$

Assuming that jointing occurred due to fold related strain, this computation indicates that jointing only cannot accommodate the 3% structural strain inferred from Figure 3.2. Therefore, only 1/100th (0.03%) of the structural strain level was chosen to be representative of the strain level responsible for the formation of the jointing in the POR reservoir. The anisotropic strain ratios as seen in the structure are still qualitatively used. Shear fractures, faulting and non-fracture grain scale deformation present in the POR structure are assumed to have accommodated the remainder of the structural strains.

Table 3.1: Calculated fracture spacing for each Point of Rocks reservoir based on FMI/OBMI data.

Set 1 N20E,58NW	**Fracture spacing (ft)**				
Well	**POR1**	**POR2**	**POR3**	**POR4**	**POR5**
7	-	-	-	-	-
10	34	-	35	20	3
2	65	26	-	35	-
74	18	42	313	-	-
Set 2 N35W,70NE	**Fracture spacing (ft)**				
Well	**POR1**	**POR2**	**POR3**	**POR4**	**POR5**
7	-	-	-	-	-
10	-	2	-	27	52
2	48	-	-	80	-
74	-	-	-	-	-
Set 3 N43E,63SE	**Fracture spacing (ft)**				
Well	**POR1**	**POR2**	**POR3**	**POR4**	**POR5**
7	-	40	-	-	-
10	-	29	-	142	-
2	-	-	-	-	-
74	-	-	-	-	-

3.5 NUMERICAL RESULTS

The input ranges necessary to start the fracture pattern simulations have been described in detail in the previous section and in Appendix A through D. Table 3.2 gives a summary of the values that were used in the sensitivity analysis presented in this section. This table also indicates the average values expected to be valid for the 2nd and 4th POR intervals. For all fracture patterns discussed in the next sections, the following properties are held constant: 1) modeled area is 20 by 20 m in map view (to reduce computation time); 2) 100 initial flaws/seeds are used; and 3) the boundary element length is 10 cm. In all following simulations the x-direction (or east-west direction) is in the horizontal direction, and the y-direction (or north-south direction) is in the vertical direction on the page.

Table 3.2: Input ranges used in the numerical simulations.

Parameter	Minimum value	Intermediate value	Maximum value	Most likely in 2ndPOR	Most likely in 4th POR
Young's modulus, GPa	18	19	20	19	19
Poisson's ratio	0.1	0.12	0.19	0.12	0.12
Bed height, m	2	9	40 m	2 m	9 m
Subcritical index	20	40	80	30	35
Strain values	0.01%	0.02%	0.03%	0.03%	<0.03%
Time, years	$6x10^6$	$12x10^6$	$24x10^6$	?	?

3.4.1 Poisson's ratio and Young's modulus

The variation of Young's modulus and Poisson's ratio within the range expected for the POR reservoir has little affect on the overall fracture pattern attributes (Fig. 3.4 and Fig. 3.5). Virtually no changes are observed when the Young's modulus is varied from 20000 MPa to 18000 MPa, and when the Poisson's ratio is varied from 0.1 to 0.19. The results are based on a 2 m thick bed with a subcritical index of 20 and an anisotropic strain of 3 to 1 applied over 24 million years. More simulations with different subcritical index, bed height and strain anisotropy values indicated that the fracture pattern characteristics change due to variations in these parameters, but that changes in Young's modulus and Poisson's ratio do not significantly alter the fracture pattern (Appendix E).

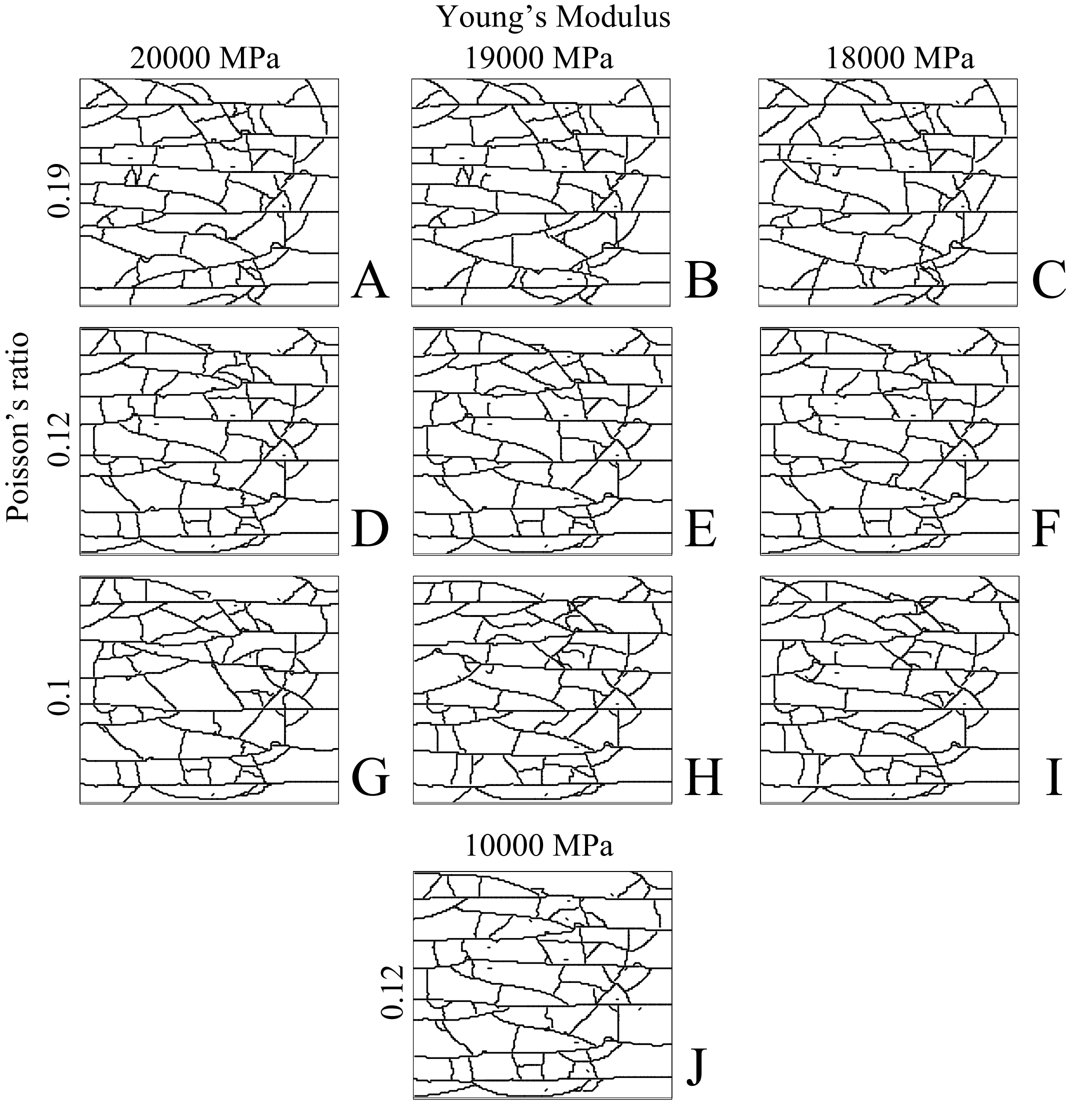

Figure 3.4: Plan view of fracture patterns generated with varying Young's modulus (horizontal direction) and Poisson's ratio (vertical direction) (Strain = 0.03% y-strain and 0.01% x-strain, subcritical index = 20, bed height = 2 m, simulated time = 24 my). Pattern J was generated using a much lower Young's modulus (10000 MPa) simulating fracturing occurring earlier in time, when the sediment has not been fully consolidated

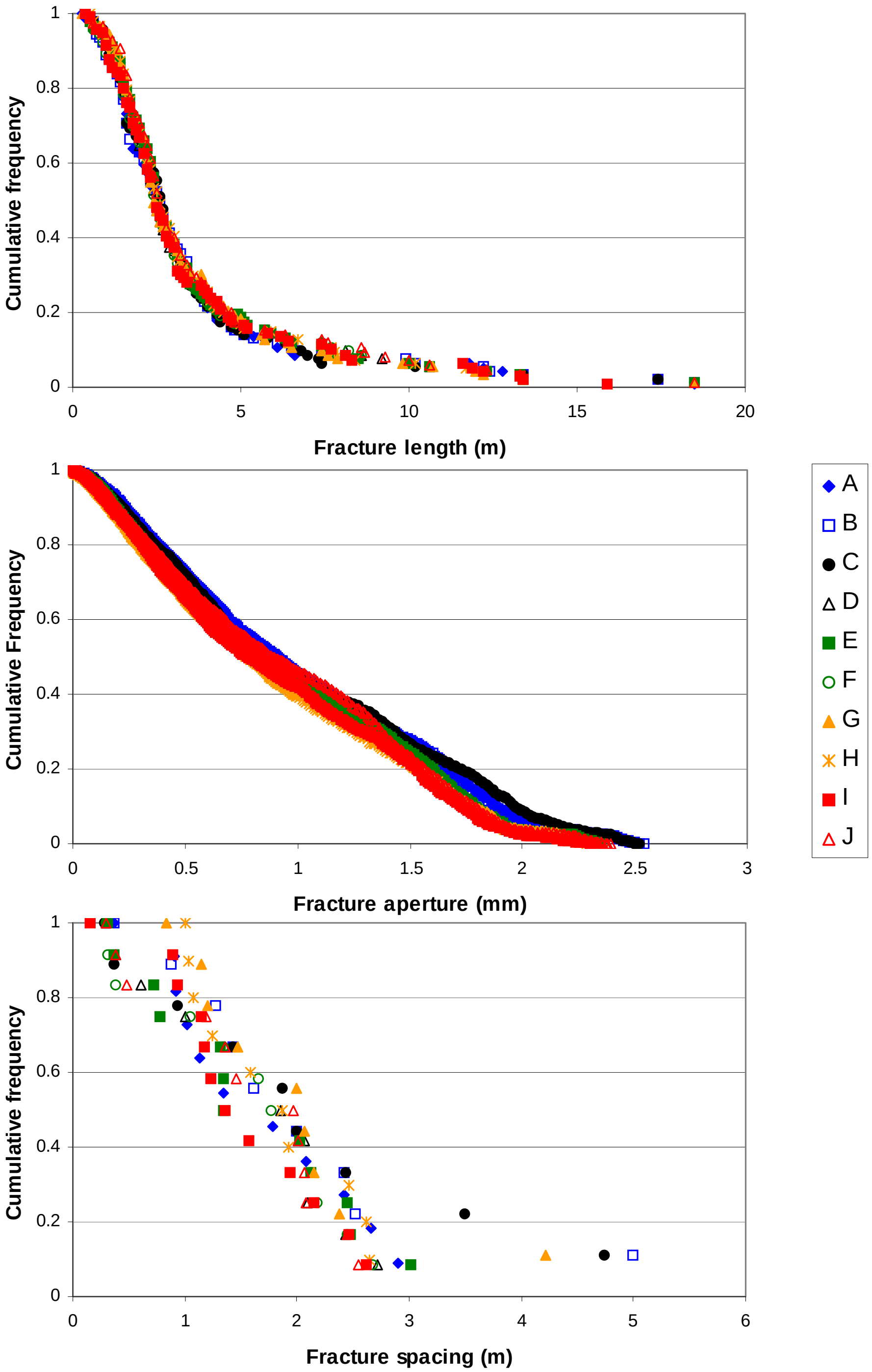

Figure 3.5: Cumulative fracture length, aperture and spacing distributions for the patterns in Fig. 3.4. Fracture spacing is based on one vertical scan-line in the middle of the pattern. Only those fractures having an angle >45 with the scan-line are counted.

Since fracturing might have occurred when the sediment was not fully consolidated, one simulation with a Young's modulus of 10000 MPa was carried out, simulating a less consolidated layer. Results show that even a 50% reduction in Young's modulus does not change the overall fracture attributes such as length, spacing and aperture (Figure 3.4J and Fig. 3.5). The largest variation in cumulative distribution is found in the spacing distribution which is attributed to the small number of sampling points. Henceforth, only the average Young's modulus (19000 MPa) and the average Poisson's ratio (0.12) are used.

3.4.2 Orientations

Under isotropic extension, random flaw or seed orientation results in an inherent unpredictability of the final fracture orientations (Fig. 3.6 and 3.7). In these models, flaws form the initiation point for fracture propagation. Five simulations were run using five different random flaw orientations (from 0 to 360 degrees with 1 degree intervals) and a subcritical index of 20. Different fracture orientations were obtained for different flaw orientations. The fracture orientations plotted are the orientations of each boundary element, excluding the initial flaws. This results in a length weighted rose diagram, since longer fractures are made up of more boundary elements with roughly the same orientation. This type of rose diagram resembles a rose diagram one would obtain from borehole or well-log data. Longer fractures are more likely to intersect the wellbore, skewing the data to the orientation of the longer fractures. In a fractured outcrop, one measurement per fracture might be taken independent of the fracture length, resulting in a bias towards the number of fractures instead of the fracture length. The observed flaw orientation dependence is not only true for a bed height of 2 m, but also for a bed height of 9 m (Fig. 3.8 and Fig. 3.9). Similar results were obtained for a variation in subcritical index (Fig. 3.10 and Fig. 3.11). The dependence of fracture orientations on the initial

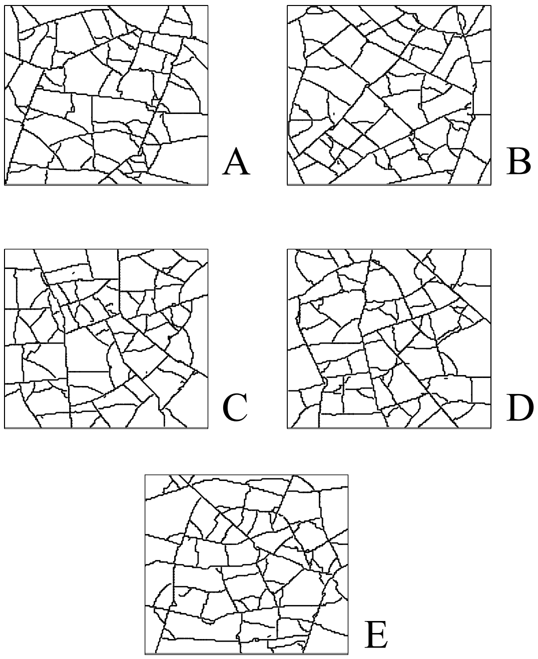

Figure 3.6

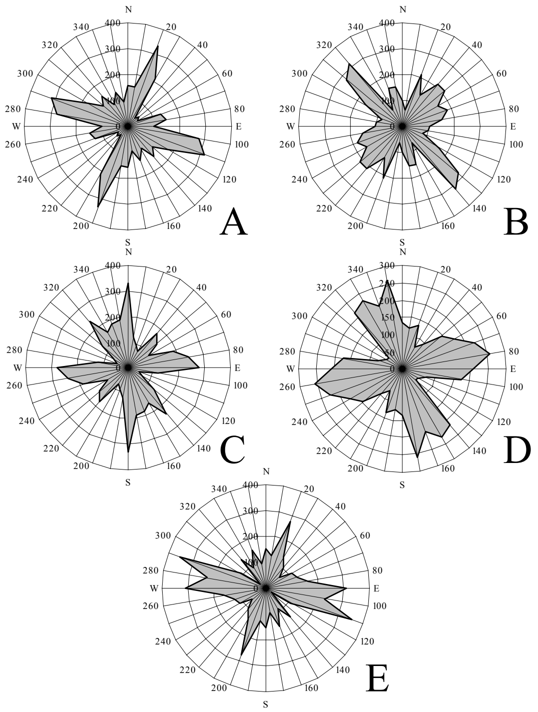

Figure 3.7

Figures 3.6-3.7: Fracture patterns generated from 100 randomly located and oriented flaws (Fig. 3.6, A through E) and their associated rose diagrams (Fig. 3.7, A-E). (Simulated time = 24 my, bed height = 2 m, subcritical index = 20, strain = 0.03% isotropic).

flaw orientation implies an inherent unpredictability of fracture orientations under isotropic strain conditions (i.e., with identical boundary conditions, different flaw configurations result in different fracture orientations). However, all patterns develop at least two dominant fractures sets at approximately 90 degree angle to each other. Sometimes a third less prominent set can be observed (Fig. 3.7A, B, and C; Fig. 3.9A, B and D). This 90 degree angle is most obvious in patterns with a subcritical index of 20 and a bed height of 2 m. Rose diagrams of fracture patterns simulated with a larger bed height and subcritical index value show broader ranges in fracture orientation (Fig. 3.8 through 3.11). A wider range in fracture orientations would be observed in the well-bore

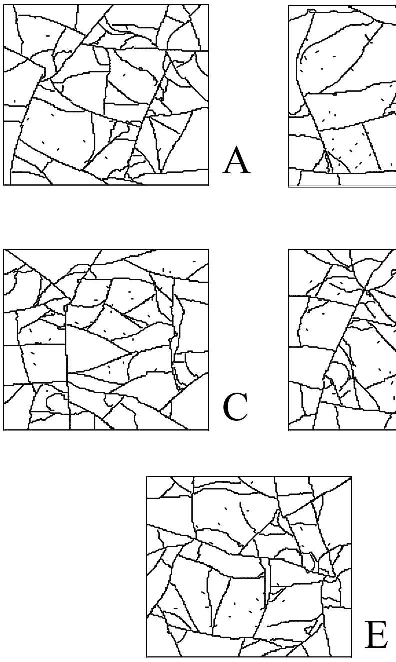

Figure 3.8

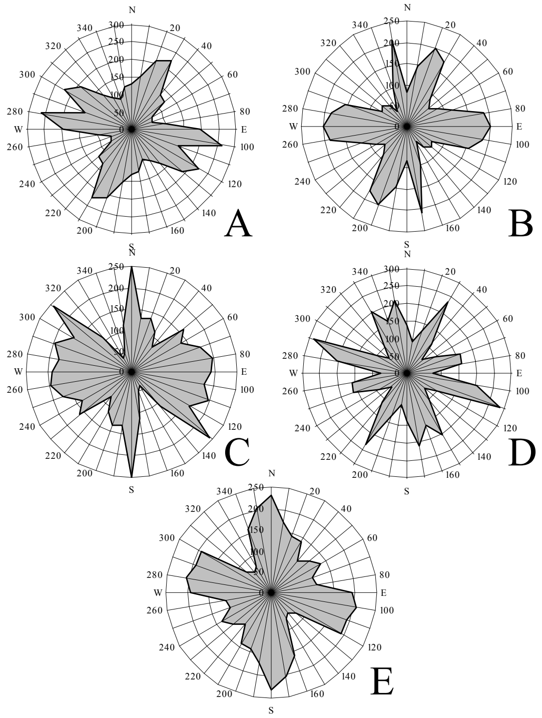

Figure 3.9

Figures 3.8-3.9: Fracture patterns generated with a greater bed height (9 m) than shown in Figures 3.6 and 3.7. All remaining conditions are identical to Figures 3.6 and 3.7.

under these conditions. The bed height dependence can be explained by the larger stress intensity factor created by taller fractures, allowing taller fractures to grow more independently of the remote or surrounding stress field, resulting in less straight fractures and thus a wider range in fracture orientation. For large subcritical index models the fracture propagation velocity is initially very low (Eq. 1.4). Propagation is delayed until more strain has accumulated, leading to larger stress intensity factors at fracture growth (Olson, 2004), allowing the fractures to propagate more independently of the remote stress field. Since the fracture orientations are believed to be accurately described within the POR reservoir, subsequent simulations use a flaw bias based on the observed fracture orientations. In other words, flaws will be oriented either in the N20E, N35W or in the N43E directions.

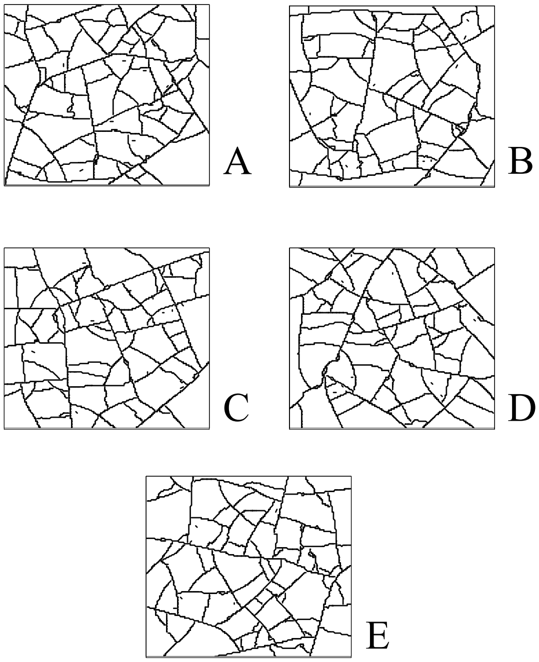

Figure 3.10

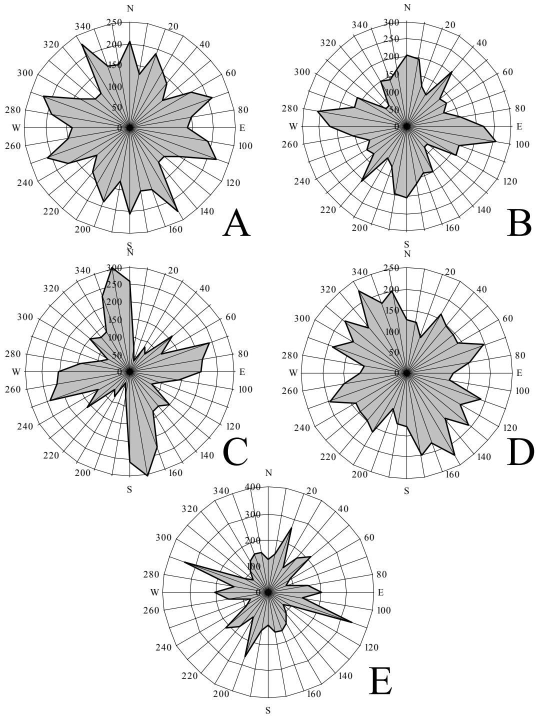

Figure 3.11

Figures 3.10-3.11: Fracture patterns generated with a greater subcritical index value (80) than shown in Figures 3.6 and 3.7. All remaining conditions are identical to Figures 3.6 and 3.7.

3.4.3 Strain/strain rate/anisotropy

Unlike strain rate, strain anisotropy has a large influence on the overall fracture pattern characteristics (Fig. 3.12 and 3.13). The strain rate changes correspond to identical strains obtained in either 6, 12 or 18 million years. The strains range from 0.03% to 0.01% in the x-direction and are kept constant at 0.03% in the y-direction, creating different levels of strain anisotropy. Very few systematic changes in the fracture pattern are observed with a change in strain rate. However, strain anisotropy does alter

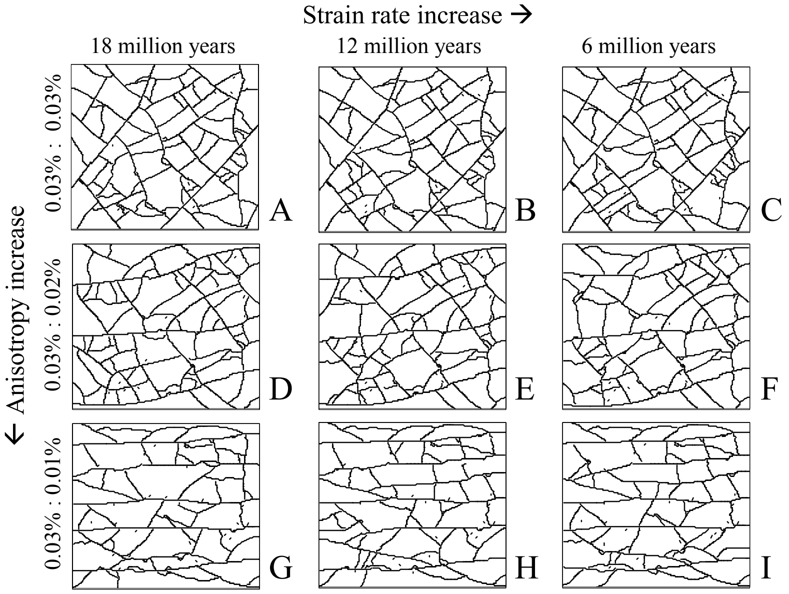

Figure 3.12

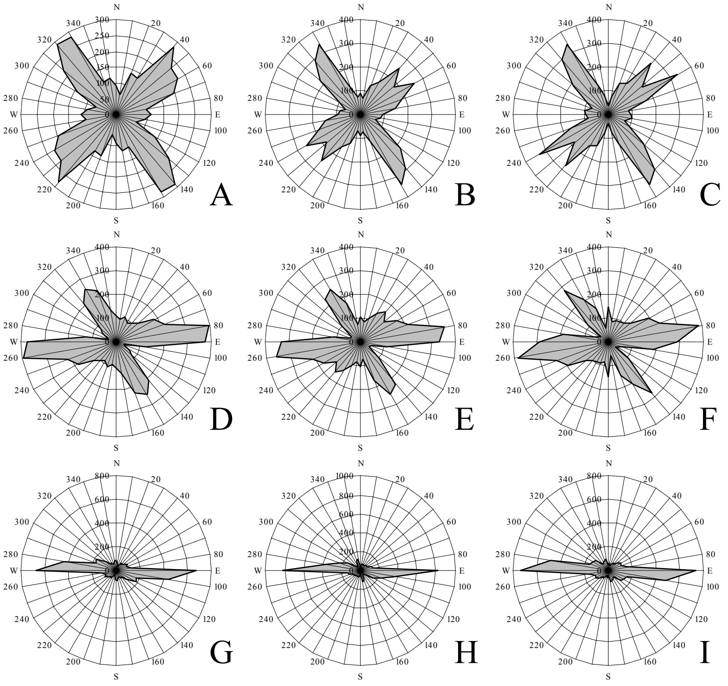

Figure 3.13

Figure 3.12-3.13: Fracture patterns generated with varying strain rate (horizontal direction) and varying strain anisotropy (vertical direction) (Fig.3.12 A through I) and their associated rose diagrams (Fig. 3.13, A-I). (Subcritical index = 40, bed height = 2 m) the fracture pattern. Rose-diagrams of the 9 patterns show that at isotropic strain, the dominant fracture orientations are 90 degree apart (Fig. 3.13A, B and C). With a 0.03% y-strain and a 0.02% x-strain, two dominant fracture orientations still develop but at an acute angle of approximately 70 degrees (Fig. 3.13D, E and F). When the strain anisotropy is further increased, one dominant through-going fracture set develops, which is parallel to the minimum strain direction (Fig. 3.13G, H and I). A second, younger set does develop at a 90 degree angle. This set is restricted in length by the dominant through-going fracture set. Noteworthy are the spacing or block size variations with a change in strain anisotropy (Fig. 3.12). For the isotropic case, two large through-going ~N50E trending fractures develop which are older than the other fracture set, because the other fracture set abuts against it. The spacing between these large through-going fractures is on the order of 10 m. As the strain anisotropy increases the spacing between the large through-going fractures diminishes from approximately 7 m to 4 m. Thus the block size between the large connecting fractures diminishes as the strain anisotropy increases. This not only influences the preferential drainage direction, it can also enhance the drainage efficiency, because more rock is exposed to the through-going fractures which are more likely to be intersected by a borehole.

Since flaw orientation influences fracture orientation, the runs were repeated using random flaw orientations (from 0 to 360 with 1 degree intervals) (Fig. 3.14 and 3.15). Like in Figure 3.13, a change in strain anisotropy changes the fracture orientation. Under isotropic strain, the fractures develop at a 90 degree angle. However, the pronounced 70 degree angle for a 3 to 2 strain anisotropy in Figure 3.13 is not obtained. Two less dominant fracture orientations develop at a ~90 and ~60 degree angle with the dominant set. Compared to Figure 3.13, the sets in Figure 3.14 are much less pronounced, indicating earlier dominance of the east-west fracture set when the flaws have random

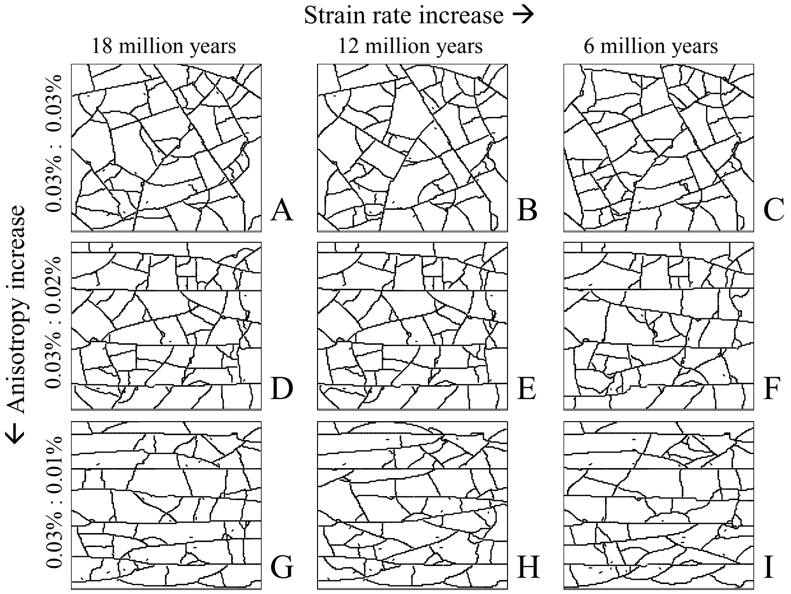

Figure 3.14

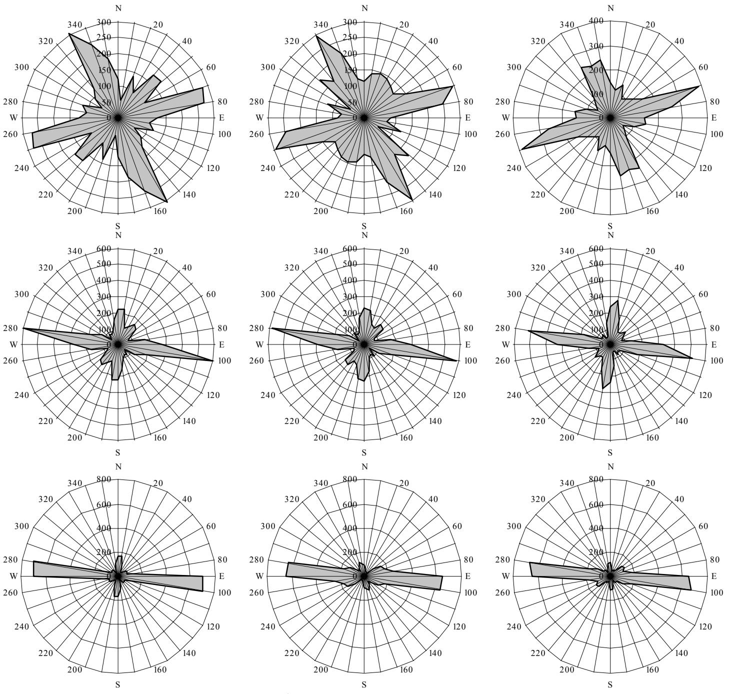

Figure 3.15

Figure 3.14-3.15: Numerical results of simulations run under identical conditions as given in Figure 3.12 and 3.13, except that random flaw orientations are used.

orientations. Since none of the flaws in Figure 3.13 are lined up in the east-west direction, aligning the fractures to this orientation is expected take a larger amount of strain anisotropy, than if the flaws have no preferential direction. Although the trends are less obvious, the decrease in spacing or block size with an increase in strain anisotropy still holds, where the spacing between the older through-going fractures is approximately 10 m, 5 m and 4 m as the strain anisotropy increases (Fig. 3.14).

The orientation changes due to an increase in strain anisotropy are not identical for all bed heights (Fig. 3.16 and 3.17). Increasing the bed height from 2 to 9 m shows that, although still very little change with strain rate is observed, the fracture orientation does not systematically change with an increase in strain anisotropy. Given the same loading, a flaw in a thick bed will propagate almost independently of the remote stress orientations, because its local, crack-induced stress regime is relatively strong. This same argument dictates that fracture orientations in a thin bed are strongly dependent on the remote stress, making orientations more systematic, as observed in Figures 3.12 and 3.13.

A decrease in absolute strain reduces the overall fracture density of the fracture pattern (Fig. 3.18 and 3.19). Fracture density is defined as the total fracture length divided by the total area. In general, Figure 3.19 shows that an increase in strain increases the fracture density and thus increases the likelihood that a vertical well-bore will intersect a fracture. The previously described increase in strain anisotropy (Figs. 3.12, 3.14 and 3.16) also decreases the mean strain. However, the change in mean strain for these cases is too small to give an observable change in fracture density. The dependence of fracture density on the absolute amount of strain implies an expected decrease in jointing with depth as the strain changes from extensional to contractional from top to bottom in the POR structure. Based on this observation alone, less fracturing is expected to be present in lower POR intervals. However, this observation can be overshadowed by

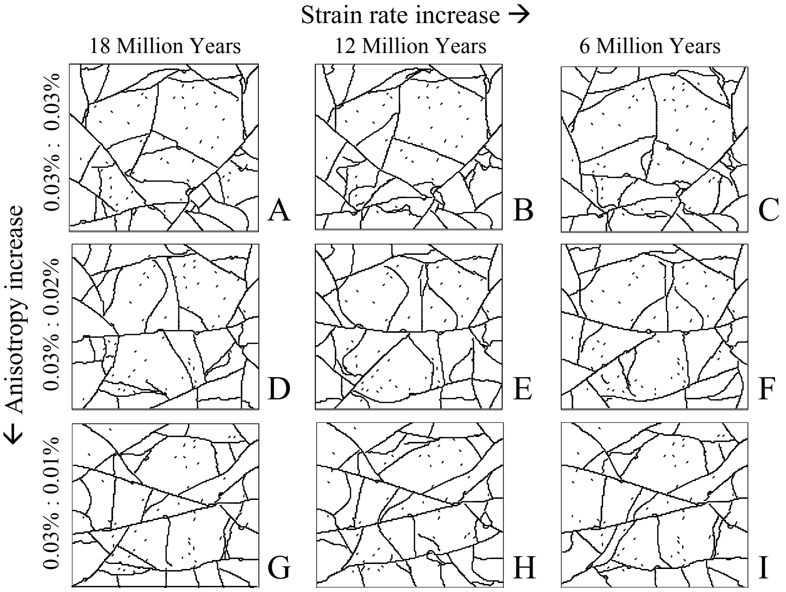

Figure 3.16

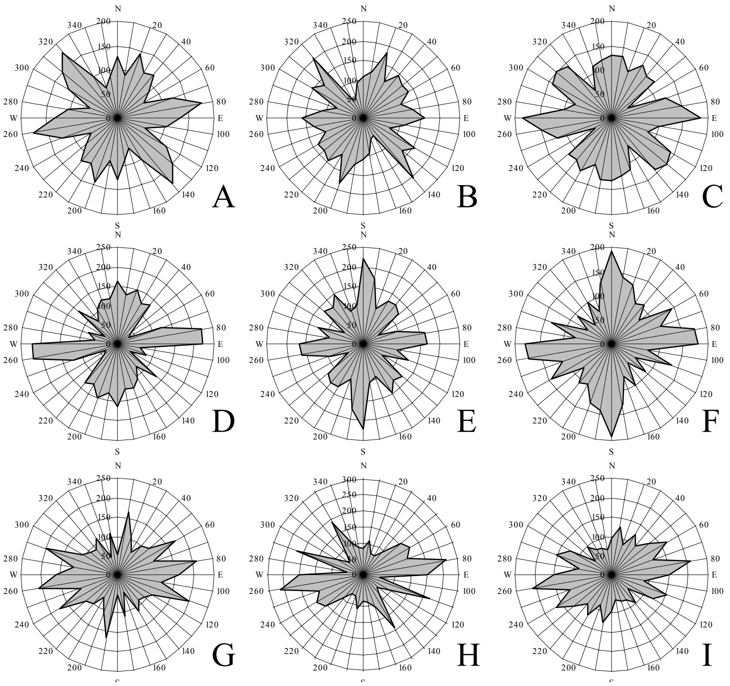

Figure 3.17

Figure 3.16-3.17: Numerical results of simulations run under identical conditions as given in Figure 3.12 and 3.13, except that larger bed thickness is used (9 m).

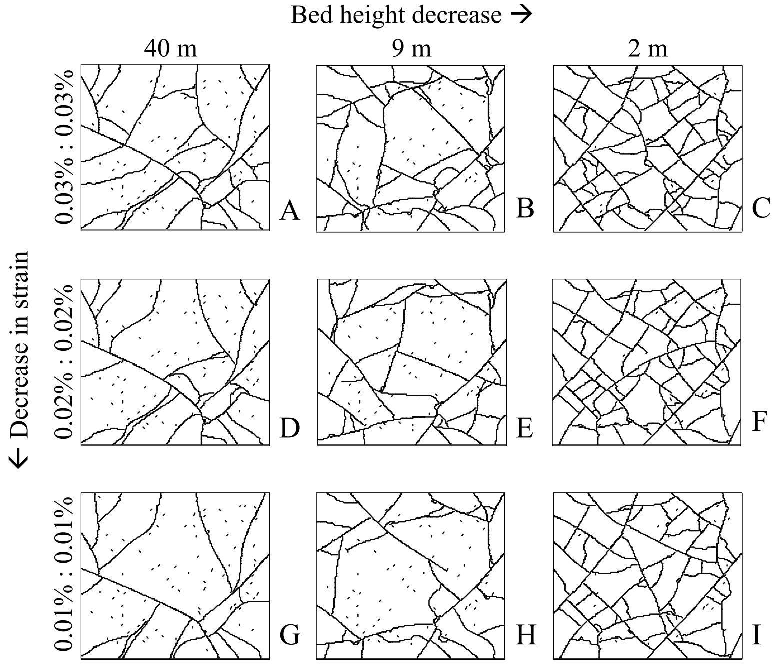

Figure 3.18

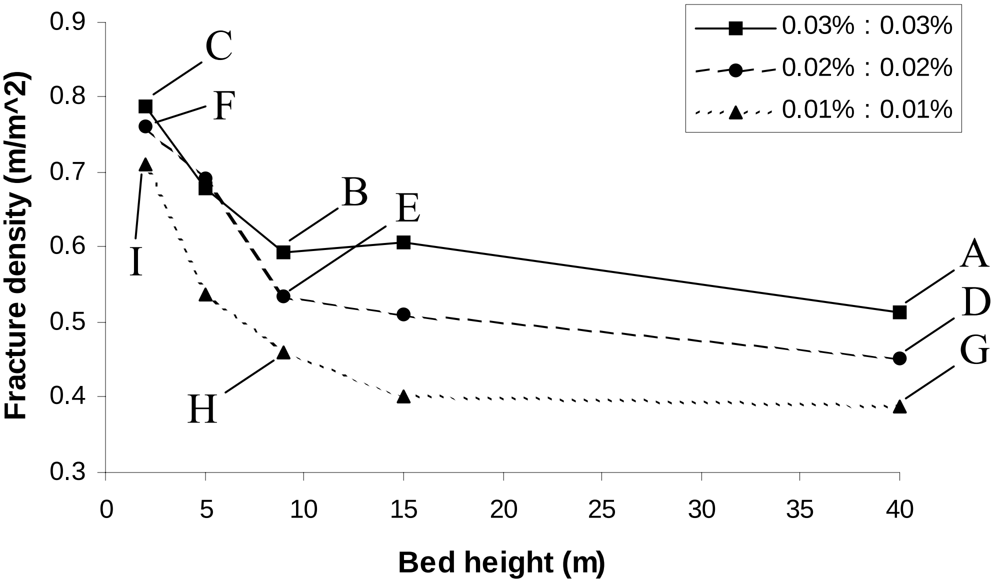

Figure 3.19

Figure 3.18-3.19: Fracture patterns generated with varying bed height (horizontal direction) and varying absolute strain (vertical direction) (Fig. 3.18, A through I) and their resulting fracture density (m/m^2) plotted vs. bed height (Fig.3.19, A-I). (Subcritical index = 40, simulated time = 24 my) a change in bed height. Figure 3.19 shows that the fracture density decreases more when the bed height increases from 2 to 9 m than when the overall strain is reduced from 0.03% to 0.01%.

3.4.4 Bed thickness

As the bed thickness increases, the fracture density decreases (Fig. 3.18 and 3.19). The reason for this behavior is that fractures are modeled to vertically span the entire bed. Thus, in the case of a 40 m thick bed, the fracture has a height of 40 m. Taller fractures will have a larger stress shadows (Pollard and Segall, 1987). In this stress shadow other fractures are hindered from growing, resulting in a sparser fracture pattern. However, as the bed thickness increases the model changes from a pseudo 3D model (a model in which variations in the third dimension, the fracture height, are indirectly taken into account) to a plane strain 2D model (a model in which variations in the third dimension, the fracture height, are considered negligible and not taken into account). Model responses from the pseudo 3D model should not be compared to results from the plane strain model. A 2D plane strain model applies to three idealized types of fracturing as described by Olson (1993): 1) fracture height growth of infinitely long blade like fractures, 2) fracture length growth of fractures confined to a bed that has freely slipping interlayer boundaries, and 3) propagation of penny shaped fractures in an infinite medium as seen from a single plane perpendicular to the propagation direction. To allow for a correct comparison the bed thickness in the pseudo 3D model should not be increased infinitely. The main difference between a 2D and a pseudo 3D approach is the value of the 3D correction factor, G^{ij} (Eq. 3.2). In other words, the 3D correction factor (Eq. 3.2) for a plane strain response would be 1. Plotting the 3D correction factor values for fractures of different height shows that a fracture in a 2 m thick bed (fracture height = 2 m) experiences a decrease in the 3D correction factor from 1 to 0.01 over the size of the pattern (= 20 by 20 m) (Fig. 3.20). However, a fracture in a 40 m thick bed (fracture height = 40 m) only experiences a decrease from 1 to 0.84 (Fig. 3.20), indicating that this simulation almost resembles a plane strain simulation. For a 15 m thick bed, deviations from plane strain are sizeable and therefore simulations with bed thicknesses of 15 m and less are considered comparable in terms of pseudo 3D behavior. Thus, the decreasing fracture density trend as bed thickness increases still holds (Fig. 3.19). This observation coincides with simulation results obtained by Olson (2004) for straight fractures with varying bed thickness values, where he observes a decrease in fracture spacing (and thus density) as the bed height increases.

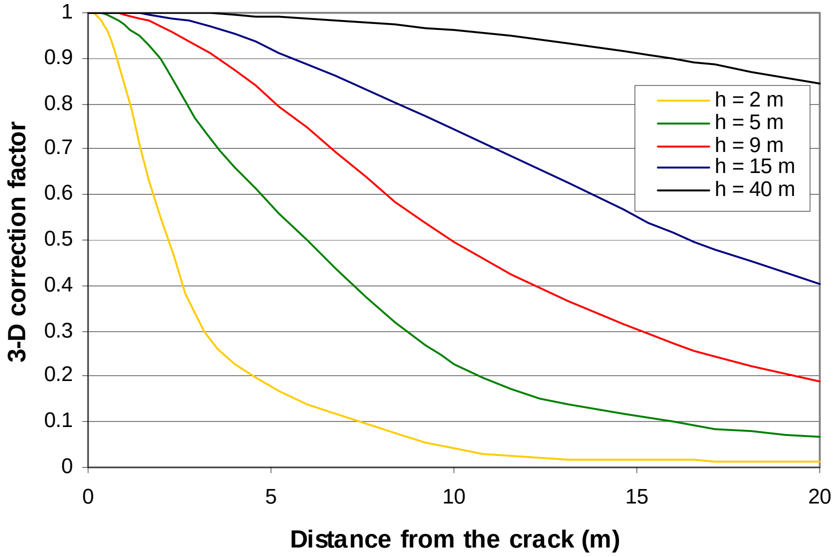

Figure 3.20: The 3D correction factor as a function of distance from the crack (m) for different bed thicknesses (h).

3.4.5 Subcritical index

Olson (1993, and 2004) has investigated the influence of subcritical index on straight fracture growth and found substantial variations in fracture pattern characteristics with subcritical index changes. A fracture spacing equal to bed thickness was observed for intermediate subcritical index values (n=20). Fracture spacing tended to become irregular and much less than the mechanical bed thickness as the subcritical index was lowered (n=5). For a subcritical index of 80, fractures were observed to cluster, where the spacing between the clusters was very large. This implies that an increase in subcritical index decreases the fracture density. Multi-orientation fracture simulations also show an increase in fracture density with a decrease in subcritical index, but only for thick beds (15-5 m) (Fig. 3.21 and 3.22). For thin beds (2 m), a change in subcritical index does not significantly change the fracture density. The limited number of flaws that are used in the simulation can explain this observation. The maximum attainable fracture density has been reached in this numerical setup at a bed thickness of 2 m. A decrease in the subcritical index cannot increase the fracture density as no flaws are left to propagate. For the 9 m thick bed, not all flaws have propagated and thus an increase in fracture density can occur when the subcritical index is decreased (Fig. 3.19). Thus, the lack of fracture density increase with a decrease in subcritical index for thin beds is considered to be a numerical artifact and not a physical observation. Therefore, as the subcritical index decreases the fracture density is expected to increase, irrespective of the bed thickness.

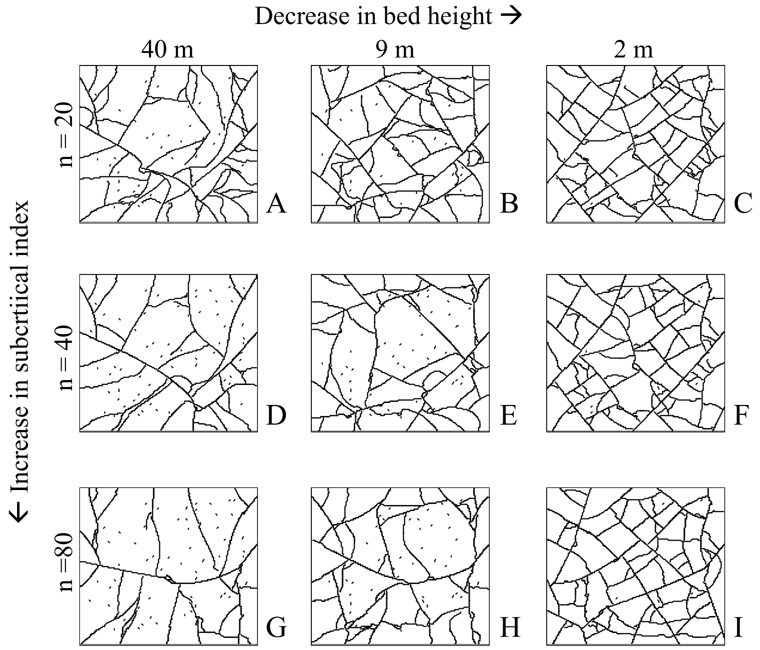

Figure 3.21

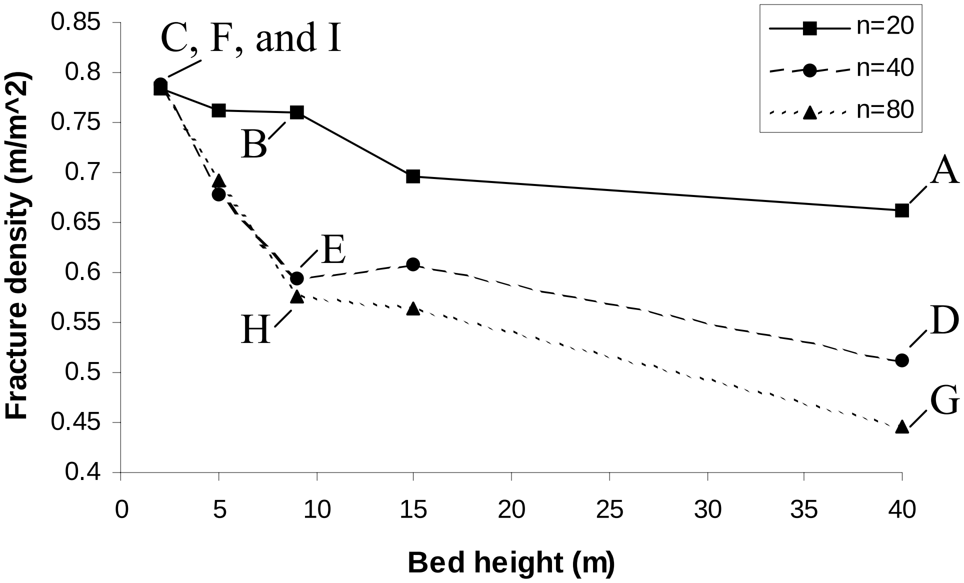

Figure 3.22

Figure 3.21-3.22: Fracture pattern generated with varying bed height (horizontal direction) and varying subcritical index (vertical direction) (Fig. 3.21, A through I) and their resulting fracture density (m/m^2) plotted vs. the bed height (Fig. 3.22, A-I). (Strain = 0.03% isotropic, Simulated time = 24 my)

3.4.6 Length, spacing and aperture distribution

From the previous sensitivity analysis, bed height, absolute strain, strain anisotropy and subcritical index have been determined to have the largest influence on the resulting fracture pattern. Therefore, a full investigation of the length and aperture distributions as well as the fracture orientations of 12 different patterns was performed. These 12 patterns can be grouped into three loading histories: 0.03% isotropic strain (Fig. 3.23 through 3.26), 0.01% isotropic strain (Fig. 3.27 through 3.30), and 0.03% strain in the x direction and 0.01% strain in the y-direction (Fig. 3.31 through 3.34). Since a subcritical index of 80 has only been observed in the calcite concretions present in the POR reservoir, only patterns with a subcritical index of 20 and 40 are simulated. Likewise, a bed height of 40 m is unlikely to be a representative value in the POR intervals under investigation (Appendix C), and thus simulations were carried out for bed heights of 2 m and 9 m.

As discussed earlier, two dominant fractures sets develop at a 90-degree angle at 0.03% isotropic strain for a bed height of 2 m (Fig. 3.23 and 3.24). In the POR reservoir, these orientations correspond to the observed the N35W and, N40E directions. For a 9 m thick bed, the fracture orientations do not cluster as nicely around the N35W and N40E directions as for the 2 m thick bed. Therefore, simulations indicate that as the bed height increases, the average fracture orientations will become more difficult to determine. At a subcritical index of 40 and a bed height of 9 m, all three fracture trends observed in FMI (N20E, 58NW; N35W, 70NE; and N43E, 63SE) are visible and even a fourth trend can be observed. Although none of these simulations shown in Figure 3.23 directly result in the 3 observed fracture orientations, the range in fracture orientations indicates that the observed fracture orientations can be recreated using the span of possible boundary conditions and rock properties. In this study, fracturing is assumed to have occurred due to a single loading event. However, fracturing might have occurred under prolonged tectonic loading prior to formation of the anticline, where the three different fracture sets might have formed due to three different remote stress fields. Since the present day stress field is aligned with the stress field responsible for formation of the anticline, no evidence exists supporting orientation changes of the remote stress field. Therefore, the single loading event approach is favored here.

All fracture length distributions were best fit using a negative exponential distribution (Fig. 3.25). The data was analyzed with a trendline in EXCEL, where the trendline with the highest R^2 is chosen to best represent the data. Normal, powerlaw, logarithmic and negative exponential fits were tried for each dataset. Olson et al. (2001) and Qiu (2002) predict a negative exponential length distribution for straight fracture propagation due to mechanical crack interaction. Numerical results show that the magnitude of the exponent depends on the subcritical index value, where an increase in subcritical index from 5 to 20 decreases the magnitude of the exponent, indicating many longer fractures and less shorter ones (Olson et al., 2001; Qiu, 2002; Olson, 2004). Higher subcritical index values result in higher velocity contrasts between fractures, resulting in a fracture pattern where fractures grow one at a time. However, this trend reverses for a subcritical index increase from 20 to 80. The larger number of shorter fractures for a subcritical index of 80 is compared to the growth of process zone across a rock body. At higher subcritical indices the initial fracture velocity is low, delaying fracturing until more strain has accumulated. This increases the stress intensity factor, resulting in critical and not subcritical fracture growth. The stress perturbation around the crack tip is large due to the high stress intensity factor, and propagation of flaws in the crack tip region is enhanced, resulting in a clustered fracture pattern with a process zone

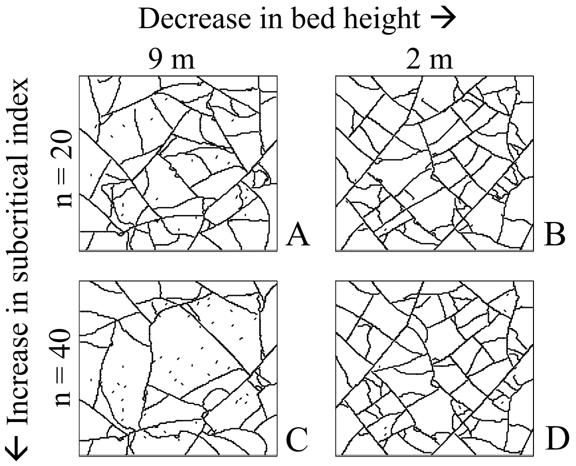

Figure 3.23

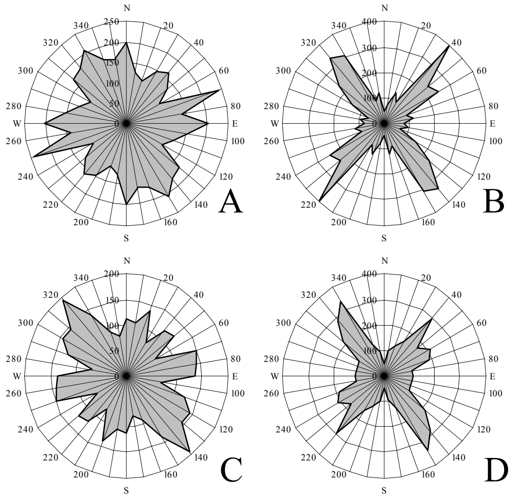

Figure 3.24

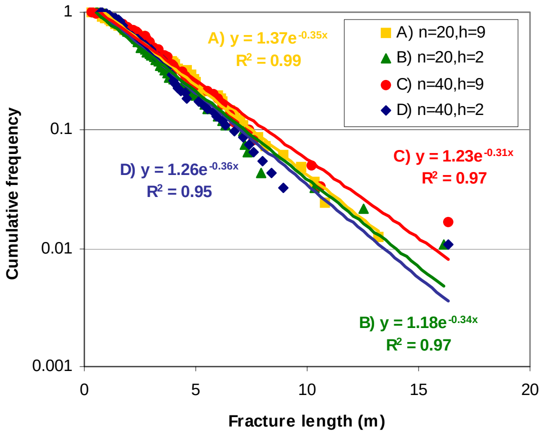

Figure 3.24

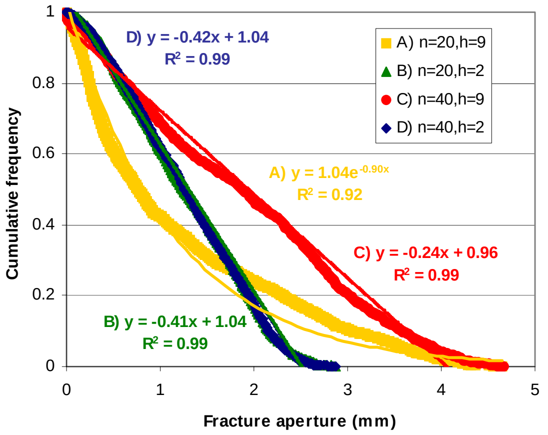

Figure 3.25

Figure 3.23-3.26: Fracture pattern generated with varying bed height (horizontal direction) and varying subcritical index (vertical direction) (Fig. 3.23, A through D) and their associated rose diagrams (Fig. 3.24, A-D), length distributions (Fig. 3.25), and aperture distributions (Fig. 3.26). (Strain = 0.03% isotropic, Simulated time = 24 my)

type appearance (Olson et al., 2001; Qiu, 2002; Olson, 2004). For the case at hand, those fractures with a large stress intensity factor (thick beds) and a large velocity contrast (high subcritical index) grow longest (Fig. 3.25 case C). The other three patterns, at lower subcritical index and bed height, exhibit almost identical length distributions. As the subcritical index decreases, multiple fractures can grow at the same time, increasing fracture interaction and reducing fracture length. Furthermore, a decrease in bed height, decreases the stress shadow and allows more cracks to propagate and interact, reducing the fracture length. However, Qiu (2002) found the exact opposite, where an increase in bed thickness resulted in a larger percentage of short fractures and a smaller percentage of long fractures. She argued that the larger bed thickness increased mechanical interaction which limited length development. Apparently in the multi-orientation simulations as presented here mechanical interaction is still large at small bed heights, resulting in shorter fractures in thinner beds. The average fracture length is approximately 3-4 m, with the mode around 2 m.

The aperture distribution at a bed height of 2 m, for both a subcritical index of 20 and 40, is best fit with a normal distribution (Fig. 3.26 case B and D). At a bed height of 9 m and a subcritical index of 20, the aperture distribution is best fit by a negative exponential distribution (Fig. 3.26 case A). However, at a bed height of 9 m and a subcritical index of 40, the distribution exhibits a larger deviation from the normal distribution than in cases B and D and exhibits a more bimodal distribution (Fig. 3.26 case C). Long, tall fractures (large stress intensity factor) open unhindered, but the opening of the surrounding smaller fractures is hampered by the nearby large fracture. This results in a considerable amount of small fracture apertures and a few large ones, explaining the exponential aperture distribution for case C of Figure 3.26. Likewise, the normal distribution, obtained for cases B and D (Fig. 3.26), indicates that the stress shadow of these smaller length and smaller height fractures is less, allowing all fractures to open almost equally, resulting in a normal distribution. The mean fracture aperture ranges from 1.2 to 1.9 mm, while the mode varies from approximately 0.45 to 1.3 mm. This is an overestimation of the 0.4 mm aperture observed in core. A possible reason for the smaller fracture aperture observed in core might be because the strain levels used for these simulations overestimate the strain levels responsible for the jointing in the POR reservoir. A lower strain level would result in an expected decrease in fracture aperture. The smaller apertures observed in the thin-bedded cases are a result of their increased fracture density. The same amount of strain is distributed over more fractures, resulting in a lower average fracture aperture.

At 0.01% isotropic strain, two dominant sets of fractures develop at a 90 degree angle (Fig. 3.27 and 3.28), similar to those observed in the 0.03% isotropic strain condition (Fig. 3.23 and 3.24). The fracture orientations do not cluster as nicely around the N35W and N40E directions for the thick versus the thin beds (Fig. 3.28). Therefore, fracture orientations appear more random as the bed thickness increases, independent of isotropic strain level. A possible explanation for the smaller fracture orientation variation observed for the case with a subcritical index of 40 and a bed height of 9 m as compared to the case with a subcritical index of 20 for a 9 m thick bed, is the larger velocity contrast for fractures at larger subcritical indices, allowing one fracture to dominate. This fracture will dominate the stress field, making the remaining fracture propagation more systematic as compared to the low subcritical index case.

Similar to the 0.03% isotropic strain cases, all simulations exhibit negative exponential length distributions, where the thin beds tend to skew more towards the short fracture lengths (Fig. 3.29). The average fracture length is approximately 3-4 m with the mode around 2-4 m (Fig. 3.29). All fracture aperture distribution are best represented by a normal distribution (Fig. 3.30). Analogous to the 0.03% isotropic case, at a bed height of 9 m, the aperture distribution deviates from the normal trend towards a negative exponential trend (Fig. 30A and 30C). It is interesting to note that the aperture distribution for a 2 m thick bed is influenced by the subcritical index value, where a

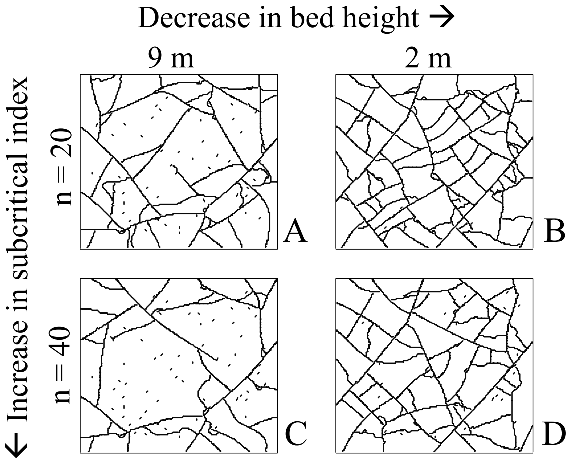

Figure 3.27

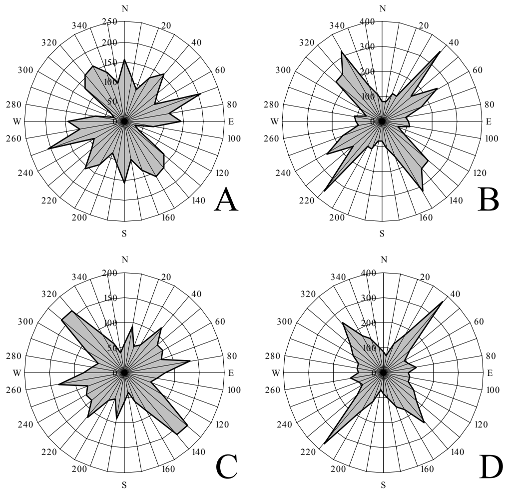

Figure 3.28

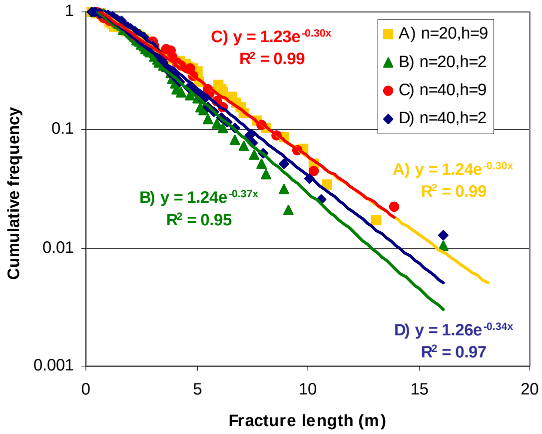

Figure 3.29

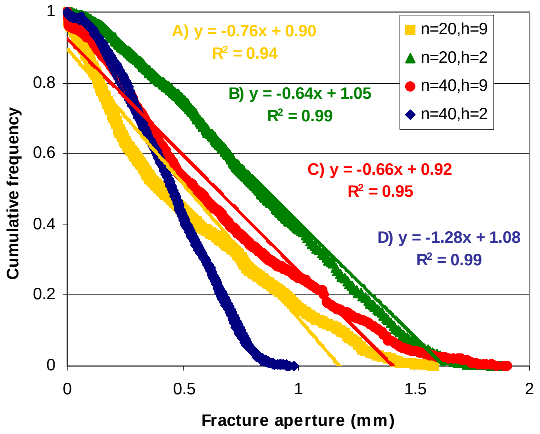

Figure 3.30

Figure 3.27-3.30: Fracture pattern generated at lower strain levels (0.01% isotropic) than shown in Figures 3.23-3.26 (Fig. 3.27, A through D), and their associated rose diagrams (Fig. 3.28, A-D), length distributions (Fig. 3.29), and aperture distributions (Fig. 3.30). (Simulated time = 24 my)

higher subcritical index results in smaller fracture apertures. As stated before, higher subcritical index cracks have lower crack velocities and do not propagate until more strain has accumulated. Thus under identical conditions these fractures are still forming whereas the ones with lower subcritical index values have already been placed. For the low subcritical index case, an additional strain increase cannot result in an additional length increase due to the limited number of flaws, effectively fattening the cracks more. The fact that this is not observed for the 0.03% isotropic strain case (Fig. 3.26) is attributed to the larger strain rate for this simulation. In the same amount of time more strain has been accumulated in the 0.03% isotropic strain case than in the 0.01% isotropic strain case, allowing fractures at higher subcritical indices to propagate earlier, reducing the contrast between the 20 and 40 subcritical index case. The average aperture is lower than that observed in the 0.03% isotropic strain case and ranges around 0.5 to 1 mm. The aperture mode value is approximately 0.15-0.75 mm (Fig 3.30). This indicates that lower strain levels produce thinner fractures.

As discussed earlier, anisotropic strain narrows the range of fracture orientations (Fig. 3.32) as compared to isotropic strain results for small bed heights (Fig. 3.24 and 3.28). One dominant through-going east-west fracture set develops (Fig. 3.32). This fracture orientation is not a dominant trend observed in wells 10 and 8. For a bed height of 9 m the E-W fracture orientation is still present, but other orientations such as the N40E and N30W-N40W direction are also observed (Fig. 3.32 case A and case C). Absence of a dominant east-west trend in the FMI-log from well 10 and Ultrasonic Borehole Image (UBI) log from well 8 might indicate that such anisotropic conditions are not representative of the strain state in the POR reservoir in those regions. Although, these strain orientations are considered representative for the POR reservoir, a slight rotation of the maximum strain orientation would influence the resulting fracture orientation. Therefore, more detailed structural strain information would be necessary to rule out this strain state.

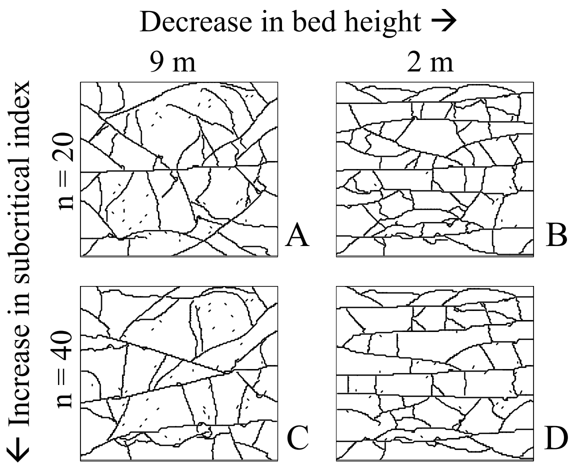

Figure 3.31

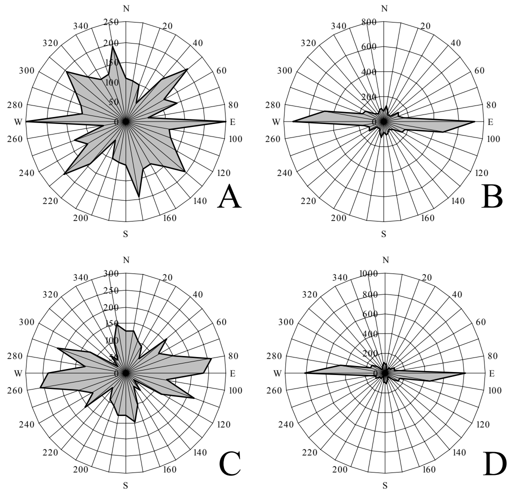

Figure 3.32

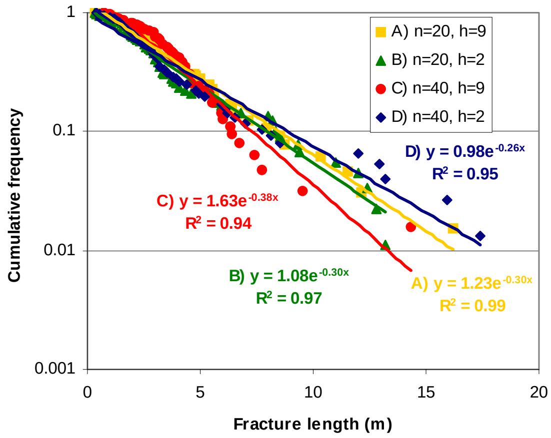

Figure 3.33

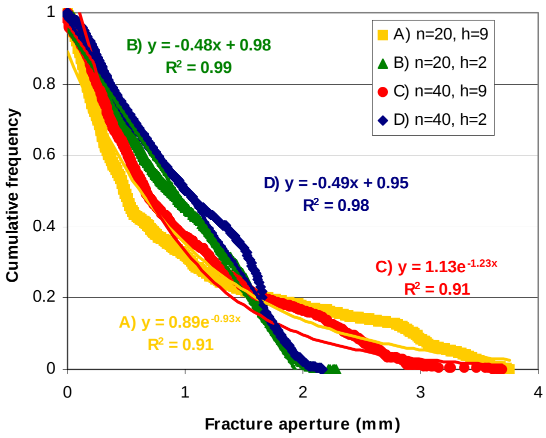

Figure 3.34

Figure 3.31-3.34: Fracture pattern generated with a 3 to 1 anistropic strain level (y strain = 0.03%, x strain = 0.01%) (Fig. 3.31, A through D) (remaining variables identical to Figure 3.23-3.26), and their associated rose diagrams (Fig. 3.32, A-D), length distributions (Fig. 3.33), and aperture distributions (Fig. 3.34). (Simulated time = 24 my)

Identical to the previous cases, all fracture length distributions are negative exponential for the 3 to 1 strain case (Fig. 3.33). However, the expected dependence of the length distribution on bed thickness and subcritical index is lost. The remote anisotropic strain field influences fracture orientation and the fracture interaction is altered from the previously described isotropic conditions, reducing the trendline fits and obscuring earlier found correlations. The average fracture length is approximately 3-4 m with the mode around 2-4 m (Fig. 3.33). The fracture aperture distribution does not remain constant dependent on the bed height and subcritical index. At a bed height of 9 m the aperture distribution is best represented by a negative exponential distribution (Fig. 3.34 case A and C), however the other simulated patterns fit normal distributions (Fig. 3.34 case B and D). This variation in aperture distribution is identical to the one found for both isotropic strain cases (Fig. 3.26 and Fig. 3.30). The average aperture is lower than that observed in the 0.03% isotropic strain case, due to the lower amount of mean strain and ranges around 1 mm.

All previous simulations were performed with the same random flaw locations and orientations. Figures 3.35 through 3.38 show results for the 0.03% isotropic strain case but with different random flaw locations and orientations (ranging from 0 to 360 with a 1 degree interval). The observed dependence for length and aperture distributions still hold, where longer fractures develop in thicker beds, and where the fracture aperture distribution becomes more negative exponential as the bed height increases.

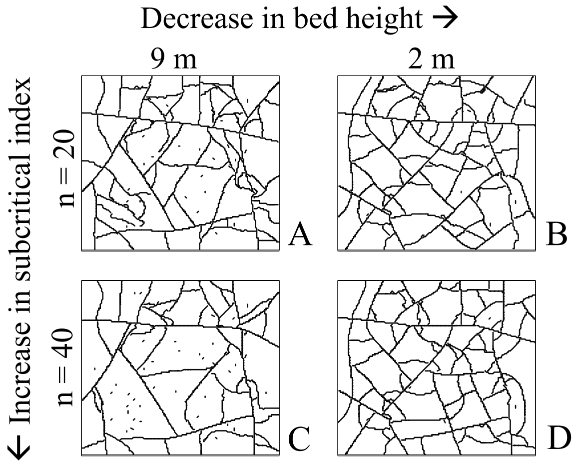

Figure 3.35

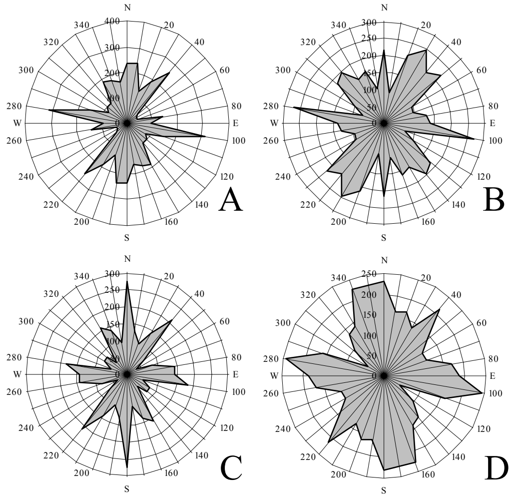

Figure 3.36

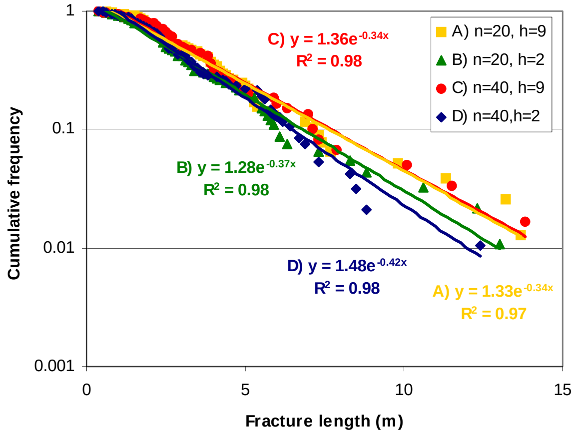

Figure 3.37

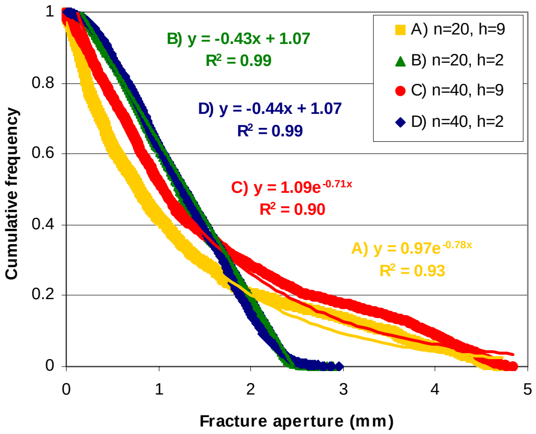

Figure 3.38

Figure 3.35-3.38: Fracture pattern generated using random flaw locations (Fig. 3.35, A through D) (remaining parameters are identical to the conditions as described in Figures 3.23 through 3.26), and their associated rose diagrams (Fig. 3.36, A-D), length distributions (Fig. 3.37), and aperture distributions (Fig. 3.38).

Spacing is defined as the perpendicular distance between two fractures. Some difficulty was encountered estimating the fracture spacing of the fracture patterns in Figures 3.23 and 3.27. Specifically for the thick-bedded simulation results, since these fracture patterns are not very systematic. Therefore, only the spacing distributions of the thin-bedded simulations were analyzed. To obtain correct spacing values each set was analyzed separately. Spacing values were determined using 5 scan-lines perpendicular to the orientation under investigation. The orientations considered are the fracture sets trending N40E and N35W for Figure 3.23 case B and D, and Figure 3.27 case B and D and the fracture sets trending east-west for Figure 3.31 case B and D. The distance between each scan-line is 4 m with the center scan-line going through the center of the fracture pattern. Only those fractures belonging to the fracture set under investigation were considered. The fracture spacing distributions obtained are highly variable even within each orientation. For the N40E orientation (Fig. 3.39A), the spacing distributions are in general best represented with a negative exponential distribution. However, for 0.01% isotropic strain, pattern D, a logarithmic distribution gives the best fit. For the N35W orientation (Fig. 3.39B), both normal and negative exponential distributions are obtained without any observed systematics as to why one is normal or negative exponential. Both east-west fracture trends (Fig. 3.39C), however, follow a normal distribution. For all isotropic patterns, the N40E set is the oldest set against which the N40W-N30W set abuts. The N40E set was free to develop under the applied strain regime and subcritical index. However, the development of the N40W-N30W set depends on the N40E set. This explains both the dependence of the N40E set on the amount of strain and subcritical index, where the larger the subcritical index and the smaller the strain the larger the spacing, as well as the independence of the N40W-N30W set to these two variables. Smaller strain values lead to smaller stress intensity factors, explaining the increase in spacing. Olson (1993, 2004) found that fracture spacing values increase with an increase in subcritical index, which coincides with the trend observed in Figure 3.39A.

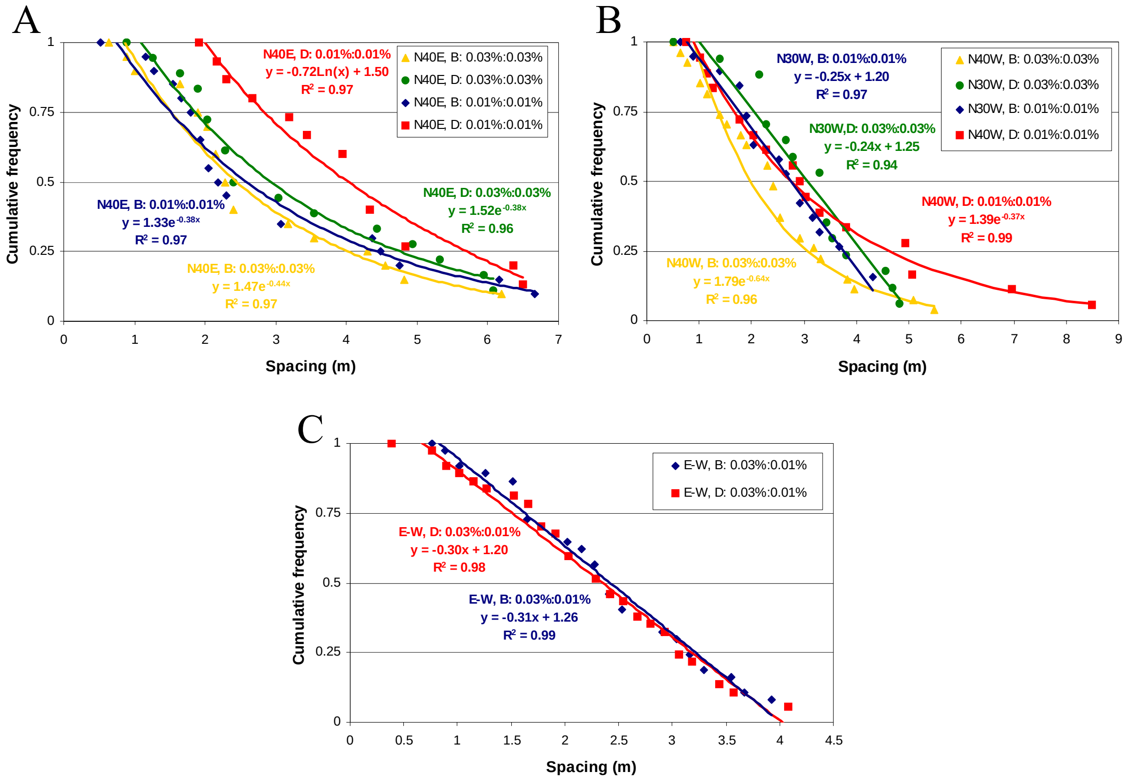

Figure 3.39: Fracture spacing distributions for: A) the N40E fracture set shown in Figures 3.23B and D, and 3.27B and D, B) the N35W fracture set shown in Figures 3.23B and D, and 3.27B and D, and C) the E-W fracture set shown in Figure 3.31B and D. Spacing values are determined using 5 scan-lines perpendicular to the orientation under investigation. The distance between each scan-line is 4 m with the center scan-line going through the center of the fracture pattern. Only those fractures belonging to the fracture set under investigation were considered.

The average fracture spacing for the N40E orientation is simulated to be approximately 3-4 m, and for the N35W orientation to be approximately 2-3 m. For the east-west orientation the average spacing is simulated to be around 2.3 m. Firstly, it should be noted that the area of investigation is relatively small. This leads to a limited number of spacing observations making the statistical fits less significant. Therefore, the distributions given in Figure 3.39 should be used with caution, as larger sampling areas are necessary to increase the degree of confidence in the overall distribution. Secondly, it should be noted that fracture spacing is highly dependent on the initial flaw density, where an increase in flaw density decreases the fracture spacing. The overall orientation characteristics of the fracture patterns do not change. Thus, increasing the flaw density should result in a similar distribution, but the mean should be shifted towards smaller spacing values.

Two types of fractures important to fluid flow are believed to be present in the POR reservoir. Small or meso-fractures, which break the reservoir up into small blocks and allow drainage of the source rock and large or macro-fractures which connect these fractured zones. The predicted fracture distributions only model the meso-fractures in the POR reservoir and do not model macro-fractures which cross multiple bed boundaries. The expected changes in subcritical index between the 2nd and the 4th POR, range from 30 to 35 respectively (in aqueous conditions). Based on the low variation in the subcritical index values measured in the POR reservoir, I do not expect that subcritical index variations have a large impact on the fracture pattern characteristics if both reservoirs fractured when water was present in the reservoir. However, if hydrocarbon migration occurred, prior to fracturing, to fill the structure up to the 2nd POR reservoir with oil and leave the remainder brine saturated, then the governing subcritical index in the 2nd POR reservoir would be 54 (Appendix D). This would lead to an expected decrease in fracture density in the 2nd POR reservoir as compared to the 4th POR reservoir (if all other boundary conditions remain constant). This however is not observed in the POR reservoir, where the 2nd POR reservoir is more heavily fractured than the 4th POR reservoir. Given this information it could be assumed that fracturing in the POR reservoir structure occurred prior to hydrocarbon migration. However, strain and bed height are likely to overpower the subcritical index dependence, where both a decrease in expected strain level and an increase in bed height result in a lower fracture density in the 4th POR reservoir than in the 2nd POR reservoir. Therefore, it is unclear if fracturing occurred before or after hydrocarbon migration in the POR reservoir. Based on the expected values for the 2nd and the 4th POR reservoir interval, the meso-fractures in the 4th POR reservoir should most closely resemble Figure 3.27C and the meso-fractures in the 2nd POR pattern should most closely resemble Figure 3.23B/D, even though the simulated orientations do not exactly match all the orientations observed in FMI. Simulated fracture orientations are predicted to change as we move towards the flanks of the structure, because of an expected increase in strain anisotropy.

In addition to the parameters discussed in this chapter, shale thickness might also influence fracture growth. Thicker shale layers can accommodate more strain than thin shale layers relieving the adjacent brittle layers of some of the strain and not allowing fractures to grow (Rijken and Cooke, 2001). This observation might not only lower the fracture connectivity, but might also reduce the fracture density.

3.5 CONCLUSIONS

A sensitivity study, motivated by the input parameters expected to be present in the POR reservoir, shows that the mechanical bed thickness has the largest influence on the fracture pattern characteristics. Mechanical bed thickness variations influence fracture orientations, fracture length distributions, fracture density and fracture aperture distributions. An increase in bed thickness, decreases the fracture density and increases the range in fracture orientations. As the bed thickness increases, the aperture distribution deviates from normal towards negative exponential. For all bed thickness values the length distribution follows a negative exponential, but larger fracture lengths develop in thicker beds. Bed thickness variations may overshadow changes in fracture pattern attributes due to other variables such as strain level, strain anisotropy and subcritical index. The sensitivity analysis also shows that fracture orientation, length, and spacing are independent of Young’s modulus, Poisson’s ratio and strain rate.

Strain anisotropy has a large influence on fracture orientation, where an increase in strain anisotropy reduces the number of dominant fracture sets from at least 2 sets to 1 dominant through-going fracture set. The spacing between through-going fractures depends on the level of strain anisotropy, where the spacing decreases as the strain anisotropy increases. This not only influences the preferential drainage direction, it can also enhance the drainage efficiency, because more rock is exposed to the through-going fractures which are more likely to be intersected by a borehole.

Both a decrease in strain level and an increase in subcritical index have been shown to decrease the fracture density. A decrease in absolute amount of strain also decreases the total fracture aperture achieved. In any anticline, one can expect the extensional strain levels to decrease as one descends into the structure, assuming no layer parallel slip, decreasing the fracture density. However, if the structure were partially filled with oil, one would expect a decrease in subcritical index with depth, since oil in the top of structure leads to larger expected subcritical index values than the bottom of the structure which is expected to be brine saturated, leading to an increase in fracture density as one descends into the anticline. Therefore, two opposing mechanisms exist as one descends into the center of an anticline: 1) extensional strain decrease, which decreases the fracture density, and 2) subcritical index decrease which increases the fracture density. One should evaluate on a case by case basis which mechanism is overpowering.

Two types of fractures are believed to be important to fluid flow in the POR reservoir: small or meso-fractures, and large or macro-fractures. Small or meso-fractures are defined as fractures that are contained within individual sandstone beds. These meso-fractures break the reservoir up into small blocks and allow drainage of the source rock. The large or macro-fractures are defined as fractures which cross multiple bed boundaries. These macro-fractures connect the meso-fracture zones. The predicted fracture distributions presented in this study only model the meso-fractures in the POR reservoir and do not model fractures which cross multiple bed boundaries.

Both the 2nd and the 4th POR intervals are expected to exhibit at least 2 dominant fracture orientations in the crest of the anticline. Towards the flanks of the structure the strain anisotropy is expected to increase, which reduces the number of dominant fracture orientations. The numerical simulations indicate fracture density is expected do decrease with depth due to an increase in bed thickness and a decrease in tensile strain from the 2nd to the 4th POR. All the fracture length distributions are modeled to follow a negative exponential distribution. Even though observations are restricted by the uncertainty in initial flaw location, flaw density and flaw orientation, it is expected that due to the smaller bed heights in the 2nd POR interval, fracture length distribution of the 2nd POR reservoir will be more skewed towards shorter fractures than the 4th POR. The smaller mechanical bed height of the 2nd POR also influences the expected fracture aperture distribution, which is expected to be normal for the 2nd POR and tend towards negative exponential for the 4th POR. The modeled fracture apertures overestimate the average fracture aperture observed in core, which is approximately 0.4 mm. A possible explanation for this discrepancy is an overestimation of the strain accommodated by the jointing present in the POR reservoir.

Chapter 4 Flow Simulation of Fractured Reservoirs Using a Finite Difference Simulator

Based on the experimental data from Chapter 2, realistic fracture patterns were created in Chapter 3. Because of their high permeability contrast with the matrix, fractures have a large impact on flow in the subsurface. Therefore, this study sets out to determine the most appropriate method to simulate flow in natural fracture patterns using an industry standard reservoir simulator (ECLIPSE) and regularly used flow simulation techniques for (fractured) hydrocarbon reservoirs. The chapter starts with a brief discussion of the available analytical and numerical methods to model naturally fractured reservoirs. Subsequently, flow simulations performed on detailed fracture patterns created in Chapter 3 are discussed. Finally, upscaling techniques are contrasted to determine which is best suited to model flow in naturally fractured reservoirs.

4.1 TRANSIENT RATE ANALYSIS – CONSTANT PRESSURE PRODUCTION

Unlike homogeneous reservoirs, fractured reservoirs typically exhibit very high initial flow rates followed by very steep declines (Da Prat, 1990). After the initial decline, however, more modest production rates can persist for very long periods. The decline behavior of a well plays an important role in deciding whether to complete or abandon (Da Prat, 1990). If interpreted as a homogeneous reservoir, fractured reservoir test response may result in the unjustified abandonment of an economic well (Da Prat, 1990). The basic equations to model fluid flow in a double porosity system were first presented by Warren and Root (1963). Mavor and Cinco-Ley (1979) extended their theory to include wellbore storage and skin effects. Here the model as introduced by Da Prat (1980) and Da Prat et al. (1981) is presented. The initial and boundary of the system are as follows:

$$P_{fD}\left(r_D,0\right)=0 \text{ (initial condition), } \ldots\ldots \text{Eq. 4.1}$$

$$P_{fD}-S\left(\frac{\partial P_{fd}}{\partial t_D}\right)_{r_D=1}=1 \text{ (inner boundary condition), } \ldots\ldots \text{Eq. 4.2}$$

$$\left.\frac{\partial P_{fd}}{\partial r_D}\right|_{r_D=r_{eD}}=0 \text{ (outer boundary condition), } \ldots\ldots \text{Eq.4.3}$$

where P_{fD} is the dimensionless pressure, r_D is the dimensionless radius (r/r_w), S is the skin factor (= 0 in this study), t_D is dimensionless time. For a closed radial reservoir under constant bottom hole pressure production the solution for the dimensionless flow rate in Laplace space is given by (Da Prat et al., 1981):

$$\bar{q}_D=\frac{\left(F\left[I_1(M)K_1(F)-K_1(M)I_1(F)\right]\right)}{\left(s\left[K_1(M)I_0(F)+I_1(M)K_0(F)\right]-FS\left[K_1(M)I_1(F)+K_1(M)I_1(F)\right]\right)}, \ldots\ldots \text{Eq. 4.4}$$

with

$$F=\sqrt{sf(s)}, \ldots\ldots \text{Eq. 4.5}$$

$$M=Fr_{eD}, \ldots\ldots \text{Eq. 4.6}$$

and

$$f(s)=\frac{\omega'(1-\omega')s+\lambda}{(1-\omega')s+\lambda}, \ldots\ldots \text{Eq. 4.7}$$

where K_n is the modified n^th^ order Bessel function of the second kind, I_n is the modified n^th^ order Bessel function of the first kind, r_{eD} is the dimensionless outer boundary radius (r_e/r_w), and s is the Laplace space variable. As specified earlier, λ is defined by:

$$\lambda=\alpha\frac{k_m}{k_f}r_w^2, \ldots\ldots \text{Eq. 4.8}$$

where α is the shape factor, k_m is the matrix permeability, k_f is the fracture permeability, and r_w is the wellbore radius. The variable ω' is defined as:

$$\omega'=\frac{\varphi_f V_f}{\varphi_f V_f+\varphi_m V_m}, \ldots\ldots \text{Eq. 4.9}$$

where V_f is the ratio of total fracture volume to bulk volume, and V_m is the ratio of total matrix volume to bulk volume the subscripts.

4.1.1 Early times

For early times, a solution of Equation 4.4 is obtained by using the asymptotic expansion of the Bessel functions. At early time, as *s* goes to infinity t_D (dimensionless time) goes to zero. For large values of the argument (z) the Bessel functions reduce to:

$$I_1(z) = I_0(z) \approx \frac{e^z}{\sqrt{2\pi z}}, \qquad \text{Eq. 4.10}$$

and

$$K_0(z) = K_1 \approx \frac{\pi}{2z} e^{-z} \qquad \text{Eq. 4.11}$$

By substituting Equations 4.10 and 4.11 in Equation 4.4, an equation for infinite acting early time behavior is obtained:

$$q_D = \frac{\sqrt{\pi}}{\pi} \left(\frac{t_D}{\omega'} \right)^{-1/2} \qquad \text{Eq. 4.12}$$

In Equation 4.12 dimensionless time, t_D, is defined as:

$$t_D = \frac{2.637 \times 10^{-4} \times k_f \times t}{\left[(\phi C)_m + (\phi C)_f \right] \times \mu \times r_w}, \qquad \text{Eq. 4.13}$$

where k_f is the fracture permeability in mD, *t* is time in hours, ϕ is the porosity fraction, *C* is the compressibility Psi^{-1}, μ is the viscosity in cp, and r_w is the wellbore radius in ft. The dimensionless flow rate, q_D, is defined as:

$$q_D = \frac{141.2 \times \mu \times B \times q}{h \times \Delta P \times k_f}, \qquad \text{Eq. 4.14}$$

where *B* is the formation volume factor in RB/STB, *q* is the volumetric rate (bbl/day), *h* is the formation thickness in ft, and ΔP is the pressure gradient in Psi. Equation 4.12 shows that the initial decline is inversely dependent on the square root of dimensionless time and ω', where ω' relates fracture storage to total storage. Equation 4.12 also shows that infinite-acting early time is expected to follow a half slope on a log-log plot of dimensionless time and flow rate.

4.1.2 Late times

The modified Bessel functions for small argument values are:

$$K_0(z) = -\left(\ln\frac{z}{2} + \gamma\right), \qquad \text{Eq. 4.15}$$

$$K_1(z) \sim \frac{1}{z}, \qquad \text{Eq. 4.16}$$

$$I_0(z) = 1 + \frac{1}{4}z^2, \qquad \text{Eq. 4.17}$$

and

$$I_1(z) = -\frac{1}{2}z + \frac{1}{8}z^3, \qquad \text{Eq. 4.18}$$

where γ is the Euler constant. Using Equation 4.15 through 4.18 and substituting them in Equation 4.4 results in:

$$q_D(t_D) = \left(\frac{r_{eD}^2 - 1}{2}\right)\lambda \exp\left(-\frac{\lambda}{1-\omega'}t_D\right) \qquad \text{Eq. 4.19}$$

Equation 4.19 shows that the late time solution follows an exponential decline.

4.1.3 Full solution

Equation 4.4 is given in Laplace space and the solution in real space is obtained by applying the Stehfest numerical algorithm (Stehfest, 1970) (Fig. 4.1). Figure 4.1 illustrates the expected flow rate characteristics of a fractured reservoir, where the initial decline mainly depends on the fracture storage as compared to the total storage (ω') (Fig. 4.1, red curve). As time progresses, a sharp decline is observed after which the rate stabilizes to a value dependent on the contrast between the fracture and matrix permeability (λ) (Fig. 4.1, Dimensionless production = 1.2×10^{-2}). Eventually the reservoir goes into its final decline, depending on λ, ω' and r_{eD} (Fig. 4.1, blue curve). This behavior is inherently different from a homogeneous reservoir, where no second decline is observed (Fetkovich, 1980). Fetkovich (1980) observed that in a homogeneous reservoir at the onset of depletion (a type of pseudo-steady state), all solutions for varying r_{eD} develop a single exponential decline.

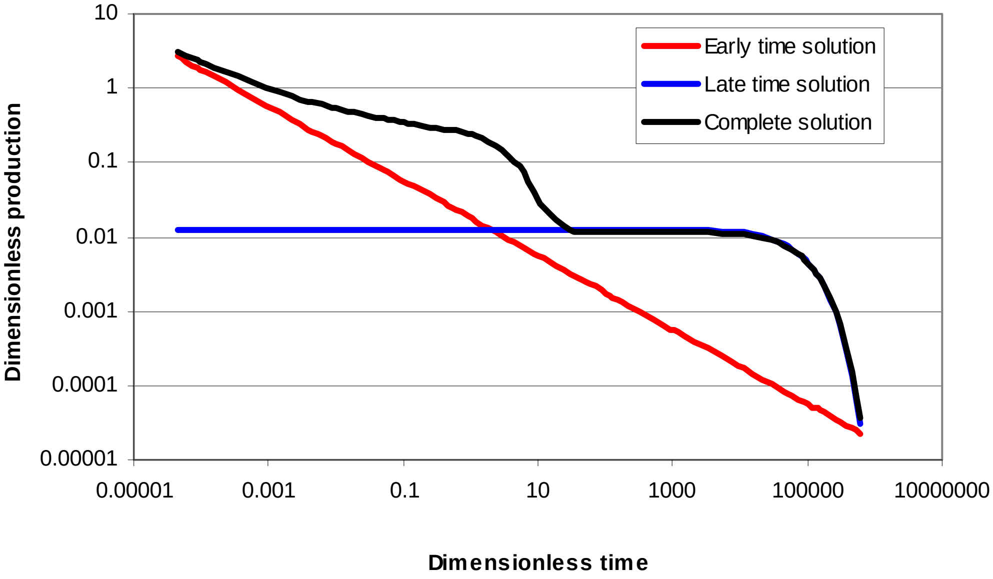

Figure 4.1: Dimensionless time vs. dimensionless production for a double porosity radial closed reservoir with the following characteristics: $k_f = 0.15$ mD, $\mu = 1$ cp, B = 1 RB/STB, S = 0, h = 480 ft, $\Delta P = 6500$, $r_{eD} = 50$, $\omega = 1\text{x}10^{-3}$, $\lambda = 1\text{x}10^{-5}$. The black curve is the full solution as given in Equation 4.4. The red and the blue curves are the early and late time approximations respectively.

There are several assumptions made for the double porosity model that are not necessarily reasonable for most naturally fractured reservoirs. In a naturally fractured reservoir: 1) the matrix porosity is not contained in a system of identical, rectangular parallelepipeds, 2) the system of fractures is not uniform, nor aligned with the principle axis, and 3) flow from matrix block to matrix block is not restricted. The lack of flow between matrix blocks is remedied in what is called the *double permeability* approach (Chen, 1989 and 1990). Figure 4.2, shows the numerical results for the numerical double permeability/double porosity runs in ECLIPSE in a closed square under constant bottom hole pressure production with reservoir and fluid characteristics as given in Table 4.1.

Figure 4.2 shows the reservoir response for varying values of the shape factor, σ, defined by Kazemi et al. (1976) as:

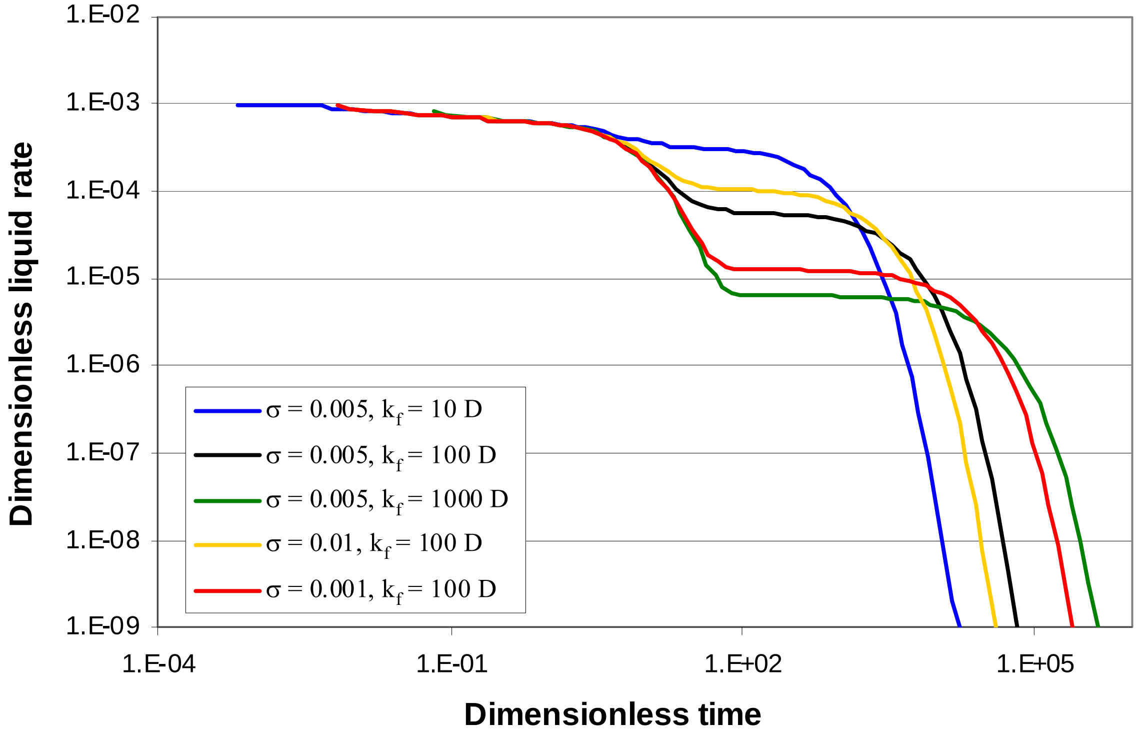

Figure 4.2: Dual permeability ECLIPSE runs for varying σ and fracture permeability values (k_f). Dimensionless production and time are calculated using Eq. 4.14 and 4.21 respectively.

Table 4.1: Numerical reservoir properties

Property	**Value**	**Unit**
Bed thickness	10	ft
Matrix permeability	0.1	mD
Fracture porosity	0.005	fraction
Matrix porosity	0.2	fraction
Reservoir pressure	4900	Psi
Well pressure	4000	Psi
Fluid compressibility	3.0E-05	1/Psi
Viscosity	1	cp
Formation volume factor	1	RB/STB
Drainage area	87188	ft^2
Well diameter	0.03	ft

$$\sigma = 4\left(\frac{1}{L_x^2}+\frac{1}{L_y^2}+\frac{1}{L_z^2}\right), \qquad \text{Eq. 4.20}$$

where L is the length of the matrix block (in ft), and the subscripts x, y or z stand for the coordinate direction. Production rate is non-dimensionalized using Equation 4.14. Time is non-dimensionalized using (Earlougher, 1977):

$$t_{Da} = \frac{0.0002637 \times k_f \times t}{\varphi \times \mu \times c_t \times A}, \qquad \text{Eq. 4.21}$$

where k_f is the fracture permeability (mD), t is time (hours), ϕ is the matrix porosity (fraction), μ is the viscosity (cp), c_t is the total compressibility (1/Psi), and A is the drainage area (ft^2). Values of σ and fracture permeability are chosen to emphasize the effect of these variables on the reservoir response. The time range is the same time range used in future numerical simulations.

At early times, the fractured reservoir initially does not detect the presence of the matrix and behaves like an infinite, homogeneous, high permeability reservoir, explaining the initial decline (Fig. 4.2 up to a dimensionless time of ~30). As soon as the matrix starts to support the flow in the fractures the rate response becomes constant, where the value depends on the shape factor and the matrix-to-fracture permeability ratio

(λ). At late times the system is depleting both the fractures and the matrix and resumes its decline. Comparing constant shape factor cases, the contrast in rates between initial and intermediate time production scales with the fracture permeability, where the 1000 D case (Fig. 4.2, green curve) has a much lower plateau rate than the 10 D case (Fig. 4.2, blue curve). The duration of the plateau value also scales with the fracture permeability, where it takes a longer amount of dimensionless time to deplete the reservoir as the matrix-to-fracture permeability contrast increases. This observation is explained by the knowledge that a limited amount of fluid is present in a closed (fractured) reservoir and that at late times the flow rate goes to zero. The larger the matrix-to-fracture permeability ratio, the larger the initial decline and the lower the intermediate plateau value. Lower intermediate plateau rates lead to prolonged production to drain all the fluids in the system. Therefore, the duration of the intermediate time behavior scales with the fracture permeability, where higher permeability fractures extend production at much lower rates. It is important to note that both dimensionless time and flow rate are a function of the fracture permeability (Eq. 4.21 and 4.14). Thus, even though higher fracture permeability values result in extended dimensionless depletion time, in dimensional time higher permeability fractures drain a reservoir more rapidly and at higher rates. For the cases with a fracture permeability of 100 D, increasing sigma from 0.001 to 0.005 to 0.01 (Fig. 4.2 red, black and yellow curve respectively) represents a decrease in the matrix block size, resulting in more efficient drainage of the reservoir because of an increase in fracture surface area. The largest shape factor shows the smallest drop in rate when fracture drainage ends (early time), indicating that the matrix flow portion of the response is able to support fracture flow rates. Because the system is more efficient in draining the matrix, pseudo-steady state begins earlier, as compared to the lower sigma cases. The shown dual permeability results closely resemble the double porosity results, because of the high contrast between the matrix and the fracture permeabilities.

4.2 DISCRETE FRACTURE GRIDDING

The analytical solutions provide a reference frame for looking at the numerical solutions. The fracture patterns of Chapter 3 were imported into a finite difference reservoir simulator, following Philip's (2003) gridding scheme. Some modifications were made to his technique to accommodate for fractures which are not aligned to the gridblock sides. To start, the fracture network is overlain by a uniform square grid. Each gridcell side has the length of one boundary element. Gridcells not containing a fracture are assigned the matrix permeability. Based on a solution of the Navier-Stokes equations for flow in a uniform slit, the intrinsic permeability of a fracture, k_f, can be written as (Snow, 1969):

$$k_f = \frac{w^2}{12}, \qquad \text{Eq. 4.22}$$

where w is fracture aperture. Although surface roughness can affect the pressure drop in very thin slits (Sharp and Maini, 1972; Warpinski, 1985), that effect is not addressed in this study. To compute the permeability of a fractured gridcell (not just the fracture), the contributions of the fracture and matrix must be combined in parallel as (van Golf-Racht, 1982):

$$\bar{k} = \frac{w \times k_f + k_m \times (\Delta L - w)}{\Delta L}, \qquad \text{Eq. 4.23}$$

where k_m is the matrix permeability and ΔL is the size of the gridcell or boundary element.

Equation 4.23 assumes that the fracture is oriented parallel to the principal grid directions. In some instances, fractures may run diagonally across the grid (Fig. 4.3). The initial assignment of fractured gridcells for diagonal fractures will result either in cells stair-stepping across the grid in a diagonal fashion, or with fractured grids meeting corner to corner. Because flow occurs only through gridcell sides, making the stair-step pattern a continuous high permeability pathway requires assigning the calculated average fracture permeability in both the x and y directions. In the case of fractured cells meeting at the corners (Fig. 4.4A), this accommodation is not enough as flow has to go from the high permeability fractured cell into the adjacent matrix cell and back into the fractured cell (4.4C). A similarly artificial flow configuration results for two fracture tips that almost intersect (come within one boundary element length of one another) (Fig. 4.4B). Fractures within one boundary element of each other are labeled intersected and restricted from further growth in the geomechanical model to prevent element crossing and numerical instability. Gridding these configurations also results in a non-connected flow pathway (Fig. 4.4C). A remedy for the corner to corner fractured cells is to change an adjacent matrix cell into a fractured cell to create a connected fracture flowpath (Fig. 4.5B, 1_diag). This can also be accomplished by changing both adjacent matrix cells to fractured cells (Fig. 4.5B, 2_diag).

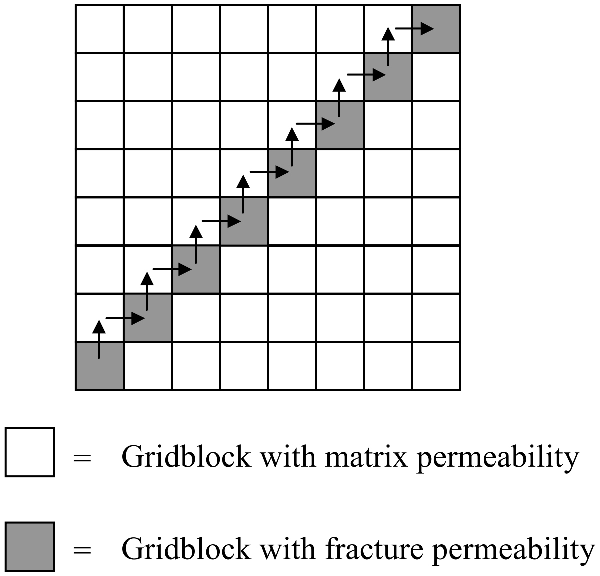

Figure 4.3: Gridding of a diagonal fracture.

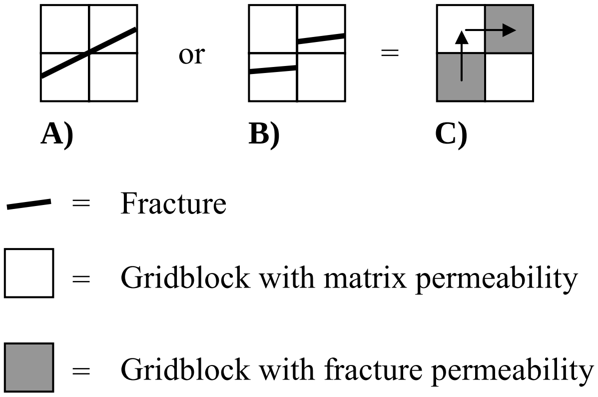

Figure 4.4: Gridding of diagonal fractures. Situations A or B lead to a permeability grid as seen in C.

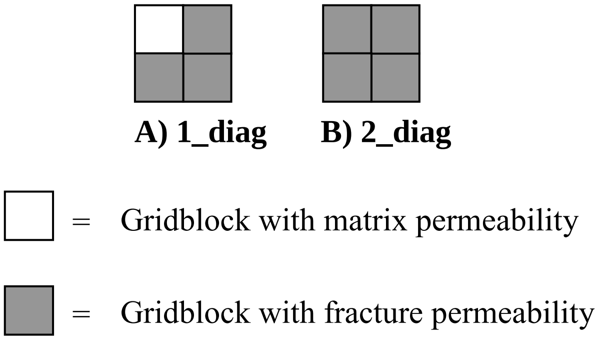

Figure 4.5: Gridding of diagonal fractures. Cells with fracture permeability can be added to ensure connectivity of the fracture. Either one (A) or two (B) cell permeability values can be changed.

Numerical experiments were conducted to validate this diagonal fracture gridding method. A pattern of 5 fractures at equal spacing in a 10 m by 10 m block (thickness = 10 m) was modeled at varying angles, β (Fig. 4.6). The fracture aperture was 0.01 mm, fractured cell permeability was assigned according to Equation 4.23 in both the x and y directions, and the matrix permeability was set to 0.1 mD. The flow was modeled with incompressible fluid under constant pressure drop boundary conditions (1000 psi) imposed with a row of producers at one end of the model and a row of injectors at the other (Fig. 4.6). The grid is oriented in the x-y direction and flow is at a 45 degree angle with the x (or y) axis. Using Darcy's law, the permeability of this medium was calculated as:

$$\bar{k} = \frac{Q \times \mu \times B \times L}{W \times t \times \Delta P}, \qquad \text{Eq. 4.24}$$

where Q is the total flow rate, μ is the viscosity, B is the formation volume factor, L is the model length (Fig. 4.6), W is the model width, t is the model thickness, and ΔP is the pressure gradient. The calculated fractured media permeability values were compared to the analytical solution (derived from Equation 4.23):

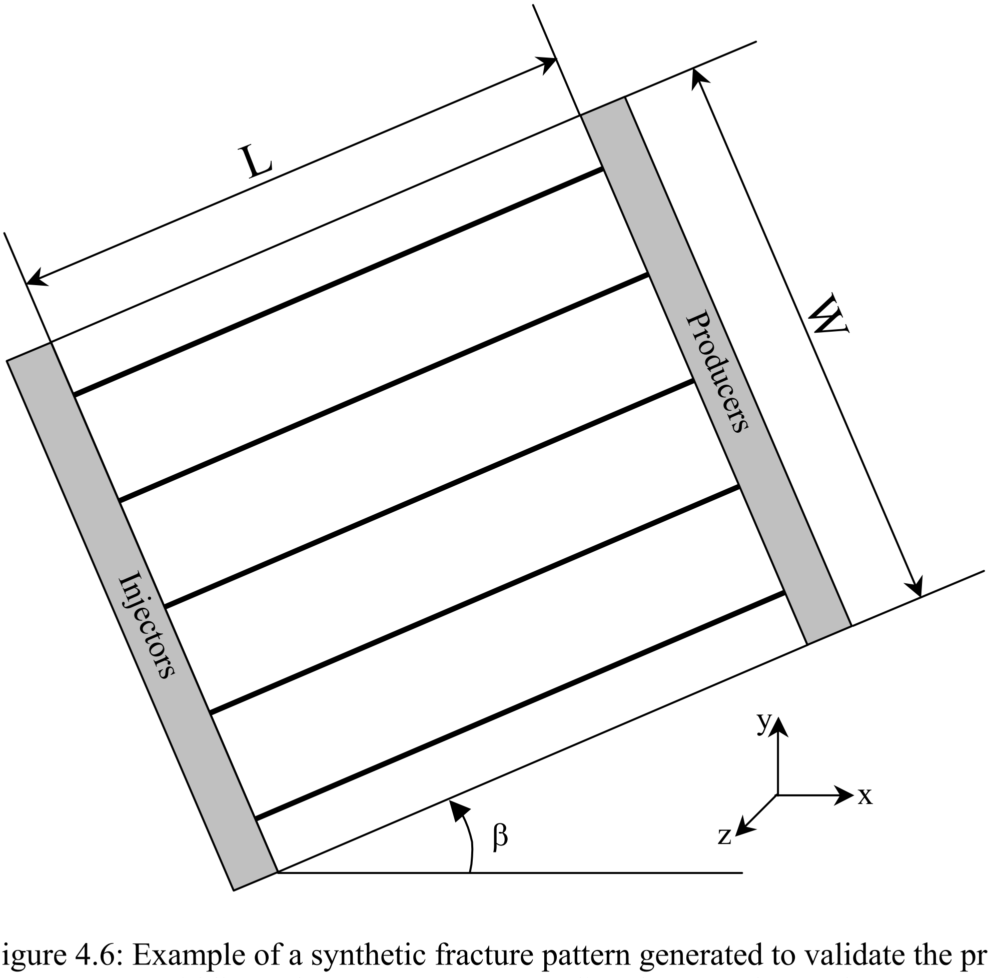

Figure 4.6: Example of a synthetic fracture pattern generated to validate the proposed gridding scheme. A pressure gradient is created over the fracture pattern by a row of constant bottom hole injectors and producers. The fracture pattern is tilted at 10, 30, and 45 degree angles (β) respectively.

$$\bar{k} = \frac{n \times \frac{w^3}{12} + k_m \times (W - n \times w)}{W} \qquad \text{Eq. 4.25}$$

where *n* equals the number of fractures. For w<<W, this reduces to the sum of the more familiar-looking expression for fracture permeability and matrix permeability,

$$\bar{k} = \frac{w^3}{12S} + k_m , \qquad \text{Eq.4.26}$$

where S is the fracture spacing (W/n). Numerically generated permeability values were normalized by the analytical value so that a value of 1 indicates agreement between the two approaches.

The model was first rotated to an angle of β = 45 degrees (Fig. 4.7). The number of gridcells was varied to see if the solutions would converge to the right answer for very fine scale grids. A distinct difference in effective permeability values was observed for each diagonal gridding method (1_diag or 2_diag, Fig. 4.7) and the uncompensated grid (no_diag, Fig. 4.7). As expected, the uncorrected grid underestimated flow because of the artificial discontinuities introduced by the diagonal fracture orientation. Changing the permeability of both adjacent matrix cells overestimated the effective permeability (2_diag Fig. 4.7). Changing only one adjacent cell gave the best approximation, within 10% of the analytical solution (1_diag Fig. 4.7), and was therefore the method chosen for subsequent simulations.

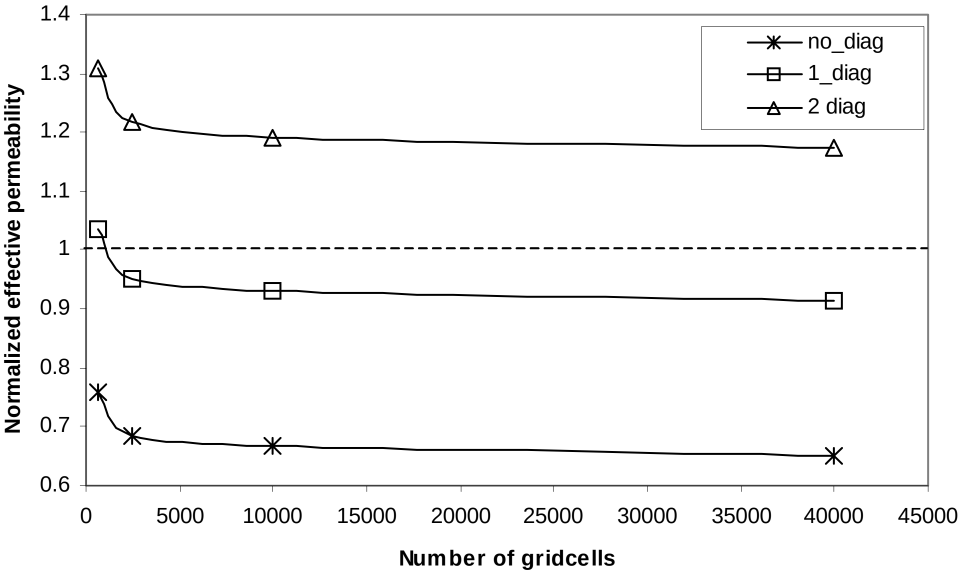

Figure 4.7: Number of gridcells vs. normalized effective permeability for a fracture pattern at an angle of 45 degrees. A larger number of gridcells represents a greater degree of detail. The results of three different gridding schemes as outlined in Figures 4.4C and 4.5A and B are given. The dashed line delineates the correct value. The 1_diag method is chosen as the best gridding method as it introduces an error less than 10% for each model investigated.

Additional simulations, adding only one diagonal cell, show that the error increases as β increases from 10° to 45° (Fig. 4.8). The reason for the observed error is fourfold: 1) the flow is not aligned with the gridcells resulting in an inherent gridding error not associated with the fracturing, 2) the off diagonal terms, most important for a 45 degree angle fracture are not taken into account, effectively lowering the calculated flow rate and thus effective permeability value, 3) fracture cell permeability in the x-direction is calculated as if the fracture is aligned with the gridcell, overestimating the true gridcell permeability, and 4) in adding fracture cells to ensure connectivity, one increases the width of the fracture and thus the flow rate. These last two point results in an overestimation of the permeability value, offsetting the underestimation occurring due to the second error. Mitigation of point 1 would require that the grid axes and fractures are always aligned, which can be difficult to achieve in multi-orientation fracture patterns. Mitigation of point 4 is not possible due to the inherent discretization necessary to import fractures into ECLIPSE. A full tensor approximation of the fracture permeability would alleviate points 2 and 3. However, calculating full tensor permeabilities is computationally much more intensive. Given the fact that the error in the current gridding scheme is less than 10%, full tensor permeabilities were not used.

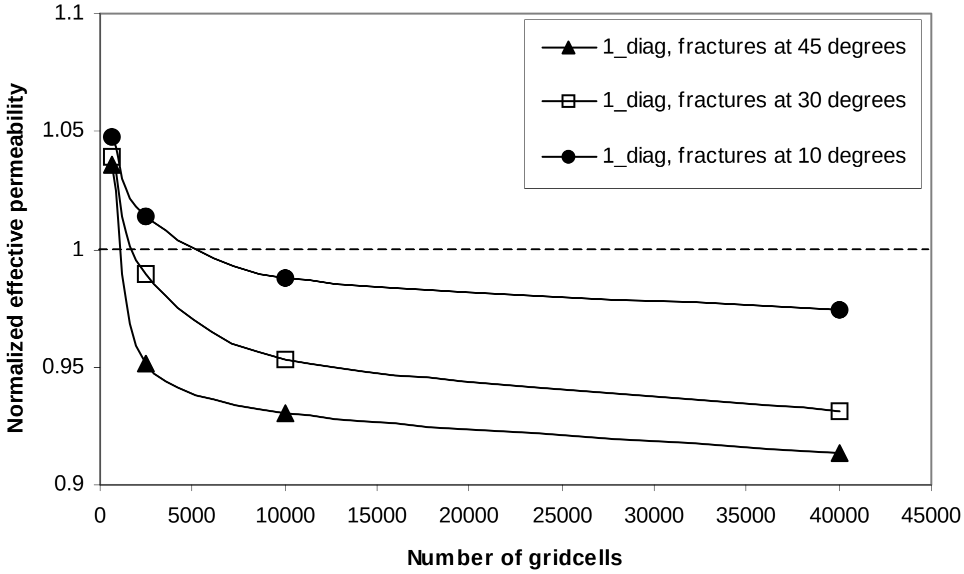

Figure 4.8: Number of gridblocks vs. normalized effective permeability for the 1_diag gridding scheme (Fig. 4.5A). The model is rotated 10, 30 and 45 degrees respectively. The dashed line delineates the correct value.

4.3 DETAILED FRACTURE SIMULATIONS

A practical computational limit on the geomechanical fracture pattern size is 40 by 40 m at the level of detail shown in Chapter 3, which is small compared to the reservoir scale. A mirroring symmetry technique was applied to increase the model size. The central, original pattern was translated and rotated in a fashion that maintained fracture connectivity (Fig. 4.9). Unfortunately, 120 by 120 m fracture pattern with a gridblock size of 15 cm (determined by the boundary element length) resulted in an ECLIPSE grid with 641,601 gridcells, too big to run on available computers. Consequently, the reservoir size was reduced to 90 by 90 m, resulting in 360,000 gridcells. The initial 40 by 40 m model was cropped to 30 by 30 m, after which the mirroring scheme was applied. This detailed 90 by 90 m case is set to be the true or reference case. An example of such a detailed grid is shown in Figure 4.10.

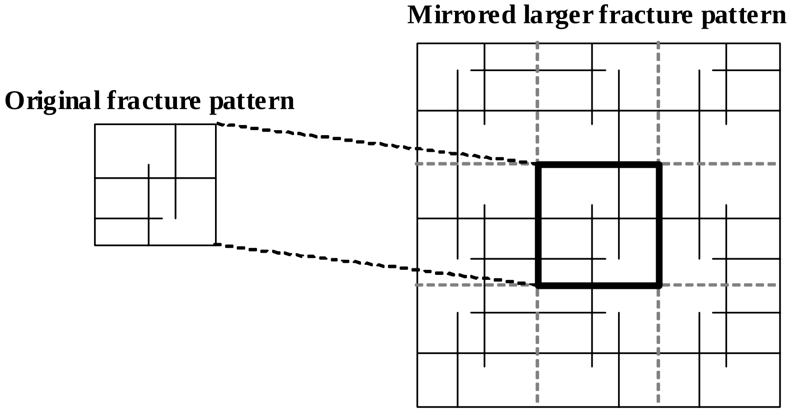

Figure 4.9: Mirroring technique used to create larger fracture patterns. The center block contains the original fracture pattern. The blocks on the edges are rotated and translated to ensure connectivity of the fractures.

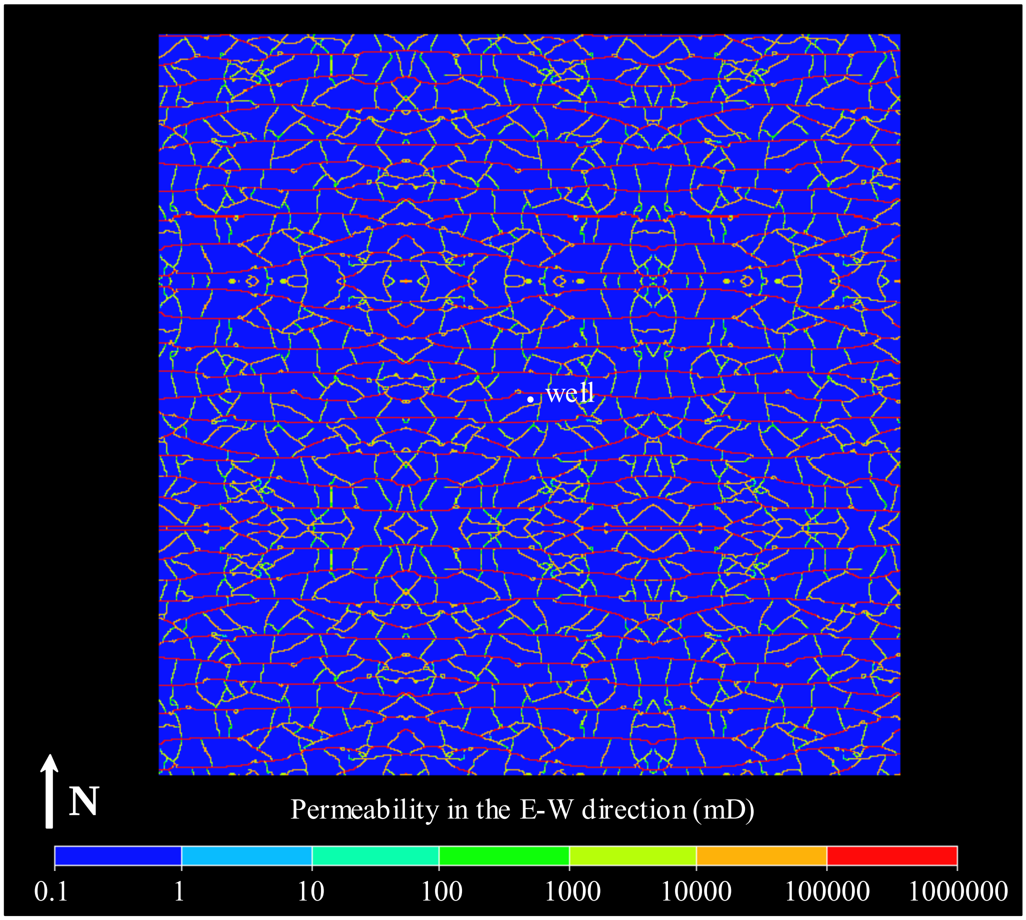

Figure 4.10: Example of a detailed permeability field for a fracture pattern created under 3 to 1 strain anisotropy. The resultant grid is 600 by 600 cells with a cell dimensions of 15 by 15 cm.

4.3.1 Fracture pattern geometry

Detailed fracture models were created using numerical fracture patterns simulated under different anisotropic strain levels (Fig. 4.11). Figure 4.11 only shows the 40 by 40 meter pattern, which will be used to create the larger 90 by 90 m pattern. The reservoirs are produced under constant pressure drawdown, with a well in the center of the model and reservoir and fluid characteristics as given in Table 4.1. However, the porosity in the cells containing a fracture is set equal to the matrix porosity, since the fracture only accounts for a small percentage of the gridcell. The well is located in a matrix cell and is thus not directly connected to the fracture network. Simulation results show that the overall changes in production rate are limited (Fig. 4.12). The initial decline from 1×10^{-6} to 1×10^{-3} days is the early fracture response, governed by the fracture network capacity. As the strain anisotropy increases, the amount of mean strain reduces, reducing the fracture aperture. This results in smaller gridcell permeability values for the highly anisotropic model. However, this decrease in fracture permeability with an increase in strain anisotropy does not result in the expected decrease in production. The exact opposite is seen, where the lower permeability pattern results in the higher flow rates. This is attributed to the distance of the well to the nearest fracture. In all models the well was placed in same cell (cell x = 300 and y = 300). This resulted in a fracture being exactly adjacent to the well for the 3 to 1 anisotropic case, a fracture being 1 gridblock away for the 3 to 2 anisotropic case, and a fracture being 2 gridcells away for the isotropic case, explaining the larger production rates for the most anisotropically loaded pattern (Fig. 4.12). In this case, the expected flow rate differences due to fracture network permeability variations are overshadowed by the proximity of the well to the nearest fracture.

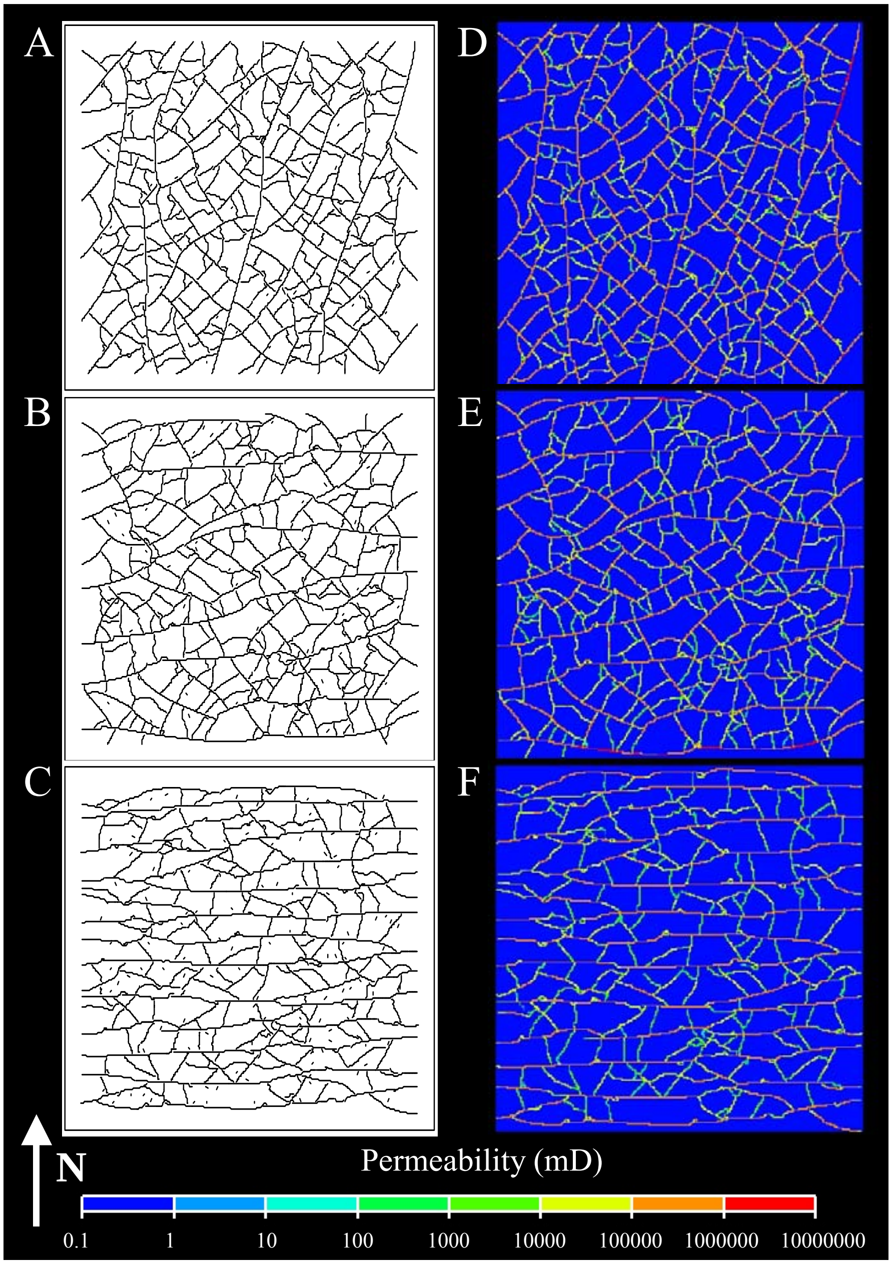

Figure 4.11: Numerically generated fracture patterns and their calculated permeability fields, where pattern A) is created under 0.03% isotropic strain, B) is created under 0.03% strain in the north-south direction and 0.02% in the east-west direction, and C) is created under 0.03% strain in the north-south direction and 0.01% in the east-west direction. Figures D through F show the corresponding ECLIPSE permeability grids.

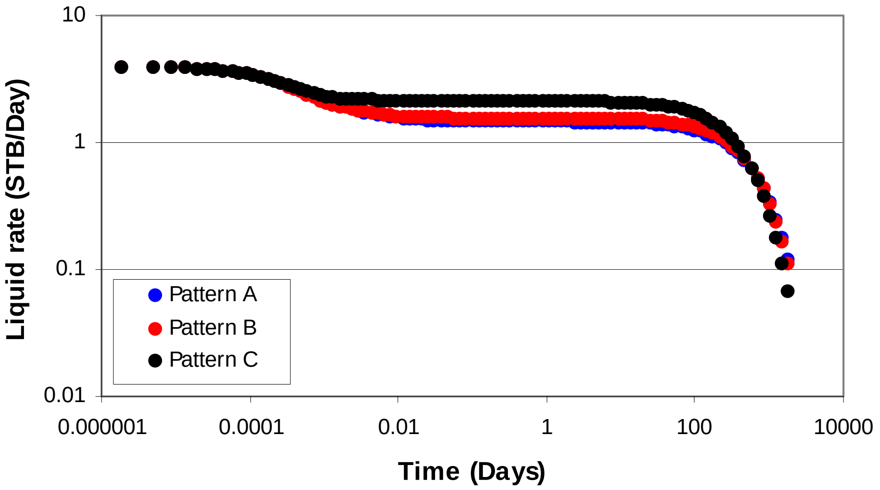

Figure 4.12: Time vs. liquid rate for the detailed numerical fracture models shown in Figure 4.11.

An alternative to discretely incorporating the detailed fracture pattern in flow modeling is to use the continuum dual permeability/dual porosity approach. Figure 4.13 shows that a reasonable match to the "true" response can be obtained by varying fracture permeability, shape factor and fracture porosity. However, the fracture properties resulting in a good production match misinterpret the true fractured reservoir considerably. The matched fracture permeability of 210 D implies a fracture aperture of 0.05 mm, which is an order of magnitude smaller than the actual average aperture of the fracture pattern (0.51 mm). Marrett (1996, 1997) suggests that the single largest aperture fracture accounts for most of the total fracture permeability, assuming the parallel plate law and a powerlaw distribution of fracture aperture. The fracture aperture estimated using the dual porosity/dual permeability approach (0.05 mm) does not compare well with the maximum fracture aperture of the detailed fracture pattern (1.24 mm). The matched shape factor is 0.00005, which indicates a blocksize of ~120 m (assuming 2 sets of fractures), which is far larger than the ~3 m blocksize of the actual fracture pattern.

The fracture porosity value, obtained using the dual permeability/dual porosity approach, is 0.0002%, which is extremely low compared to the 0.04% fracture porosity determined for the detailed model, where the fracture porosity is obtained by summing the area of each fracture element and dividing it by the total area of the pattern. The mismatch between the observed fracture pattern characteristics and the modeled characteristics points towards the disconnect between the geologic reality and the capability of the numerical tool with which fractured reservoirs are managed.

In this study, the detailed fractured reservoir response is matched using uniform dual permeability input values for the entire model. However, an alternative approach is to combine the detailed fracture pattern knowledge as determined in chapter 3 with the dual permeability approach, where different regions can be constructed in which the dual permeability parameters are varied to more closely resemble the "true" fracture network. This approach should result in a better liquid production match and obviously a better fracture pattern match, however in using such an approach the main advantage of the dual permeability approach, i.e. much shorter modeling and computation time, is lost. Therefore, this approach is not pursued in this study.

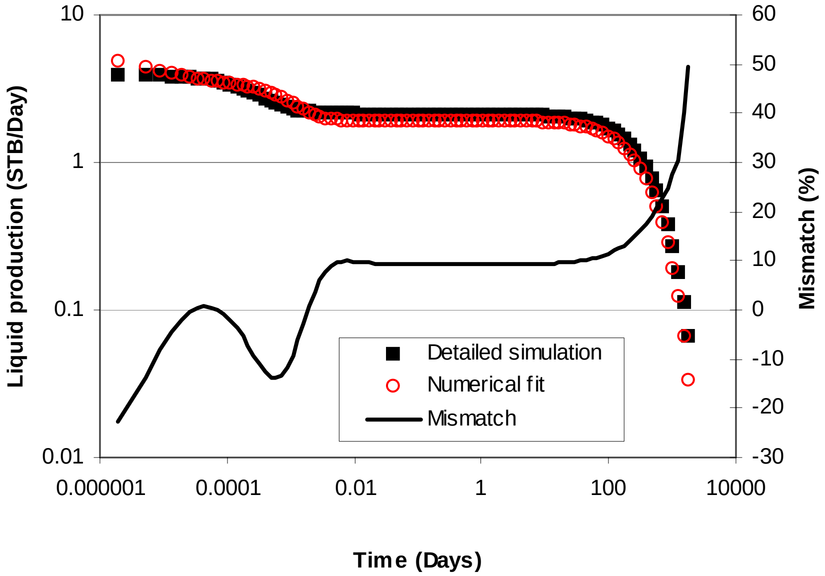

Figure 4.13: Time (Days) vs. liquid production (STB/Day) for the fracture pattern generated with 3 to 1 anisotropic loading. A match was obtained using a dual porosity/dual permeability approach, where $\phi_f = 0.0002\%$, $k_f = 210$ D, and $\sigma = 0.00005$.

4.3.2 Network connectivity

Cementation, contemporaneous with fracturing, has the ability to completely or partially close fractures (Laubach, 1997; Laubach et al, 2000; Laubach, 2003), potentially altering the fluid flow characteristics of the fracture network. Laubach (2003) observed that fractures with apertures below a certain threshold value were predominantly cemented shut, but that fractures above this threshold value were mostly conductive. He coined this threshold value the emergent threshold. To investigate the influence of cementation on fractured reservoir production, an emergent threshold of 30% and 50% of the maximum aperture was applied to the fracture pattern created with a 3 to 1 strain anisotropy (Fig. 4.14). This effectively created fracture patterns with varying degrees of connectivity. The well responses for these detailed patterns are shown in Figure 4.15, where the well is located in a matrix block and thus not directly connected to the fracture pattern. The initial flow rate remains the same since the large aperture fractures are maintained (Fig. 4.15). However, the initial decline lasts longer for more poorly connected patterns, and they consequently plateau at lower rates, corresponding to both an overall decrease in permeability value of the pattern as a substantial amount of fracture length is eliminated by cement infilling as well as to an increased distance of the well to the nearest fracture. The dual decline curve with two distinct horizontal plateaus is slowly lost as the fracture pattern becomes more disconnected.

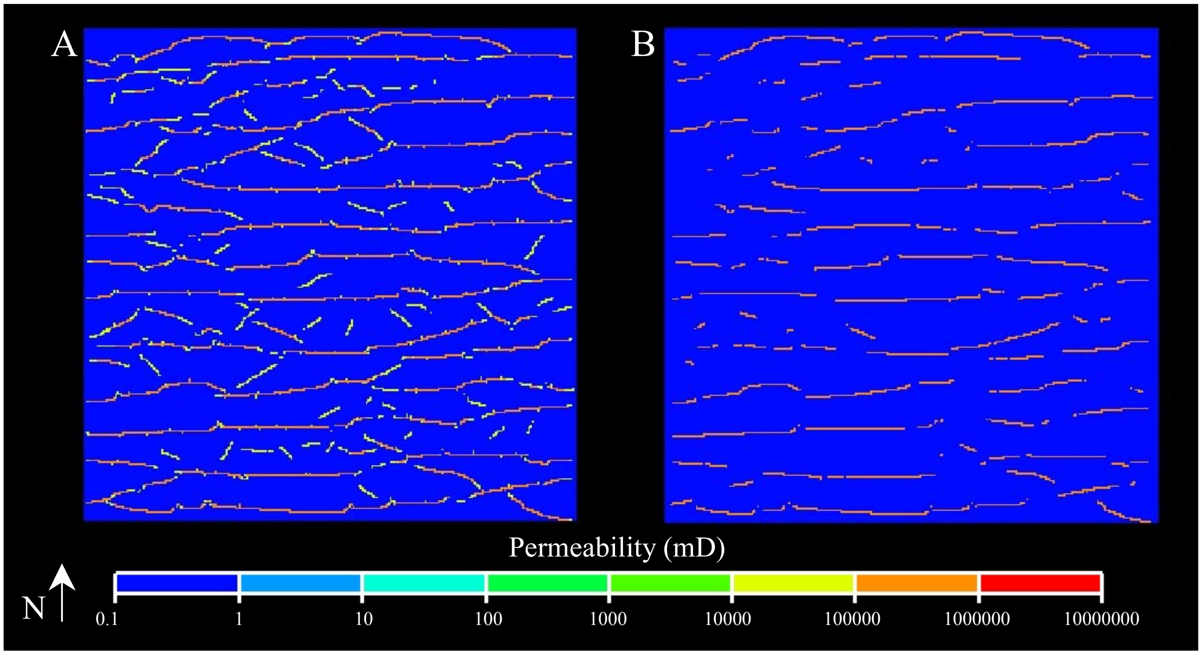

Figure 4.14: ECLIPSE permeability grids for the fracture pattern created using an anisotropy strain of 3 to 1 with A) an emergent threshold of 30%, and B) an emergent threshold of 50% of the maximum aperture.

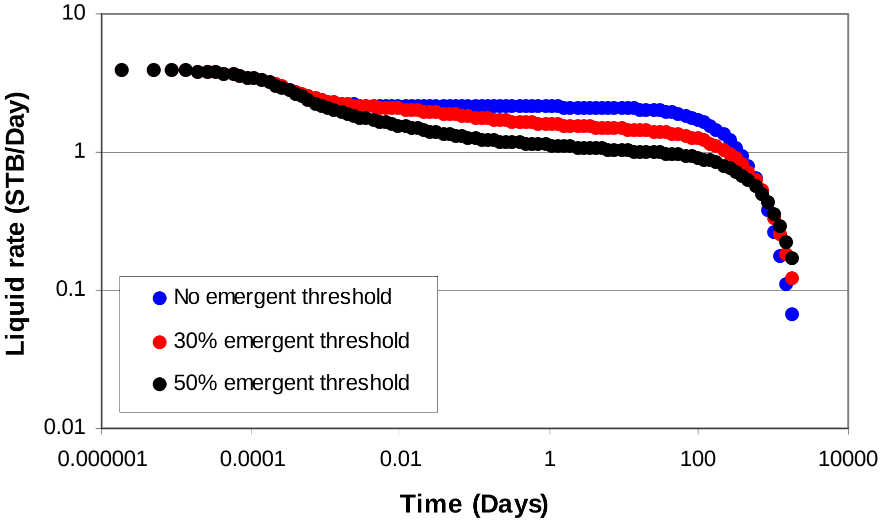

Figure 4.15: Time vs. liquid rate for detailed fracture patterns with varying emergent threshold values, for a fracture pattern created using an anisotropic strain of 3 to 1.

4.3.3 Well placement

In the previous sections, the well was not connected to the fracture pattern. However, it was shown that well location still had an impact on the well production rate. To investigate the influence of the well placement, the detailed patterns of Figure 4.12 are rerun but with the well directly connected to the fracture network (Fig. 4.16). As expected, an increase in initial flow rate is observed as the well is linked to the fracture pattern. The pattern is drained more quickly for the isotropic strain case than for the more anisotropic cases, a result of the higher fracture apertures for the isotropic versus anisotropic loading. These fracture aperture variations also control the plateau level value, which decreases with an increase in strain anisotropy. As expected, the observed liquid rate variations are larger than when the well was not connected to the fracture network. It is noteworthy that the more isotropic the pattern, the more it resembles a homogeneous reservoir, since only a single decline is observed. One expects that a match could be obtained using a homogeneous reservoir approach, where the average reservoir permeability would greatly overestimate the true matrix permeability.

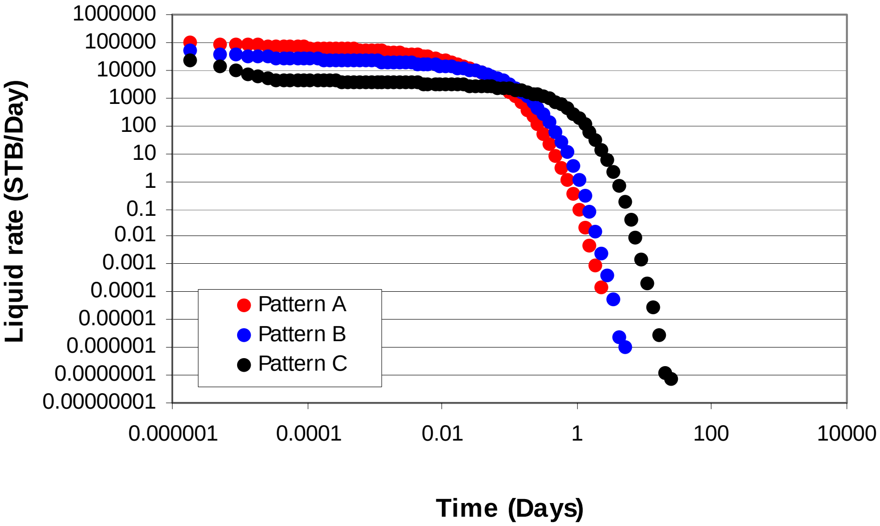

Figure 4.16: Time vs. liquid rate for the detailed fracture patterns with varying degrees of strain anisotropy, where the well is connected to the fracture network. The models correspond to pattern A through C from Figure 4.11.

In this case, history matching using a dual permeability/dual porosity approach resulted in a reasonable approximation of the fracture network (Fig. 4.17). The fracture permeability of k_f = 25000 D indicates a fracture aperture of 0.54 mm, which is in excellent agreement with the average actual aperture value of 0.51 mm. Comparing the fracture aperture estimated using the dual porosity/dual permeability approach (0.54 mm) with the maximum fracture aperture of the detailed fracture pattern (1.24 mm) increases the mismatch, but the estimated aperture value is still reasonable given the level of uncertainty. The history-match shape factor $\sigma = 0.04$ corresponds to a blocksize of ~4 m (assuming 2 sets of fractures), not far from the actual average spacing value of ~3 m. The history-match fracture porosity is 0.01%, only slightly smaller than the true fracture porosity for this model (= 0.04%). Assuming the parallel plate law, fracture porosity and permeability are related, since they both are a function of fracture aperture and spacing.

However, the numerical model allows all variables to be changed independently, resulting in a fracture porosity value which does not correspond with the fracture spacing and aperture values.

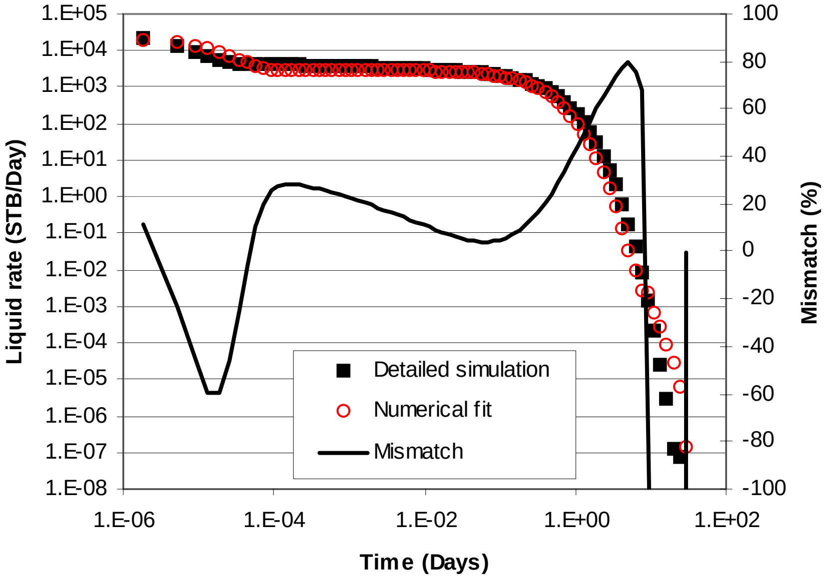

Figure 4.17: Time (Days) vs. liquid production (STB/Day) for the fracture pattern with 3 to 1 anisotropic loading the well connected to the pattern. A match was obtained using a dual porosity/dual permeability approach, where ϕ_f = 0.01%, k_f=25000 D, and σ=0.04.

In the case of a non-percolating fracture network, whether the well is directly connected to the fractures or not has less impact than for the well-connected case (Fig. 4.16 and 4.18). In disconnected patterns, the radius of influence is marginally increased by the presence of a limited length fracture at the well. This isolated fracture provides large initial flow rates for a very limited time (from 1×10^{-6} to 1×10^{-5} days). After this initial decline the flow rate exhibits a gradual dual decline.

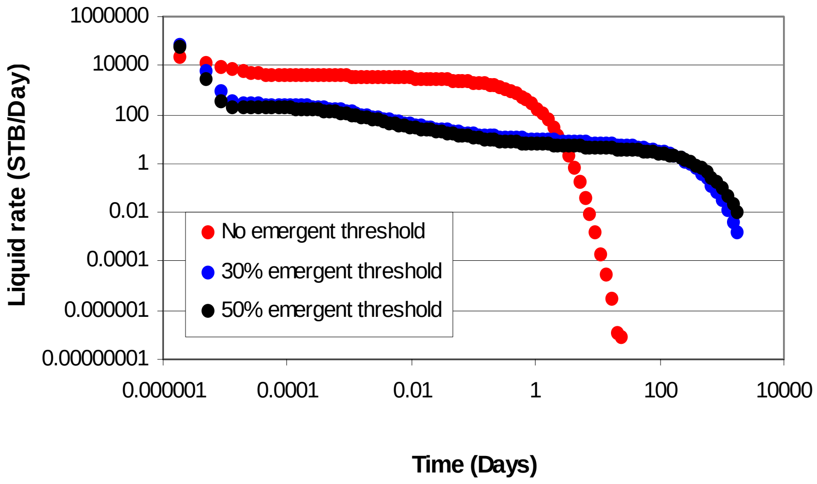

Figure 4.18: Time vs. liquid rate for detailed fracture patterns with varying emergent threshold values, for a fracture pattern created using an anisotropic strain of 3 to 1, where the well is connected to the fracture network.

The continuum model history-match for the pattern with a 50% emergent threshold could not match all 3 stages of the production data (Fig. 4.19). The dual permeability approach assumes a well connected fracture pattern, where production initially occurs through drainage of the (connected) fracture network. After this initial response, the matrix supports the fracture production and the matrix and fractures produce together. However, as stated above the non-percolating pattern exhibits 3 stages of flow: 1) drainage of the limited length fracture, 2) enhanced flow due to the permeability enhancement from the disconnected fractures, and 3) final decline where the fractures and matrix drain together. Since this does not resemble the assumptions made in the dual permeability approach it is not surprising that a poor match is obtained using the dual permeability approach (Fig. 4.19). The values of the intermediate and late time plateaus could be matched, but the shape of the production curve could not be honored. The match parameters were $\phi_f = 0.02\%$, $k_f = 100$ D, and $\sigma = 0.00005$, corresponding to a fracture aperture of 0.03 mm (0.87 mm average actual aperture, and 1.24 mm maximum actual aperture) and a matrix blocksize of ~90 m assuming 1 set fracture (3 m actual). Only the fracture porosity gave a good match (0.02% actual). Thus, the dual permeability/dual porosity approach for this type of fracture pattern failed both in matching the production response and in estimating the correct fracture pattern characteristics. Noteworthy is the fact that although the fracture pattern with 30% emergent threshold seems still well connected its response is almost identical to the 50% emergent threshold case, showing that a small amount of cementation can have a large impact on the well response.

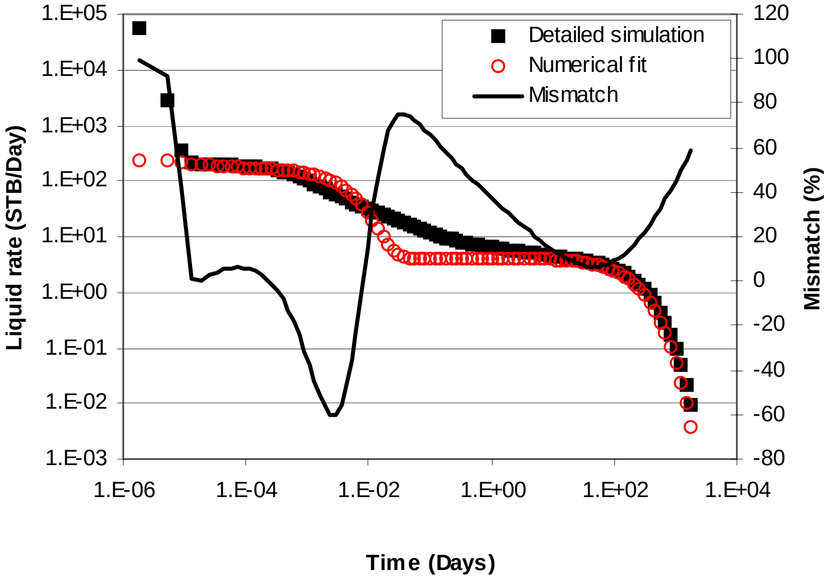

Figure 4.19: Time (Days) vs. liquid production (STB/Day) for the fracture pattern created with an anisotropic loading of 3 to 1 and the well connected to the fracture pattern. A match was obtained using a dual porosity/dual permeability approach, where $\phi_f = 0.02\%$, k_f=100 D, and σ=0.00005.

4.4 UPSCALING OF DISCRETE FRACTURE PATTERNS

The detailed numerical fracture models shown in the previous sections are computationally very expensive, where performing multiple model realizations is prohibitive. This problem would be alleviated if the models could be accurately upscaled, where upscaling is defined as a process which transforms a fine-scaled grid into an equivalent coarse grid which can be used as input in a numerical flow simulator. This section starts with a brief overview of some of the upscaling techniques presented in literature and is followed by a summary of the methods used in this study. The detailed or measurement scale is referred to as the cell-scale and the upscaled or numerical scale is referred to as the block scale.

4.4.1 Upscaling techniques used in literature

Many upscaling techniques start with the assumption that the property to be upscaled can be treated as a material property. This means that the large upscaled block permeability is directly related to the small detailed cell permeability. Simple averaging is one of the techniques that has been used in literature (Warren and Price, 1961; Bouwer, 1969; Dagan, 1982, 1985; Clifton and Neuman, 1982; Hoeksema and Kitanidis, 1984, 1985). Several techniques based on this assumption are discussed in detail by Wen and Gómez-Hernández (1996) and by Renard and Marsily (1997). The observation that the block permeability is a function of the applied boundary conditions indicates that the assumption that the block permeability can be estimated using some kind of scalar averaging of the cell permeability values is not strictly valid.

An alternative approach solves the flow equations on the block scale to estimate the block permeability value. Constant pressure-no flow boundary conditions are often used to determine the gridblock permeability value (e.g. Warren and Price, 1961; White and Horne, 1987; Kasap and Lake, 1990; Panda and Kulatitilake, 1999; Jourde et al., 2002; Flodin et al., 2004). A pressure gradient is applied on two opposing sides and a no flow boundary is placed on the two remaining sides (Fig. 4.20). The permeability in the direction of the pressure gradient can be obtained using Equation 4.24. To obtain the permeability in the perpendicular direction, the numerical experiment is repeated with the whole system of boundary conditions rotated 90 degrees. This approach assumes that the block principal permeability values are aligned with the block faces. In other words, this method does not provide a full permeability tensor. Panda and Kulatilake (1999) circumvented this drawback by performing flow experiments every 30 degrees to obtain a full permeability tensor. Holden et al. (1989) developed a technique to reduce the computation time by calculating the conductivity tensor after each iteration step in the flow simulation. They found that the conductivity tensor converged faster than the flow equations, allowing them to stop the numerical experiment earlier and reducing the required computation time.

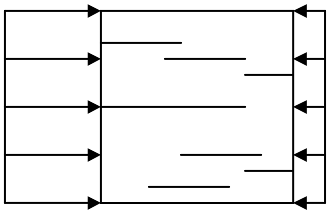

Figure 4.20: Constant pressure-no flow boundary conditions. Pressure boundaries are delineated with arrows, where the size of the arrow indicates the relative magnitude of the applied pressure. No specification on the boundary symbolizes a no flow boundary.

White (1987) and White and Horne (1987) were the first to propose that the pressure gradient and flow rate applied on the block scale should resemble the pressure gradient and flow rate present on the cells during the full field flow simulation. This of course requires a full field simulation to be run which defeats the purpose of upscaling. However, if the objective is multiphase simulation, then such full scale single phase simulations are justified. The main problem with this method is that it is computationally expensive. At least four full scale flow simulations need to be conducted with varying boundary conditions to obtain the full block permeability tensor. To reduce computation time, Gómez-Hernández (1990, 1991) proposed a method similar to White and Horne (1987). However, instead of performing multiple full field simulations, he proposed the same simulation on a smaller sub-region that is 4 times the block-size.

Durlofsky and Chung (1990) and Durlofsky (1991) present a method that always yields fully positive definite permeability tensors. Non positive definite permeability tensors result in an ill posed flow problem with no or a non-unique solution. The boundary conditions require that the flow rates through opposing sides of the gridblock are identical. The only requirement on the pressure field is that there exists a pressure gradient between two opposing sides and that the pressure distributions on the two remaining sides are equal. Using these periodic boundary conditions results in a flow regime which responds as if the region of interest is infinitely repeated. To obtain the full permeability tensor, the flow experiment has to be repeated with the boundary conditions rotated 90 degrees. This method provides the full permeability tensor for truly periodic media (Durlofsky, 1991). Pickup et al. (1992) showed that Durlofsky's approach is robust enough to be valid in situations where the media is not strictly periodic.

Zhang and Sanderson (2002) investigated fluid flow in naturally fractured rocks. They propose a constant pressure drop on two opposing sides. On the two remaining sides a pressure gradient is applied (Fig. 4.21). In a truly periodic system, the flow rates through each set of opposing sides should be identical in order to simulate the full periodic boundary condition set as described by Durlofsky (1991). However, in naturally fractured reservoir the inherent heterogeneity of the fractured medium creates flow rates which are not identical through each set of opposing sides (Zhang and Sanderson, 2002). To circumvent this problem, Zhang and Sanderson (2002) propose to average the in-flow

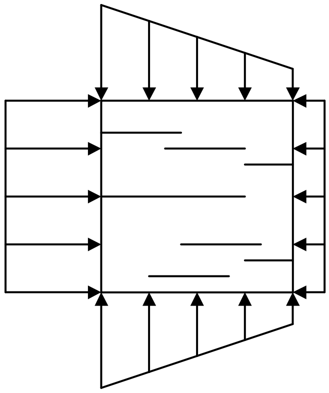

Figure 4.21: Pseudo periodic boundary conditions. Pressure boundaries are delineated with arrows, where the size of the arrow indicates the relative magnitude of the applied pressure.

and out-flow across the sides with the pressure drop to obtain the principal permeability components. The remaining four flow rates from the two orthogonal flow simulations are averaged to obtain 1 cross-component.

Except for the Zhang and Sanderson (2002) method, the previously described methods were not specifically created with fractured reservoirs in mind. In fractured media, upscaled permeabilities have been found to be highly dependent on the applied boundary conditions (Philip, 2003; Flodin et al., 2004). Upscaling is based on the homogenization principle. The homogenization principle requires the heterogeneities to be small compared to the region of interest. Fractured reservoirs often do not meet these requirements, leading to ambiguities in the permeability determination. Philip (2003) and Flodin et al. (2004) investigated the appropriateness of different boundary conditions in fractured and faulted models. Both found that the constant pressure-no flow boundary conditions are most appropriate in the presence of large through-going fractures, but that those boundary conditions typically overestimate the permeability value of other fracture patterns (Philip, 2003; Flodin et al., 2004). Philip (2003) and Flodin et al. (2004) both use a thought experiment to illustrate this point. Assume a disconnected fracture pattern as shown in Figure 4.22. If upscaling separately determines the permeability of block A and B, using constant pressure no flow boundary conditions, the upscaled permeability of the 2 block system will be as if the model contains one through-going fracture. This would greatly over-predict the effective permeability for a low permeability matrix situation, considering the two fractures are not actually connected.

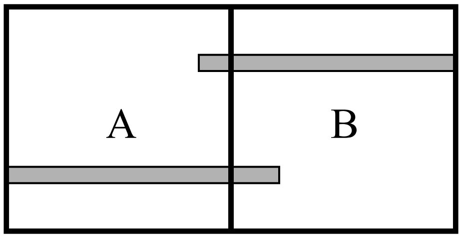

Figure 4.22: Disconnected fracture pattern after Philip (2003) and Flodin et al. (2004). Both gridblocks would have an infinite permeability if constant pressure-no flow boundary conditions are used to estimate the permeability of each gridblock. This significantly overestimates the permeability of the model.

For a non-percolating fracture pattern, Philip (2003) proposed that uniform flux boundary conditions are more appropriate. Uniform flux boundary conditions ensure that the flow rate through the fracture is limited. Flow can still divert into the fracture, but only at the expense of flow moving orthogonally to the main pressure gradient through the matrix, lowering the estimated permeability value.

Flodin et al. (2004) found the periodic boundary conditions most applicable in disconnected fracture networks. Periodic conditions act as if the entire model is infinitely repeated. If a fracture bisects a gridblock at an angle, repetition of this block without rotation (= pure translation) leads to a disconnected fracture pattern (Fig. 4.23). In this case, the estimated permeability field resembles that of a disconnected fracture pattern. However, if repetition of the gridblock leads to linking of the fracture over the repeated area, the estimated permeability field will resemble through-going fractures.

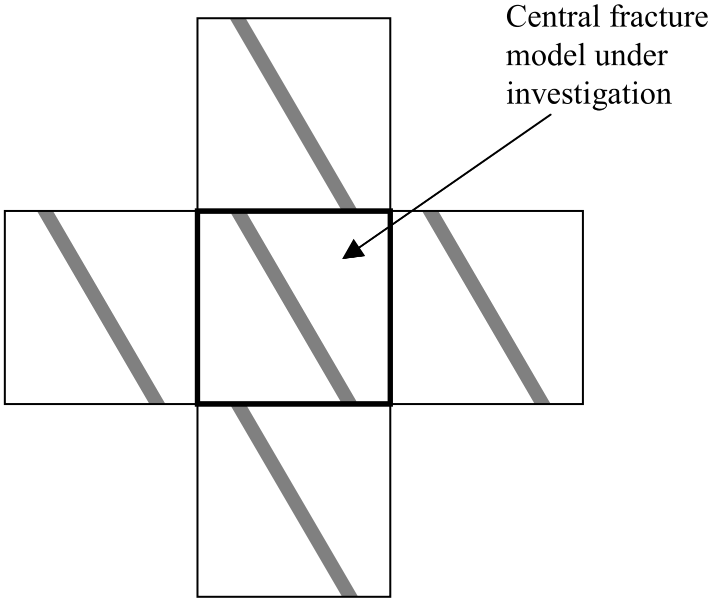

Figure 4.23: Schematic representation of the infinite model repetition, resulting from the periodic boundary conditions.

Flodin et al. (2004) propose an interesting upscaling scheme similar to Lee et al. (2001). Both approaches split the fractured model into different submodels based on fracture characteristics. Lee et al. (2001) subdivide the model into: 1) short fractures, where the length of the fracture is much smaller than the gridblock length, 2) medium length fractures, where the length of the fractures is approximately equal to the gridblock length, and 3) long fractures, where the fracture length is much larger than the gridblock length. Flodin et al. (2004) divide the model up into through-going fractures and background features. Both methods use different techniques to calculate the permeability fields of each submodel, consisting of matrix and fractures. These fields are later combined to form a full field picture, where both Lee et al. (2001) and Flodin et al. (2004) explicitly model the large through-going fractures in the final model. Although interesting, these approaches are not suitable for the fracture patterns in this study. The fracture patterns modeled in Chapter 3 do not show a fracture hierarchy which would lend itself to the described submodels, rendering this approach ineffective.

4.4.2 Boundary conditions as used in this study

A priori knowledge of the most appropriate boundary condition is often not possible. Therefore, this study does not restrict itself to one boundary condition but chooses to investigate the suitability of different boundary conditions. The first type of boundary condition is the constant pressure no flow boundary condition. This boundary condition is selected because of its wide use in literature (e.g. Warren and Price, 1961; White and Horne, 1987; Kasap and Lake, 1990; Panda and Kulatitilake, 1999; Jourde et al., 2002; Flodin et al., 2004). The objective of this study is to use an industry standard reservoir simulator (ECLIPSE) to simulate fractured reservoirs. In ECLIPSE, constant pressure boundary conditions can be maintained by a variety of methods; 1) a strip of cells is placed adjacent to the model with constant pressure injectors or producers located in each cell, 2) a strip of cells having infinite permeability is placed adjacent to the model and one constant pressure injector or producer is placed in the center of one cell, and 3) an infinite constant pressure aquifer is linked to the sides of the model. In this study, the aquifer method is preferred over the other methods. A producer will shut in if the reservoir pressure drops below the well pressure (at the outlet of the of the flow experiment). This is often the case if the well is in direct contact with a high permeability fracture. As soon as the well is shut in, the constant pressure boundary is no longer maintained. Infinite aquifers maintain the same pressure regardless of the reservoir pressure. The flow direction will merely be reversed if the reservoir pressure falls below the aquifer pressure.

The second type of boundary conditions chosen is similar to the one proposed by Zhang and Sanderson (2002), here coined the pseudo-periodic boundary condition (Fig.

4.21). This boundary condition is chosen since it resembles the periodic boundary conditions as proposed by Durlofsky (1991). The full periodic boundary conditions cannot be set in ECLIPSE, since either pressures or rates are specified on a boundary, but not both. However, specifying the pressures as shown in Figure 4.21 closely follows the method as described by Durlofsky (1991) and will give identical results if the model is periodic. Using two aquifers, a constant pressure drop is prescribed over the model. On the remaining two sides, pressure gradients are applied using multiple aquifers with varying pressure. This honors the pressure specifications of periodic boundary conditions, but not necessarily the flow conditions. Flow in does not necessarily equal flow out for any two opposing sides (Zhang and Sanderson, 2002). Using the method as proposed by Zhang and Sanderson (2002), the unequal flow rates can be averaged to obtain a symmetric permeability tensor. However, averaging flux terms from different flow experiments to obtain 1 homogeneous cross diagonal term is not considered physical. Therefore, the permeability field in this study is calculated using the described pressure boundaries, but without averaging. Moreover, the cross-terms are neglected, since they result in non-physical permeability tensors. This introduces an *a priori* error into the simulation, since the off-diagonal terms are known not to be zero. However, unlike the constant pressure-no flow boundary conditions, the pseudo-periodic approach has the ability to incorporate flow from fractures which connect two adjacent gridblock sides. Such a fracture orientation signifies a poor grid choice, but is inevitable for multi-orientation fracture networks (networks with 2 or more fracture orientations). In such an instance, the pseudo-periodic boundary condition will correctly increase the x and y permeability values, whereas the constant pressure-no flow boundary condition will not. Therefore, the permeability values computed using the pseudo-periodic boundary condition are expected to be greater than those obtained from the constant pressure-no flow boundary conditions.

Uniform flow rate boundary conditions are difficult to set in fractured reservoirs. The flux into the model needs to be balanced with the flux out of the model. This is easily established in homogeneous reservoirs, but is almost impossible in heterogeneous fractured reservoirs. Since upscaling requires a boundary condition to be set twice over multiple gridblocks, this approach is not feasible. An alternative to true constant flow rate boundary conditions is to place matrix buffers between the constant pressure boundary and the model (Fig. 4.24). An intuitive value for the buffer permeability would be the matrix permeability. The buffers are assumed to supply a pseudo-uniform flow rate to the fracture pattern. An equivalent permeability value is calculated by averaging the pressures and flow rates at the contact between the buffers and the fractured medium and applying Equation 4.24. However, this approach is highly sensitive to the buffer permeability, where the calculated equivalent permeability value increases as the buffer permeability increases (Fig. 4.25). This indicates that the uniform flux boundary conditions are not strictly maintained. It also indicates that the equivalent permeability value calculated is highly dependent on the boundary conditions set. This advocates the White and Horne (1987) approach, which requires that the boundary conditions set on the upscaled block resemble the boundary conditions on that same block during the full field

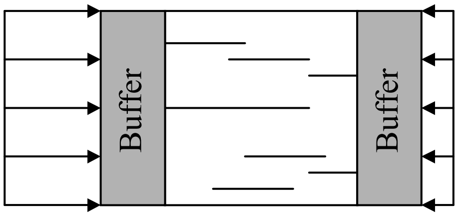

Figure 4.24: Pseudo-uniform flow rate boundary conditions. Buffers are placed between the pressure boundary and the fracture pattern to simulate uniform flow rate boundaries.

fine scale simulation. As stated before, one would not be upscaling if full field simulations were an option. Since *a priori* knowledge of the appropriate buffer permeability value is not possible, this approach is abandoned. Following Philip (2003), instead of the buffer approach, mixed boundary conditions are used, where constant fluxes are set at the inlet and constant pressures are set at the outlet of the model. This is achieved by placing a row of constant flow rate injectors at the inlet end of the model and a row of constant pressure producers at the outlet end of the model, creating a uniform flow-rate edge at the inlet end and a uniform pressure edge at the outlet of the model. The equivalent permeability values are calculated as described for the buffer boundary conditions, where the average pressures and flow rates at the edges of the model are used in Equation 4.24. Like Philip (2003), the calculated equivalent permeability value is observed to be independent of the specified flow rate.

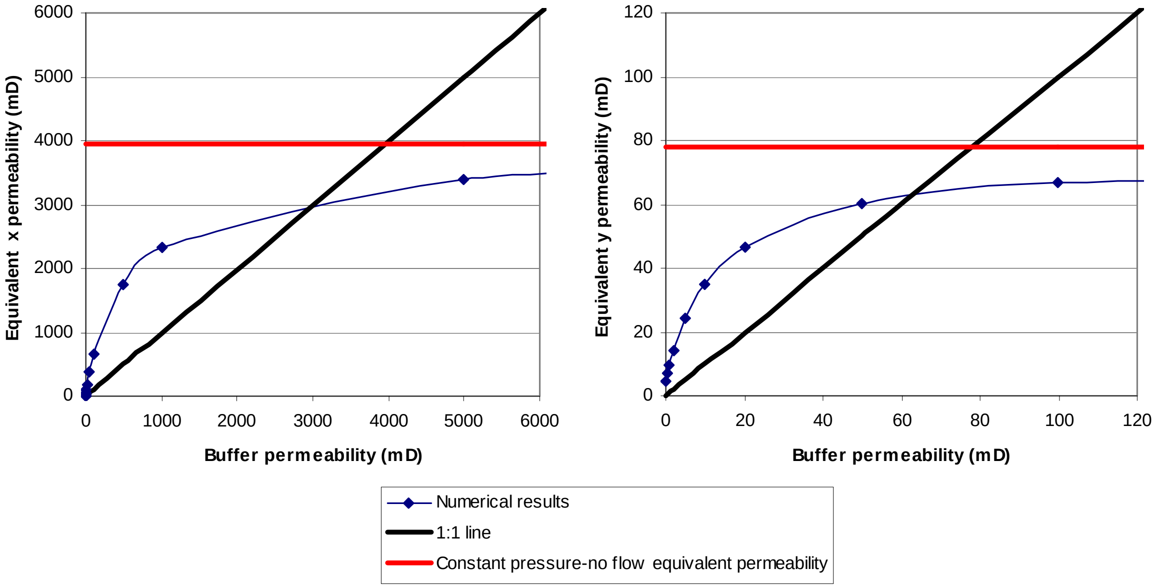

Figure 4.25: Buffer permeability as a function of the calculated equivalent permeability.

In summary, the three boundary conditions that will be utilized for permeability upscaling calculations are: 1) constant pressure-no flow, 2) pseudo-periodic boundary conditions, and 3) mixed uniform flow rate and constant pressure boundary conditions. For brevity in the remainder of the text these boundary conditions will be referred to as 1) pressure, 2) periodic, and 3) mixed boundary conditions.

4.5 REPRESENTATIVE ELEMENTARY VOLUME

Bear (1972) first introduced the idea of a Representative Elementary Volume (REV) based on rock porosity. A REV is the smallest volume of material that can be used as a representation of the whole volume. Bear (1972) states that the porosity of a steadily increasing spherical volume around an arbitrary point displays a stabilizing value for homogeneous media, once the volume is large enough (Fig. 4.26). For small volumes the porosity fluctuates (Fig. 4.26). As the averaging volume increases, a plateau is reached which corresponds to the porosity value representative for the whole volume. The volume at which this happens is called the REV. In other words, existence of a REV would mean that a further scale increase would not alter the hydraulic behavior (e.g. Wang et al., 2002). If the medium is not homogeneous, an increase in volume size beyond the REV eventually leads to gradual changes in the plateau value (Fig. 4.26) (Bear, 1973). However, the existence of a REV in fractured reservoirs is still disputed (Kunkel, 1988; Kulatilake and Panda, 2000). Anderson and Dverstorp (1987) showed that the existence of a REV in fractured media depends on the fracture size and frequency. Long et al. (1982) stipulated that high fracture density, non-uniform orientation distributions, and the absence of large through-going fractures enhance the likelihood of the existence of a REV. Likewise, Kunkel et al. (1988) showed that a spacing increase increases the likelihood of the existence of a REV. Similarly, a non-uniform aperture distribution makes the existence of a REV less likely (Long et al., 1982).

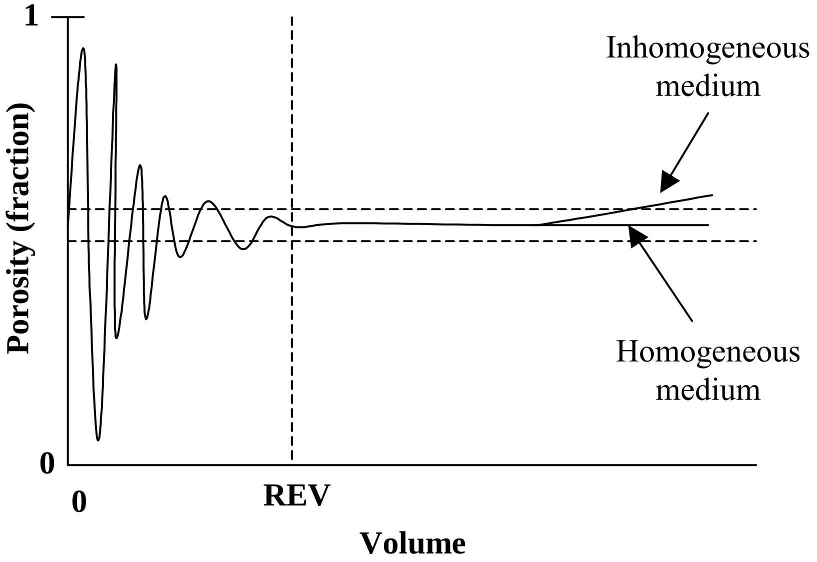

Figure 4.26: Definition of a Representative Elementary Volume (REV), adapted from Bear (1972).

Brace (1980) and Clauser (1992) observed a permeability increase from laboratory to borehole scale. Furthermore, Clauser (1992) shows that permeability becomes scale independent from borehole to regional scale. On a laboratory scale, material is taken from sound intervals, introducing a bias towards low permeabilities (unfractured rock) (Brace, 1980; Clauser, 1992). If a REV is not reached on the scale of investigation, usage of the equivalent continuum approach is not appropriate (Wang et al., 2002). Kunkel et al. (1988) describe a REV in fractured rock as that volume beyond which the fluctuations in hydraulic response diminish (Fig. 4.27). However, the high degree of heterogeneity makes determination of a REV in fractured reservoir difficult.

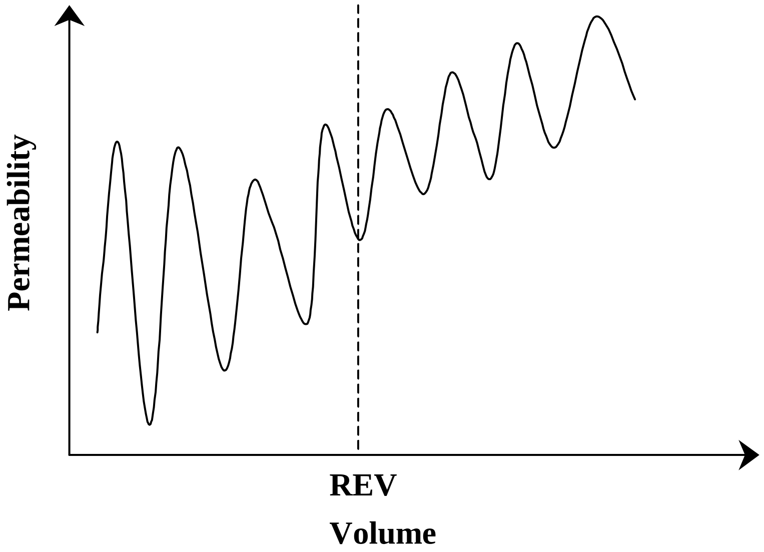

Figure 4.27: Representation of REV in fractured rock (after Kunkel et al., 1988).

A common technique to determine the size of a REV is to apply the constant pressure-no flow boundary condition over varying blocksizes and calculating the effective permeability (Panda and Kulatilake, 2000; Wang et al., 2002). If the effective permeability stabilizes with further increase of the blocksize, the REV has been reached (Wang et al., 2002). The size of the REV must be small compared to the total volume under consideration (Long et al., 1982). An identical approach is used in this study to determine the size of the REV in the fracture patterns of interest, except that all three described types of boundary conditions are used to investigate the existence of a REV. To honor the assumption that a REV is small compared to the total volume under investigation, the REV calculation is limited to a size of $1/5^{th}$ of the total volume. The fracture pattern created with 3 to 1 anisotropic strain was used to investigate the existence of a REV. The gridding scheme as described in section 4.2 was used. The detailed grid was overlain by a coarser grid which divided the pattern into 5x5, 10x10, 20x20 or 25x25 pieces respectively. The effective permeability in the east-west and north-south direction for each subdivision was calculated using the three different boundary conditions.

Results show that determination of a REV depends on the applied boundary conditions (Fig. 4.28). The calculated permeability values are plotted against the volume fraction of the subdivision, where the dashed horizontal line delineates the permeability value obtained using the same boundary conditions on the entire pattern. The numerical permeability values obtained for the entire pattern are given in Table 4.2. A narrowing of the permeability range is observed when using the pressure or periodic boundary conditions (Fig. 4.28). However, the standard deviation is still large for a REV which has a size equivalent to 20% of the total pattern (east-west permeability standard deviation was ~5000 mD for both boundary conditions, the north-south permeability standard deviation was ~640 mD for the periodic boundary condition and ~40 mD for the pressure boundary condition), suggesting that a REV has not been reached. The mixed boundary conditions give a different response from the pressure and periodic boundary conditions. First of all, the range in permeability values calculated does not span the values calculated for the full field simulation (Fig. 4.28). Secondly, the REV analysis based on the mixed boundary conditions follows the model as described by Kunkel et al. (1988), where an increase in model volume leads to an increase in permeability and a decrease in standard deviation (Fig. 4.28E), indicating that equivalent permeability value is size dependent. The north-south permeability exhibits an identical trend, but a few relatively large permeability values obscure this trend. The reason for these outlying values is that the block over which the boundary conditions are applied has a fracture located at the edge of the model directly adjacent to the constant flux producers. A second orthogonal fracture connects the injector side to the producer side. Since the x and y permeability are very high in the fracture, the flow rate of all the wells is redistributed into the single fracture. This results in a much higher flow rate than in a case were only a few fracture cells are directly adjacent to the constant flow rate injectors. Due to the anisotropic loading history of this pattern, this configuration of fractures and wells more often happens in the y-direction, than the x direction. The standard deviations for the mixed boundary conditions are much lower than for the pressure and periodic cases (standard deviation = 0.6 mD for the east-west permeability, and standard deviation = 0.5 mD for the north-south direction), suggesting that an REV has been reached using the mixed boundary conditions, although the permeability value doesn't match the permeability value for the entire pattern, when using the same mixed boundary conditions.

Table 4.2: Reference permeability values for the entire fracture pattern.

Pattern: 0.03%:0.01% anisotropic strain		
Boundary condition	**E-W permeability (mD)**	**N-S permeability (mD)**
Pressure	3953	78
Periodic	4812	462
Mixed	6	5
Pattern: 0.03%:0.01% anisotropic strain with 50% emergent threshold		
Boundary condition	**E-W permeability (mD)**	**N-S permeability (mD)**
Pressure	0.4	0.1
Periodic	0.6	0.1
Mixed	0.3	0.1

Constant pressure-no flow boundary conditions

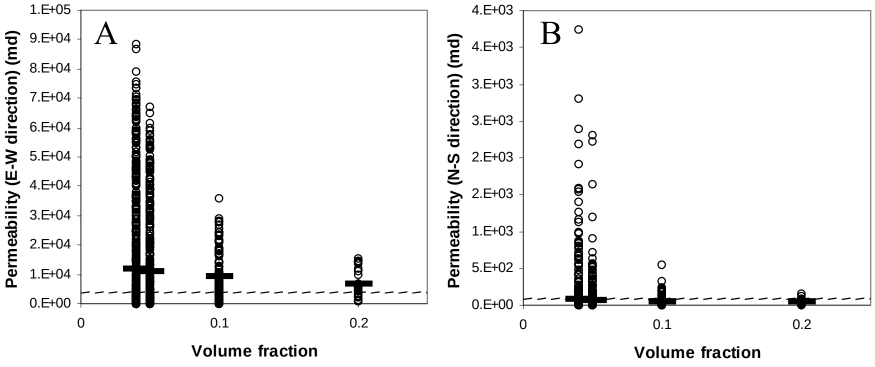

Pseudo periodic boundary conditions

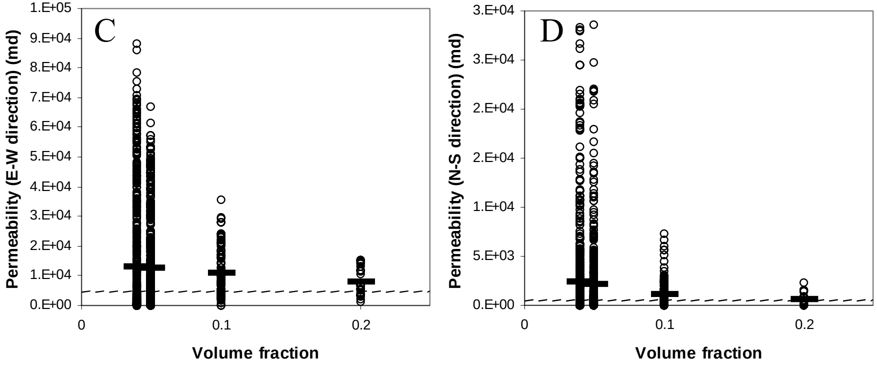

Mixed uniform flux-constant pressure boundary conditions

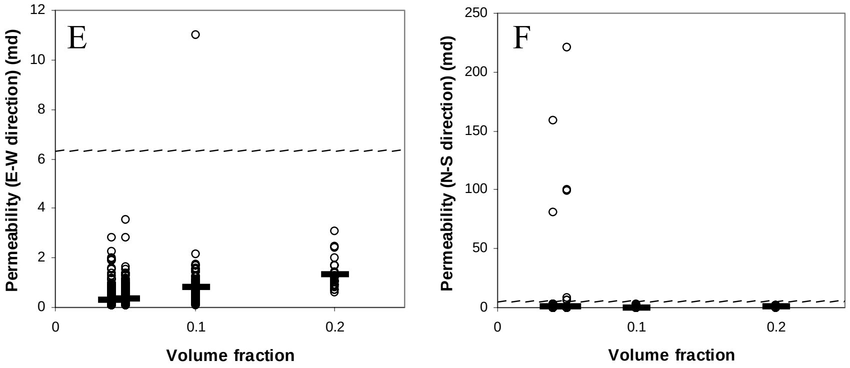

Figure 4.28: Determination of the existence of a REV for a fracture pattern created at a 3 to 1 anisotropic strain level, where A and B are the east-west and north-south permeability values obtained using constant pressure-no flow boundary conditions, C and D are the east-west and north-south permeability values obtained using pseudo periodic boundary conditions, and E and F are the east-west and north-south permeability values obtained using the mixed boundary conditions.

The analysis was repeated for the same pattern but now subjected to an emergent threshold of 50% of the maximum aperture (Fig. 4.29 and Table 4.2), resulting in elimination of fractures having an aperture smaller than 50% of the maximum aperture. This creates a pattern which is no longer percolating in either the east-west or north-south direction (Fig. 4.14), resulting in a reduction of the permeability values of the entire pattern (Table 4.2). Furthermore, north-south oriented fractures are predominantly eliminated (Fig. 4.14), leading to a larger reduction in the estimated north-south permeability values (Fig. 4.29 and Table 4.2). For the pressure and periodic boundary conditions, the range in east-west permeability values is not reduced since the largest capacity fractures, resulting in the largest permeability values, are maintained. Likewise, the lower permeability bounds are maintained since the smallest permeability values result from matrix only models. Since the range in permeability values is identical, no REV exists based on these boundary conditions. However, the mixed boundary condition indicates that an REV has been reached, since very small ranges in permeability values are obtained in both the east-west and north-south direction, suggesting that an average value of ~0.3 mD (east-west direction) and ~0.1 mD (north-south direction) can be used as representative values to simulate this reservoir. However, if such a method is applied to a fractured reservoir the dual decline behavior as seen in Figure 4.15 will be lost. A single permeability (and porosity) reservoir would exhibit a single exponential decline (Fetkovich, 1980), and thus would not be able to recreate the signature dual decline response of a fractured reservoir.

Constant pressure-no flow boundary conditions

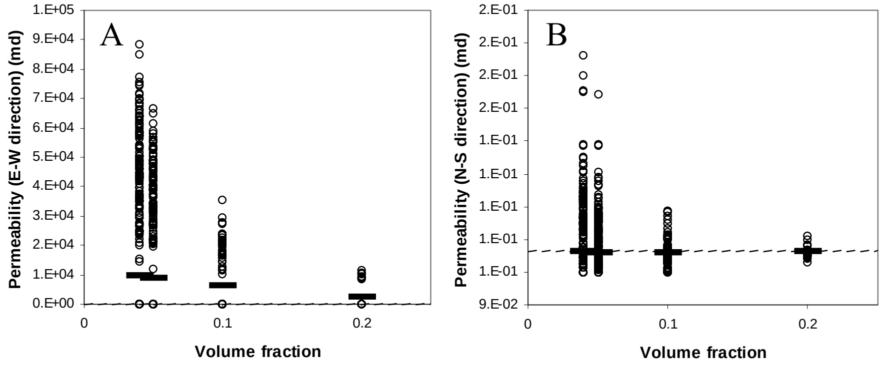

Pseudo periodic boundary conditions

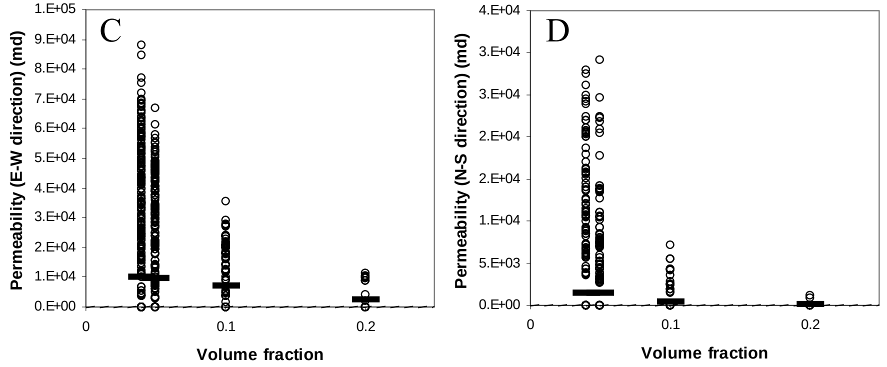

Mixed uniform flux-constant pressure boundary conditions

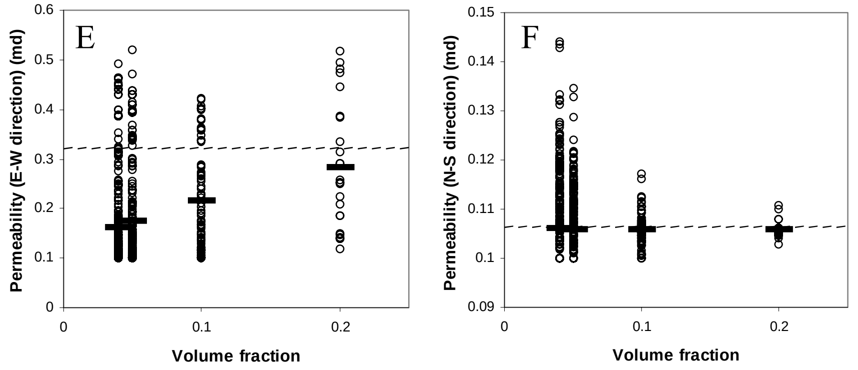

Figure 4.29: Determination of the existence of a REV for a fracture pattern created at a 3 to 1 anisotropic strain level and an emergent threshold of 50% of the maximum aperture, where A and B are the east-west and north-south permeability values obtained using constant pressure-no flow boundary conditions, C and D are the east-west and north-south permeability values obtained using pseudo periodic boundary conditions, and E and F are the east-west and north-south permeability values obtained using the mixed boundary conditions.

4.6 CALCULATED PERMEABILITY FIELDS

The previous section suggests that upscaled permeability values will depend on the boundary conditions used. Gridblock permeability distributions were generated using pressure, periodic and mixed boundary conditions for the fracture pattern of Fig. 4.11C to explicitly demonstrate this boundary condition effect. The 30 x 30 m fracture pattern was divided into 5x5, 10x10, 20x20 and 25x25 gridblocks, and each gridblock's permeability was computed using the three specified boundary conditions to generate different east-west and north-south permeability distributions for the fracture pattern (Fig. 4.30).

The periodic (black curves) and mixed (blue curves) boundary conditions results have the largest difference in permeability values (they define the maximum and minimum values, respectively) (Fig. 4.30). All of the boundary conditions used show that the coarsest gridding of the fracture pattern (5x5) results in the highest median permeability values. Finer gridding results universally increase the number of low permeability gridblocks, since more gridblocks exist that do not contain any fractures. Comparing extreme values, even though the median is highest for the coarse gridding, the highest individual permeability values result from the fine grid. The constant pressure results exhibit a bimodal behavior, matching the large values of the periodic boundary conditions for about half of the distribution and the small values of the mixed boundary condition for the other half of the distribution. This is most evident for the east-west permeabilities. For the north-south distribution, the pressure results still follow the mixed boundary condition distribution for the low values part of the distribution (for the relatively unfractured blocks), but higher permeabilities (for blocks containing fractures) for pressure boundary conditions are substantially less than the periodic results. This difference is due to the alignment of the fractures with the flow direction. The east-west fractures have very little orientation variation (Fig. 4.11C), whereas the north-south fractures show more deviation, resulting in more fractures connecting not opposing block sides but adjacent sides. Since the periodic boundary condition can account for the contribution of diagonal fractures (connecting adjacent gridcell sides), it estimates larger permeability values than the pressure boundary conditions. One last general aspect of the permeability distributions is that the east-west values are on average higher than the north-south values. This can be attributed to the fact that the east-west fractures have higher apertures on average than the north-south fractures, a consequence of the higher strain imposed perpendicular to the east-west fractures.

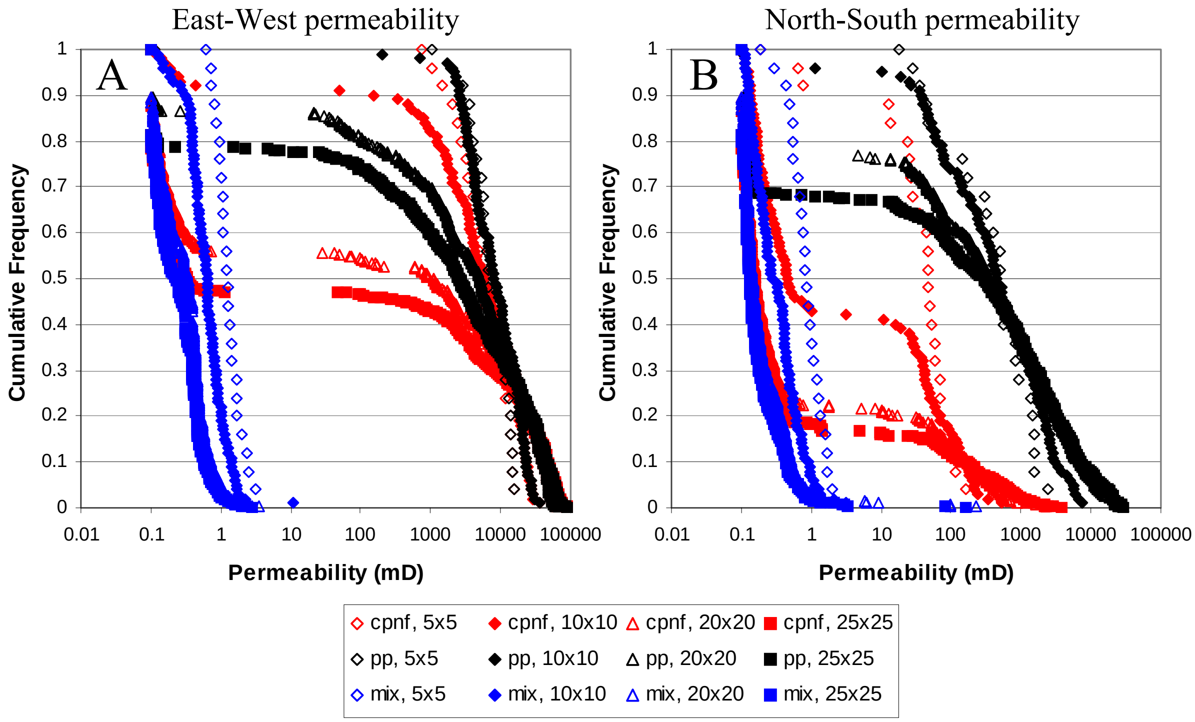

Figure 4.30: Cumulative frequency distributions of the permeability values calculated using different sets of boundary conditions: 1) cpnf = constant pressure-no flow, 2) pp = pseudo-periodic, and 3) mix = mixed, where the pattern under investigation is created using a 3 to 1 strain anisotropy. The coarseness of the upscaling is varied from 5x5, to 10x10, to 20x20, and 25x25 gridblocks for a 30 by 30 m model.

When a 50% emergent threshold is applied to the pattern created under 3 to 1 strain anisotropy, large portions of the thinner north-south fractures are eliminated (Fig. 4.14B). Since the fracture pattern has essentially reduced to a single orientation fracture pattern, the permeability distribution of the periodic and constant pressure boundary conditions are virtually identical for the east-west direction, both returning a bimodal distribution representing fractured and unfractured gridblocks (Fig. 4.31). For the north-south direction, the periodic boundary condition still returns high permeability values for

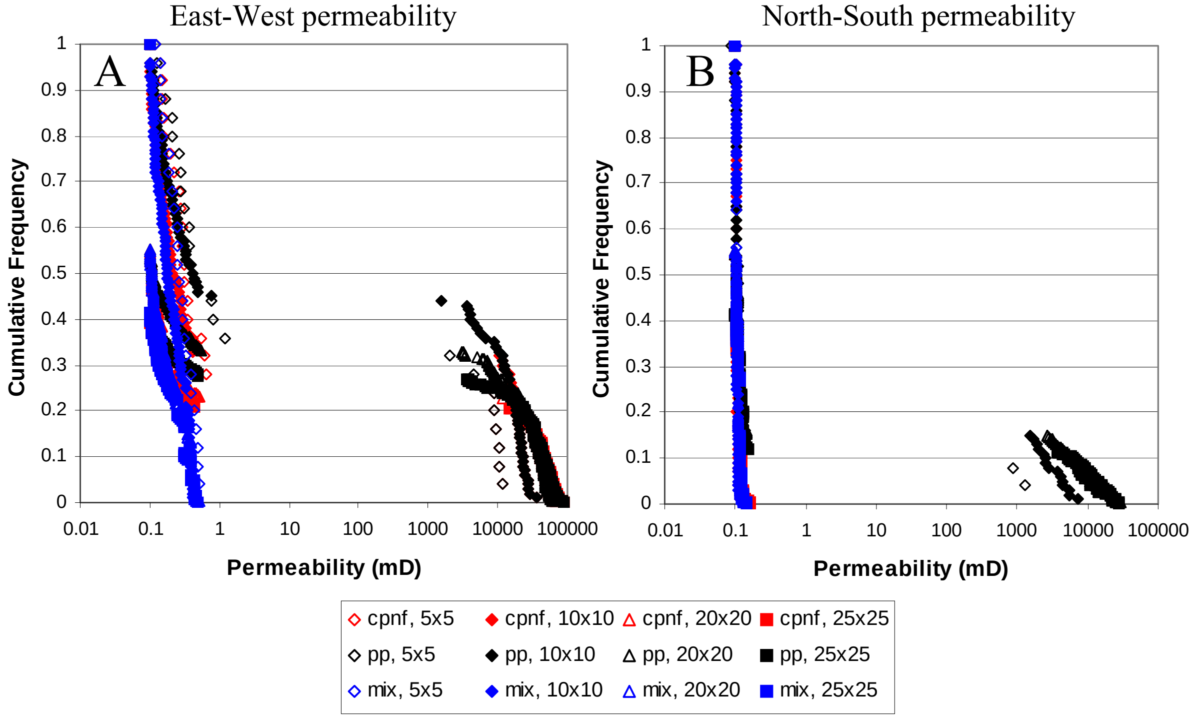

Figure 4.31: Cumulative frequency distributions of the permeability values calculated using different sets of boundary conditions: 1) cpnf = constant pressure-no flow, 2) pp = pseudo-periodic, and 3) mix = mixed, where the pattern under investigation is created using a 3 to 1 strain anisotropy and an emergent threshold of 50%. The coarseness of the upscaling is varied from 5x5, to 10x10, to 20x20, and 25x25 gridblocks for a 30 by 30 m model.

~15% of the gridblocks, corresponding to those cases where fractures slightly deviate from the east-west trend and thus connect two adjacent gridblock sides. The mixed boundary condition returns the same permeability value for all blocks, which could be interpreted as the REV permeability.

4.7 PRIMARY RECOVERY

The objective of this section is to determine which of the selected upscaling techniques is best suited for fractured reservoir simulation. Attempts to model a fractured reservoir with a single permeability (and porosity) value, determined from a REV analysis, will always result in an oversimplification of the problem, since using a single permeability and porosity value would lead to a single exponential decline (Fetkovich, 1980). The proposed method has the objective to create a permeability field which still honors the dual rate decline behavior signature of a fractured reservoir, but reduces the computational requirements. The investigation focuses on a closed square reservoir in primary recovery with a constant bottom hole pressure well placed its center. The upscaled model consists of the original detailed pattern in the center around the well and upscaled cells at the edge (Fig. 4.32). First the 40 by 40 m pattern is trimmed down to 30 by 30 m, to fit within the detailed grid size requirements. This 30 by 30 m model is then subdivided into smaller gridblocks (i.e. 5 by 5 gridblocks, 10 by 10 gridblocks, 20 by 20 gridblocks, and 25 by 25 gridblocks) which are upscaled using one of the three different boundary conditions: 1) pressure, 2) periodic, and 3) mixed. The upscaled field is placed at the edge of the detailed pattern in accordance with Figure 4.9. The reservoir is produced as a single phase reservoir. Table 4.1 gives a complete set of data used to create a simulation run. The pattern under 3 to 1 anisotropic loading is investigated as well as that same pattern with an emergent threshold of 50%.

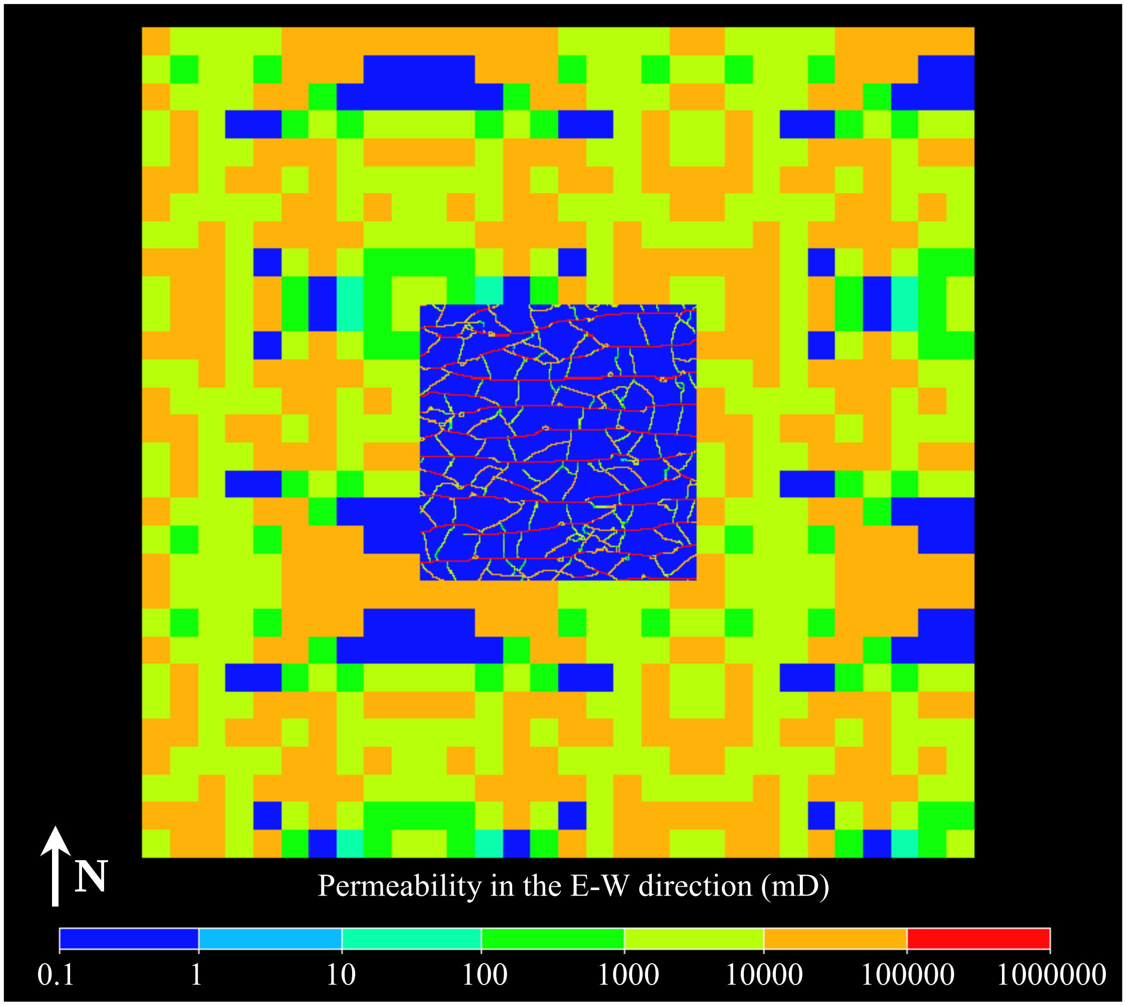

Figure 4.32: Example of an upscaled grid for the fracture pattern created under 3 to 1 anisotropic strain. Upscaling has been performed based on the constant pressure-no flow boundary conditions. The upscaled grid consists of 10 by 10 cells. The local grid refinement (LGR) around the well consists of 200 by 200 cells. Cell permeabilities on the edges are placed in accordance with Figure 4.9.

4.7.1 LGR: well not connected to the fracture pattern

For all upscaling techniques (pressure, periodic, and mixed), the mismatch up to 10 days is negligible (Fig. 4.33) with the reference model (section 4.3) for a fracture pattern created under 3 to 1 anisotropic loading with the well not connected to the fracture network. All boundary conditions match very well with only some discrepancies occurring at pseudo steady state. Since all errors are small, no real preference exists for any one boundary condition. The fact that all methods and coarseness levels give a close match indicates that the model is relatively insensitive to the permeability field outside the local grid refinement (LGR). Figures 4.30 and 4.31 clearly show that the different methods and coarseness levels result in drastically different permeability fields. This indifference to the remote permeability field is also observed for a disconnected fracture pattern (Fig. 4.34). Applying an emergent threshold of 50% and repeating the upscaling procedure shows that all upscaling techniques match the detailed results.

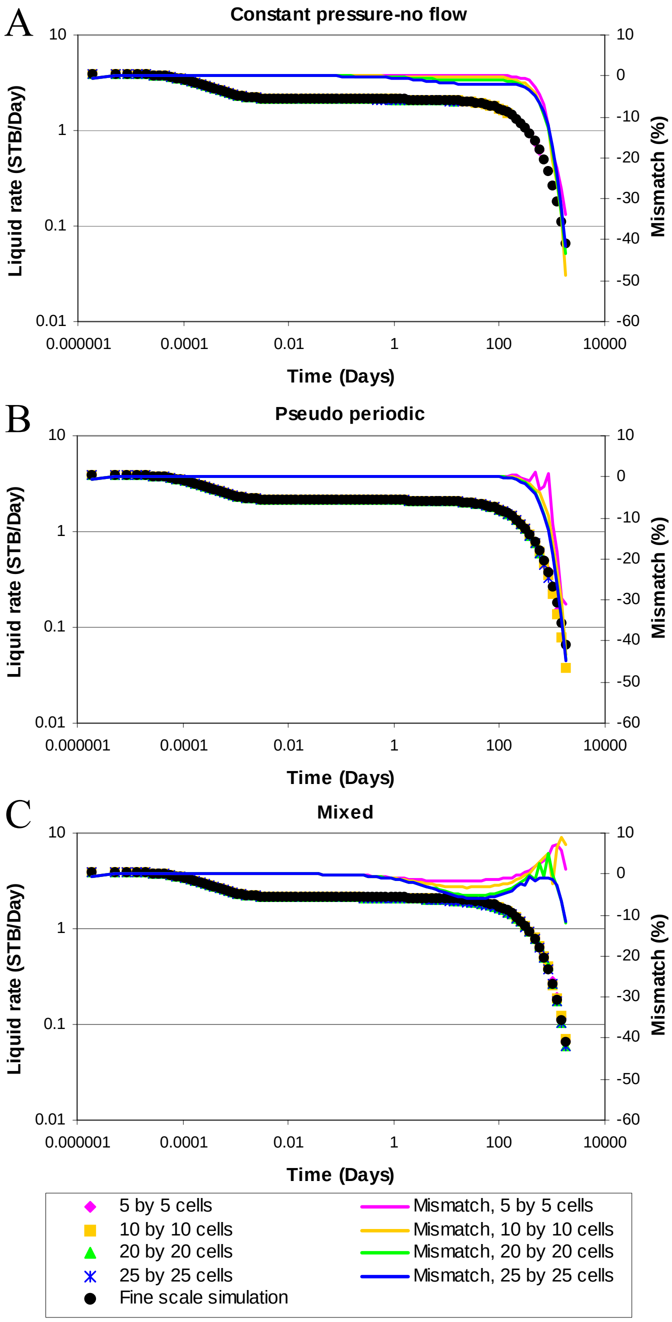

Figure 4.33: Time vs. liquid rate for the upscaled fracture pattern created under 3 to 1 anisotropic strain. The mismatch of the upscaled results with the detailed or fine scale simulation is also given. The coarseness of the upscaling is varied from 5x5, to 10x10, to 20x20, and to 25x25 gridblocks, for a 30 by 30 m pattern. Each plot shows the results for a different boundary condition: A) pressure, B) periodic, and C) mixed.

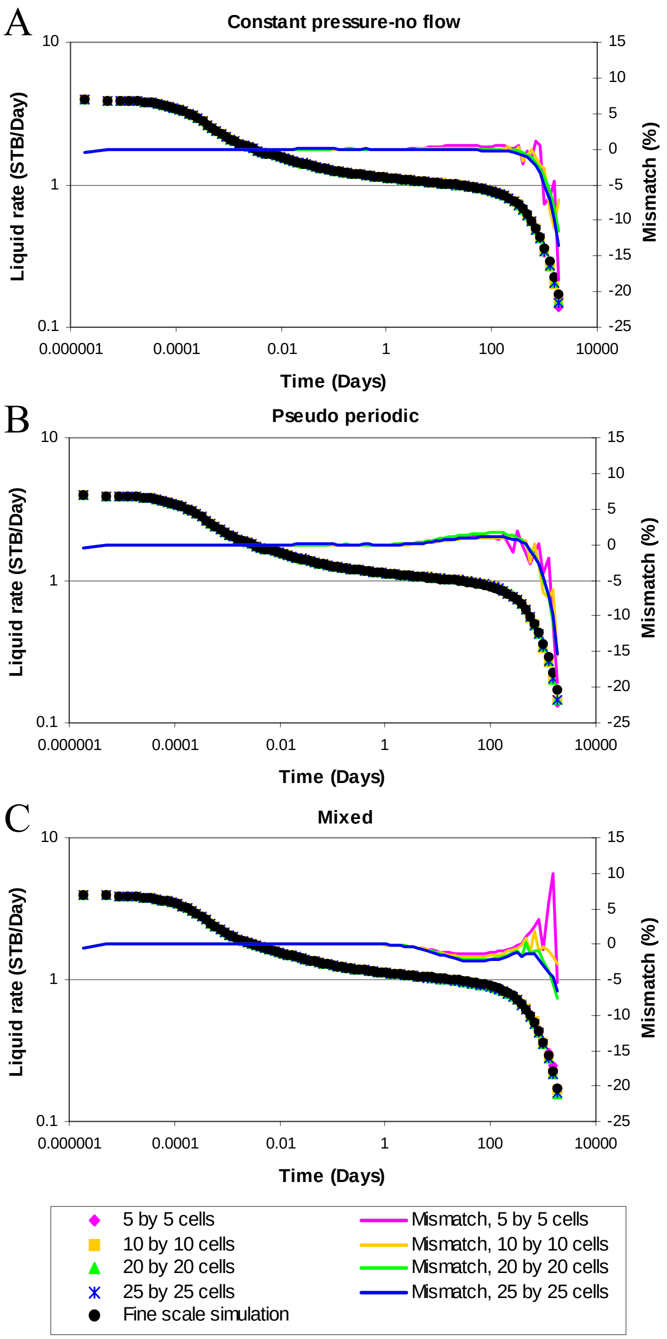

Figure 4.34: Time vs. liquid rate for the upscaled fracture pattern created under 3 to 1 anisotropic strain with a 50% emergent threshold. The mismatch of the upscaled results with the detailed or fine scale simulation is also given. The coarseness of the upscaling is varied from 5x5, to 10x10, to 20x20, and to 25x25 gridblocks, for a 30 by 30 m pattern. Each plot shows the results for a different boundary condition: A) pressure, B) periodic, and C) mixed.

4.7.2 LGR: well connected to the fracture pattern

Unlike the case where the well was not connected to the fracture network, the upscaling technique does influence the simulation results when the well is connected the fracture pattern (Fig. 4.35). In connecting the well to the fracture network, the radius of influence of the well effectively increases, making the far field permeability values more important. In general, none of the upscaling techniques give a 100% match with the true case. The best match is obtained for the coarsest level of upscaling, using the constant pressure-no flow boundary conditions. However, increasing the level of detail significantly deteriorates the match. Fine upscaling does a better job at placing high permeability streaks, but it does not necessarily honor the connectivity of these high permeability streaks. In the detailed fractured models, fracture connectivity was ensured by the special gridding scheme outlined in Figure 4.5, but this is not done for the upscaled fields. As upscaling becomes more detailed the resulting permeability field exhibits places where the connectivity of the system is not specifically honored. For large block sizes, there will never be a block which does not contain a fracture, ensuring that all permeability values are high (for the pressure and periodic boundary condition). Since the fracture pattern is highly connected, and since the well is connected to the fractures, a high permeability value is appropriate. Although the coarsest pressure boundary condition case gives the best match, the pseudo periodic boundary condition matches the shape of the curves best at all levels of upscaling. This is not true for the other two boundary conditions under investigation. It is not surprising that the periodic boundary condition gives this superior shape match, since connecting the well to the fracture network makes the local boundary conditions resemble a constant pressure boundary condition. The fact that the pressure boundary condition does not give a good match at all gridding refinements is attributed to the fact that it does not take into account flow from fractures at an angle with the gridblock sides. Even though the periodic boundary condition is able to match the shape of the curve, it would not be recommended to use this approach given that the dual permeability approach is able to obtain a similar match with significantly less effort, while still honoring the fracture data obtained from core and outcrop (Fig. 4.17).

If the well is connected to a non-percolating fracture pattern, the well response is once more insensitive to the upscaling technique (Fig. 4.36). This is not surprising since connecting the well to a fracture only marginally increases the radius of influence, rendering the well response insensitive to the remote permeability field. All upscaling methods give exact matches up to about 1 day into the simulation. The match remains good up to 100 days after which all methods start to deviate. These results are clearly superior to the dual permeability/dual porosity approach, which could not match the production data profile nor be related to realistic fracture parameters for this kind of case (see Fig. 4.19).

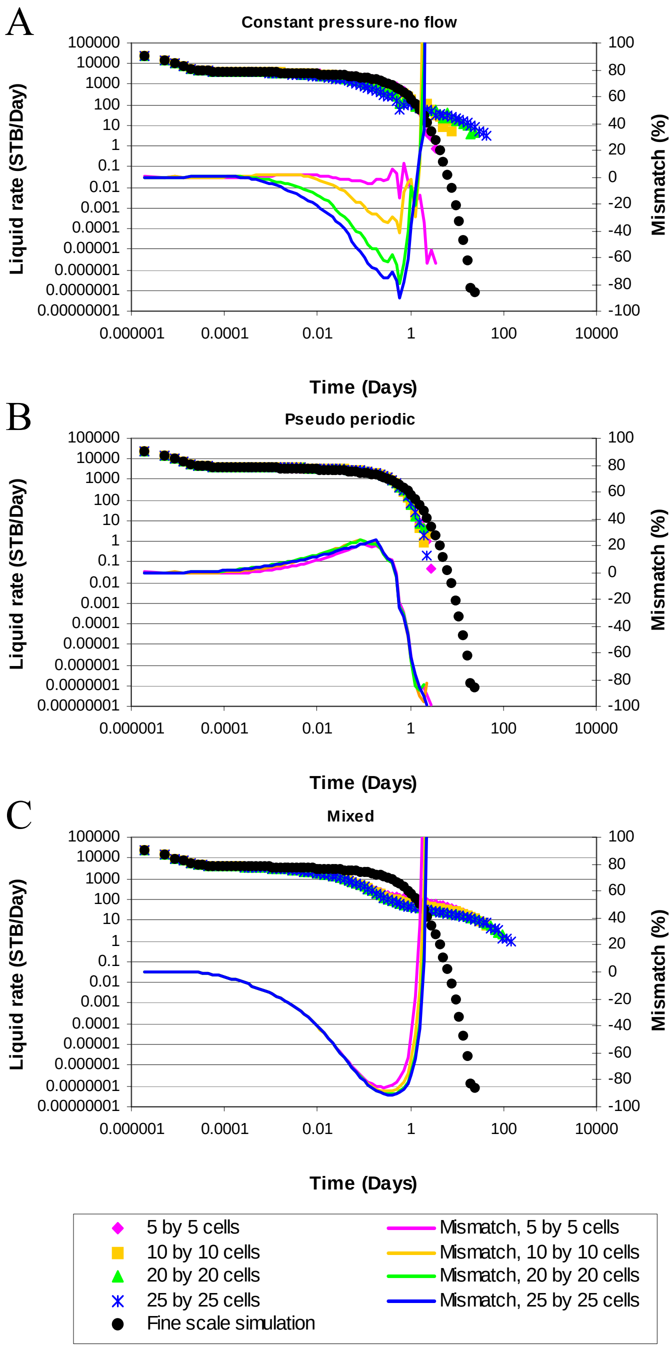
A Constant pressure-no flow

B Pseudo periodic

C Mixed

Figure 4.35: Time vs. liquid rate for the upscaled fracture pattern created under 3 to 1 anisotropic strain, where the well is connected to the fracture pattern. For each plot the mismatch of the upscaled result with the detailed or fine scale simulation is given. The coarseness of the upscaling is varied from 5x5, to 10x10, to 20x20, and to 25x25 gridblocks, for a 30 by 30 m pattern. Each plot shows the results for different boundary conditions: A) pressure, B) periodic, and C) mixed.

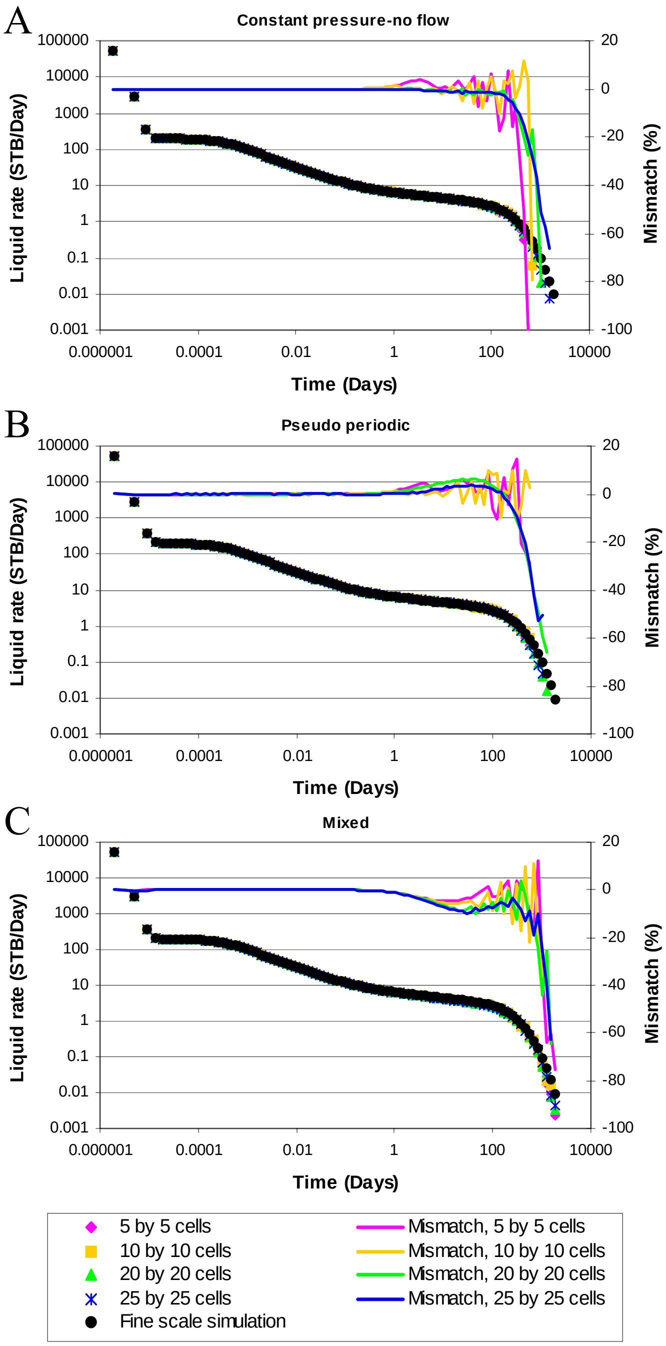

Figure 4.36: Time vs. liquid rates for the upscaled fracture pattern created under 3 to 1 anisotropic strain with a 50% emergent threshold, where the well is connected to the fracture pattern. For each plot the mismatch of the upscaled result with the detailed or fine scale simulation is given. The coarseness of the upscaling is varied from 5x5, to 10x10, to 20x20, and to 25x25 gridblocks, for a 30 by 30 m pattern. Each plot shows the results for different boundary conditions: A) pressure, B) periodic, and C) mixed.

4.7.3 No LGR

The previous two sections illustrated that as long as the well is not linked to a well-connected fracture pattern, the farfield upscaling technique has little effect on the model response. This indicates that the model with a local grid refinement (LGR) around the well is insensitive to the permeability field outside the LGR. In the absence of good fracture characterization, or to reduce the computational requirements, the LGR around the well might be eliminated. To test the impact of such a simplification, the 30 x 30 m region around the well was replaced by upscaled gridblocks (Fig. 4.37). Clearly, as the coarseness level increases the level of detail diminishes. Previous sections showed that the well response is dependent on its connectivity to the fracture pattern. Therefore, separate runs were created with the well connected and not connected to the fracture network. Wells were placed in cells with a permeability value close to the matrix permeability value to simulate a disconnected well. Wells were placed in cells with permeability values close to the average fracture permeability value to simulate a connected well. As the upscaling becomes coarser this distinction is more and more difficult to make (Fig. 4.37).

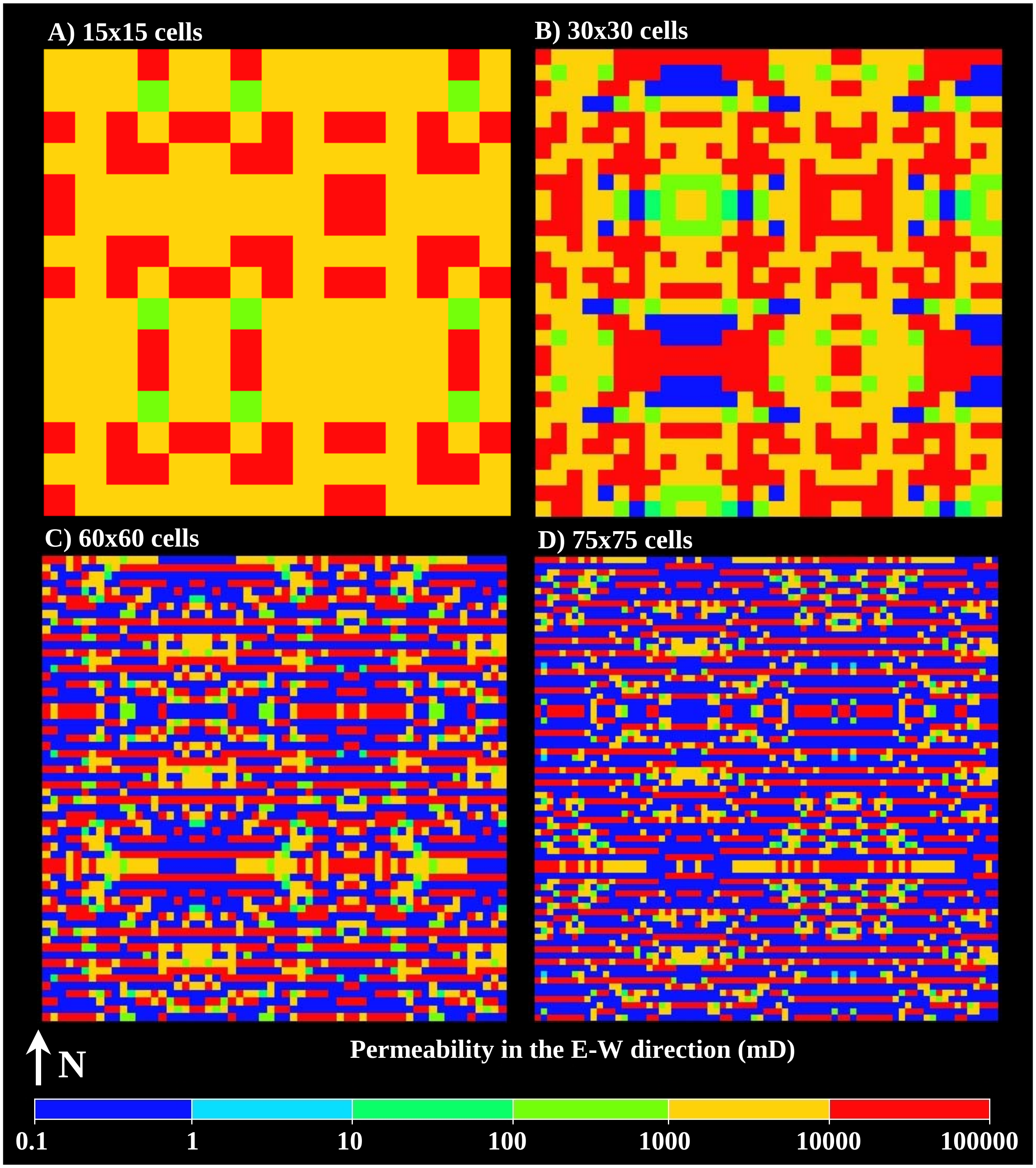

Figure 4.37: Permeability fields for the 90 by 90 m upscaled pattern without the LGR around the well, based on the pattern shown in Figure 4.10. The degree of coarseness is varied: A) 15 by 15 cells, B) 30 by 30 cells, C) 60 by 60 cells, and D) 75 by 75 cells.

4.7.3.1 No LGR: well not connected to the fracture pattern

The fracture pattern generated using a 3 to 1 anisotropic strain is investigated with varying levels of upscaling coarseness, where the well was not connected to the fracture network (Fig. 4.38). The results show the expected decrease in accuracy with an increase in upscaling coarseness. They also show that all methods perform poorly at early times. This is not surprising since the primary decline is an artifact of the detailed fracture pattern, which is no longer explicitly honored. The poor fit at early times indicates that not enough detail is preserved during upscaling, even at fine levels of upscaling. Early time matches would provide information about the near wellbore reservoir and fluid characteristics and are important in characterizing the near wellbore fracture pattern. Late time matches give information on the far field reservoir characteristics such as size of the reservoir and the distance to the boundaries. Given that the well response is insensitive to the farfield permeability values if the LGR is maintained for a percolating fracture network with the well not connected to the fractures (Fig. 4.33), and given that significantly different rates are obtained (dependent on the boundary conditions used) if the LGR is eliminated (Fig. 4.38), one has to conclude that the LGR dominates the well response in this model. This indicates that knowledge of the fracture pattern at the well can provide accurate production prediction. At the coarsest gridding, the mixed boundary conditions give the best results, but the only acceptable results are for the finer pressure boundary conditions, where the 20 by 20 grid performs better than the 25 by 25 grid (Fig. 4.38). As stated before, upscaling does not specifically honor the connectivity of the pattern. High permeability gridblocks are more likely to occur at coarser upscaling levels in highly connected fracture patterns, resulting in better connectivity. This point is further illustrated in Figure 4.39, where the same pattern at two different levels of upscaling is shown for the pressure boundary condition. The white lines illustrate the number of paths

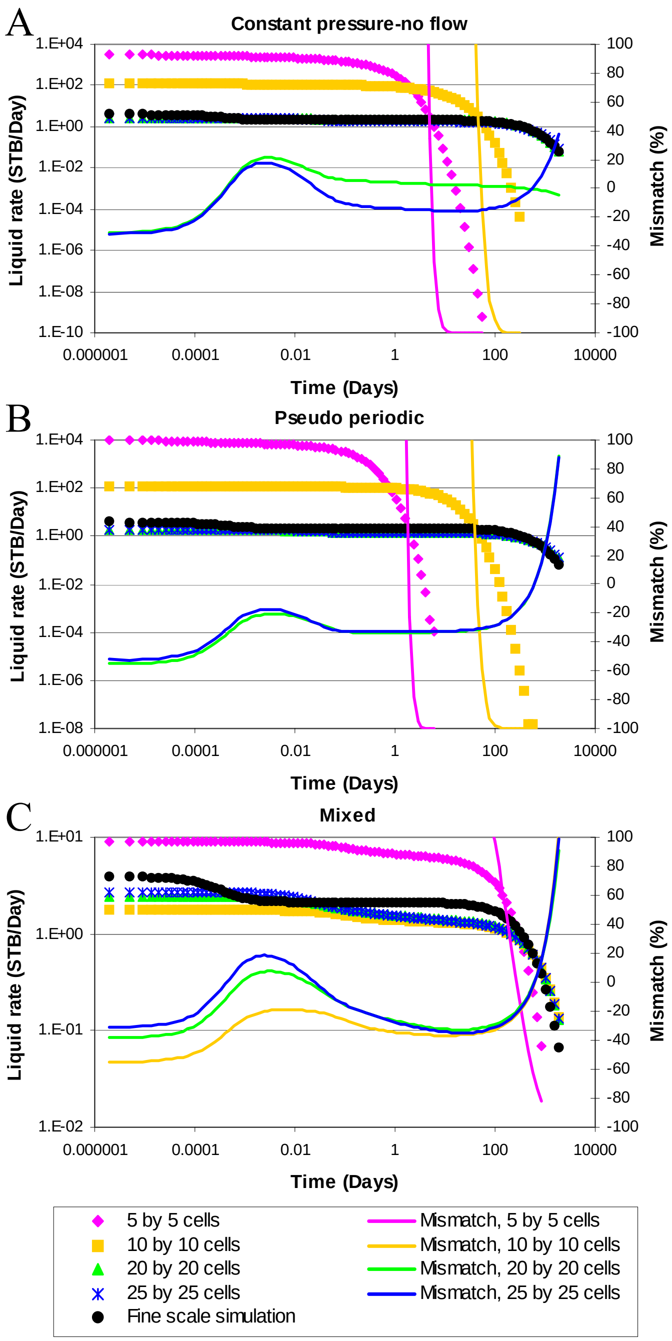

Figure 4.38: Time vs. liquid rates for the upscaled fracture pattern created under 3 to 1 anisotropic strain, where the well is not connected to the fracture pattern. For each plot the mismatch of the upscaled result with the detailed or fine scale simulation is given. The coarseness of the upscaling is varied from 5x5, to 10x10, to 20x20, and to 25x25 gridblocks, for a 30 by 30 m pattern. Each plot shows the result for a different upscaling method: A) pressure, B) periodic, and C) mixed.

connecting two sides, where multiple paths are not allowed to go through the same gridblock. Three such paths can be found for an upscaling level of 20 by 20 gridblocks and only two of those paths can be found for 25 by 25 gridblocks, indicating a larger degree of connectivity at coarser upscaling levels. With such a high fracture permeability, connectivity is the most important parameter and not the permeability value calculated in the fracture. Both a 1000 mD fracture gridblock and a 10000 mD fracture gridblock will have an infinite capacity compared to the 0.1-1 mD matrix blocks. The poorer match obtained using the periodic boundary condition is attributed to the difference in well location. For the periodic boundary condition fewer cells are present which resemble the matrix permeability, making well placement more restricted. Locating the well in the same block as used for the pressure boundary condition results in a larger mismatch, since the periodic boundary condition does not return a permeability value resembling the matrix permeability for that gridblock. This points to an inherent drawback when comparing the well responses of the different models, since the well location can not be kept constant between models without leading to an unfair comparison.

One might argue that the mismatch obtained using the pressure or periodic boundary conditions can be attributed to the fact that no full tensor permeability was used. However, Figure 4.38 clearly shows acceptable matches occurring at late times, indicating that even without a full tensor representation late time behavior can be adequately modeled for the fracture pattern under investigation. Furthermore, the early time mismatch is not considered an artifact of the permeability representation. A full tensor permeability representation would also homogenize the reservoir, resulting in a similar expected loss of the signature naturally fractured reservoir dual decline behavior.

For the same fracture pattern but with a 50% emergent threshold, all upscaling boundary condition methods have similar shortcomings in matching the reference results when run without the LGR around the well (Fig. 4.40). Early time behavior is not matched because the detailed fracture pattern is not explicitly modeled around the well. Although all the boundary conditions return different permeability estimates for the fractured gridblock permeability, this variation does not result in vastly different production differences. In this non-percolating fracture network with the well not connected to the fracture network, the flow rate is dependent on the permeability of the matrix gridblocks, which is approximately the same for all boundary conditions, explaining the similar well responses.

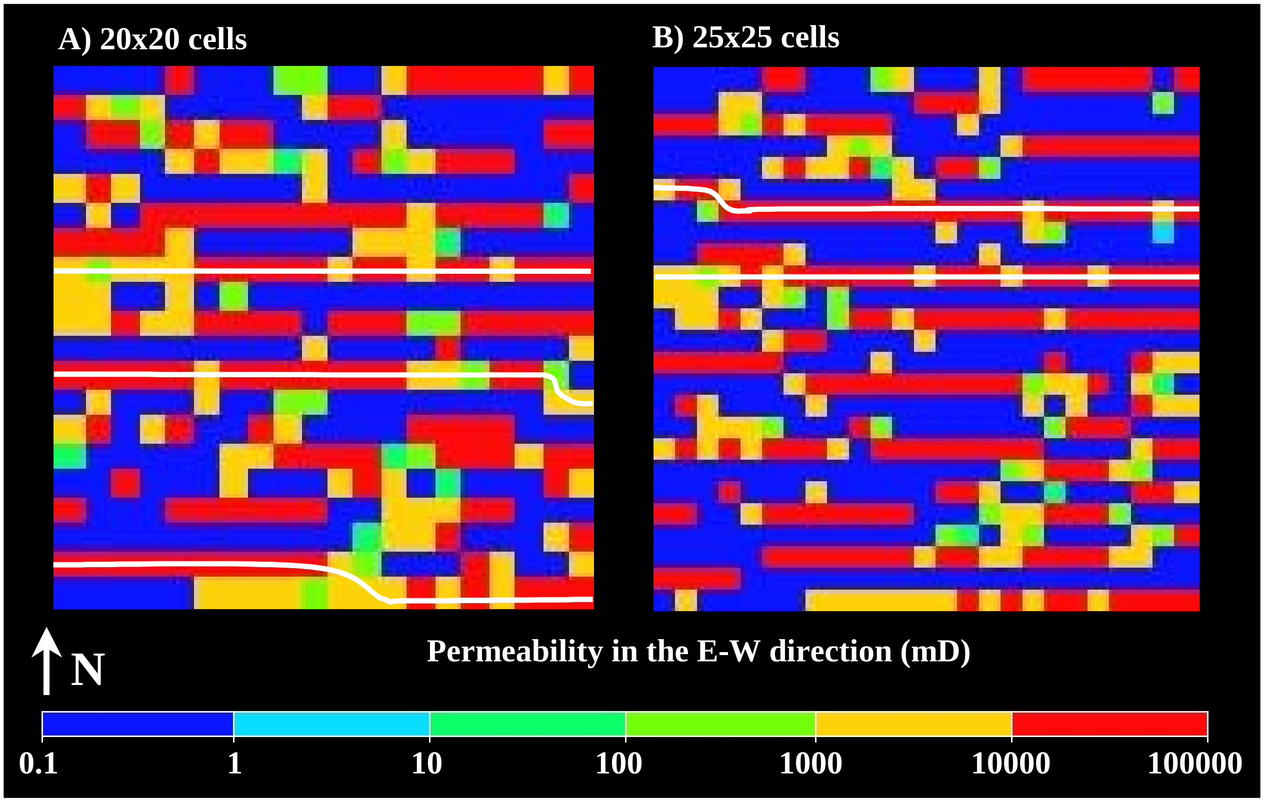

Figure 4.39: Connectivity of the permeability field at different upscaling levels. Upscaled permeability fields resemble the pattern created with a 3 to 1 anisotropic strain level. The white lines delineate the flow paths connecting two opposite sides, where no paths are allowed to use the same fracture gridblock twice.

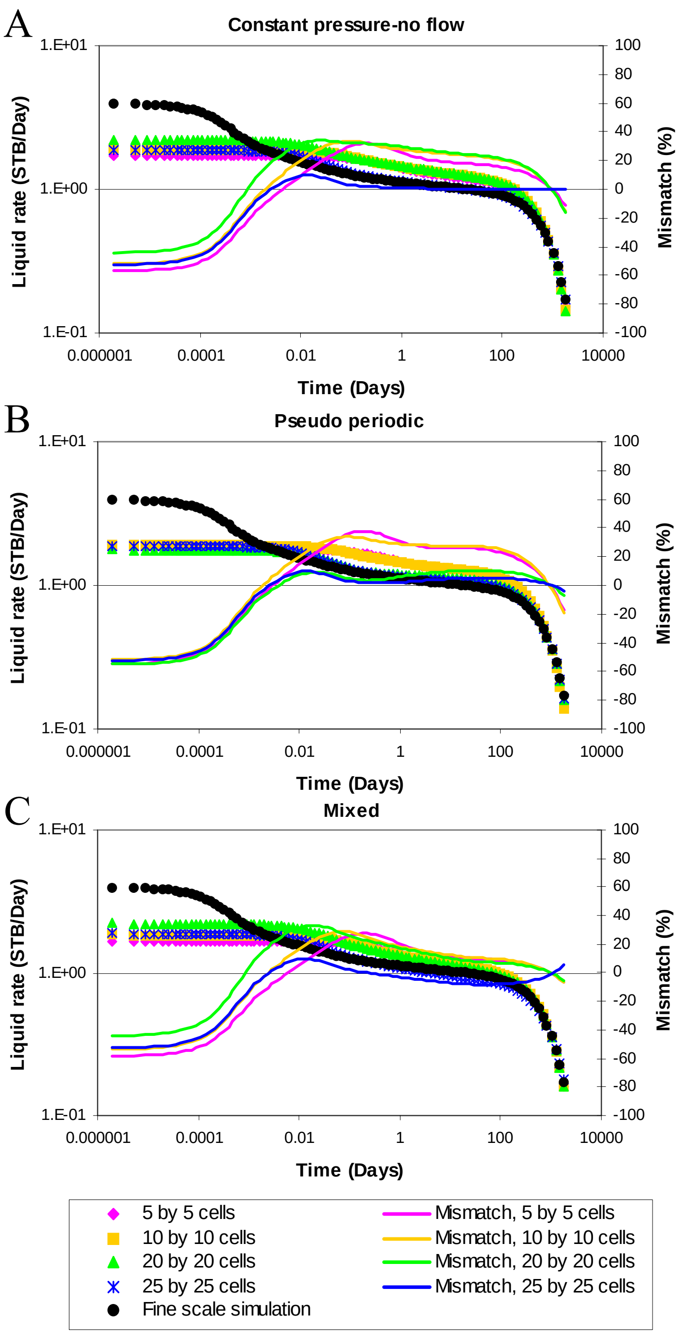

Figure 4.40: Time vs. liquid rate for the upscaled fracture pattern created with a 3 to 1 strain anisotropy and a 50% emergent threshold, where the well is not connected to the fracture pattern. For each plot the mismatch of the upscaled result with the detailed or fine scale simulation is given. The coarseness of the upscaling is varied from 5x5, to 10x10, to 20x20, and to 25x25 gridblocks, for a 30 by 30 m pattern. Each plot shows the results for a different boundary condition: A) pressure, B) periodic, and C) mixed.

4.7.3.2 No LGR: well connected to the fracture pattern

The response for the non-LGR case where the well is located in a fractured cell does not exhibit the expected decrease in accuracy as the upscaling becomes coarser (Fig. 4.41). As explained earlier, this is attributed to the lack of connectivity in the upscaled models (Fig. 4.39). In the detailed fracture models, fracture connectivity was ensured by a special gridding scheme. As upscaling becomes more detailed the resulting permeability field exhibits places were the connectivity of the system is not specifically honored, resulting in larger mismatches. This lack of connectivity makes the model relatively more disconnected, explaining why the finer models sense the boundary later. Due to the low estimated permeability values, the mixed boundary condition shows an extremely poor match for all levels of upscaling, indicating that this boundary condition is poorly suited for this case. The periodic boundary condition results most closely resemble the shape of the detailed model response at most levels of upscaling (the pressure boundary condition results are better at the coarsest level of upscaling). The error is large, but not unexpected given the complexity of the modeled fracture patterns. The superior performance can be explained by the resemblance of this boundary condition to the boundary conditions present in the detailed model. Since the well is directly connected to the fracture network flow is not limited by the capacity of the of the matrix rock. Also, periodic boundary conditions honor connectivity best for all upscaling levels since very few gridblocks exist with matrix permeability values, explaining the superior shape match. However, as stated before, if the fracture pattern is highly connected and if the well is hydraulically linked to the fracture pattern, the described upscaling techniques are not recommended since the dual permeability/dual porosity approach will both adequately match the well response and the fracture network characteristics.

Taking the previous case (non-LGR, well is in a fractured block, 3 to 1 anistropy fracture pattern) and adding the effects of a 50% emergent threshold degrades the already poor matches shown in Figure 4.41 (Fig. 4.42). The relatively large mismatch observed using the mixed boundary conditions, is due to the much lower permeability values obtained for fractured gridblocks. These fractured gridblock values do not resemble those present in the detailed model, and therefore the mixed boundary condition results show large deviations from the reference case. Both pressure and periodic boundary conditions give similarly poor results at early time, but the pressure boundary condition is able to match the pseudo-steady state decline at all grid refinements. The periodic boundary conditions overestimate the gridblock permeability values, since any fracture connecting two adjacent gridblock sides will create a substantial flow rate and thus a large permeability value. When a well is connected to a fracture in a disconnected fracture pattern the source configuration resembles that of a line (or plane in 3D). In the upscaled models this source configuration is not honored, i.e. the length and width of the fracture are not identical leading to well response differences, explaining the substantial errors at early times.

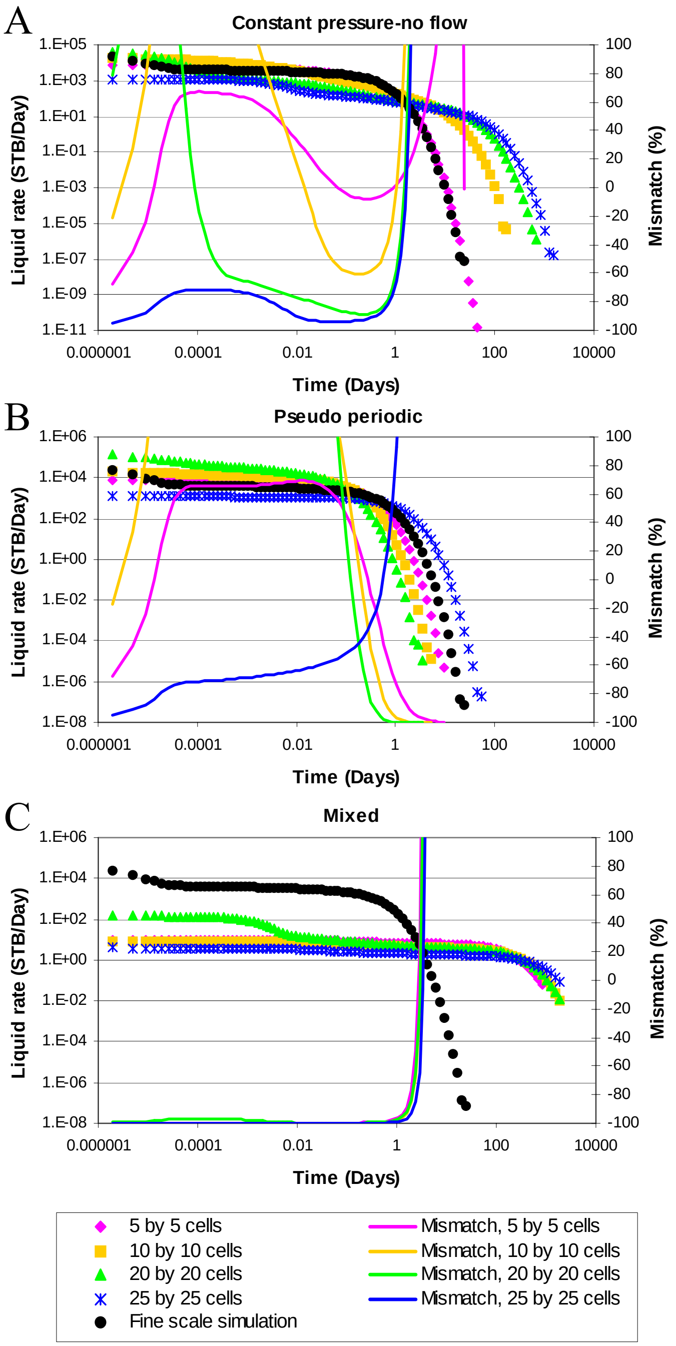

Figure 4.41: Time vs. liquid rates for the upscaled fracture pattern created under a 3 to 1 anistropic strain, where the well is connected to the fracture pattern. For each plot the mismatch of the upscaled result with the detailed or fine scale simulation is given. The coarseness of the upscaling is varied from 5x5, to 10x10, to 20x20, and to 25x25 gridblocks, for a 30 by 30 m pattern. Each plot shows the result for a different upscaling method: A) pressure, B) periodic, and C) mixed.

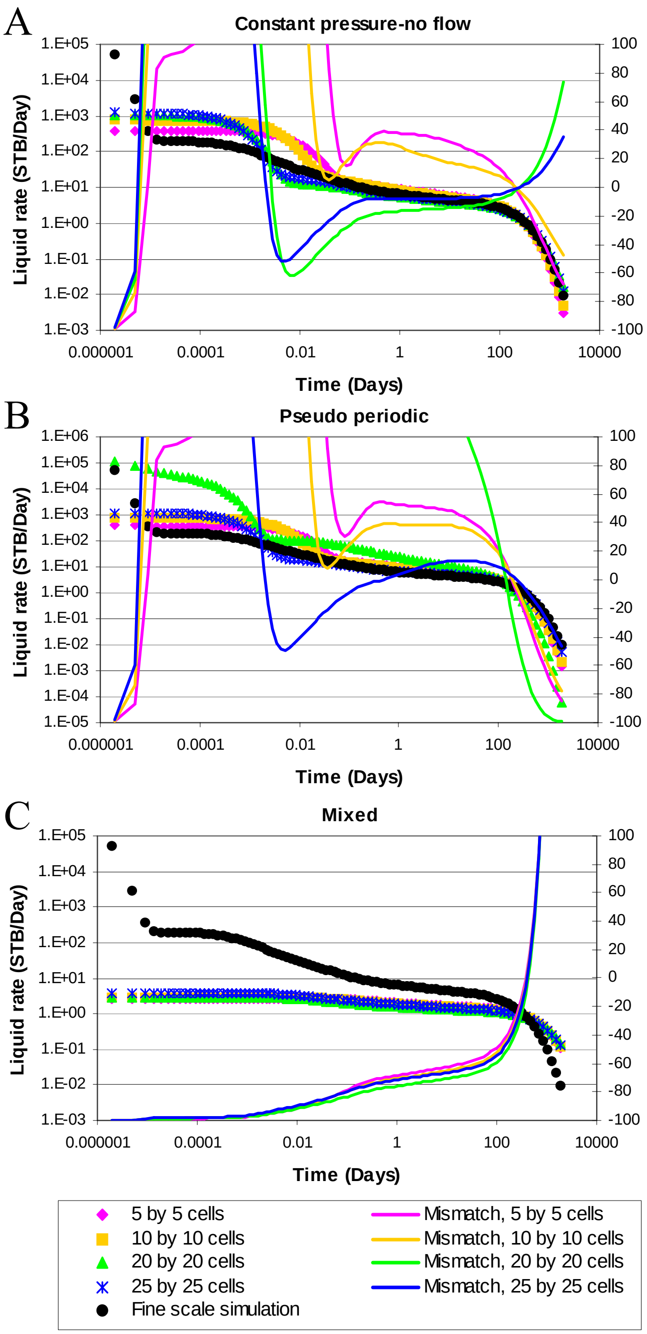

Figure 4.42: Time vs. liquid rates for the upscaled fracture pattern created under 3 to 1 anisotropic strain with a 50% emergent threshold, where the well is connected to the fracture pattern. For each plot the mismatch of the upscaled result with the detailed or fine scale simulation is given. The coarseness of the upscaling is varied from 5x5, to 10x10, to 20x20, and to 25x25 gridblocks, for a 30 by 30 m pattern. Each plot shows the result for a different upscaling method: A) pressure, B) periodic, and C) mixed.

4.8 CONCLUSIONS

The conventional dual permeability/dual porosity approach has the ability to match production results in only a limited number of fractured reservoir configurations. However, unless the well is connected to a highly connected fracture network, the estimated fracture network characteristics are not consistent with the actual fracture pattern. This misinterpretation of the fracture pattern can have a large negative economic impact, since future well placement, completion design and reservoir development may be based upon it. Using a local grid refinement around the well allows for a close match of the well production data, independent of upscaling technique used to populate the far field permeability values. Accurate results using a LGR around the well, however, presume an accurate characterization is available for the near wellbore fracture pattern. In Chapter 3, a procedure was presented which allows for the determination of the fracture pattern characteristics present in the subsurface based on readily available data. Creating a suite of patterns based on the most likely input parameters will result in a well production prediction based on geologic data, which should at least span the observed well production. This is preferred over the dual permeability/dual porosity approach which would be able to match the production data, but would not give a realistic representation of the fracture pattern present in the subsurface, potentially having a large impact on reservoir economics. Only in the case where one knows that the well is in hydraulic contact with a highly connected fracture network, is the dual permeability/dual porosity approach recommended. In this study, a relatively large LGR was used and it is recommended that a sensitivity study be performed with respect to the size of the LGR and its influence on the well response. The expectation is that there exists a minimum LGR size which needs to be maintained to ensure accuracy.

Representing the fractured reservoir with a single permeability (and porosity) value based on a representative elementary volume (REV) will inevitably lead to a considerable loss of early time resolution. The signature dual decline behavior is impossible to match with a single permeability (and porosity) value, since a homogeneous reservoir will exhibit only 1 decline. Furthermore, determination of a representative permeability value depends heavily on the boundary conditions used in heterogeneous systems such as naturally fractured reservoirs.

Attempts to simulate fractured reservoirs using 3 different upscaling techniques and four different levels of upscaling, without the use of a LGR, showed that the best late time matches were obtained using the constant pressure-no flow boundary conditions in almost all cases, except for when the well was connected to a highly connected fracture network. However, as stated before, for that particular situation, the dual permeability/dual porosity approach is preferred, since the production data match is better than the one obtained using any of the investigated boundary conditions, and since the method is able to match the fracture network characteristics as well. The investigated approach showed that any level and method of upscaling results in a loss of resolution at early times. Early time production is a direct response of the hydraulic characteristics of the fracture network. Any level of upscaling will homogenize the near wellbore region, leading to a loss in resolution and inevitably a loss in the ability to match the true production data.

Chapter 5 Method and Conclusions

This study gives a robust and practical workflow to obtain a mechanically consistent naturally fractured reservoir model without direct sampling of the fracture network. The employed workflow presented in this study can be used as a blue print to model many of the naturally fractured reservoirs in the world. The three main tiers of the workflow are: 1) subcritical testing, 2) geomechanical modeling, and 3) flow modeling (Fig. 5.1).

The first stage of the workflow requires the determination of the subcritical index present during fracturing. The subcritical index and the relative fracture strength (RFS) both depend on the rock's microstructure and the chemical environment. The average subcritical index tested in ambient air for sandstones is around 62, whereas the average value for comparable carbonates samples is 120. Thin-section analysis shows that an increase in cement content increases the subcritical index, where the largest increase in subcritical index is observed for (ferroan) calcite cement.

Tests performed in fresh water, brine and oil show that oil and ambient air tests cluster at higher RFS and subcritical index values than tests performed in fresh water or brine. Clay rich sandstones which are (ferroan) calcite cemented respond strongest to environment changes, where a large drop in subcritical index is observed as the environment is changed from ambient air or oil to fresh water or brine.

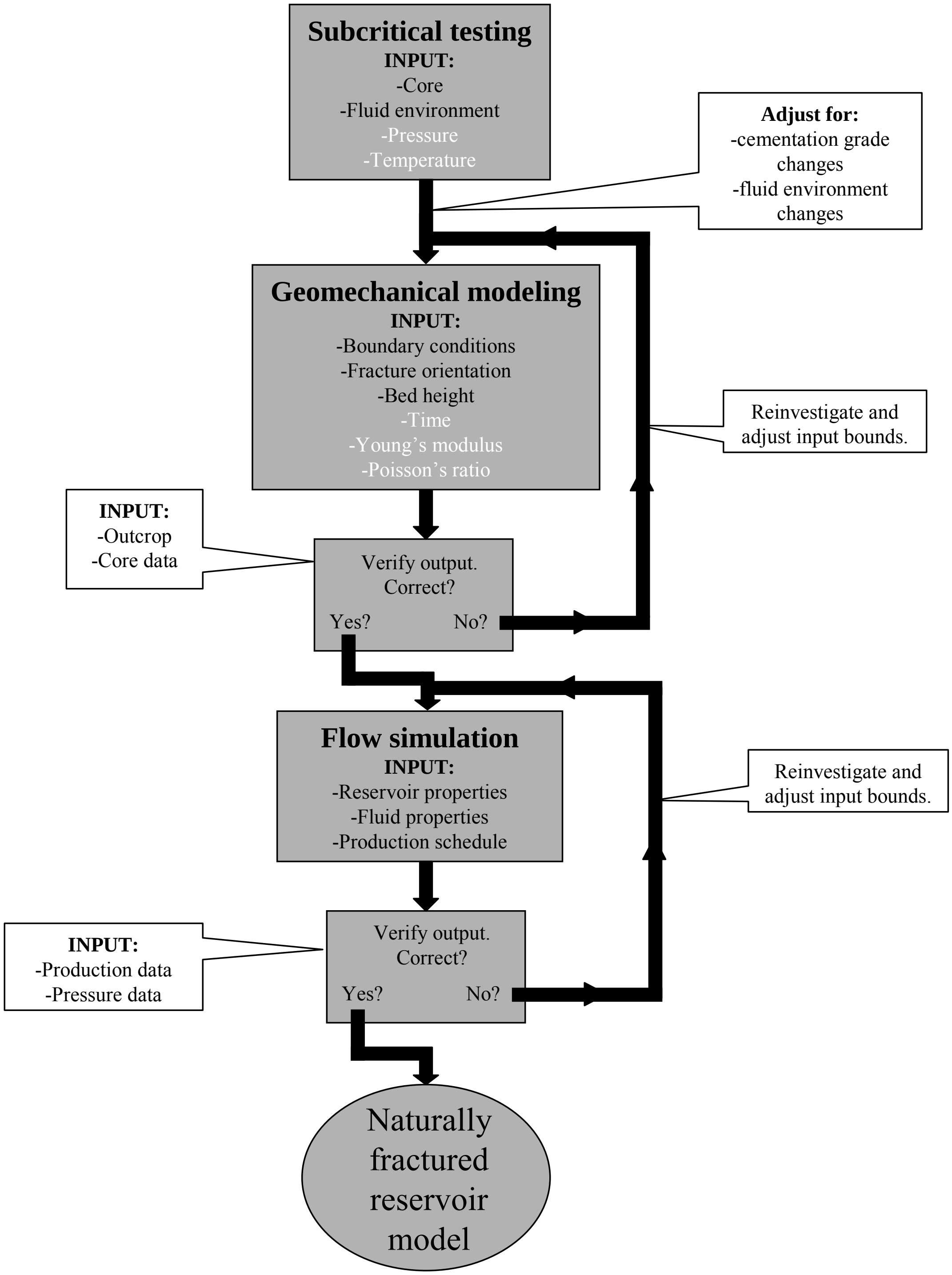

Figure 5.1: Workflow to characterize and flow-simulate naturally fractured reservoirs.

Given these observations, predictions can be made regarding subcritical index values for reservoir rocks. In general, two processes are expected to occur as the reservoir matures: 1) cementation, and 2) influx of hydrocarbons displacing water. If fracturing occurred prior to these maturing processes, the subcritical index measured in the laboratory will be too high. Specifically, if the later cement consists of (ferroan) calcite, the increase in subcritical index and RFS will be considerable. Therefore, once subcritical testing has been performed, adjustments have to be made for changes in cementation and fluid environment which occurred after fracture formation before geomechanical modeling can commence (Fig. 5.1).

Geomechanical modeling has shown that fracture orientation, length, and spacing are independent of Young's modulus, Poisson's ratio and strain rate over the limited ranges tested. However, mechanical bed thickness has a large influence on the fracture pattern. An increase in bed thickness, decreases the fracture density and increases the range in fracture orientations. As the bed thickness increases, the aperture distribution deviates from normal towards negative exponential. For all bed thickness values the length distribution follows a negative exponential, but larger fracture lengths develop in thicker beds. Bed thickness variations may overshadow pattern changes due to other variables such as strain level, strain anisotropy and subcritical index. Therefore, it is important to have a good understanding of the mechanical bed thickness in the reservoir.

Strain anisotropy has a large influence on fracture orientation, where an increase in strain anisotropy reduces the number of dominant fracture sets from at least 2 to 1 dominant through-going fracture set. The spacing between through-going fractures depends on the level of strain anisotropy, where the spacing decreases as the strain anisotropy increases. This not only influences the preferential drainage direction, it can also enhance the drainage efficiency, because more rock is exposed to the through-going fractures which are more likely to be intersected by a borehole.

Many hydrocarbon reservoirs are anticlines. This study has shown that one can expect the fracture density to decrease as one descends into an anticline due an expected decrease in the extensional strain levels, assuming no layer parallel slip. Towards the flanks of the structure, the strain anisotropy might increase, reducing the number of fracture orientations and decreasing fracture spacing. Oil saturated rocks have higher subcritical indices than brine or water saturated rocks. Therefore, if the structure were partially filled with oil, one would expect a decrease in subcritical index as one descends into the anticline. This results in an increase in fracture density with depth, since lower subcritical index patterns have higher fracture densities. Therefore, two opposing mechanisms exist as one descends into the center of an anticline: 1) an extensional strain decrease which decreases the fracture density, and 2) a subcritical index decrease which increases the fracture density. These effects should be evaluated on a case by case basis to see which mechanism is more important.

After creating the fracture model, it must be imported into the reservoir simulator (Fig. 5.1). However, prior to this step the output from the geomechanical model should be checked against core and outcrop data. Core data can give information on fracture aperture as well as give a rough estimate on fracture spacing. Similarly, outcrop data gives an indication of fracture spacing and possibly fracture length. If the model does not match the data, the input values and their bounds should be reexamined.

The level of detail provided by the geomechanical model greatly exceeds the level of detail normally used in reservoir simulation. Therefore, upscaling of the geomechanical patterns is necessary. This study has shown that different upscaling methods can lead to large variations in permeability prediction. Using a Local Grid

Refinement (LGR) around the well is recommended and will almost always improve production prediction accuracy. The exception to this rule is a well hydraulically linked to a highly connected fracture network. In such a case, the conventional dual permeability/dual porosity approach is just as accurate. Information necessary to maintain an LGR around the well can be difficult to obtain. The procedure of geomechanically generating a suite of patterns based on the most likely input parameters and simulating the end members will result in a well production prediction based on realistic geologic data, which should at least span the observed well production. This is preferred over the dual permeability/dual porosity approach which would be able to match the production data, but would not give a realistic representation of the fracture pattern, potentially having a large economic impact.

This study has shown that characterization of naturally fractured reservoirs is not a trivial exercise that can easily be automated. Fractures have a large influence on reservoir production and are inherently difficult to quantify. This study gives a robust and practical workflow to obtain a mechanically consistent naturally fractured reservoir model, without extensive sampling of the fracture network.

Appendices

APPENDIX A: STATIC YOUNG'S MODULUS

The general workflow to obtain a static Young's modulus (E_{stat}) curve is to use sonic data to create a dynamic Young's modulus (E_{dyn}) curve. This dynamic Young's modulus curve is transformed into a static Young's modulus curve through a static to dynamic Young's modulus transform, determined from core. Using the log data available in well 10 the dynamic Young's modulus values were calculated using:

$$E_{dyn} = 1.34 \times 10^{10} \left(\frac{\rho}{\Delta t_s^2} \right) \quad \text{Eq. A.1}$$

where ρ is the density in g/cm^3 and Δt_s is the shear travel time in μs/ft.

Since no sonic data was available in wells 8 and 4, a dynamic Young's modulus transform based on other logs, available in all 3 wells, was created. The logs used to create this transform were: depth in ft (D), caliper in inches (Cal), Gamma ray response in GAPI (Gr), and deep resistivity in Ωm ($Dres$). Marginally better fits were obtained when more log types were included (e.g. V-shale, water saturation, gas saturation). However, this smaller subset was preferred, because it consists of independent measurements, whereas a V-shale curve, for instance is a direct derivative of either the spontaneous potential curve or the gamma ray curve. Spontaneous potential curves were not available in all three wells and were therefore not used. Also, shallow resistivities were not used because well 10 was drilled with a water based mud while wells 4 and 8 were drilled with an oil based mud. The resulting transform for the dynamic Young's modulus is:

$$E_{dyn} = -1644686 + 443 \times D + 942328 \times \rho + 15267 \times Cal - 174078 \times Gr + 40279 \times Dres \quad \text{Eq. A.2}$$

This transform gives a close fit with the calculated dynamic Young's modulus calculated from the sonic log (Fig. A.1). Using this transform (Eq. A.2), continuous dynamic Young's modulus curves were created for wells 4 and 8.

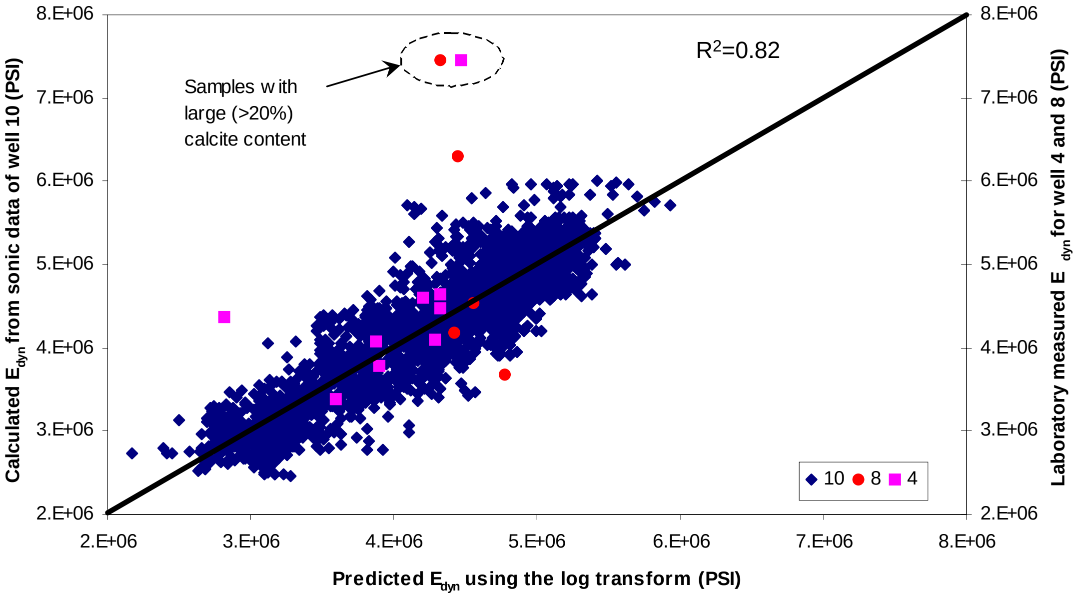

Figure A.1: Predicted dynamic Young's modulus using the log transform from eq. A.2 vs. either the calculated dynamic Young's modulus using the sonic data in well 10 or the measured dynamic Young's modulus from the lab for wells 4 and 8. A good correlation is obtained for all points except those laboratory samples, which contained large (>20%) amounts of calcite.

Using the laboratory measurements of static Young's modulus in wells 4 and 8 and the calculated dynamic Young's modulus values, a static to dynamic conversion was determined:

$$E_{stat} = 0.1844 \times E_{dyn} + 2 \times 10^{6} \quad \text{Eq. A.3}$$

Figure A.2 shows the obtained fit, where the two core samples containing a large (>20%) percentage of calcite were not included in the fit. A third point was not included in the fit because of its outlying position. It is currently unknown why this point forms an outlier. The static to dynamic Young's modulus fit is poor (Fig. A.2). Using the laboratory measurements of static Young's modulus produces a similarly poor fit, when the data of well 8 and 4 are combined. A possible reason for the poor fit is the high variability in sample type and the sparseness of the data set. Of the 9 samples from well 4, 3 are shale samples and one contains a large percentage of calcite (~21%). Of the 5 samples from well 8, one contains a large percentage of calcite (~29%) and one contains more than 50% clay. This creates 3 groups of samples, each with very few data points. Therefore, the fit is not improved if these sets are separated.

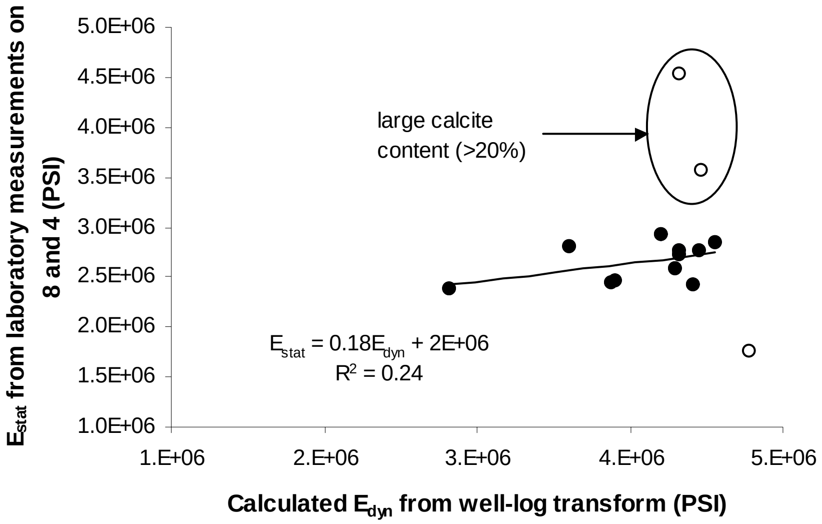

Figure A.2: Dynamic to static Young's modulus correlation. The solid circles delineate the points upon which the regression is based. The open circles are the outliers not incorporated in the correlation. The two outliers in the big oval have a large calcite (>20%) content explaining their outlying position. It is unclear why the third point is an outlier.

Utilizing the static to dynamic conversion of equation A.3, continuous static Young's modulus curves were constructed for all three wells (Fig. A.3). The static Young's modulus curves can easily be correlated from well to well as is outlined in Figure A.3. The resultant curves indicated that the static Young's modulus varies from approximately 2.6 MPsi (18000 MPa) to 2.9 MPsi (20000 MPa) with an average value of approximately 2.8 MPsi (19000 MPa).

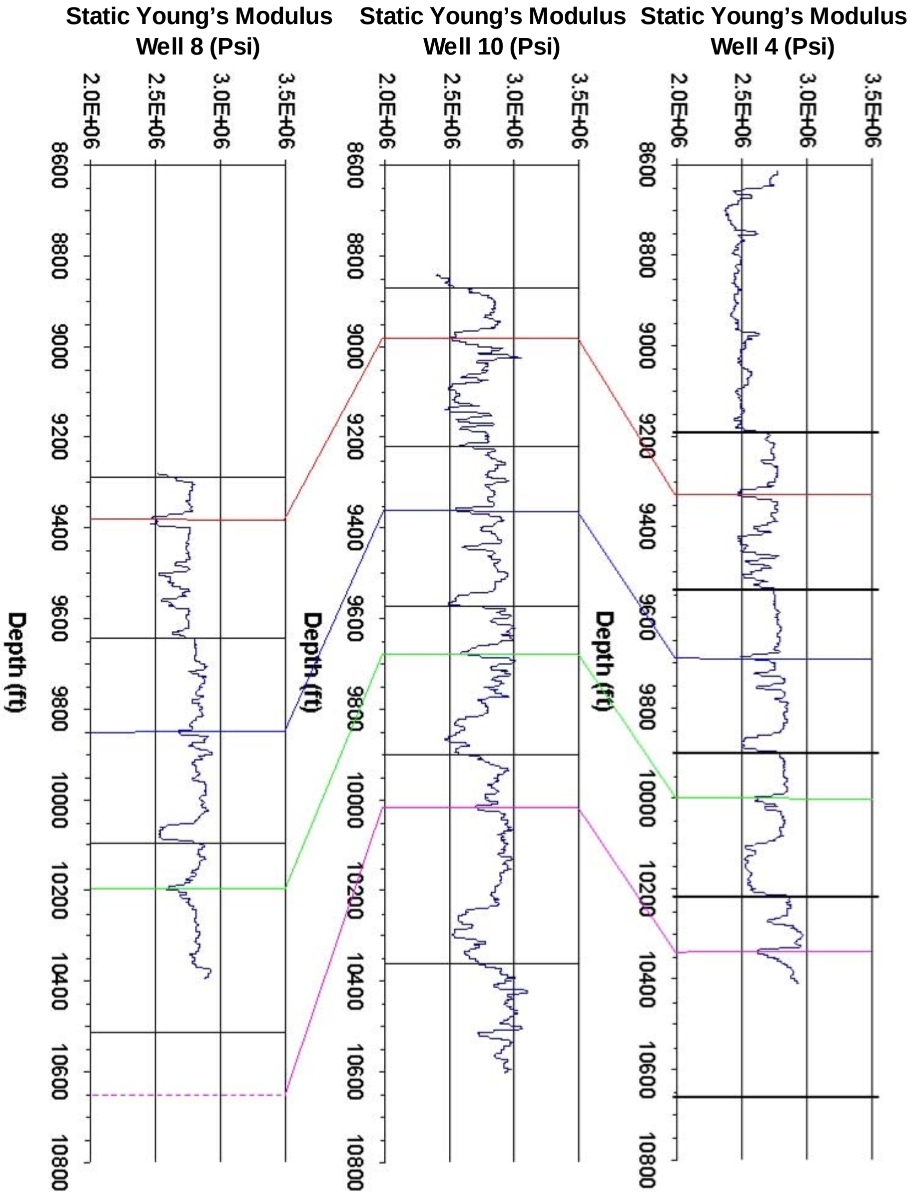

Figure A.3: Static Young's Modulus Curves for wells 8, 10 and 4. The black horizontal lines delineate the POR tops. The different colored lines show features, which correlate across the three wells.

APPENDIX B: STATIC POISSON'S RATIO

Similar to the static Young's modulus determination (Appendix A), the dynamic Poisson's ratio (ν_{dyn}) is determined through sonic log information from well 10 by using the following expression:

$$\nu_{dyn} = \frac{0.5 \times \left(\frac{\Delta t_s}{\Delta t_c} \right)^2 - 1}{\left(\frac{\Delta t_s}{\Delta t_c} \right)^2 - 1} \text{ .... Eq. B.1}$$

where Δt_c is the compressional wave travel time in μs/ft and Δt_s is the shear travel time in μs/ft.

To extrapolate the dynamic Poisson's ratio data to wells 8 and 4, a transform based on log data available in all 3 wells was constructed. For reasons described in the Young's modulus analysis (Appendix A), the following parameters were used to create the transform: depth in ft (*D*), caliper in inches (*Cal*), Gamma ray response in GAPI (*Gr*) and the deep resistivity in Ωm (*Dres*). The resulting transform for the dynamic Poisson's ratio is:

$$\nu_{dyn} = 0.6 - 6.5 \times 10^{-5} \times D + 0.1 \times \rho - 9.5 \times 10^{-3} \times Cal + 1.2 \times 10^{-4} \times Gr - 3.4 \times 10^{-3} \times Dres$$

.... Eq. B.2

This transform gives a reasonable fit to the calculated dynamic Poisson's ratio based on the shear and compressional wave velocity (Fig. B.1). Using this transform (Eq. B.2) continuous dynamic Poisson's ratio curves were created for wells 4 and 8.

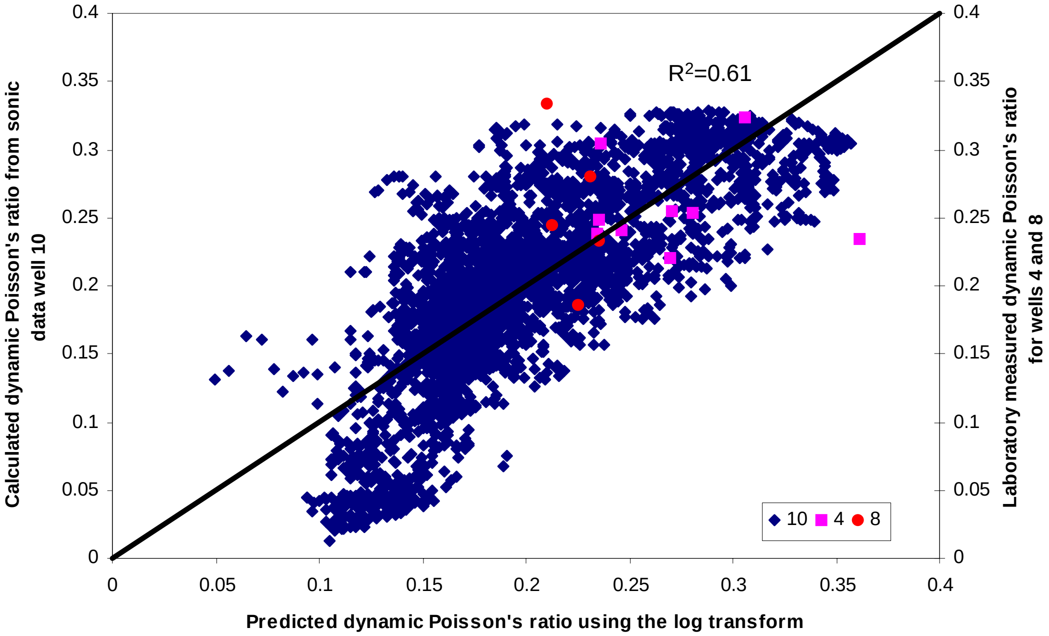

Figure B.1: Predicted dynamic Poisson's ratio using the log transform from eq. B.2 vs. either the calculated dynamic Poisson's ratio using the sonic data in well 10 or the measured dynamic Poisson's ratio in the laboratory for well 4 and 8. A reasonable correlation is obtained for all points.

Utilizing the laboratory measurements of static Poisson's ratio (ν_{stat}) in wells 4 and 8 and the calculated dynamic Poisson's ratio values, a static to dynamic conversion is determined:

$$\nu_{stat} = 0.4842 \times \nu_{dyn} + 0.0039 \quad \text{Eq. B.3}$$

Figure B.2 shows the obtained fit. One point is an obvious outlier and has not been incorporated in the fit. It is currently unclear why this point is an outlier. The static to dynamic Poisson's ratio fit is poor (Fig. B.2). Using the laboratory measurements of static Poisson's ratio and combining the data from well 8 and 4, produces an even worse fit. Similar to the analysis performed in Appendix A, a possible reason for the poor fit is the high variability in sample type and the sparseness of the data set. Of the 9 samples from well 4, 3 are shale samples and one contains a large percentage of calcite (~21%).

Of the 5 samples from well 8, one contains a large percentage of calcite (~29%) and one contains more than 50% clay. This creates 3 groups of samples each with very few data points. Therefore, the fit is not improved if these sets are separated.

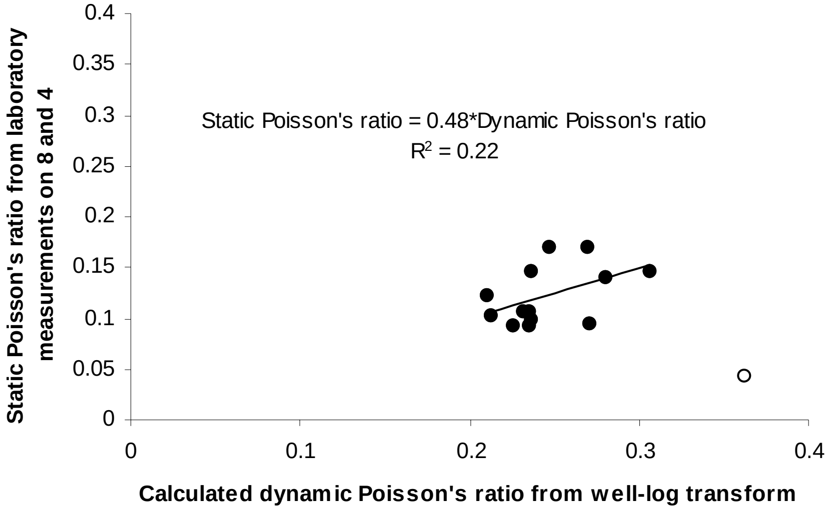

Figure B.2: Dynamic to static Poisson's ratio correlation. The solid circles delineate the points upon which the regression is based. The open circle is the outlier, which has not been incorporated in the linear regression fit.

Equation B.3 allows for creation of continuous static Poisson's ratio curves in wells 10, 4 and 8 (Fig. B.3). Figure B.3 shows that correlation of Poisson's ratio across beds/mechanical layers is not as clear as for the static Young's modulus logs (Fig. A.3). This is attributed to the relatively high scatter in the static to dynamic Poisson's ratio conversion. Figure B.3 shows that the Poisson's ratio varies from approximately 0.1 to 0.19 with an average value of 0.12.

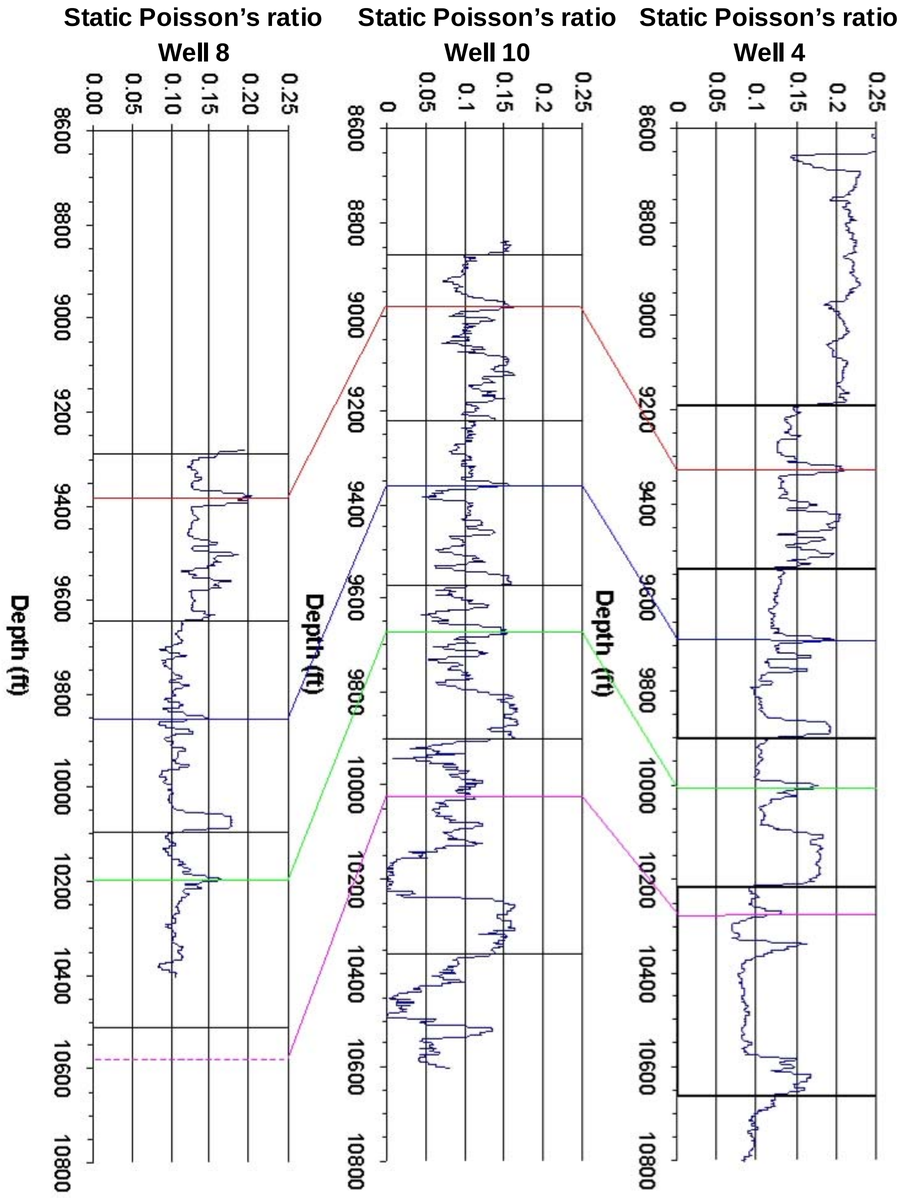

Figure B.3: Static Poisson's ratio curves for wells 8, 10 and 4. The black horizontal lines delineate the POR tops. The different colored lines show features, which correlate, across the three wells.

APPENDIX C: BED THICKNESS

Establishing a correct bed thickness is important for fracture growth prediction. Strong correlations exist between mechanical bed thickness and fracture spacing, where thicker beds exhibit larger fracture spacing (e.g. Pollard and Segall, 1987; Narr and Suppe, 1991; Gross, 1993). Fracture spacing is controlled by the size of the stress shadow created by a fracture (Pollard and Segall, 1987), where taller fractures create larger stress shadows than shorter fractures. In this stress shadow no joints can grow, resulting in larger fracture spacing values in thicker beds. This mechanical bed thickness dependence has also been observed in the POR reservoir (Fig 3.3).

In the fracture pattern simulator, only one value of Young's modulus is used per simulation/bed. Therefore, static Young's modulus curves are used to determine mechanical bed thickness. The static Young modulus curves closely follow the reservoir lithology, where sandstones have a higher static Young's modulus than shales. Since no continuous static Young's modulus curves are available for the 4th POR in well 8 only a close-up of the 2nd POR is shown (Fig. C.1). However, from the existing Young's modulus curves in well 10 and 4, I estimate that the average bed height of the 4th POR is larger than that of the 2nd POR. The bed height determined for the 2nd POR ranges from 6 ft to about 120 ft with an average of about 27 ft (Fig C.1). These bed heights are believed to be upper limits of the true mechanical bed height present in the POR reservoir. Numerical modeling of the Austin Chalk and outcrop observations have shown that shale layers on the order of centimeters are able to stop fractures on the order of meters (Rijken and Cooke, 2001). Therefore, shale beds which arrest fracture height growth, are most probably below the resolution of the well-logs. This idea is further corroborated by FMI from 10, which shows that fractures are mainly contained within their sandstone beds and that fracture heights are maximally on the order of several feet (maximum fracture height in 10 is ~5 ft). Figure C.1 also shows smaller mechanical bed thickness in well 10 than in wells 4 and 8. This indicates that mechanical layer thickness is not constant over the area of interest.

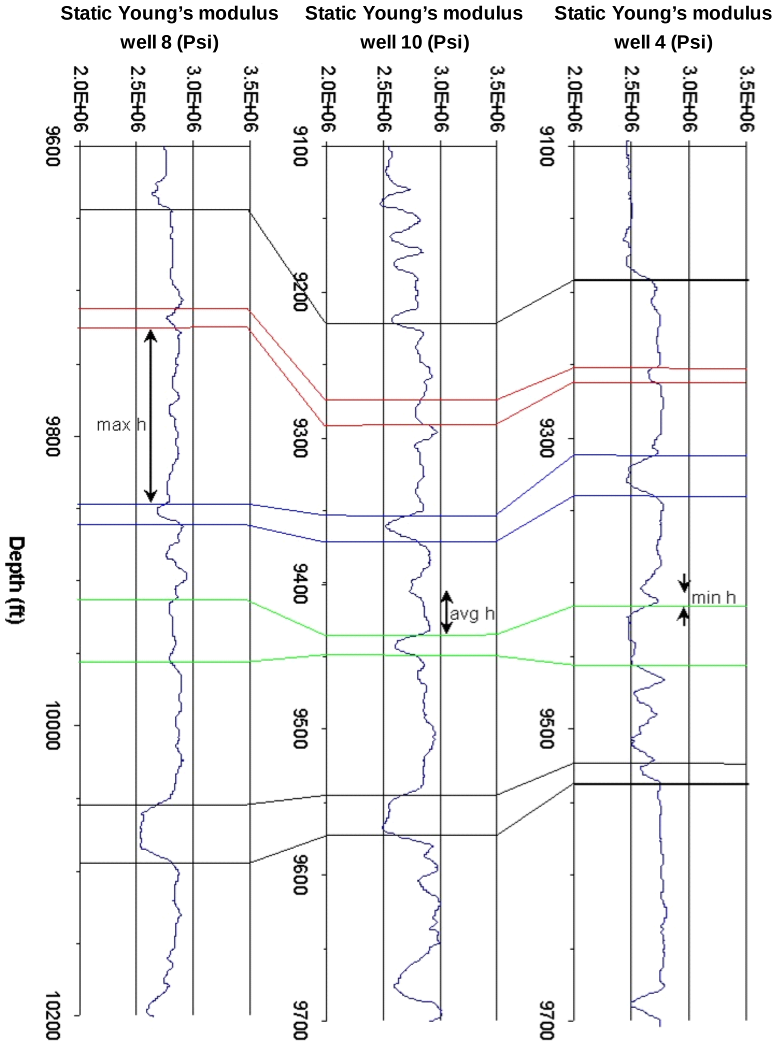

Figure C.1: Static Young's modulus curves for wells 10, 4 and 8 showing only the 2nd POR reservoir interval. The horizontal lines of differing color correlate beds across these three wells. The subdivisions shown here is the coarsest mechanical stratigraphy of the 2nd POR. The minimum maximum and average bed heights are delineated on the well logs and are determined to be 6 ft, 27 ft and 120 ft.

APPENDIX D: SUBCRITICAL INDEX

Chapter 2 discusses the average subcritical index changes dependent on the chemical environment and rock type. A summary of the subcritical indices (*n*) for the POR reservoir is given in tables D.1. For each sample, Table D.1 specifies from which POR reservoir the sample was taken. For numerical modeling, 3 subcritical index values are used: 20, 40 and 80. Values of 20 and 40 seem most reasonable for the POR reservoirs. A subcritical index of 80 would correspond to a calcite concretion, which sometimes form layer like features. An average value for the subcritical index for the 2nd POR reservoir is estimated to be approximately 30. This value is determined by averaging all the measurements in aqueous conditions. For the 4th POR reservoir the obtained average value is 35. This assumes that fracturing occurred prior to hydrocarbon migration. If fracturing occurred after hydrocarbon migration, the expected average subcritical index value for the 2nd POR reservoir would be 54 and 41 for the 4th POR reservoir.

Table D.1: Subcritical index values for the POR reservoir.

Sample number	Well	Depth (ft)	POR Member	Subcritical index			
				Air	Wet	Brine	Oil
1	10	9025.8 - 9026.3	POR1	45 ± 2	29 ± 2	38 ± 2	53 ± 2
2	10	9038.8 - 9039.3	POR1	44 ± 3	28 ± 3	35 ± 3	47 ± 3
3	10	9239.4 - 9239.9	POR2	52 ± 5	24 ± 2	40 ± 3	52 ± 6
4	10	9615.8 - 9616.3	POR3	20 ± 4			
5	10	10033.9 - 10034.4	POR4	41 ± 3	37 ± 5	33 ± 4	41 ± 3
6	8	9771.9 - 9773	POR2	34 ± 6	23 ± 4	22 ± 3	41 ± 4
7	8	9804 - 9804.7	POR2	45 ± 4		29 ± 9	46 ± 2
8	4	9707.7 - 9708.4	POR2	54 ± 2	30 ± 3	36 ± 3	49 ± 3
9	4	9710.6 - 9711.5	POR2	82 ± 9	27 ± 2	26 ± 2	74 ± 7
10	4	9738.8 - 9739.3	POR2	53 ± 3		40 ± 1	63 ± 2

APPENDIX E: INFLUENCE OF YOUNG'S MODULUS AND POISSON'S RATIO ON FRACTURE PATTERN DEVELOPMENT

Simulation results for a different strain anisotropy (Fig. E.1), bed height (Fig. E.2), and subcritical index (Fig. E.3) as compared to Figure 3.4, show that variation of these parameters result in different fracture patterns. However, no significant changes in the fracture pattern characteristics are observed due to variations in Young's modulus and Poisson's ratio.

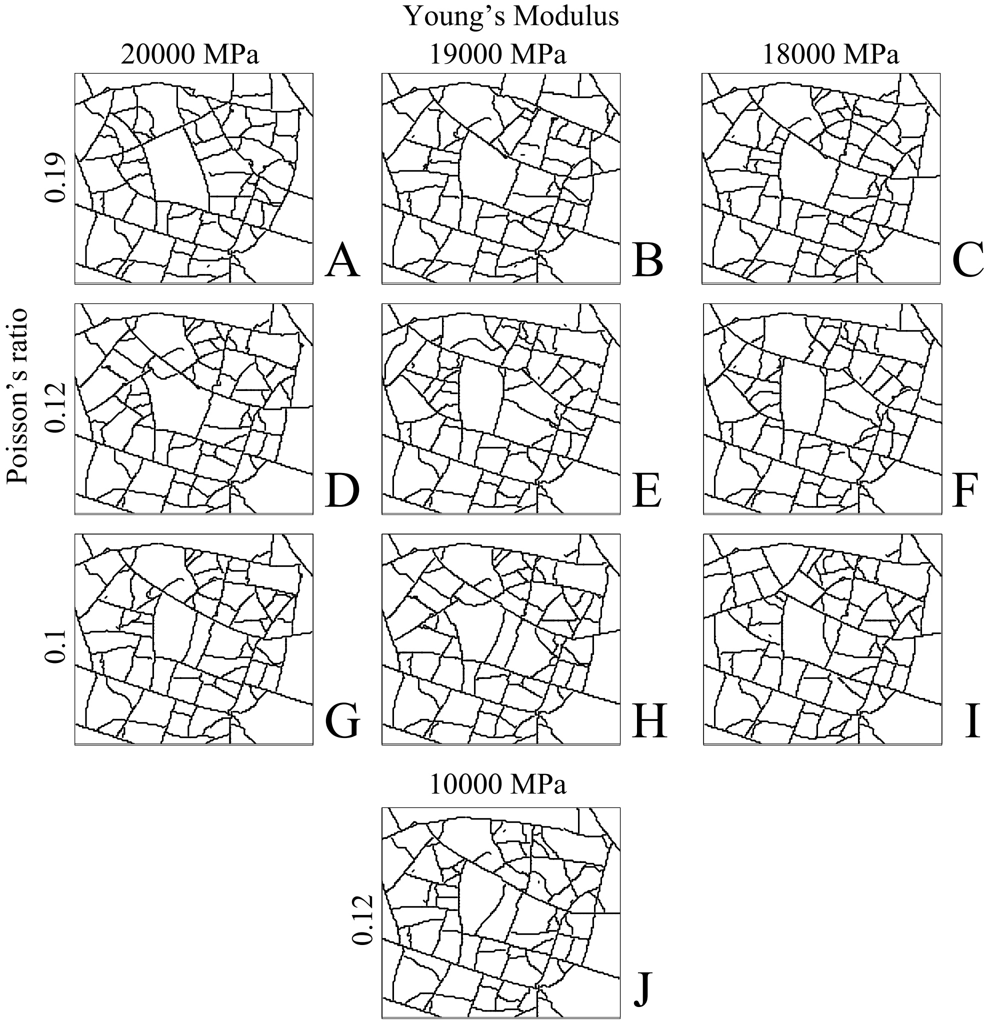

Figure E.1: Plan view of fracture patterns simulated using a 0.03% isotropic strain, a bed thickness of 2 m, a subcritical index of 20, a time of 24 million years with a varying Young's modulus (i.e. 18000, 19000 and 20000 MPa) and Poisson's ratio (i.e. 0.1, 0.12, and 0.19). Pattern J was generated using a much lower Young's modulus (10000 MPa) simulating fracturing occurring earlier in time, when the sediment has not been fully consolidated. The resulting fracture patterns are almost identical (A through J).

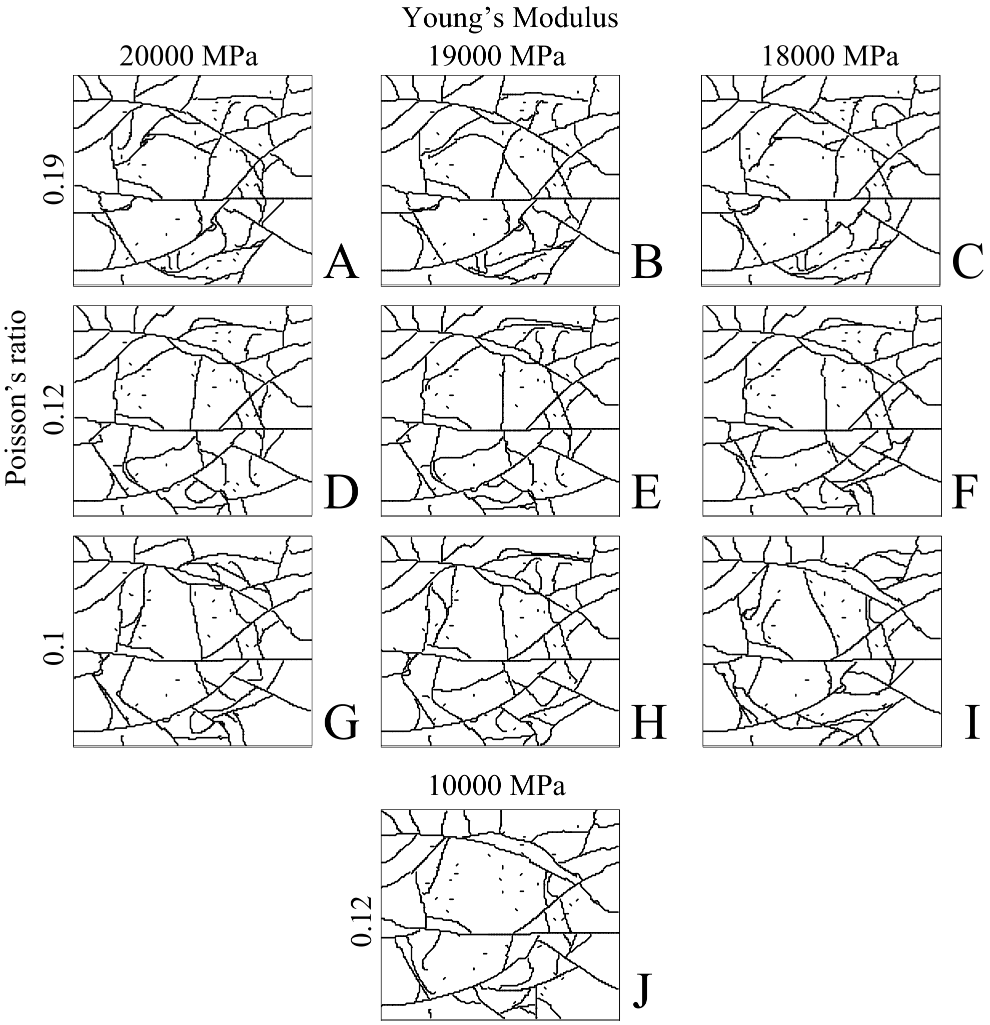

Figure E.2: Plan view of fracture patterns simulated using a 0.03% strain in the y-direction and a 0.01% strain in the x-direction, a bed thickness of 9 m, a subcritical index of 20, a time of 24 million years with a varying Young's modulus (i.e. 18000, 19000 and 20000 MPa) and Poisson's ratio (i.e. 0.1, 0.12, and 0.19). Pattern J was generated using a much lower Young's modulus (10000 MPa) simulating fracturing occurring earlier in time, when the sediment has not been fully consolidated. The resulting fracture patterns are almost identical (A through J).

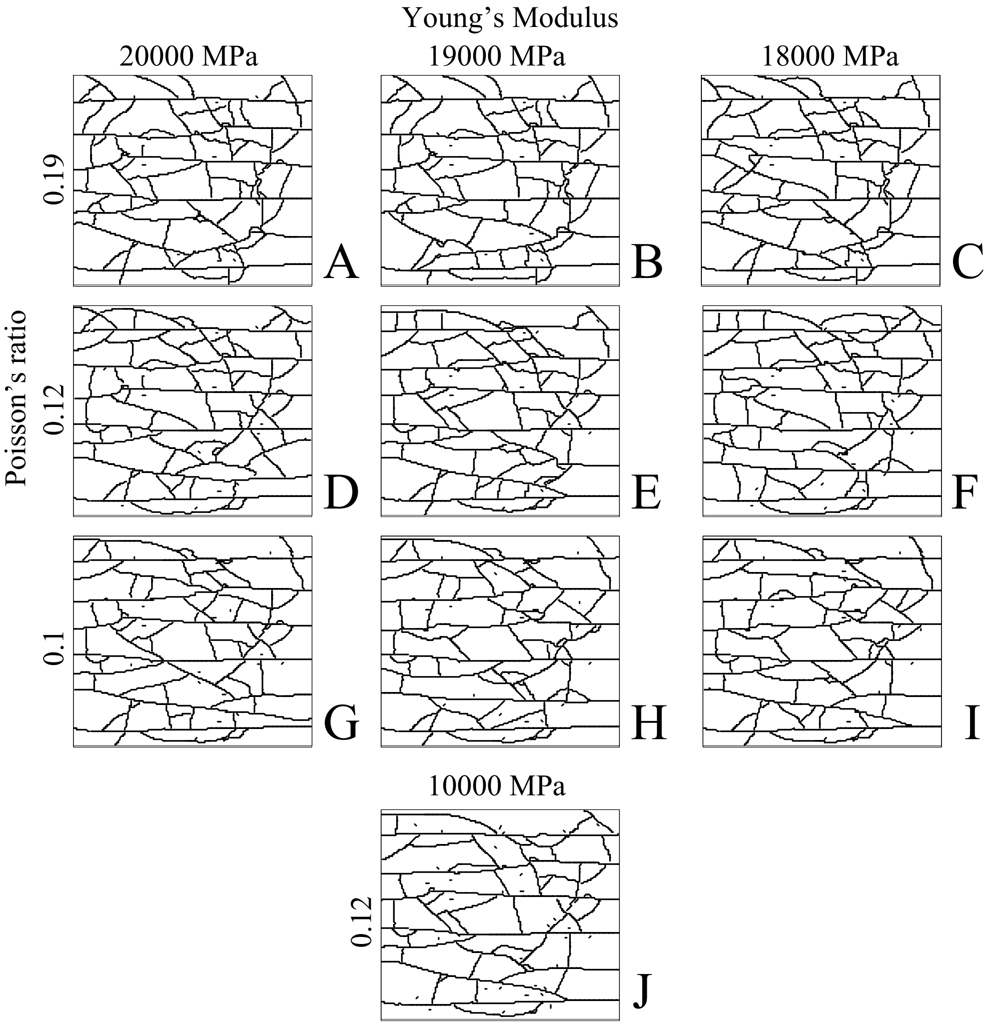

Figure E.3: Plan view of fracture patterns simulated using a 0.03% strain in the y-direction and a 0.01% strain in the x-direction, a bed thickness of 2 m, a subcritical index of 40, a time of 24 million years with a varying Young’s modulus (i.e. 18000, 19000 and 20000 MPa) and Poisson’s ratio (i.e. 0.1, 0.12, and 0.19). Pattern J was generated using a much lower Young’s modulus (10000 MPa) simulating fracturing occurring earlier in time, when the sediment has not been fully consolidated. The resulting fracture patterns are almost identical (A through J).

References

Aguilera, R., 1980, *Naturally Fractured Reservoirs,* The Petroleum Publishing Company, Tulsa, Oklahoma, 703 p.

Anderson, T.L., 1995, *Fracture Mechanics, Fundamentals and Applications,* 2nd edition, CRC Press, Boca Raton, 688 p.

Anderson, O.L., and Grew, P.C., 1977, Stress Corrosion Theory of Crack Propagation with Applications to Geophysics, *Reviews of Geophysics and Space Physics,* Vol. 15, No. 1, February, p. 77-104.

Andersson, J., and Dverstorp, B., 1987, Conditional Simulations of Fluid Flow in Three-Dimensional Networks of Discrete Fractures, *Water Resources Research,* Vol. 23, No. 10, p. 1876-1886.

Atkinson, B.K., 1979, A Fracture Mechanics Study of Subcritical Tensile Cracking of Quartz in Wet Environments, *Pure and Applied Geophysics,* Vol. 117, No. 5, p. 1011-1024.

Atkinson, B.K., 1980, Stress Corrosion and the Rate-Dependent Tensile Failure of a Fine-Grained Quartz Rock, *Tectonophysics,* Vol. 65, p. 281-290.

Atkinson, B.K., 1982, Subcritical Crack Propagation in Rocks: Theory, Experimental Results and Applications, *Journal of Structural Geology,* Vol. 4, No. 1, p. 41-56.

Atkinson, B.K., 1984, Subcritical Crack Growth in Geological Materials, *Journal of Geophysical Research*, Vol. 89, No. B6, p. 4077-4114.

Atkinson, B.K., and Meredith, P.G., 1981, Stress Corrosion Cracking of Quartz: a Note on the Influence on Chemical Environment, *Tectonophysics,* Vol. 77, p. T1-T11.

Atkinson, B.K., and Rawlings, R.D., 1981, Acoustic Emission During Stress Corrosion Cracking in Rocks, *Maurice Ewing Series, Earthquake Prediction; an International Review,* Editors: Simpson, D.W., and Richards, P.C., American Geophysical Union, Issue 4, p. 605-616.

Atkinson, B.K., and Meredith, P.G., 1987a, The Theory of Subcritical Crack Growth with Applications to Minerals and Rocks, *In: Fracture Mechanics of Rock*, Editor: Atkinson, B.K., Academic Press Geology Series, p. 111-166.

Atkinson, B.K., and Meredith, P.G., 1987b, Experimental Fracture Mechanics Data for Rocks and Minerals, *In: Fracture Mechanics of Rock*, Editor: Atkinson, B.K., Academic Press Geology Series, p. 477-525.

Atkinson, B .K, Price, N.J., Dennis, S.M., Meredith, P.G., and Holloway, R.F., 1980, Mechanisms of Fracture and Friction of Crustal Rocks in Simulated Geological Environments, *Semi-annual Technical Report to the Managers of U.S. National Earthquake Hazards Reduction Program,* Contract no.: 14-08-0001-18325, U.S. Geological Survey, Menlo Park, CA.

Atkinson, B.K., Dennis, S.M., Meredith, P.G., and Zheng, J., 1984a, Stress Corrosion and Microseismic Activity During Tensile, Shear and Compressive Failure of Rocks, *Final Technical Report to the Managers of the U.S. National Earthquake Hazard Reduction Program,* Contract no.: 14-08-0001-21287. U.S. Geological Survey, Menlo Park, CA.

Atkinson, B.K., MacDonald, D., and Meredith, P.G., 1984b, Acoustic Response and Fracture Mechanics of Granite Subjected to Thermal and Stress Cycling Experiments, *Proceedings of the Third Conference; Acoustic Emission/Microseismic Activity in Geologic Structures and Materials*, Editors: Hardy, H.R., Jr., and Leighton, F.W., p. 5-18.

Bai, T., and Pollard, D.D., 2000, Fracture Spacing in Layered Rocks: a New Explanation Based on the Stress Transition, *Journal of Structural Geology,* Vol. 22, p. 43-57.

Barenblatt, G.I., and Zheltov, Y.P., 1960, On Fundamental Equations of Flow of Homogeneous Liquids in Naturally Fractured Rocks, *Dokl. Akad. Nauk. SSSR,* Vol. 132, No. 3, p. 545-548. (in Russian)

Bear, J., 1972, *Dynamics of Fluid Flow in Porous Media,* Environmental Science Series, American Elsevier Publishing Company, New York, p. 19-20.

Bear, J., 1993, Modeling Flow and Contaminant Transport in Fractured Rocks, *In: Flow and Contaminant Transport in Fractured Rock,* Editors: Bear, J., Tsang, C.F., and Marsily, G., Academic Press, New York, p. 1-37.

Beaudoin, J.J., 1985a, Effect of Humidity on Subcritical Crack Growth in Cement Paste, *Cement and Concrete Research,* Vol. 15, p. 871-878.

Beaudoin, J.J., 1985b, Effect of Water and Other Dielectrics on Subcritical Crack Growth in Portland Cement Paste, *Cement and Concrete Research,* Vol. 15, p. 988-994.

Beaudoin, J.J., 1987, Subcritical Crack Growth in Low-Porosity Cement Systems, *Journal of Materials Science Letters,* Vol. 6, No. 2, February, p. 197-199.

Becker, A., and Gross, M.R., 1996, Mechanism for Joint Saturation in Mechanically Layered Rocks: an Example from Southern Israel, *Tectonophysics,* Vol. 257, p. 223-237.

Berkowitz, B., 1995, Analysis of Fracture Network Connectivity Using Percolation Theory, *Mathematical Geology,* Vol. 27, No. 4, p. 467-483.

Bhatnagar, A., Hoffman, M.J., and Dauskardt, R.H., 2000, Fracture and Subcritical Crack-Growth Behavior of Y-Si-Al-O-N Glasses and Si_3N_4 Ceramics, *Journal of American Ceramic Society,* Vol. 83, No. 3, p. 585-596.

Bogdanov, A.A., 1947, The Intensity of Cleavage as Related to the Thickness of Beds, *Soviet Geology,* Vol. 16, p. 102-104.

Bouwer, H., 1969, Planning and Interpreting Soil Permeability Measurements, *Journal of the Irrigation and Drainage Division of the A.S.C.E.,* IE(3), p. 391-402.

Brace, W.F., 1980, Permeability of Crystalline and Argillaceous Rocks, *International Journal of Rock Mechanics, Mining Science & Geomechanics Abstracts*, Vol. 17, p. 241-251.

Charles, R.J., 1958a, Static Fatigue of Glass I, *Journal of Applied Physics,* Vol. 29, No. 11, p. 1549-1553.

Charles, R.J., 1958b, Static Fatigue of Glass II, *Journal of Applied Physics,* Vol. 29, No. 11, p. 1554-1560.

Charles, R.J., and Hillig, W.B., 1961, The Kinetics of Glass Failure by Stress Corrosion, *In: Symposium on Mechanical Strength of Glass and Ways of Improving It*, Union Scientifique Continentale due Verre, Charleroi, Belgium, p. 511-527.

Cheema, T., Al-Harthy, A., Al-Aghbari, M., and Al-Aufi, M., 2004, Influence of Grain Size and Mineralogy on the Strength of Weak Rocks, *Geotechnical Practice Publication*, Vol. 1, p. 239-249.

Chen, Z.-X, 1989, Transient Flow in Slightly Compressible Fluids Through Double-Porosity, Double-Permeability Systems – A State-of-the-Art Review, *Transport in Porous Media,* Vol. 4, p. 147-184.

Chen, Z.-X., 1990, Analytical Solutions for Double-Porosity, Double-Permeability and Layered Systems, *Journal of Petroleum Science and Engineering,* Vol. 5, p. 1-24.

Clauser, C., 1992, Permeability of Crystalline Rocks, *EOS, Transactions, American Geophysical Union,* Vol. 73, No. 21, p. 233-236.

Clifton, M.P., and Neuman, S.P., 1982, Effect of Kriging and Inverse Modeling on Conditional Simulation of the Avra Valley Aquifer in Southern Arizona, *Water Resources Research*, Vol. 18, No. 4, p. 1215-1234.

Cook, R.F., and Liniger, E.G., 1993, Kinetics of Indentation Cracking in Glass, *Journal of the American Ceramic Society,* Vol. 76, No. 5, p. 1096-1105.

Costin, L.S., and Mecholsky, J.J., 1983, Time Dependent Crack Growth and Failure in Brittle Rock, *Proceedings of the 24th U.S. Symposium on Rock Mechanics; Theory, Experiment, Practice*, Editor: Mathewson, C.C., p. 385-394.

Crampin, S., 1987, Geological and Industrial Implications of Extensive-Dilatancy Anisotropy, *Nature*, Vol. 328, p. 491-496.

Crampin, S., and Lovell, J.H., 1991, A Decade of Shear-Wave Splitting in the Earth's Crust: What Does It Mean? What Use Can We Make of It? And What Should We Do Next?, *Geophysical Journal International*, Vol. 107, p. 387-407.

Crouch, S.L., and Starfield, A.M., 1983, *Boundary Element Methods in Solid Mechanics,* George Allen & Unwin Ltd., London, 322 p.

Dagan, G., 1982, Analysis of Flow through Heterogeneous Random Aquifers, 2: Unsteady Flow in Confined Formations, *Water Resources Research*, Vol. 18, p. 1571-1585.

Dagan, G., 1985, Stochastic Modeling of Groundwater Flow by Unconditional and Conditional Probabilities, 2: The Inverse Problem, *Water Resources Research*, Vol. 21, No. 1, p. 65-72.

Da Prat, G., 1980, *Well Test Analysis for a Naturally Fractured Reservoir,* Ph.D. Thesis, Stanford University, California.

Da Prat, G., 1990, *Well Test Analysis for Fractured Reservoir Evaluation, Developments in Petroleum Science 17*, Editor: Chilingarian, G.V., Elsevier, Amsterdam, 210 p.

Da Prat, G., Ci.nco-Ley, H., and Ramey, H.J., Jr., 1981, Decline Curve Analysis using Type Curves for Two-Porosity Systems, *Society of Petroleum Engineers,* p. 354-362.

Darot, M., and Gueguen, Y., 1986, Slow Crack Growth in Minerals and Rocks: Theory and Experiments, *Pure and Applied Geophysics,* Vol. 124, No. 4/5, p. 677-692.

Delaney, P.T., and Pollard, D.D., 1981, Deformation of Host Rocks and Flow of Magma During Growth of Minette Dikes and Breccia-Bearing Intrusions near Ship Rock, New Mexico, *U.S. Geological Survey Professional paper,* No. 1202, 61 p.

Dershowitz, W.S., and Einstein, H.H., 1988, Characterizing Rock Joint Geometry with Joint System Models, *Rock Mechanics and Rock Engineering,* Vol. 21, p. 21-51.

Desbarats, A.J., 1992, Spatia Averaging of Hydraulic Conductivity in Three-Dimensional Heterogeneous Porous Media, *Math. Geology,* Vol. 24, No. 3, p. 249-267.

Draper, N.R., and Smith, H., 1981, *Applied Regression Analysis,* 2nd Edition, John Wiley & Sons, p. 307-311.

Durlofsky, L.J., 1991, Numerical Calculation of Equivalent Grid Block Permeability Tensors for Heterogeneous Porous Media, *Water Resources Research,* Vol. 27, No. 5, p. 699-708.

Durlofsky, L.J., and Chung, E.Y., 1990, Effective Permeability of Heterogeneous Reservoir Regions, *2nd European Conference on the Mathematics of Oil Recovery,* Paris, p. 57-64.

Dverstorp, B., and Andersson, J., 1989, Application of the Discrete Fracture Network Concept with Field Data: Possibilities of Model Calibration and Validation, *Water Resources Research,* Vol. 25, No. 3, p. 540-550.

Eberhardt, E., Stimpson, B., and Stead, D., 1999, Effects of Grain Size on the Initiation and Propagation Thresholds of Stress-Induced Brittle Fractures, *Rock Mechanics and Rock Engineering*, Vol. 32, No. 2, p. 81-99.

Evans, A.G., 1972, A Method for Evaluating the Time-Dependent Failure Characteristics of Brittle Materials – and Its Application to Polycrystalline Alumina, *Journal of Materials Science,* Vol. 7, p. 1137-1146.

Evans, A.G., Linzer, M., and Russell, L.R., 1974, Acoustic Emission and Crack Propagation in Polycrystalline Alumina, *Materials Science and Engineering,* Vol. 15, No. 2-3, p. 253-261.

Fetkovich, M.J., 1980, Decline Curve Analysis Using Type Curves, *Society of Petroleum Technology,* June, p. 1065-1077.

Flodin, E.A., Durlofsky, L.J., and Aydin, A., 2004, Upscaled Models of Flow and Transport in Faulted Sandstone: Boundary Condition Effects and Explicit Fracture Modeling, *Petroleum Geoscience,* Vol. 10, p. 173-181.

Fouché, O., and Diebolt, J., 2004, Describing the Geometry of 3D Fracture Systems by Correcting for Linear Sampling Bias, *Mathematical Geology,* Vol. 36, No. 1, p. 33-63.

Freiman, S.W., 1984, Effects of Chemical Environment on Slow Crack Growth in Glasses and Ceramics, *Journal of Geophysical Research,* Vol. 89, No. B6, p. 4072-4076.

Freiman, S.W., McKinney, K.R., and Smith, H.L., 1974, Slow Crack Growth in Polycrystalline Ceramics, *Fracture Mechanics of Ceramics Volume 2,* Editors: Bradt, R.C., Hasselman, D.P.H., and Lange, F.F., Plenum Press, New York, p. 659-676.

Gesing, A.J., and Bradt, R.C., 1983, A Micocracking Model for the Effect of Grain Size on Slow Crack Growth in Polycyrstalline Al_2O_3, *Fracture Mechanics of Ceramics Volume 5,* Editors: Bradt, R.C., Evans, A.G., Hasselman, D.P.H., and Lange, F.F., Plenum Press, New York, p. 569-590.

Grenet, L., 1899, Mechanical Strength of Glass, *Bull. Soc. Enc. Industr. Nat. Paris,* Serie 5, No. 4, p. 838-848.

Golf-Racht, T.D. van, 1982, *Fundamentals of Fractured Reservoir Engineering, Developments in Petroleum Science 12,* Elsevier, Amsterdam, 710 p.

Gómez-Herenández, J.J., 1990, Simulation of Block Permeabilities Conditioned upon Data Measured at a Different Scale. In: *ModelCARE 90: Calibration and Reliability in Groundwater Modeling,* IAHS, Publ. No. 195, p. 407-416.

Gómez-Herenández, J.J., 1991, *A Stochastic Approach to the Simulation of Block Conductivity Fields Conditioned upon Data Measured at a Smaller Scale,* Ph.D. Thesis, Stanford University, CA.

Griffith, A.A., 1921, The Phenomena of Rupture and Flow in Solids, *Philosophical Transactions of the Royal Society of London, Series A, Containing Papers of a Mathematical or Physical Character,* Vol. 221, p. 163-198.

Griffith, A.A., 1924, The Theory of Rupture, *Proceedings of the First International Congress for Applied Mechanics,* Delft, p. 55-63.

Gross, M.R., 1993, The Origin of Cross Joints: Examples from the Monterey Formation, Santa Barbara Coastline, California, Journal of Structural Geology, Vol. 15, No. 6, p. 737-751.

Gross, M.R. and Engelder, T., 1995, Strain Accommodated by Brittle Failure in Adjacent Units of the Monterey Formation, U.S.A.: Scale Effects and Evidence for Uniform Displacement Boundary Conditions, *Journal of Structural Geology,* Vol. 17, p. 1303-1318.

Gross, M.R., Fischer, M.P., Engelder, T., and Greenfield, R.J., 1995, Factors Controlling Joint Spacing in Interbedded Sedimentary Rocks: Integrating Numerical Models with Field Observations from the Monterey Formation, USA, *From: Fractography: Fracture Topography as a Tool in Fracture Mechanics and Stress Analysis,* Editor: Ameen, M.S, Geological Society Special Publication No. 92, p. 215-233.

Gudmundsson, A., 2000, Fracture Dimensions, Displacement and Fluid Transport, *Journal of Structural Geology,* Vol. 22, p. 1221-1231.

Hillig, W.B., and Charles, R.J., 1964, Surfaces, Stress-Dependent Surface Reactions, and Strength, *Chapter 17 in: High-Strength Materials,* Editor: Zackay, V.F., John Wiley & Sons, New York, Proceedings of the Second Berkeley International Materials Conference, p. 682-705.

Hobbs, D.W., 1967, The Formation of Tension Joints in Sedimentary Rocks: An Explanation, *Geological Magazine,* Vol. 104, No. 6, p. 550-556.

Hoeksema, R.J., and Kitanidis, P.K., 1984, An Application of the Geostatistical Approach to the Inverse Problem in Two-Dimensional Groundwater Modeling, *Water Resources Research*, Vol. 20, No. 7, p. 1003-1020.

Hoeksema, R.J., and Kitanidis, P.K., 1985, Comparison of Gaussian Conditional Mean and Kriging Estimation in the Geostatistical Solution of the Inverse Problem, *Water Resources Research,* Vol. 21, No. 6, p. 825-836.

Holden, L., Hoiberg, J., and Lia, O., 1989, Homogenization of Absolute Permeability, *Norwegian Computer Centre (NCC), report.*

Holder, J., Philip, Z., and Olson, J., 1999, Experimental Study of Subcritical Crack Growth in Porous Rock, *EOS, Transactions, American Geophysical Union,* Vol. 80, No. 46, Suppl., p. 1036.

Holder, J., Olson, J.E., and Philip, Z., 2001, Experimental Determination of Subcritical Crack Growth Parameters in Sedimentary Rock, *Geophysical Research Letters,* Vol. 28, No. 4, p. 599-602.

Huang, Q., and Angelier, J., 1989, Fracture Spacing and Its Relation to Bed Thickness, *Geological Magazine,* Vol. 126, p. 355-362.

Ito, S., and Tomozawa, M., 1982, Crack Blunting of High-Silica Glass, *Journal of the American Ceramic Society*, Vol. 65, No. 8, p. 368-371.

Jaeger, J.C., and Cook, N.G.W., 1979, *Fundamentals of Rock Mechanics,* 3rd edition, Chapman and Hall Ltd., London, 593 p.

Ji, S., and Saruwatari, K., 1998, A Revised Model for the Relationship between Joint Spacing and Layer Thickness, *Journal of Structural Geology,* Vol. 20, p. 1495-1508.

Jourde, H., Flodin, E.A., Aydin, A., Durlofsky, L.J., and Wen, X.-H., 2002, Computing Permeability of fault zones in Aeolian Sandstone from Outcrop Measurements, *American Association of Petroleum Geologists Bulletin,* Vol. 86, p. 1187-1200.

Kasap, E., and Lake, L.W., 1990, Calculating the Effective Permeability Tensor of a Gridblock, *Society of Petroleum Engineers Formation Evaluation*, SPE 18434, June, p. 192-200

Kazemi, H., 1969, Pressure Transient Analysis of Naturally Fractured Reservoirs with Uniform Fracture Distribution, *Society of Petroleum Engineers Journal,* SPE 2156A, p. 451-462.

Kazemi, H., Merrill, L.S. Jr., Porterfield, K.L., and Zeman, P.R., 1976, Numerical Simulation of Water-Oil Flow in Naturally Fractured Reservoirs, *Society of Petroleum Engineers Journal,* SPE 5719, p. 317-326.

Kies, J.A., and Clark, A.B.J., 1969, Fracture Propagation Rates and Times to Fail Following Proof Stress in Bulk Glass, *Fracture: Proceedings of the Second International Conference on Fracture,* Brighton, April, p. 483-491.

Kirby, S.H., 1984, Introduction and Digest to the Special Issue on Chemical Effects of Water on the Deformation and Strengths of Rocks, *Journal of Geophysical Research,* Vol. 89, No. B6, p. 3991-3995.

Kulatilake, P.H.S.W., and Panda, B.B., 2000, Effect of Block Size and Joint Geometry on Jointed Rock Hydraulics and REV, *Journal of Engineering Mechanics,* Vol. 126, No. 8, p. 850-858.

Kunkel, J.R., Way, S.C., and McKee, C.R., 1988, Comparative Evaluation of Selected Continuum and Discrete-Fracture Models, *US Nuclear Regulatory Commission,* NUREG/CR-5240.

Lachenbruch, A.H., 1961, Depth and Spacing of Tension Cracks, *Journal of Geophysical Research,* Vol. 66, p. 4273-4292.

Laubach, S.E., 1988, Subsurface Fractures and Their Relationship to Stress History in East Texas Basin Sandstone, *Tectonophysics*, Vol. 156, p. 37-49.

Laubach, S.E., 1997, A Method to Detect Natural Fracture Strike in Sandstones, *American Association of Petroleum Geologists Bulletin,* Vol. 81, No. 4, p. 604-623.

Laubach, S.E., 2003, Practical Approaches to Identifying Sealed and Open Fractures, *American Association of Petroleum Geologists Bulletin,* Vol. 87, No. 4, p. 561-579.

Laubach, S.E., Marrett, R.A., Olson, J.E., and Scott, A.R., 1998, Characteristics and Origins of Coal Cleat: A Review, *International Journal of Coal Geology,* Vol. 35, p. 175-207

Laubach, S., Marrett, R., and Olson, J., 2000, New Directions in Fracture Characterization, *The Leading Edge,* Vol. 19, No. 7, p. 704, 706, 708, 710-711.

Laubach, S.E., Olson, J.E., and Gale, J.F.W., 2004, Are Open Fractures Necessarily Aligned with Maximum Horizontal Stress?, *Earth and Planetary Science Letters,* Vol. 222, p. 191-195.

Lawn, B.R., 1975, An Atomistic Model of Kinetic Crack Growth in Brittle Solids, *Journal of Materials Science,* Vol. 10, p. 469-480.

Lawn, B.R., and Wilshaw, T.R., 1975, *Fracture of Brittle Solids,* Cambridge University Press, p. 65-72.

Lee, S.H., Lough, M.F., and Jensen, C.L., 2001, Hierarchical Modeling of Flow in Naturally Fractured Formations with Multiple Length Scales, *Water Resources Research,* Vol. 37, p. 443-455.

Lee, M.K., and Farmer, I., 1993, *Fluid Flow in Discontinuous Rocks,* Chapman and Hall, London, 169 p.

Long, J.C.S., and Witherspoon, P.A., 1985, The Relationship of the Degree of Interconnection to Permeability in Fracture Networks, *Journal of Geophysical Research,* Vol. 90, No. B4, p. 3087-3098.

Long, J.C.S., and Billaux, D., 1987, From Field Data to Fracture Network Modeling: An Example Incorporating Spatial Structure, *Water Resources Research,* Vol. 23, No. 7, p. 1201-1216.

Long, J.C.S., Remer, J.S., Wilson, C.R. and Witherspoon, P.A., 1982, Porous Media Equivalents for Networks of Discontinuous Fractures, *Water Resources Research,* Vol. 18, No. 3, p. 645-658.

Long, J.C.S., Gilmour, P., and Witherspoon, P.A., 1985a, A Model for Steady Fluid Flow in Random Three-dimensional Networks of Disc-Shaped Fractures, *Water Resources Research,* Vol. 21, No. 8, p. 1105-1115.

Long, J.C.S., Endo, H.K., Karasaki, K., Pyrak, L., Maclean, P., and Witherspoon, P.A., 1985b, Hydrologic Behavior of Fracture Networks, paper presented at *Proceedings of the International Association of Hydrogeologists 17th International Congress,* International Association of Hydrogeologists, Tucson, Arizona, January 7-10.

Love, A.E.H., 1934, *A Treatise on the Mathematical Theory of Elasticity,* London, Cambridge University Press, 4th edition, p. 121-123.

Mann, H., 2000, Southern San Joaquin Basin Has Underexplored 'Complex Westside', *Oil & Gas Journal*, May 27th, p. 85-89.

Marrett, R., 1996, Aggregate Properties of Fracture Populations, *Journal of Structural Geology,* Vol. 18, Nos. 2/3, p. 169-178.

Marrett, R., 1997, Permeability, Porosity, and Shear-wave Anisotropy From Scaling of Open Fracture Populations, *Fractured Reservoirs: Characterization and Modeling Guidebook,* Editors: Hoak, T.E., Klawitter, A.L, and Blomquist, P.K., p. 217-226.

Marrett, R., Ortega, O.J., and Kelsey, C.M., 1999, Extent of Power-Law Scaling for Natural Fractures in Rock, *Geology,* September, Vol. 27, No. 9, p. 799-802.

Martin, R.J. III, 1972, Time-Dependent Crack Growth in Quartz and Its Application to the Creep of Rocks, *Journal of Geophysical Research,* Vol. 77, No. 8, p. 1406-1419.

Mattax, C.C., and Dalton, R.L., 1990, *Reservoir Simulation Monograph Volume 13,* Society of Petroleum Engineers, 184 p.

Mavor, M.J., and Cinco, H., 1979, Transient Pressure Behavior of Naturally Fractured Reservoirs, *Society of Petroleum Engineers,* California Regional Meeting, Ventura, CA, SPE 7977.

Mecholsky, J.J., 1981, Intergranular Slow Crack Growth in MgF_2, *Journal of the American Ceramic Society,* Vol. 64, No. 9, p. 563-566.

Meredith, P.G., and Atkinson, B.K., 1982, High-Temperature Tensile Crack Propagation in Quartz: Experimental Results and Application to Time-Dependent Earthquake Rupture, *Earthquake Prediction Research,* Vol. 1, No. 4, p. 377-391.

Meredith, P.G., and Atkinson, B.K., 1983, Stress Corrosion During Tensile Crack Propagation in Whin Sill Dolerite and Other Basic Rocks, *Geophysical Journal of the Royal Astronomical Society,* Vol. 75, p. 1-21.

Meredith, P.G., and Atkinson, B.K., 1985, Fracture Toughness and Subcritical Crack Growth During High-Temperature Tensile Deformation of Westerly Granite and Black Gabbro, *Physics of the Earth and Planetary Interiors,* Vol. 39, p. 33-51.

McQuillan, H., 1973, Small-Scale Fracture Density in Asmari Formation of Southwest Iran and Its Relation to Bed Thickness and Structural Setting, *American Association of Petroleum Geologists Bulletin,* Vol. 57, p. 2367-2385.

Michalske, T.A., Singh, M., and Frechette, V.D., 1981, Experimental Observation of Crack Velocity and Crack Front Shape Effects in Double-Torsion Fracture

Mechanics Tests, *Fracture Mechanics Methods for Ceramics, Rocks, and Concrete, ASTM STP 745,* Editors: Freiman, S.W., and Fuller, E.R., American society for Testing and Materials, p. 3-12.

Mindess, S., Nadeau, J.S., and Hay, J.M., 1974, Effects of Different Curing Conditions on Slow Crack Growth in Cement Paste, *Cement and Concrete Research,* Vol. 4, p. 953-965.

Moros, J.G., 1999, Relationship between Fracture Aperture and Length in Sedimentary Rocks, M.A. thesis, The University of Texas at Austin, Department of Geological Sciences.

Nakashima, T., Sato, K., Arihara, N., and Yazawa, N., 2000, Effective Permeability Estimation for Simulation of Naturally Fractured Reservoirs, *SPE 64286.*

Narr, W., 1996, Estimating Average Fracture Spacing in Subsurface Rock, *American Association of Petroleum Geologists Bulletin,* Vol. 80, No. 10, p. 1565-1586.

Narr, W., and Lerche, I., 1984, A Method for Estimating Subsurface Fracture Density in Core, *American Association of Petroleum Geologists Bulletin,* Vol. 66, p. 637-648.

Narr, W., and Suppe, J., 1991, Joint Spacing in Sedimentary Rocks, *Journal of Structural Geology*, Vol. 13, No. 9, p. 1037-1048.

National Research Council, 1996, *Rock Fractures and Fluid Flow, Contemporary Understanding and Applications,* National Academy Press, Washington, p. 332-351.

Navarette-Guijosa, W.P., Minnear, W.P., and Bradt, R.C., 1976, Effect of Grain Size on Subcritical Crack Growth in Alumina, *Presented at the American Ceramic Society Annual Meeting*, Cincinatti, Ohio, May 1-6.

Nelson, A., 1985, Geologic Analysis of Naturally Fractured Reservoirs, *Contributions in Petroleum Geology & Engineering*, Vol. 1, 320 *p.*

Nur, A., 1982, The Origin of Tensile Fracture Lineaments, *Journal of Structural Geology,* Vol. 4, No. 1, p. 31-40.

Olson, J.E., 1993, Joint Pattern Development: Effects of Subcritical Crack Growth and Mechanical Crack Interaction, *Journal of Geophysical Research*, Vol. 98, No. B7, p. 12251-12265.

Olson, J.E., 1997, Natural Fracture Pattern Characterization Using a Mechanically-Based Model Constrained By Geologic Data – Moving Closer to a Predictive Tool, *International Journal of Rock Mechanics and Mining Sciences & Geomechanics*

Abstracts, Vol. 34, No. 3-4, Presented at the 1997, 36th U.S. Rock Mechanics Symposium, New York, p. 391.

Olson, J.E., 2003, Sublinear Scaling of Fracture Aperture Versus Length: An Exception or the Rule?, *Journal of Geophysical Research,* Vol. 108, No. B9, p. 2413-2423.

Olson, J.E., 2004, Predicting Fracture Swarms – The Influence of Subcritical Crack Growth and the Crack-Tip Process Zone on Joint Spacing in Rock, *In: The Initiation, Propagation, and Arrest of Joints and Other Fractures,* Editors: Cosgrove, J.W., and Engelder, T., Geological Society, London, Special Publications, Vol. 231, p. 73-87.

Olson, J.E., and Pollard, D.D., 1989, Inferring Paleostresses from Natural Fracture Patterns: A New Method, *Geology,* Vol. 17, p. 345-348.

Olson, J.E., Qiu, Y., Holder, J., and Rijken, P., 2001, Constraining the Spatial Distribution of Fracture Networks in Naturally Fractured Reservoirs Using Fracture Mechanics and Core Measurements, *Society of Petroleum Engineers,* SPE 71342.

Ortega, O., and Marrett, R., 2000, Prediction of Macrofracture Properties Using Microfracture Information, Mesaverde Group Sandstones, San Juan Basin, New Mexico, *Journal of Structural Geology,* Vol. 22, No. 5, p. 571-588.

Panda, B.B, and Kulatilake, P.H.S.W., 1999, Effect of Joint Geometry and Transmissivity on Jointed Rock Hydraulics, *Journal of Engineering Mechanics,* Vol. 125, No. 1, p. 41-50.

Philip, Z. G., 2003, *Incorporating Subcritical Crack Growth Mechanics into Natural Fracture Characterization for Improved Reservoir Simulation*, Ph.D. thesis, The University of Texas at Austin, Department of Petroleum and Geosystems Engineering, 175 p.

Pickup, G.E., Jensen, J.L., Ringrose, P.S., and Sorbie, K.S., 1992, A Method for Calculating Permeability Tensors using Perturbed Boundary Conditions, *In: 3rd European Conference on the Mathematics of Oil Recovery,* Delft, The Netherlands, June.

Pletka, B.J., and Wiederhorn, S.M., 1978, Subcritical Crack Growth in Glass-Ceramics, *In: Fracture Mechanics of Ceramics,* Vol. 4, Editors: Bradt, R.C., Hasselman, D.P.H., and Lange, F.F., Plenum Press, New York, p. 745-759.

Pletka, B.J., Fuller, E.R. Jr., and Koepke, B.G., 1979, An Evaluation of Double-Torsion Testing – Experimental, *Fracture Mechanics Applied to Brittle Materials, ASTM STP 678,* Editor: Freiman, S.W., American Society for Testing and Materials, p. 19-37.

Pollard, D.D., and Segall, P., 1987, Theoretical Displacements and Stress, *Fracture Mechanics of Rock*, Editor: Atkinson, B.K., Academic Press Geology Series, Orlando, p. 277-350.

Pollard, D.D., and Aydin, A., 1988, Progress in Understanding Jointing over the Past Century, *Geological Society of America Bulletin,* Vol. 100, p. 1181-1204.

Pollard, D.D., Segall, P., and Delaney, P.T., 1982, Formation and Interpretation of Dilatant Echelon Cracks, *Geological Society of America Bulletin*, Vol. 93, p. 1291-1303.

Price, N.J., 1966, *Fault and Joint Development in Brittle and Semi-Brittle Rocks*, Pergamon Press, Oxford, 176 p.

Přikryl, R, 2001, Some Microstructural Aspecs of Strength Variation in Rocks, *International Journal of Rock Mechanics &Miniing Sciences*, Vol. 38, p. 671-682.

Qui, Y., 2002, *Natural Fracture Modeling and Characterization*, Ph.D. Thesis, The University of Texas at Austin, Department of Petroleum and Geosystems Engineering, 169 p.

Ravi-Chandar, K., 1998, Dynamic Fracture of Nominally Brittle Materials, *International Journal of Fracture*, Vol. 90, p. 83-102.

Ravi-Chandar, K., Knauss, W.G., 1984, An Experimental Investigation into Dynamic Fracture: II. Microstructrual Aspects, *International Journal of Fracture*, Vol. 26, p. 65-80.

Reinecker, J., Heidbach, O. and Mueller, B., 2003, *The 2003 release of the World Stress Map* (available online at www.world-stress-map.org).

Renard, Ph., and Marsily, G. de, 1997, Calculating Equivalent Permeability: a Review, *Advances in Water Resources,* Vol. 20, No. 5-6, p. 253-278.

Renshaw, C.E., 1996, Influence of Subcritical Fracture Growth on the Connectivity of Fracture Networks, *Water Resources Research,* Vol. 32, No. 6, p. 1519-1530.

Renshaw, C.E., 1997, Effect of Mechanical Interactions on the Scaling of Fracture Length and Aperture, *Nature,* Vol. 386, No. 6624, p. 482-484.

Renshaw, C.E., and Harvey, C.F., 1994, Propagation Velocity of a Natural Hydraulic Fracture in a Poroelastic Medium, *Journal of Geophysical Research,* Vol. 99, No. B11, p. 21667-21677.

Renshaw, C.E., and Park, J.C., 1997, Effect of Mechanical Interactions on the scaling of Fracture Length and Aperture, *Nature,* Vol. 386, p. 482-484.

Rice, R.W., Freiman, S.W., and Mecholsky, J.J. Jr., 1980, The Dependence of Strength-Controlling Fracture Energy on the Flaw-Size to Grain-Size Ratio, *Journal of the American Ceramic Society,* Vol. 63, No. 3-4, p. 129-136.

Rice, R.W., Freiman, S.W., and Becher, P.F., 1981, Grain-Size Dependence of Fracture Energy in Ceramics: I, Experiment, *Journal of the American Ceramic Society,* Vol. 64, No. 6, p. 345-350.

Rijken, P. and Cooke, M.L., 2001, Role of Shale Thickness on Vertical Connectivity of Fractures: Application of Crack-Bridging Theory to the Austin Chalk, Texas, *Tectonophysics*, Vol. 337, p. 117-133.

Rives, T., Razack, M., Petit, J.-P., and Rawnsley, K.D., 1992, Joint Spacing: Analogue and Numerical Simulations, *Journal of Structural Geology,* Vol. 14, No. 8/9, p. 925-937.

Rossmanith, H.P., 1983, *Rock Fracture Mechanics,* Springer-Verlag, 484 p.

Sageev, A., 1985, Decline Curve Analysis for Double-Porosity Systems, *Society of Petroleum Engineers,* SPE 13630, p. 435-446.

Sagy, A., Reches, Z., Roman, I, 2001, Dynamic Fracturing: Field and Experimental Observations, *Journal of Structural Geology,* Vol. 23, p. 1223-1239.

Sanderson, D.J., and Zhang, X., 1999, Critical Stress Localization of Flow Associated with Deformation of Well-Fractured Rock Masses, with Implications for Mineral Deposits, *In: Fractures, Fluid Flow and Mineralization,* Editors: McCaffrey, K.J.W., Lonergan, L., and Wilkinson, J.J., Published by the Geological Society, Special Publication, No. 155, p. 69-81.

Sano, O., and Ogino, S., 1980, Acoustic Emission During Slow Crack Growth, *Technical Report 2, Yamaguchi University*, Yamaguchi, Japan, p. 381-388.

Schardin, H., 1959, Velocity Effects in Fracture, *In: Fracture*, Editor: Averbach, B.L., MIT Press, Cambridge, MA, p. 297-330.

Scholz, C.H., 1972, Static Fatigue of Quartz, *Journal of Geophysical Research,* Vol. 77, No. 11, p. 2104-2114.

Schwartz, F.W., Smith, L., and Crowe, A.S., 1983, A Stochastic Analysis of Macroscopic Dispersion in Fractured Media, *Water Resources Research,* Vol. 19, No. 5, p. 1253-1265.

Segall, P., 1984, Rate-Dependent Extensional Deformation Resulting from Crack Growth in Rock, *Journal of Geophysical Research*, Vol. 89, No. B6, p. 4185-4195.

Segall, P., and Pollard, D.D., Joint Formation in Granitic Rock of the Sierra Nevada, *Geological Society of America Bulletin,* Vol. 94, p. 563-575.

Sharon, E., and Fineberg, J., 1996, Microbranching Instability and the Dynamic Fracture of Brittle Materials, *Physical Review*, Vol. 54, p. 7128-7139.

Sharon, E., and Fineberg, J., 1999, Confirming the Continuum Theory of Brittle Fracture for Fast Cracks, *Nature*, Vol. 397, p. 334-336.

Sharp, J.C., and Maini, Y.N.T., 1972, Fundamental Considerations on the Hydraulic Characteristics of Joints in Rocks, *Proceedings of the Symposium on Percolation through Fissured Rock,* Stuttgart, Germany, American Society of Mechanical Engineers, paper T1-F, 15 p.

Simmons, C.J., and Freiman, S.W., 1981, Effect of Corrosion Processes on Subcritical Crack Growth in Glass, *Journal of the American Ceramic Society,* Vol. 64, No. 11, p. 683-686.

Smith, L., and Schwartz, F.W., 1984, An Analysis of the Influence of Fracture Geometry on Mass Transport in Fractured Media, *Water Resources Research,* Vol. 20, No. 9, p. 1241-1252.

Snow, D.T., 1969, Anistropic Permeability of Fractured Media, *Water Resources Research*, Vol. 5, No. 6, p. 1273-1289.

Snow, D.T., 1970, The Frequency and Apertures of Fractures in Rock, *International Journal of Rock Mechanics and Mining Sciences,* Vol. 7, p. 23-40.

Stehfest, H., 1970, Numerical Inversion of LaPlace Transforms, *Communications of the ACM,* Vol. 13, No. 1, p. 47-49.

Stravrinidis, B., and Holloway, D.G., 1983, Crack Healing in Glass, *Physics and Chemistry of Glasses,* Vol. 24, No. 1, February, p. 19-25.

Sudicky, E.A., and McLaren, R.G., 1992, The Laplace Transform Galerkin Technique for Large-Scale Simulation of Mass Transport in Discretely Fractured Porous Formations, *Water Resources Research,* Vol. 28, No. 2, p. 499-514.

Swain, M.V., Williams, J.S., Lawn, B.R., and Beek, J.J.H., 1973, A Comparative Study of the Fracture of Various Silica Modifications Using the Hertzian Test, *Journal of Materials Science,* Vol. 8, p. 1153-1164.

Swanson, P.L., 1984, Subcritical Crack Growth and Other Time- and Environment-Dependent Behavior in Crustal Rocks, *Journal of Geophysical Research*, Vol. 89, No. B6, June 10, p. 4137-4152.

Taylor, P.C., and Tait, R.B., 1999, Effects of Fly Ash on Fatigue and Fracture Properties of Hardened Cement and Mortar, *Cement & Concrete Composites,* Vol. 21, p. 223-232.

Therrien, R., and Sudicky, E.A., 1996, Three-Dimensional Analysis of Variably-Saturated Flow and Solute Transport in Discretely-Fractured Porous Media, *Journal of Contaminant Hydrology,* Vol. 23, p. 1-44.

Vermilye, J.M., and Scholz, C.H., 1995, Relation Between Vein Length and Aperture, *Journal of Structural Geology,* Vol. 17, No. 3, p. 423-434.

Vosikovsky, O., Trudeau, L.P., and Rivard, A., 1980, Effect of Residual Stresses on Fatigue Crack Growth Threshold, *International Journal of Fracture,* Vol. 16, p. R187-190.

Wang, M., Kulatilake, P.H.S.W., Um, J., and Narvaiz, J., 2002, Estimation of REV Size and Three-Dimensional Hydraulic Conductivity Tensor For a Fractured Rock Mass through a Single Well Packer Test and Discrete Fracture Fluid Flow Modeling, *International Journal of Rock Mechanics & Mining Sciences*, Vol. 39, p. 887-904.

Warpinski, N.R., 1985, Measurement of Width and Pressure in a Propagating Hydraulic Fracture, *Society of Petroleum Engineers Journal*, SPE 11648, p. 46-56.

Warren, J.E., and Price, H.H., 1961, Flow in Heterogeneous Porous Media, *Society of Petroleum Engineering Journal,* Vol. 1, p. 153-169.

Warren, J.E., and Root, P.J., 1963, The Behavior of Naturally Fractured Reservoirs, *Society of Petroleum Engineers Journal*, SPE 426, p. 245-255.

Waza, T., Kurita, K., and Mizutani, H., 1980, The Effect of Water on Subcritical Crack Growth in Silicate Rocks, *Tectonophysics,* Vol. 67, p. 24-34.

Wels, C., and Smith, L., 1994, Retardation of Sorbing Solutes in Fractured Media, *Water Resources Research,* Vol. 30, No. 9, p. 2547-2563.

Wen, X-H, and Gómez-Hernández, J.J., 1996, Upscaling Hydraulic Conductivities in Heterogeneous Media: An Overview, *Journal of Hydrology,* Vol. 183, p. ix-xxxii.

White, C.D., 1987, *Representation of heterogeneity for numerical reservoir simulation,* Ph.D. Thesis, Stanford University, CA.

White, C.D., and Horne, R.N., 1987, Computing Absolute Transmissibility in the Presence of Fine Scale Heterogeneity, *Society of Petroleum Engineers,* SPE 16011, p. 209-220.

Wilkins, B.J.S., 1980, Slow Crack Growth and Delayed Failure of Granite, *International Journal of Rock Mechanics, Mining Science & Geomechanics Abstracts,* Vol. 17, p. 365-369.

Wiederhorn, S.M., 1967, Influence of Water Vapor on Crack Propagation in Soda-Lime Glass, *Journal of The American Ceramic Society,* Vol. 50, No. 8, p. 407-414.

Wiederhorn, S.M., and Bolz, L.H., 1970, Stress Corrosion and Static Fatigue of Glass, *Journal of the American Ceramic Society,* Vol. 53, No. 10, p. 543-548.

Wiederhorn, S.M., Fuller, E.R. Jr., and Thomson, R., 1980, Micromechanisms of Crack Growth in Ceramics and Glasses in Corrosive Environments, *Metal Science,* August-September, p. 450-458.

Wiederhorn, S.M., Freiman, S.W., Fuller, E.R. Jr., and Simmons, C.J., 1982, Effects of water and other dielectrics on crack growth, *Journal of Materials Science,* Vol. 17, p. 3460-3478.

Williams, D.P., and Evans, A.G., 1973, A Simple Method for Studying Slow Crack Growth, *Journal of Testing and Evaluation,* Vol. 1, No. 4, July, p. 264-270.

Wilson, C.R., and Witherspoon, P.A., 1974, Steady State Flow in Rigid Networks of Fractures, *Water Resources Research,* Vol. 10, No. 2, p. 328-335.

Winter, R.B., 1983, Bruchmechanische Gesteinuntersuchungen mit dem Bezug zu Hydraulischen Frac-Versuchen in Tiefbohrungen, *Berichte des Instituts für Geophysik der Ruhr-Universität Bochum,* Vol. 13, No. 13, 177 p.

Wu, C.Cm., Freiman, S.W., Rice, R.W., and Mecholsky, J.J., 1978, Microstructural Aspects of Crack Propagation in Ceramics, *Journal of Materials Science,* Vol. 13, p. 2659-2670.

Wu, H., and Pollard, D.D., 1995, An Experimental Study of the Relationship between Joint Spacing and Layer Thickness, *Journal of Structural Geology,* Vol. 17, p. 887-905.

Yaoguang, W., and Shengyan, L., 1982, Behavior of Slow-Propagation Cracks in Quartz Glass, *Journal of Non-Crystalline Solids,* Vol. 52, p. 377-383.

Zhang, X., and Sanderson, D.J., 2002, *Numerical Modeling and Analysis of Fluid Flow and Deformation of Fractured Rock Masses*, Pergamon, 288 p.

Zhang, X., Harkness, R.M., and Last, N.C., 1992, Evaluation of Connectivity Characteristics of Naturally Jointed Rock Masses, *Engineering Geology,* Vol. 33, p. 11-30.

Vita

Margaretha Catharina Maria Rijken was born in Oss, The Netherlands, on January 22nd, 1975. Her mother is Irene Rijken-van den Elzen and her father is Peter Rijken. Peggy started her M.Sc. degree in 1993 at the Department of Mining and Petroleum Engineering at the Technical University in Delft, The Netherlands. She specialized in engineering geology and received her M.Sc. in 1999. During her M.Sc., Peggy was an exchange student for 1.5 years in Madison, Wisconsin in the Geological Engineering department. In 2000, she started her Ph.D. at the University of Texas at Austin in the Petroleum and Geosystems Engineering department under supervision of Dr. J. E. Olson. During her time at the University of Texas at Austin, she worked as a summer hire for ChevronTexaco in Bakersfield, CA, and twice in Houston, TX. She also is the recipient of the 2003 Texas Excellence Teaching Award for Graduate Instructors in the College of Engineering.

Permanent address: Wijnruit 47
4907 HC, Oosterhout
The Netherlands

This dissertation was typed by the author.